


# Magnetic Resonance Imaging of Oxygen Nano-Carriers for the Treatment of Hypoxic Tumours

A thesis submitted for the degree of Doctor of Philosophy
January 2022

Emma Bluemke

Institute of Biomedical Engineering
University of Oxford

Supervisors: Prof Eleanor Stride, Prof Daniel Bulte



*To my family: past, present, and future.*

# Abstract

In cancer therapy, tumour hypoxia is an important predictor of disease progression, treatment outcomes, and metastatic potential. To date, methods for reducing tumour hypoxia have delivered limited success owing to either a lack of proven efficacy, unwanted side effects, or logistical limitations. Therefore, there remains an urgent requirement for an effective hypoxia reduction mechanism that is safe, cost effective, biocompatible, and easy to use. To address this, oxygen-filled micro and nanobubbles have been investigated as a method of oxygen delivery and have shown promising results in improving therapeutic response. To develop and optimise oxygen carriers and other hypoxia reduction strategies, however, consistent methods for measuring changes in tissue oxygenation need to be established. The ideal method should be noninvasive and quantitative, allowing tumour oxygen measurements to be obtained before, during, and after treatment. This thesis examines whether clinically available MRI techniques can be used to detect the change in tissue oxygenation caused by the nano-carriers.

A combination of phantom and preclinical experiments, mathematical modelling, and the analysis of data from two clinical trials are used. First, original results from phantom and preliminary in vivo MRI experiments are reported, which demonstrate the feasibility of detecting the effects of oxygen carriers. Second, three separate mathematical models are developed and presented in order of increasing complexity — first addressing simple bodily fluids, then blood, and finally, tissues — each of which are useful for areas of MRI research beyond the focus of this thesis. Third, original research results from recently completed clinical studies of oxygen-enhanced MRI are analysed and used to assess the viability of using these MRI measurements to monitor oxygen delivery from nanobubbles in a clinical MRI setting. Lastly, the broader potential applications of the conclusions and tools presented in this thesis are discussed.

# Acknowledgments

This research would not have been possible without the immense support of many people to whom I am very grateful. First, I would like to thank my excellent supervisors, Professor Eleanor Stride and Professor Daniel Bulte, for their guidance and support, and for making this project so much *fun*. Their ability to explain complex concepts has been extremely helpful for me, and I've learned more from observing their problem solving, creativity, and methodology than I could from any course or textbook. Thank you both for taking a chance on me for this project, I will always be grateful.

The experiments in this thesis required many collaborators, for whom I am very grateful. I am grateful to all of the BIOPIC and ART trial coauthors, especially Ambre Bertrand, Petra Ferencz, and Dr Ben George for help with the trial data, script debugging, and image registration. Thank you to Dr Estelle Beguin and Dr Joshua Owen, and Dr Luca Bau for teaching me how to manufacture the nanobubbles and use the equipment throughout the laboratory. A lot of the work performed by Dr Owen, Dr Beguin, and Elinor Thompson sits as the cornerstone for this project, and I thank them for their help and input throughout this project. The preclinical imaging expertise and assistance of Dr. Sean Smart and Dr Paul Kinchesh has been invaluable in these preclinical experiments. I would especially like to thank Dr Veerle Kersemans and Dr. Richard Browning for providing their expertise in preclinical models, growing and caring for the tumour model, helping run the imaging sessions, and taking the time to train me. Thank you to Jim Fisk and David Salisbury in the IBME workshop, who have always been available for the development and construction of various tools to enable this research along the way, and Liam Young for his collaboration on our phantom experiments. The ongoing chemistry knowledge and consulting provided by Dr Luca Bau has been invaluable for me, and I thank him for his patience, generosity with his time, and masterful MATLAB debugging abilities. I am very grateful to Dr Richard Sové for sharing his expertise and working with me to begin the oxygen diffusion modelling back in my first year: Richard, thank you for having the patience to teach me the concepts once again — although I used a different modelling approach and code in the end, your help allowed me to find the Goldman manuscript and figure out that different approach. Thank you to Dr Shamit Shrivastava for sharing his expertise and time to help Alexandra Vasilyeva and I perform the sonoluminescence experiments. I am greatly indebted for the help you have all provided.

Thank you to the communities that have made this experience so wonderful: the BUBBL group, the Bulte group, the ONBI-CDT, and the Clarendon community. I am immensely grateful to the Oxford-Nottingham Biomedical Imaging Centre for Doctoral Training and the Clarendon Scholarship Fund for making this opportunity possible.

I am also grateful to Professor Mark Jenksinon, Professor Steve Smith, Dr Ana Namburete, and the FMRIB community for making my CDT rotation project such a positive experience, and patiently teaching me so much about programming, modelling, and image analysis. I also thank Eoin Malins for the CDT teaching opportunities throughout my PhD, which have been an excellent experience.

This research was greatly improved by the scrupulous feedback of many anonymous reviewers, to whom I am incredibly grateful. In addition, much of this research depended heavily on open-source software packages that are thanklessly maintained by hardworking developers worldwide — thank you for your work, it is the backbone of much of modern science.

I also extend my sincere gratitude for the support and inspiration from my past academic mentors, Dr Arash Zarrine Afsar, Dr Jody Culham, and Dr Grace Parraga — thanks to the hands-on research experience opportunities you gave me, I was well prepared for this PhD and had an extremely positive and productive experience. I am also grateful for the Medical Biophysics Department at Western University, especially Dr Dwayne Jackson, Dr Charles McKenzie, Dr Aaron Ward, and Dr Abbas Samani — not only was the Medical Biophysics program fun and engaging, it prepared me very well for this PhD. I thank you all for your support and encouragement, you played a pivotal role in my educational journey.

This thesis is dedicated to my family, who have been the most supportive and loving team I could have ever asked for. Mum and Dad, my educational journey began decades before this PhD and I thank you all for always fostering a love for learning and encouraging this adventure. Thank you to my friends both in Oxford and abroad, and the Smiths: you have given me a home away from home — thank you. I will always be grateful for the support, encouragement, and humour from my partner Andy Smith, whose calm disposition and fun-loving approach to life has helped make these years so wonderful. I am grateful to Andy, Louie, and Scout for their wonderfully uplifting companionship while writing these many manuscripts and chapters in lockdown.

Lastly, Dan — thank you for responding to my cold email back in 2016. I simply would have never applied to the ONBI-CDT had it not been for your suggestion and encouragement, and for this I will always be grateful.

# Research Dissemination

## Peer-Reviewed Publications & Manuscripts In Progress

*The following chapters of this thesis contain material that has been disseminated in the following manuscripts:*

**Chapter 1**

1. **E Bluemke**, E Stride, D Bulte. A review of imaging methods for measuring tumour oxygen levels. *In preparation.*

**Chapter 2**

2. **E Bluemke**, L Young, J Owen, S Smart, P Kinchesh, D Bulte, E Stride. Determination of oxygen relaxivity in oxygen nanobubbles at 3 and 7 Tesla. *Magnetic Resonance Materials in Physics, Biology and Medicine (MAGMA), 2022. DOI:10.1007/s10334-022-01009-3*

**Chapter 4**

3. **E Bluemke,** E Stride, D Bulte. A simplified empirical model to estimate oxygen relaxivity at different magnetic fields. *NMR in Biomedicine, 2021. DOI:10.1002/nbm.4625*

**Chapter 5**

4. **E Bluemke,** E Stride, D Bulte. A general model to calculate the spin-lattice relaxation rate (R1) of blood, accounting for hematocrit, oxygen saturation, oxygen partial pressure, and magnetic field strength under hyperoxic conditions. *Journal of Magnetic Resonance Imaging (JMRI), 2021. DOI:10.1002/jmri.27938*

**Chapter 6**

5. **E Bluemke,** E Stride, D Bulte. Modelling the effect of hyperoxia on the spin-lattice relaxation rate R1 of tissues. *Magnetic Resonance in Medicine, 2022. DOI:10.1002/mrm.29315.*
6. **E Bluemke,** E Stride, D Bulte. The effect of oxygen on longitudinal relaxation: a review of oxygen-enhanced MRI. *In preparation.*

**Chapter 7**

7. **E Bluemke*,** D Bulte*, A Bertrand, B George, R Booke, K Chu, L Durrant, V Goh, C Jacobs, S Ng, V Strauss, M Hawkins, R Muirhead; Oxygen-Enhanced MRI MOLLI T1 Mapping during Chemoradiotherapy in Anal Squamous Cell Carcinoma. *Clinical and Translational Radiation Oncology, 2020. DOI:10.1016/j.ctro.2020.03.001*
8. **E Bluemke**, A Bertrand, K Chu, A Murchison, T Greenhalgh, B Burns, N Taylor, K Shah, F Gleeson, D Bulte. Using Variable Flip Angle (VFA) and Modified Look Locker Inversion Recovery (MOLLI) T1 Mapping in Clinical OE-MRI. *Magnetic Resonance Imaging, 2022. DOI:10.1016/j.mri.2022.03.001*
9. **E Bluemke**, A Bertrand, K Chu, A Murchison, T Greenhalgh, B Burns, N Taylor, K Shah, F Gleeson, D Bulte. Oxygen-enhanced MRI and radiotherapy in patients with oropharyngeal squamous cell carcinoma. *Under review.*
10. **E Bluemke**, D Bulte, A Bertrand, P Ferencz, B George, R Cooke, K Chu, L Durrant, V Goh, C Jacobs, SM Ng, VY Strauss, MA Hawkins, and R Muirhead. Oxygen-enhanced MRI and chemoradiotherapy in patients with anal squamous cell carcinoma. *In preparation.*

## Public Code Repositories

1. **OxygenRelaxivityModel:** A simplified empirical model to estimate oxygen relaxivity at different magnetic field strengths. *Open-source (MIT License) at GitHub.com/BulteGroup/OxygenRelaxivityModel*

2. **R1BloodModel:** A general model to calculate the spin-lattice relaxation rate (R1) of blood. *Open-source (MIT License) at GitHub.com/BulteGroup/R1BloodModel*

3. **TissueR1Model:** A general model to calculate the changes in spin-lattice relaxation rate (R1) of tissue in response to oxygen changes. *Open-source (MIT License) at GitHub.com/BulteGroup/TissueR1Model*

## Conferences

1. **E Bluemke,** E Stride, D Bulte. A general model to calculate the spin-lattice relaxation rate (R1) of blood, accounting for hematocrit, oxygen saturation, oxygen partial pressure, and magnetic field strength under hyperoxic conditions. **British Chapter of International Society for Magnetic Resonance in Medicine MR-Fest, 2021. Digital Poster.**
    - *1st Place Poster Award in "Body MR" Category*

2. **E Bluemke**, A Bertrand, K Chu, A Murchison, T Greenhalgh, B Burns, N Taylor, K Shah, F Gleeson, D Bulte. Using Variable Flip Angle (VFA) and Modified Look Locker Inversion Recovery (MOLLI) T1 Mapping in Clinical OE-MRI. **Presented at the International Society for Magnetic Resonance in Medicine (ISMRM), 2021. Digital Poster.**

3. **E Bluemke**, D Bulte, A Bertrand, B George, R Booke, K Chu, L Durrant, V Goh, C Jacobs, S Ng, V Strauss, M Hawkins, R Muirhead; Oxygen-Enhanced MOLLI T1 Mapping during Chemoradiotherapy in Anal Squamous Cell Carcinoma. **International Society for Magnetic Resonance in Medicine (ISMRM), Sydney (Virtual) 2020.**

4. **E Bluemke**, D Bulte, P Kinchesh, S Smart, E Stride. Magnetic Resonance Imaging of Oxygen Micro and Nanobubbles. **The 25th European Symposium on Ultrasound Contrast Imaging, Rotterdam 2020**.

5. **E Bluemke**, J Owen, E Thompson, P Kinchesh, S Smart, E Stride, D Bulte. Magnetic Resonance Imaging of Oxygen Carriers in Treatment of Hypoxic Tumours. **International Society for Magnetic Resonance in Medicine (ISMRM), Montreal 2019**.

6. **E Bluemke**, J Owen, E Thompson, P Kinchesh, S Smart, E Stride, D Bulte. Magnetic Resonance Imaging of Oxygen Nano-Carriers In Vitro and In Vivo. **Postgraduate British Chapter of ISMRM Symposium, Birmingham UK 2019**.
    - *1st Place Poster Award*
    - *2nd Place Best Power Pitch Award*

# Table of Contents

**Abbreviations and Definitions** ..... **5**
**Chapter 1. Thesis Introduction** ..... **6**
**1.1. Tumour Hypoxia and Therapy** ..... **7**
1.1.1. Hypoxia in Tumours ..... 7
1.1.2. Resistance to Therapy ..... 8
**1.2. Approaches for Mitigating Hypoxia** ..... **9**
1.2.1. Previous Approaches for Mitigating Hypoxia ..... 9
1.2.2. Oxygen Delivery Techniques ..... 10
1.2.3. Oxygen Nanobubbles for Therapy ..... 11
**1.3. Measuring Oxygen Delivery** ..... **12**
1.3.1. Current Challenges in Oxygen Measurement ..... 12
1.3.2. Oxygen Measurement Needed for Research and Clinic ..... 13
1.3.3. Oxygen in the Body ..... 14
**1.4. Non-Invasive Methods for Measuring Oxygen Delivery** ..... **16**
1.4.1. Positron Emission Tomography (PET) ..... 16
1.4.2. Photoacoustic/Optoacoustic Imaging ..... 18
1.4.3. Magnetic Resonance Imaging (MRI) ..... 18
1.4.3.1. MRI — T2*, R2*, and BOLD ..... 19
1.4.3.2. MRI — T1 and R1 of Water protons ..... 21
1.4.3.2.1. MRI — T1 Mapping Techniques ..... 23
1.4.3.3. MRI — Relaxivity of Lipid protons ('MOBILE' Method) ..... 24
1.4.3.4. MRI — DCE-MRI ..... 24
1.4.3.5. MRI — $^{19}$F-MRI Oximetry ..... 25
1.4.3.6. MRI — $^{17}$O-MRI Oximetry ..... 26
1.4.4. Electron Paramagnetic Resonance ..... 26
1.4.5. Measuring Oxygen from Nanobubble Delivery ..... 27
**1.5. Thesis Outline** ..... **29**
**Chapter 2. Oxygen Relaxivity in Nanobubbles** ..... **32**
**2.1. Introduction** ..... **33**
**2.2. Methods** ..... **34**
2.2.1. Phantom Design ..... 34
2.2.2. Nanobubble Preparation ..... 35
2.2.3. MRI Acquisition Details ..... 36
2.2.4. Oxygen Measurements ..... 37
2.2.5. Calculation of Limit of Detection ..... 37
**2.3. Results** ..... **38**
2.3.1. Oxygen Relaxivity ..... 38
2.3.2. Limit of Detection ..... 38

2.3.3. Nanobubbles and R1 ..... 39
**2.4. Discussion ..... 42**
2.4.1. Relaxivity ..... 42
2.4.2. Limit of Detection ..... 43
2.4.3. Additional Confounding Effects ..... 45
2.4.4. Experiment Limitations ..... 46
**2.5. Conclusion ..... 47**
**Chapter 3. Pre-Clinical Pilot Experiments ..... 48**
**3.1. Introduction ..... 49**
**3.2. Methods ..... 49**
3.2.1. Experiment Design ..... 49
3.2.2. MRI Acquisition Details ..... 52
**3.3. Results ..... 53**
3.3.1. Experiment 1 Results ..... 53
3.3.2. Experiment 2 Results ..... 54
3.3.3. Experiment 3 Results ..... 56
**3.4. Discussion ..... 58**
3.4.1. Experiments 1 & 2 ..... 59
3.4.2. Experiment 3, Repeatability, & Temperature ..... 59
3.4.3. Post-Experiment Troubleshooting ..... 60
**3.5. Conclusion ..... 64**
**Chapter 4. A Model of Oxygen Relaxivity in Bodily Fluids ..... 65**
**4.1. Introduction ..... 66**
**4.2. Methods ..... 67**
4.2.1. Model Theory ..... 67
4.2.2. Data Collection and Analysis ..... 70
**4.3. Results ..... 70**
**4.4. Discussion ..... 75**
4.4.1. Limitations ..... 76
4.4.2. Implications for Measurement of Nanobubble Oxygen Delivery ..... 77
**4.5. Conclusion ..... 80**
**Chapter 5. A Model of Blood R1 in Response to Hyperoxia ..... 81**
**5.1. Introduction ..... 82**
**5.2. Methods ..... 83**
5.2.1. Background Theory ..... 83
5.2.2. New Model ..... 85
5.2.3. Data Analysis ..... 88
5.2.4. Statistical Analysis ..... 89
**5.3. Results ..... 89**
5.3.1. Akaike Information Criterion ..... 89

5.3.2. Model Fitting ..... 90
5.3.3. Model Behaviour ..... 93
**5.4. Discussion ..... 98**
5.4.1. Limitations ..... 100
5.4.2. Implications for Measurement of Nanobubble Oxygen Delivery ..... 101
**5.5. Conclusion ..... 101**
**Chapter 6. A Model of Tissue R1 Response to Oxygen Delivery ..... 103**
**6.1. Introduction ..... 104**
**6.2. Theory and Methods ..... 105**
6.2.1. Model Background and Overview ..... 105
6.2.2. Step 1: Calculating $PO_2$ Along Capillary Length ..... 110
6.2.3. Step 2: Estimating ΔPO2 in the 3 Compartments ..... 111
6.2.3.1. Blood Compartments ..... 111
6.2.3.2. Tissue Compartment - Oxygen Diffusion ..... 111
6.2.3.3. Tissue Compartment - Oxygen Consumption ..... 112
6.2.3.4. Tissue Compartment - Estimating $R_t$ from Blood Volume ..... 113
6.2.3.5. Tissue Compartment - Estimating Oxygen Consumption ..... 114
6.2.4. Step 3. Calculating ΔR1 in the 3 Compartments ..... 116
6.2.4.1. Blood Compartments ..... 116
6.2.4.2. Tissue Compartment ..... 116
6.2.5. Step 4. Calculating Weighted Voxel ΔR1 ..... 116
6.2.6. Applying Model to Simulate ΔR1 from OE-MRI ..... 117
6.2.6.1. Model Variables and Constants ..... 117
6.2.6.2. Comparison with Empirical OE-MRI Results ..... 120
6.2.7. Applying Model to Simulate ΔR1 from Nanobubble Delivery ..... 121
**6.3. Results ..... 121**
6.3.1. Model Behaviour ..... 121
6.3.2. Applying Model to Simulate ΔR1 from OE-MRI ..... 122
6.3.3. Applying Model to Simulate ΔR1 from Nanobubble Delivery ..... 126
**6.4. Discussion ..... 126**
6.4.1. Model Design and Behaviour ..... 126
6.4.2. Applying Model to Simulate ΔR1 from OE-MRI ..... 128
6.4.3. Limitations ..... 128
6.4.4. Implications for Measurement of Nanobubble Oxygen Delivery ..... 130
6.4.5. Optional expansion: Inclusion of a Capillary Compartment ..... 131
**6.5. Conclusion ..... 132**
**Chapter 7. Conclusions, Clinical Translation, and Future Work ..... 133**
**7.1. Main Findings ..... 134**
**7.2. Clinical Translation ..... 136**
7.2.1. Background ..... 136

7.2.2. Discussion of Relevant Results ..... 138
7.2.3. Implications for Measurement of Nanobubble Oxygen Delivery ..... 141
**7.3. Future Work and Broader Applications ..... 141**
**7.4. Thesis Conclusion ..... 146**
**Appendices ..... 147**
**Appendix A ..... 147**
A.1. Figures ..... 147
A.2. Tables ..... 149
**Appendix B ..... 150**
B.1. Figures ..... 150
B.2. Tables ..... 155
**Appendix C ..... 159**
C.1. Figures ..... 159
C.2. Tables ..... 165
**Appendix D ..... 168**
D.1. Figures ..... 168
**Appendix E ..... 169**
E.1. Figures ..... 169
E.2 Tables ..... 171
**References ..... 177**

# Abbreviations and Definitions

| | |
|---|---|
| AIC | Akaike Information Criterion |
| B0 | Main magnetic field of MRI scanner |
| B1 | Radiofrequency field (perpendicular to the main magnetic field B0). |
| BV | Blood Volume |
| $CaO_2$ | Total blood oxygen content |
| CSF | Cerebrospinal fluid |
| Hb | Haemoglobin |
| Hct | Haematocrit |
| IR | Inversion Recovery |
| LOD | Limit of Detection |
| MOLLI | Modified Look-Locker Inversion Recovery |
| MSE | Mean Squared Error |
| NB | Nanobubble |
| OEF | Oxygen Extraction Fraction |
| OE-MRI | Oxygen-Enhanced Magnetic Resonance Imaging |
| P50 | Half-saturation $PO_2$ |
| $PO_2$ | Partial pressure of oxygen |
| R1 | Proton relaxation rate in $s^{-1}$ |
| r1 | R1 relaxivity of a contrast agent |
| $r1_{Ox}$ | R1 relaxivity of oxygen in $s^{-1}$/mmHg |
| R2* | Apparent transverse relaxation rate in $s^{-1}$ |
| ShMOLLI | Shortened Modified Look-Locker Inversion Recovery |
| $SO_2$ | Blood oxygen saturation |
| T1 | Proton longitudinal relaxation time in ms |
| T2 | Transverse relaxation time constant in ms |
| T2* | Apparent transverse relaxation time constant in ms |
| VFA | Variable Flip Angle |

# Chapter 1. Thesis Introduction

---

*This thesis aims to examine whether clinically available MRI techniques can be used to detect oxygen delivery from nanobubbles developed for the treatment of tumour hypoxia. In this chapter, the motivation of this thesis research is introduced by providing background information regarding the problem of tumour hypoxia and the development of oxygen carriers to aid tumour therapy. The challenge of measuring the oxygen delivery from these carriers is discussed, and a review of possible imaging-based methods that could be used to measure the oxygen delivery is provided. Lastly, the thesis outline is presented, highlighting the research objectives and the resulting significant original contributions to knowledge.*

*This chapter includes edited material from the following manuscript:*

- ***E Bluemke,*** *E Stride, D Bulte. A Review of Imaging Methods for Measuring Oxygen Delivery. In preparation.*

---

## 1.1. Tumour Hypoxia and Therapy

### 1.1.1. Hypoxia in Tumours

Tumour hypoxia is a predictor of disease progression, treatment failures, and metastatic potential in multiple types of cancer [1]–[4]. Hypoxia, typically defined as levels of the partial pressure of oxygen ($PO_2$) below 10 mmHg, arises in tumours due to defective or atypical vasculature in combination with rapidly proliferating cancer cells [5], [6]. The aggressive growth of the tumour cell population and over-expression of pro-angiogenic factors lead to the development of dysfunctional blood vessel networks, including chaotic vascular architecture, leakiness, and incomplete endothelial lining [7]. As the tumour cells continue to require oxygen to fulfil metabolic needs, some regions fail to receive enough oxygen. Although the tumour can recruit new blood vessels, these often form a dense network along the tumour periphery and fail to cover regions within the tumour core, leaving it hypoxic or necrotic [8], [9]. These hypoxic regions tend to be heterogeneously distributed throughout the tumour core [10], [11].

Hypoxia is dynamic, highly heterogeneous temporally and spatially, and influenced by many factors. It can be broadly classified as either chronic or acute (Figure 1.1). Diffusion-related or chronic hypoxia is a characteristic of cancer cells existing further away from blood vessels than the limit of oxygen diffusion (100 to 150 μm is approximately the diffusion distance of oxygen through respiring tissue [12]–[14]. However, hypoxia in tumours can also occur by a temporary obstruction or variable blood flow in the tumour vessels — this short term oxygen deprivation is known as perfusion-related, or acute, hypoxia, and the hypoxic-normoxic cycles can last several minutes to a few hours [15], [16]. These types of hypoxia are caused by separate phenomena, and this distinction is important as some hypoxia measurement techniques may be sensitive to one type but not the other.

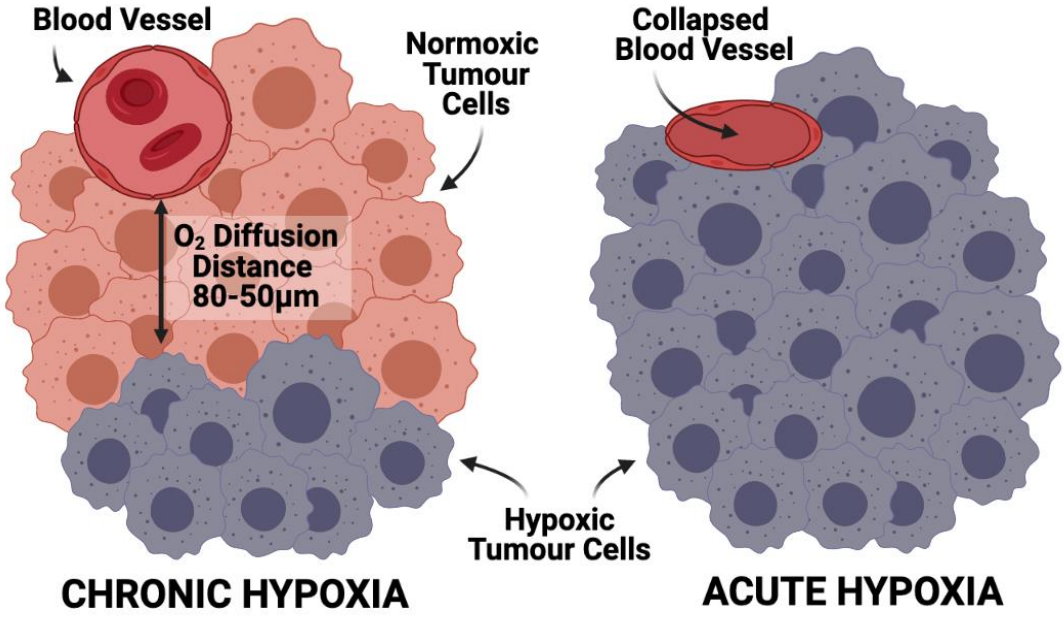


***Figure 1.1.*** *Hypoxia can be broadly classified as either chronic (left) or acute (right).*

### 1.1.2. Resistance to Therapy

Tumour cells existing in hypoxic environments have long been known to be resistant to therapy and display an aggressive phenotype [17]. Tumour hypoxia plays a pivotal role in malignant tumour progression [18], as the heterogeneous vasculature allows for the circulation and relocation of tumour cells to new and unaffected tissues to escape the hypoxic environment [7], [19], [20]. Cells under hypoxic conditions have been shown to be more resistant to photodynamic therapy, sonodynamic therapy, radiation therapy, and chemotherapy than fully oxygenated tissues [21], and this resistance has been attributed to the need for molecular oxygen to generate free radicals during treatment [11], [22]. Since the presence of oxygen is a key requirement for the generation of reactive oxygen species in sonodynamic therapy and photodynamic therapy, treating hypoxic tumours is a challenge [23], [24]. It is well established that providing oxygen to an excited sensitizer during photodynamic therapy can enhance the amount of reactive oxygen species generated, particularly under hypoxic conditions [23], [24]. In addition to the need for molecular oxygen, hypoxic cells are considered to be resistant to many anticancer drugs for several other

reasons, including that they are simply distant from blood vessels and as a result, do not receive adequate drug exposure [12], [18], [25], [26].

In radiation therapy, the hypoxic resistance to therapy is mainly the result of the physicochemical free radical reaction between the target of radiation damage (DNA) and oxygen. Radiation affects tumours by causing DNA damage in cells via both direct and indirect effects [27]. In the presence of oxygen, free radical attack can enhance the radiation-induced DNA damage by oxygen fixation. Radiation resistance is most pronounced at $PO_2$ levels below 20 mmHg, however it can be overcome almost instantaneously via localized oxygen delivery [12], [28]. Fortunately, well-established radiation sensitization curves have demonstrated that increasing the $PO_2$ from low hypoxic levels to just 20 mmHg can double or triple the relative radiosensitivity, making tumours nearly as sensitive to radiation therapy as healthy tissues [13]. In fact, a meta-analysis review of 10,000 patients showed that hypoxia modification in solid tumours undergoing radiotherapy leads to improved outcomes [17]. Due to these promising results of oxygen delivery improving therapy response, much research and attention has been focused on methods to increase the amount of oxygen in hypoxic tumours.

## 1.2. Approaches for Mitigating Hypoxia

### 1.2.1. Previous Approaches for Mitigating Hypoxia

Initial strategies for treating hypoxia focused on directly improving oxygenation through methods including blood transfusions and high oxygen content breathing, although more recently, hypoxia-selective drugs have been developed as well to mitigate or even exploit the effects of hypoxia [29]. The primary methods for oxygen delivery have generally focused on: hyperbaric oxygen or high oxygen content breathing therapy, oxygen-generating materials, and oxygen-carrying materials [30]–[32].

Administering blood transfusions to increase red blood cell count was practical and effective for treatment outcomes, but its use greatly declined in the 1980s since it was reliant

on supplies of donated blood [17], [33]. It was replaced by strategies such as erythropoietin therapy, which has been tentatively associated with a decrease in survival rather than improvement [34], [35]. In hyperbaric chamber therapy, due to the increased partial pressure, the amount of oxygen dissolved in plasma was shown to significantly increase independently of haemoglobin saturation [17]. However, these chambers were largely discontinued due to cases of oxygen poisoning, fires, and patient discomfort [36]. In high oxygen-content breathing, to mitigate the vasoconstriction caused by breathing 100% oxygen, 'carbogen' (95-8% $O_2$, 2-5% $CO_2$) is sometimes used as an alternative breathing gas. Carbogen effectively reduces chronic hypoxia but has little or no impact on acute hypoxia, but when used in combination with nicotinamide (to increase blood flow), the combination improves clinical outcomes [17]. However, clinical trials using nicotinamide have encountered considerable toxicities and some undesirable side effects [37]. Lastly, a drawback of oxygen-generating materials is that they might produce reactive oxygen species in concentrations that are cytotoxic to cells or induce local inflammation, release ions, and could cause hyperoxia [38]. To date, these approaches have delivered limited success owing to either a lack of proven efficacy, unwanted side effects, or logistical limitations [39], [40]. Therefore, in summary, there is still an urgent requirement for an oxygen source or delivery mechanism that is safe, effective, cost-effective, biocompatible, and easy to use in the clinic [25], [26], [41].

### 1.2.2. Oxygen Delivery Techniques

More recent approaches to hypoxia mitigation have taken advantage of developments in drug delivery systems to deliver oxygen to the tumour. Of these drug delivery approaches, therapeutic and diagnostic applications of nano and micro-materials are playing increasingly important roles [42]. Various types of synthetic nano and micro-particles, including liposomes and micelles, are being engineered to encapsulate or carry drugs [43]. By encapsulating the desired drug (such as a chemotherapy drug or oxygen), higher concentrations and improved stability can be achieved than via direct dissolution in a

fluid such as water [40]. Lipid-based nanoparticles and microparticles are often preferred for medical applications because of their biocompatibility and biodegradability [41]. Microbubbles, for example, have been used as contrast agents for ultrasound imaging for decades [44]. These nanoparticle/microparticle delivery systems are widely investigated pre-clinically and some formulations have already been introduced in clinical trials [45].

### 1.2.3. Oxygen Nanobubbles for Therapy

Oxygen-filled micro and nanobubbles (illustrated in Figure 1.2) have also specifically been investigated as a method of oxygen delivery [46]. Several groups have shown that microbubbles can be used to encapsulate oxygen, and have shown varied results on their efficacy at reducing hypoxia in vitro [47]–[51].

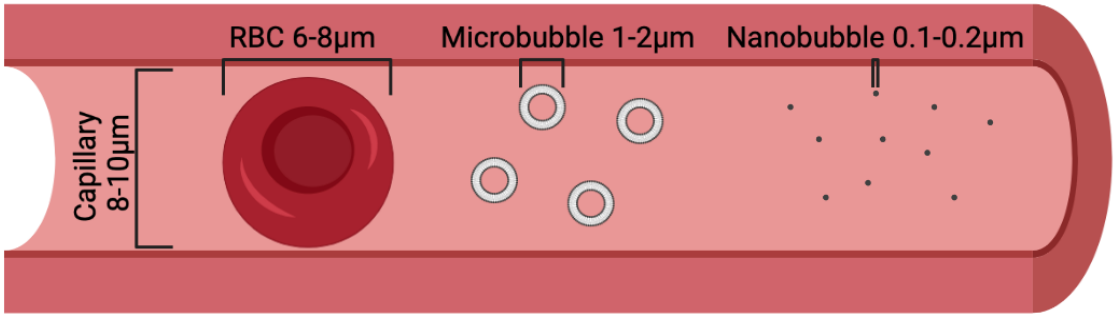


***Figure 1.2.*** *An illustration of the relative diameters of an average capillary, red blood cell, the therapeutic microbubbles used by McEwan et al. [49], and the therapeutic nanobubbles used by Owen et al. [40], [52].*

McEwan et al. have shown impressive results using microbubble-delivered oxygen for improving sonodynamic therapy in pancreatic tumours [49], Eisenbrey et al. successfully increased breast tumour oxygenation levels in vitro by 20 mmHg [53], [54], and Owen et al. demonstrated that oxygen nanobubbles enhanced tumour response to sonodynamic therapy [52]. These studies have illustrated the potential of oxygen loaded nano and microbubbles to deliver oxygen to the tumour microenvironment, reduce tumour hypoxia, and improve clinical outcomes, and no adverse side effects were observed.

## 1.3. Measuring Oxygen Delivery

### 1.3.1. Current Challenges in Oxygen Measurement

Although previous studies have illustrated the potential of oxygen loaded nano and microbubbles to improve clinical outcomes, *statistically significant* changes in *tumour oxygenation* were not always able to be detected [40], [49], [52], [53]. In each of these instances, the absence of oxygen detection was potentially due to the method used to measure the change in oxygenation.

For example, perhaps the technique lacks the spatial resolution required: Owen et al. [40] used a single fibre optic probe; however, tumours are highly heterogeneous and it is possible that some of the probes were placed in a poorly perfused area of the tumour. Alternatively, perhaps the technique measures the wrong type of oxygen, whether it be dissolved or bound to haemoglobin. For example, Eisenbrey et al. [53] were unable to detect any change in oxygenation using photoacoustic imaging — since the delivery of oxygen using micro and nanobubbles is independent of haemoglobin transport, photoacoustic imaging is not ideal to measure the changes in tissue oxygenation from micro and nanobubbles as it relies on comparing ratios of oxygenated and deoxygenated haemoglobin [55], [56]. Therefore, to continue effective research on promising oxygen carriers and hypoxia reduction, robust methods for measuring oxygen release from these carriers is needed.

In addition, traditional invasive methods of $PO_2$ measurement such as electrodes may not be an accurate gold-standard of true tissue oxygen levels. Weiner has argued that "classical concepts based on 'tissue $PO_2$' values derived from venous blood or oxygen electrodes inserted into tissue need re-evaluation": he explains that as an oxygen electrode moves slowly through a muscle, the observed $PO_2$ fluctuates widely from levels under 10 mmHg to typical capillary $PO_2$ values of 30 mmHg [57]. Weiner suggests that "although the value of greatest interest is the intracellular $PO_2$, many of our traditional oxygen

measurements include the capillaries, intracellular, and extracellular components that differ considerably in $PO_2$ [57].

### 1.3.2. Oxygen Measurement Needed for Research and Clinic

> *"Monitoring [tumour] oxygenation status is valuable, not just for better understanding of cancer physiology… but also for obtaining information on the status and behaviour of tumour node(s) in the clinical setting.*
>
> *To study tumour hypoxia,* ***simple and robust quantification of tissue oxygenation levels in vivo is necessary.****"*
>
> *American Association for Cancer Research, Sept 2019 [58]*

In addition to the need for tumour oxygen quantification for the research and development of hypoxia therapies, there is also a great need for tumour oxygen measurement in the clinic. For example, much research effort has focused on detecting which tumours are hypoxic and might need an increased dose or different therapy. If hypoxic regions of a tumour could be identified, mapped and/or quantified ahead of time, it would both aid in treatment planning and also in the ongoing research for therapies that mitigate or reduce hypoxia.

To both address this clinical need, and to study the effect of these oxygen carriers, methods can either measure the presence of oxygen (to confirm oxygen delivery) or the presence or absence of hypoxia. For example, some approaches to this problem detect hypoxia by measuring markers of the hypoxic environment (i.e. HIF-1 alpha) [59], or techniques that directly or indirectly measure anaerobic metabolism (i.e. pH and lactate). However, there are drawbacks to this approach: first, the detrimental effect that hypoxia has on therapy is not due to the presence of HIF-1 or lactate, but rather due to the fact that there was not enough oxygen present to create reactive oxygen species & DNA damage. In addition, the expression of these metabolic markers can also be triggered by factors other than hypoxia, including changes in pH [17]. Lastly, many treatments to reduce hypoxia focus on increasing the oxygen in the environment, rather than reducing any of these other factors — this temporary delivery of oxygen would not be detected by a metabolic marker.

Therefore, the ideal tool for hypoxia measurement would be able to quantitatively measure the $PO_2$ of oxygen in the tumour tissue, rather than indirectly inferring a state of hypoxia via other factors. If a technique could measure changes in $PO_2$ in tissue, it would enable researchers to properly measure the effectiveness of their hypoxia-reducing (or oxygen-delivering) therapy and develop the optimal therapy.

Typical methods to measure dissolved oxygen include electrochemical sensing and fibre optic-based sensing [26], [60], and the Eppendorf Histograph electrode system, which has been applied extensively in pre-clinical studies but is highly invasive, and technically challenging [2], [61]–[66]. A significant impediment to the clinical application of many of the hypoxia-detecting and oxygen-sensing approaches has been the invasive nature of probes or the need to use biopsy samples. To provide a non-invasive alternative, much research has focused on the development of hypoxia imaging markers for non-invasive detection methods that can determine spatial and temporal changes in oxygenation, such as PET, MRI, and CT imaging. Therefore, the ideal method for measuring oxygen in tissues would be non-invasive and quantitative, and would allow tumour $PO_2$ measurements to be obtained before, during, and after treatment. Because of this, it seems that non-invasive imaging approaches will lead the way for both clinical and research hypoxia measurements.

### 1.3.3. Oxygen in the Body

Since information about oxygenation status holds such importance for both medical care and research, a great variety of methods have been developed to measure oxygenation. While these techniques can differ in sensitivity, temporal and spatial resolution, penetration depth, and feasibility, what also makes it difficult to identify the ‘optimal’ technique is that these methods can measure different types of oxygen levels in the body — arterial oxygen versus tissue oxygen, haemoglobin saturation versus dissolved oxygen, and more. In addition, sometimes a technique *indirectly* measures the desired type of oxygenation — for example, although the desired measurement is the oxygenation status of

the tissue, this is sometimes inferred from changes in blood oxygenation. Therefore, deciding which is the 'best' technique depends on the desired use-case at hand.

In the use-case of tumour therapy, it is specifically the low amounts of oxygen in the tumour *tissue* that affects therapy — hence, tumour tissue oxygenation is the desired measurement. However, tumour tissue oxygenation can be broken down into the measurements of interstitial oxygen and intracellular oxygen. In addition, the oxygen reaches the tissues via diffusive transport from the oxygen concentrations in the bloodstream, so the blood oxygen concentrations — the arterial $PO_2$ ($PaO_2$), oxygen saturation ($SO_2$), and oxygen content ($CaO_2$) — can also give an indication of the levels of oxygen in the tissue (illustrated in Figure 1.3).

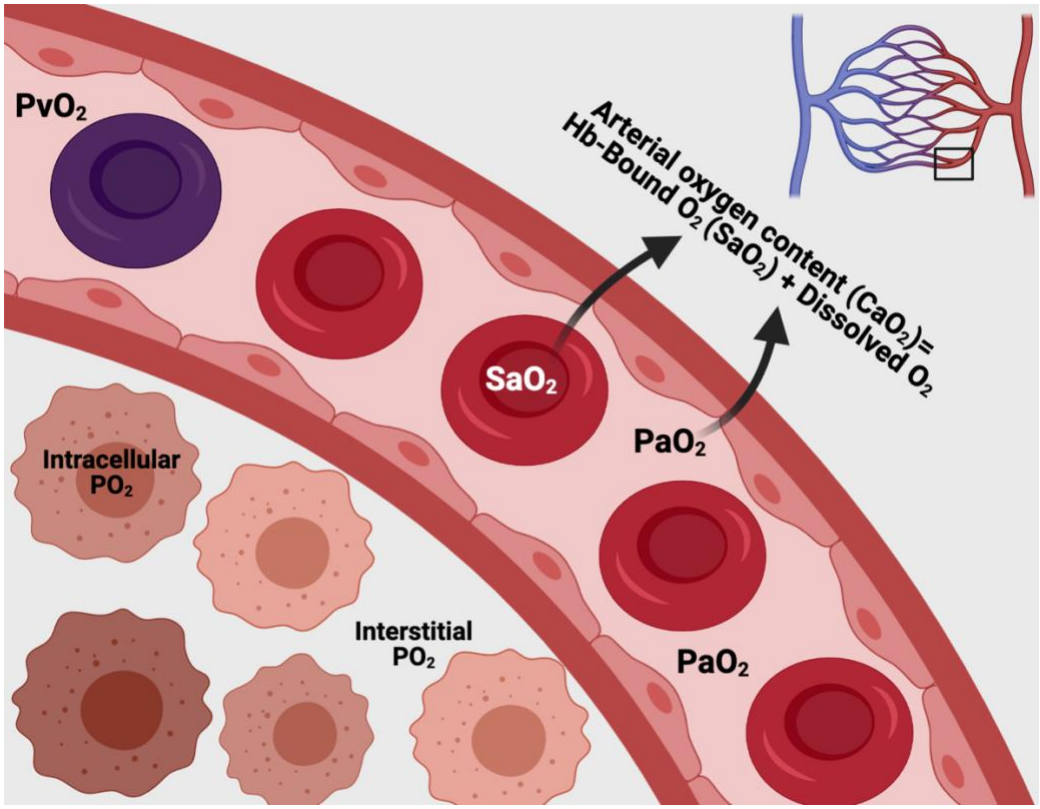


***Figure 1.3.*** *Oxygen in the body: oxygen can be dissolved in the tissues, either intracellularly or interstitially, or carried in the blood vessels as either unbound dissolved oxygen ($PaO_2$) or bound to haemoglobin in the red blood cells. The total oxygen content, $CaO_2$, can be calculated as the sum of the Hb-bound oxygen and dissolved unbound oxygen.*

The arterial $PO_2$ ($PaO_2$) and venous $PO_2$ ($PvO_2$) refers to the oxygen molecules dissolved in plasma — in other words, oxygen not bound to the haemoglobin in the red

blood cells. This distinction is important, since once oxygen is bound to haemoglobin, oxygen molecules can no longer be measured by certain methods, such as an electrode that senses dissolved oxygen molecules.

Most of the oxygen in our blood, however, is carried in the haemoglobin of the red blood cells. The percentage of haem-binding sites saturated with oxygen is described as the oxygen saturation, or $SO_2$. The relationship between $SO_2$ and $PO_2$ levels in the blood is described by equations for the oxygen dissociation curve, and the total oxygen content of the blood is therefore the sum of all bound and unbound (dissolved) oxygen carried in the blood. The arterial oxygen content ($CaO_2$) for example can be calculated by $CaO_2 = (O_2$ carried by Hb) + ($O_2$ in solution) = (1.34 x Hb x $SO_2$) + (0.003 x $PaO_2$), where $SO_2$ is in percent saturation (from 0-1), Hb is haemoglobin concentration in grams per 100 ml blood, and 0.003 is ml of $O_2$ dissolved per mmHg. Although a certain technique might only measure $SO_2$, other levels of oxygen can sometimes be inferred by using this relationship. The methods for measuring oxygen delivery discussed in this chapter will either directly or indirectly measure at least one of these forms of oxygen in the body, and this will be summarized in Table 1.1 at the end of this chapter.

## 1.4. Non-Invasive Methods for Measuring Oxygen Delivery

Due to the broad importance of hypoxia in the clinic, there is a vast body of research on hypoxia measurement and detection including all areas of the body, such as hypoxia caused by stroke or ischaemic heart disease [67]–[73]. This literature review section focuses on the most prevalent non-invasive imaging approaches to measuring oxygenation and/or hypoxia in *clinical tumour tissues* specifically and discusses the strengths and limitations of each method.

### 1.4.1. Positron Emission Tomography (PET)

The most widely established method for imaging hypoxia is with Positron Emission Tomography (PET). This is based on using hypoxia-specific radiotracers: $^{18}$F-MISO, $^{18}$F-

FAZA, $^{18}$F-FETNIM, $^{60}$CU-ATSM. It identifies hypoxic regions by the following method: inside cells, the radiotracer undergoes a succession of reduction steps [74]. In the presence of oxygen, the reduced nitroimidazole is quickly reoxidized and washed out from tissues — without oxygen, the reoxidation is slowed, and the compound is retained inside cells. Hence, the tracer is retained in low-oxygen — or hypoxic — tissues [69].

As opposed to specifically measuring oxygen, PET tracers identify regions of hypoxia. For example, the regions are not reported as a measure of $PO_2$, but instead as a ratio of mean tumour uptake compared to normoxic tissue (called tumour to background ratio) [69]. Imaging with PET hypoxia tracers is a promising hypoxia imaging method as it is widely established, specific to hypoxia, has a full-body penetration depth, and uses devices already in the clinical workflow. Note that the hypoxia is measured by the presence/absence of oxygen, rather than a specific hypoxia metabolite, which would make it hypothetically possible to confirm oxygen delivery with this technique. PET methods have the potential to be sensitive to both chronic and acute hypoxia, and in fact, may be able to be used to differentiate between chronic and acute hypoxia based on $^{18}$F-FMISO PET serial images [75]. However, in clinical studies using the $^{18}$F-FMISO tracer, it was not possible to correlate the hypoxia PET measurements with $PO_2$ measurements from Eppendorf electrodes in head and neck tumours [76].

Another drawback of imaging hypoxia with PET is time: the major limitation of hypoxia-PET is that image contrast develops slowly, and, therefore, scans can result in different tumour hypoxia rankings depending on the post-injection time scanned [74], [77].

Another type of PET radiotracer is $^{15}$O water, where injections of radioactive $^{15}$O have been used to measure oxygen extraction fraction (OEF) and myocardial flow [78]. Although the oxygen measurement is made from the $^{15}$O, this technique also requires inspired molecular oxygen (to measure OEF), and inspired carbon monoxide (to measure cerebral blood volume). However, since $^{15}$O is a short-lived radioisotope with an approximately 2-

minute half-life, it must be made on site using a cyclotron, and there are unfortunately few sites in the world capable of this type of PET measurement [79].

### 1.4.2. Photoacoustic/Optoacoustic Imaging

Photoacoustic imaging combines ultrasound and optical imaging techniques to non-invasively map $SO_2$ with excellent spatial resolution (0.1 mm spatial resolution) [58], [80]. This method exploits the difference in optical absorption of haemoglobin when it is oxygenated versus deoxygenated to quantify blood oxygen saturation. Photoacoustic imaging can also be combined with hypoxia-sensitive probes to image the tissue oxygenation [81]. In addition, photoacoustic imaging combined with gas challenge experiments may be a suitable method to differentiate chronic from acute hypoxic tumors [82]. Unfortunately, despite rapid advances to this technique, at the current time, it is only applicable up to cm depth which limits its use for clinical tumours. Moreover, it has limited applicability in the context of this thesis, since the delivery of oxygen using microbubbles is independent of haemoglobin transport. For example, Eisenbrey *et al.* were unable to detect any change in oxygenation using this method when trying to measure the changes in tissue oxygenation from microbubbles [53].

### 1.4.3. Magnetic Resonance Imaging (MRI)

The effect of oxygen on MR signals has been known and exploited for various purposes for decades [83]–[85]. Oxygen can affect the recovery of both magnetization in the x-y plane (known as spin-spin, or transverse relaxation) and along the z-axis (known as spin-lattice, or longitudinal relaxation) after a radiofrequency pulse [86]. The recovery of the longitudinal magnetization and the decay of the transverse relaxation is approximated by exponential functions with the decay constant ‘T1’ for longitudinal relaxation and ‘T2’ for transverse relaxation (Figure 1.4). In the body, oxygen affects MR signals mainly through two different mechanisms: a paramagnetic property of deoxyhaemoglobin and a paramagnetic property of molecular oxygen itself.

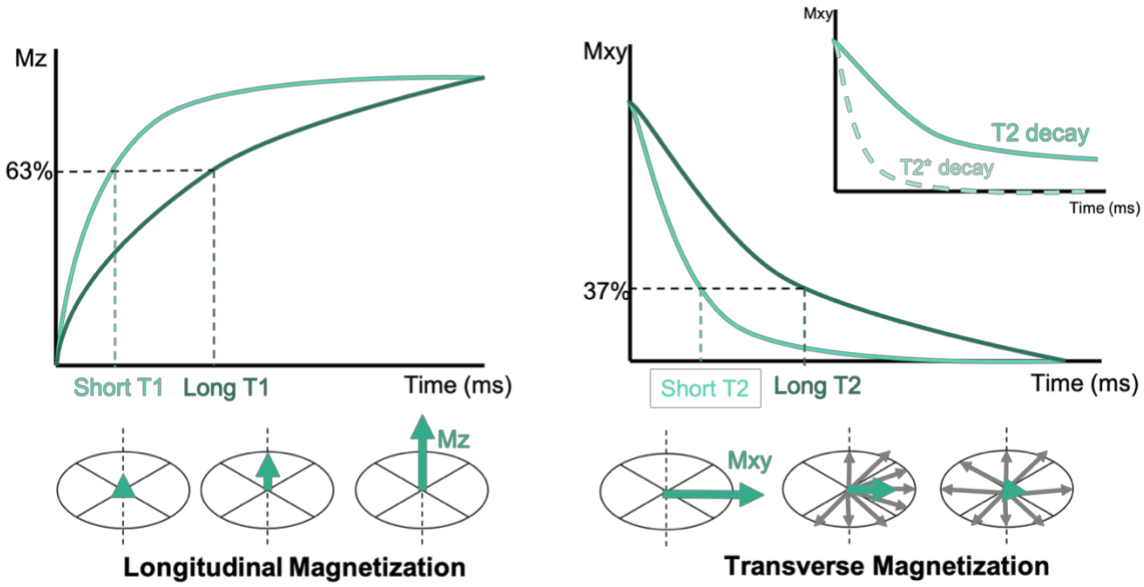


***Figure 1.4.*** *The recovery of the longitudinal magnetization and the decay of the transverse relaxation is approximated by exponential functions with the decay constant 'T1' for longitudinal relaxation and 'T2' for transverse relaxation. While T2 is the time constant, the transverse magnetization decays much faster than the "true" T2 mainly due to inhomogeneities in the magnetic field, and this rate is denoted T2* (top right corner).*

### *1.4.3.1. MRI — T2*, R2*, and BOLD*

Otherwise known as intrinsic susceptibility imaging or blood oxygenation level-dependent (BOLD) contrast, the T2* or R2* (1/T2*) contrast induced by changes in blood oxygen content is one of the most popular uses of oxygen contrast in MRI. While oxyhaemoglobin has no unpaired electrons, deoxyhaemoglobin has four unpaired electrons, making it strongly paramagnetic. This paramagnetism creates local magnetic field distortions in and around blood vessels, resulting in increased dephasing, causing a shortening of T2* — in other words, a drop in blood saturation (and therefore an increase in levels of deoxyhaemoglobin) will shorten T2*, or increase R2*. This T2*-shortening effect is the basis of BOLD contrast used in functional MRI [83], [84], and has been proposed as an imaging biomarker of tissue oxygenation status in preclinical and clinical studies [71], [87], [88].

Results of using tumour R2* and BOLD signal to infer oxygenation status are varied. While Chopra et al. reported that human prostate tumour R2* itself demonstrated a (non-

significant) trend with tumour $PO_2$ (at 1.5T), and Hoskin et al. reported that human prostate tumours with higher R2* (at 1.5T) were more likely to be hypoxic [89], [90], other experiments have confirmed that the initial T2* value did not reliably predict tumour oxygenation at the beginning of the experiment (at 4.7 T in mouse tumours) [91].

However, in addition to measuring initial R2* or T2*, several experiments measured *changes* in R2* or BOLD signal induced by changes in oxygenation by acquiring measurements while breathing air and then again breathing high percentages of oxygen, an experiment known as a 'hyperoxic challenge' (Figure 1.5). While some studies measure the BOLD signal intensity changes and some measure changes using quantitative T2* mapping, making it difficult to compare results across studies, the BOLD signal response and quantitative %ΔR2* response to hyperoxia *has* been shown to negatively correlate significantly ($R^2$=0.88) [92]. However, the *magnitude* of changes seen from the hyperoxic challenge is very variable: the hyperoxic challenge has been shown to decrease R2* on carbogen by -21.6% in preclinical tumours (at 4.7T) and -5-6% in human tumours (at 1.5T) [93]; in human intracranial tumours at 1.5T, some tumours showed a decrease in R2* some showed no change [94]; and 11 human head & neck tumours showed decreases in R2* ranging from 0-8% (at 1.5T) [95]. From the hyperoxic challenge with oxygen, the T2*-weighted signal changes ranged from -1 to +3.6%, and R2* has been shown to change by -1% in human tumours but -5% in uterus tissue (at 3T) [92]. As demonstrated by these experiments, ΔR2* may vary between experiments on high-field preclinical scanners in comparison to lower-field clinical scanners, since the relaxivity effect of deoxyhemoglobin on R2* is vastly stronger at 7T than 1.5T — Blockley et al. [96] measured a 200 $s^{-1}$ versus only 20 $s^{-1}$ ΔR2* for the same change in deoxyhemoglobin concentration, at 7T and 1.5T respectively. Furthermore, in addition to magnitude, the *direction* of signal change induced by hyperoxia has been variable as well, and while many studies have reported negative ΔR2* in response to hyperoxia, more recently there have also been reports of positive ΔR2* changes from hyperoxia [97].

While the BOLD signal change *has* been shown to *temporally* correlate with $PO_2$ changes, repeated studies have shown that the *magnitude* of BOLD changes do not correlate with quantitative $PO_2$ changes. For example, in an experiment by Baudelet et al, a given change in signal intensity corresponded to a 25 mmHg $PO_2$ change in one tumour, but to a 100 mmHg change in another [91], and Hoskin et al. have reported that BOLD changes did not correlate with tumour $PO_2$ levels [90]. Unfortunately, while R2* is definitely influenced by changing ratios of deoxy and oxyhaemoglobin, R2* signal change is also affected by alterations in blood flow, hematocrit, and vascular volume, once named the FLOOD effect [88], [98], and therefore BOLD has poor specificity for hypoxia [88], [91], [99], and would be an insufficient method to measure oxygen delivery from nanobubbles if used alone.

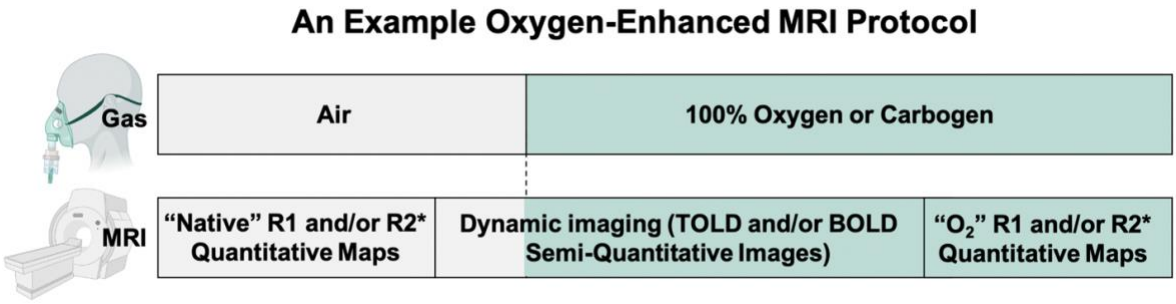


***Figure 1.5.*** *An example of an OE-MRI protocol. The gas used in the hyperoxic challenge is typically 100% oxygen or carbogen, and further measurements may be acquired as the patient returns to air breathing to capture the oxygen wash-out dynamics. A 'cyclic' gas challenge may repeat this gas protocol several times. Additional metrics such as blood flow, blood volume, and arterial blood oxygen levels may be required (during both air and oxygen states). Gadolinium DCE-MRI is sometimes also added to the end of the protocol to examine the vasculature in the tissue.*

### *1.4.3.2. MRI — T1 and R1 of Water protons*

The spin-lattice relaxation described by the relaxation time T1 or relaxation rate R1 (1/T1) occurs because of interactions between nuclear magnetic dipoles and the randomly fluctuating magnetic fields generated by the movement of molecules and nuclei in the nearby environment [86]. Consequently, the rate at which the spin magnetization recovers to its equilibrium state depends on the nearby environment, and the presence of paramagnetic moments nearby can greatly increase R1. Molecular oxygen, with two unpaired electrons in

the outermost molecular orbital, is paramagnetic, and acts as a paramagnetic relaxation agent to the surrounding nuclear spins [100], thus increasing R1.

It has been demonstrated experimentally repeatedly that the contribution of dissolved oxygen in water to R1 is linearly proportional to its concentration [85], [86], [101]. This linear, reproducible relationship between $PO_2$ and R1 has been used to infer oxygen levels in vitreous fluid as a non-invasive alternative to the highly invasive oxygen electrodes used to measure retinal hypoxia [102]–[105], bladder urine [105] and urine in the renal pelvis to create a non-invasive detection of renal dysfunction [106], cerebrospinal fluid [105], [107], brain tissue, and blood, including foetal blood [108]–[110]. The main limitation of using R1 to infer $PO_2$ is that the change in R1 is not specific to oxygen: R1 can be affected by the temperature, pH, and numerous other changes in the chemical environment. In addition, unless the specific $PO_2$-R1 relationship was measured in that material previously (with consistent temperature, MRI methods, etc.), the absolute oxygen levels cannot be inferred from R1, only a relative change in oxygenation. This technique will be covered in more detail throughout this thesis.

In addition to using the linear R1-$PO_2$ relationship to infer quantitative oxygen changes, the *presence or absence* of an R1 change — in combination with DCE-MRI and R2* changes — has been used to differentiate regions of hypoxia from healthy tissue. The hyperoxic challenge used in BOLD/R2* experiments is also commonly applied in studies measuring R1 changes — this technique is the basis of a developing hypoxia-biomarker technique called oxygen-enhanced MRI (OE-MRI), which aims to detect regions of hypoxia by distinguishing regions that do or do not exhibit R1 signal change in response to the hyperoxic breathing challenge. The changes in R1 induced during hyperoxia in the oxygen-enhanced MRI literature are the most analogous to the changes induced by increasing dissolved oxygen levels via nanobubble delivery, and therefore this body of literature will be consulted repeatedly throughout this thesis.

#### *1.4.3.2.1. MRI — T1 Mapping Techniques*

By obtaining a measurement of T1 at each voxel across an image, the resulting image is a quantitative map, rather than a qualitative T1-weighted image – this is called T1 mapping. The 'gold standard' method for T1 mapping is inversion recovery [111], but there are widely accepted alternative methods, such as the Look-Locker [112], Modified Look-Locker (MOLLI) [113], and Shortened Modified Look-Locker (ShMOLLI) variations [114], and Variable Flip Angle (VFA) methods [115]–[117]. Although there are a variety of T1 mapping techniques, the underlying principle remains the same: if the equations that relate T1 to the image signal intensity are known, we can acquire several images while tweaking one variable of that equation (such as the flip angle, inversion time, etc.), so that we obtain a variety of measurements of signal intensity for a variety of settings of that variable. We can then use the equations that describe the relationship between T1 and signal intensity to fit the acquired data and calculate T1, the unknown value. This fitting process is repeated across every voxel in the image, creating a 2D or 3D map of T1 values.

For example, to produce a T1 map from inversion recovery, the magnetization is first inverted with a 180° pulse, and then observed after a period of delay. This is repeated several times, each with a varied delay, allowing the signal to be recorded at several time points after inversion. Since the signal from each repetition ($S_n$) and various set waiting times ($t_n$) are known, the equation $S_n = a + be^{-tn/T1}$ can be fit to calculate T1.

The inversion recovery procedure requires several repetitions and waiting for each inversion time, so standard inversion recovery sequences can be incompatible with measuring effects arising from real-time oxygen delivery. However, some alternative methods greatly reduce the acquisition time required, offering a practical alternative for pre-clinical and clinical experiments [118]. For example, modified Look-Locker inversion recovery (MOLLI) pulse sequence [9] is standard for myocardial T1-mapping where much faster imaging is required. The Look-Locker variants take multiple readouts following an inversion and then merge images from 3 consecutive inversion-recovery experiments, allowing for a much shorter scan time [114], and short breath holds which are more easily achievable for patients.

Rather than altering the inversion times, the variable flip angle methods are based on two or more spoiled gradient echo sequences which are each acquired with different flip angles [115]. The equation $S_n = \frac{M_0(1-e^{\mathrm{TR}/T1})\sin\alpha_n}{1-\cos\alpha_n\, e^{-\mathrm{TR}/\mathrm{T1}}}$, which describes the signal in a spoiled gradient echo sequence, can be manipulated and reduced to the linear equation $\frac{S}{\sin\alpha} = E \ \frac{S}{\tan\alpha} + M_0(1-E)$. The T1 values can be calculated by a linear least-squares fit where $E = e^{-TR/T1}$ is the slope. The VFA method can be used to acquire 3D T1 maps in a faster timescale more compatible with measuring effects arising from oxygen delivery, so it is a suitable T1 mapping method for the aims of this research. Further strengths and weaknesses of each technique used in this thesis are discussed throughout this thesis, particularly in Chapter 7.

#### *1.4.3.3. MRI — Relaxivity of Lipid protons ('MOBILE' Method)*

In similar reasoning to using proton R1 to measure $PO_2$, since oxygen is 11 times more soluble in lipids than in water, it is also possible to measure tissue oxygenation using the R1 of the lipid proton peak rather than water protons [119]. This method has been called 'Mapping Oxygen By Imaging Lipids Relaxation Enhancement (MOBILE)" [120], and has been examined for mapping $PO_2$ in liver, muscles, brain, mammary tumours [69], and hypoxia in stroke areas [121].

While the ability of MOBILE method to quantitatively map $PO_2$ has been demonstrated on mammary tumour models with a high lipid content, a major drawback is that the method was not applicable to tumours with low lipid content [122]. To address this, an alternative MOBILE method based on the deconvolution of global T1 in fat and water components was developed, however, the lipid R1 only weakly correlated with the quantitative measurements of $PO_2$ [123].

#### *1.4.3.4. MRI — DCE-MRI*

Dynamic contrast-enhanced MRI uses the acquisition of T1-weighted images in combination with gadolinium-based contrast agents to visualize the injection dynamics and

image the tissue vasculature. The presence of gadolinium increases the R1 in that voxel, resulting in a change in T1-weighted signal [124]. The Tofts model [125] is commonly used to extract a variety of parameters, the most common being $K^{trans}$, $v_e$, $v_p$, and $k_{ep}$. $K^{trans}$ represents the volume transfer constant of the contrast agent between the blood plasma and the extravascular extracellular space, which is assumed to be proportional to tumour blood perfusion [126]. $V_p$ is the blood plasma volume per unit volume of tissue; ve is the distribution volume of the contrast agent per unit volume of tissue; and $k_{ep}=K^{trans}/v_e$, or the rate constant of the contrast agent between the extravascular extracellular space and the blood plasma [126]. Ultimately, none of these parameters measure oxygen; however by the assumption that low-perfused tumour regions suffer from an insufficient supply of oxygen and are therefore hypoxic, DCE-MRI parameters are very indirect estimates of hypoxia [71].

It is important to note that in the case of additional oxygen delivery to the tumour, the presence of increased oxygen would not be detected by these measures, therefore DCE-MRI is unsuitable for the purpose of oxygen delivery measurement. However, DCE-MRI *has* been very useful for distinguishing perfused tissue from non-perfused tissue to aid the interpretation of signal changes from other methods such as oxygen-induced changes in R1 and R2*, where tissues can be distinguished by regions that *are* perfused (by DCE measures) but do or do not show oxygen enhancement (known as Perfused Oxy-E and Perfused Oxy-R, respectively, which will be discussed further in Chapter 6).

#### *1.4.3.5. MRI — $^{19}$F-MRI Oximetry*

In similar reasoning to using proton R1 to measure $PO_2$, $^{19}$F-MRI takes advantage of the linear relationship between R1 of $^{19}$F and $PO_2$. Although this method requires an injection of a fluorinated substance, the linear relationship between $^{19}$F R1 and $PO_2$ has a slope of 0.0016 $s^{-1}$/mmHg, which is an order of magnitude greater than that of water proton R1 [127]. $^{19}$F-MRI oximetry is capable of directly measuring the $PO_2$ of the tissue [127], and these $PO_2$ measurements have been validated by direct comparison to multiple polarographic electrode measurements [127], [128].

Unfortunately, intravenous injection of the PFC tracer is largely sequestered by the liver and spleen [129], resulting in levels of $^{19}F$ that are too low to provide an adequate signal to noise ratio for measurement, especially in poorly vascularized regions where the PFC does not reach [127]. While direct injection of the PFC into the tumour can solve this SNR issue, direct tumour injection is an inconvenient requirement for the measurement of tumour oxygen levels in real patients.

#### *1.4.3.6. MRI — $^{17}$O-MRI Oximetry*

Another type of magnetic resonance imaging uses the non-radioactive isotope oxygen-17, which can be administered as an enriched gas [130]. When $^{17}O$-enriched oxygen gas is administered to a patient or subject, $^{17}O$ does not affect the MR signal intensity until it is converted to $^{17}O$-enriched water as the final step in oxygen metabolism [131]. When $^{17}O_2$ combines with hydrogen as $^{17}O$-enriched water, it is then detectable to the MRI and leads to a corresponding change in signal intensity [132].

Similar to the experimental design for the hyperoxic gas challenge, $^{17}O$ imaging is performed while the subject is breathing room air as a baseline, inhaling $^{17}O$-enriched oxygen gas for a fixed period, and then breathing room air again during a washout period [133]. Although $^{17}O$-enriched gas would be safe for human applications [130], $^{17}O$-enriched gas is currently very expensive, which likely has limited its uptake in the clinical MR research community.

### 1.4.4. Electron Paramagnetic Resonance

Once again, in a similar reasoning to using proton R1 to measure $PO_2$, Electron paramagnetic resonance (EPR) oximetry takes advantage of the linear relationship between relaxation rates and $PO_2$. However, instead of measuring the relaxation of water or lipid protons like in MRI, EPR imaging measures unpaired electron spins [134], [135]. While molecular oxygen has two unpaired electrons, their relaxation is too fast to directly measure, so instead, an oxygen spin probe is used. An oxygen spin probe is a molecule injected into

the subject that contains a relatively stable unpaired electron that interacts with the two unpaired electrons of oxygen molecules [134], [136], [137]. The EPR imager can detect the relaxation rates of the spin probes, and there is a linear relationship between the relaxation rate of the spin probe and dissolved oxygen levels [135], [137]–[140]. The EPR measurements can also be influenced by the probe concentration, however this issue was successfully addressed by Epel et al. [138].

EPR is a very promising technique with great spatial resolution, and has shown potential for distinguishing chronic hypoxia from acute hypoxia [141]. However, to be able to use this method in humans, there is still much research needed on (1) technical development in order to image at depths needed for humans, and (2) research on the toxicity and safety of the spin probe in human subjects [135].

### 1.4.5. Measuring Oxygen from Nanobubble Delivery

The key points of each oxygen measurement method discussed in this chapter are summarized in Table 1.1. As the aim of this thesis is specifically measuring oxygen from nanobubble delivery in both preclinical and clinical settings, the ideal method would be easy to fit into the clinical workflow and be able to acquire measurements at the depth needed for clinical tumours noninvasively. Specifically, the ability to detect a change in dissolved oxygen levels in the tumour tissues, either directly or indirectly, is required. The imaging method needs to be able to acquire measurements within the nanobubble peak delivery time, which could be in the range of 10-30 minutes. In addition, for ease of use in potential clinical trials, it is preferable to use an imaging method that requires sequences already installed on hospital scanners and requires no additional tracers or equipment.

For these reasons, this thesis has focused on proton MRI methods, specifically investigating the use of the reported linear relationship between R1 and $PO_2$ for the direct measurement of dissolved oxygen in tumour tissues.

***Table 1.1.*** *A summary of the key points of each oxygen measurement method discussed in this chapter.*

| Technique | Temporal resolution | Tracer or Contrast Agent Needed? | Spatial resolution | Measurement | Depth | Clinical compat-ibility |
|---|---|---|---|---|---|---|
| **Photoacoustic Imaging** | Real-time, or seconds to minutes | Sometimes | 0.1mm | Quantifying ratio of oxyHb to deoxyHb, i.e. $SO_2$ changes | Shallow - up to cm depth | Not yet ready |
| **PET** | Slow (waiting for tracer uptake) | Yes, tracer injection | 2.36mm for clinical, 0.83mm for preclinical (Moses, 2011) | Tumour-to-background ratio of hypoxia tracer uptake (unitless) - hypoxia measured by presence of oxygen | Whole body | Good |
| **MRI T2*** | Seconds | No | Approx. 1mm | Detecting $SO_2$ changes as changes in R2* ($s^{-1}$) | Whole body | Good |
| **MRI T1 Water** | Seconds to minutes | No | Approx. 1mm | Detecting dissolved O2 changes as changes in water proton R1 ($s^{-1}$) | Whole body | Good |
| **MRI T1 Lipids** | Seconds to minutes | No | Approx. 1mm | Detecting dissolved O2 changes as changes in lipid proton R1 ($s^{-1}$) | Whole body | Good |
| **$^{19}$F-MRI Oximetry** | Seconds to minutes | Yes, $^{19}$F injection | Approx. 1mm | Detecting dissolved $O_2$ changes as changes in $^{19}$F proton R1 ($s^{-1}$) from an $^{19}$F injection | Whole body | Concen-trations too low |
| **$^{17}$O MRI** | Need tracer to be metabolised | Yes, $^{17}$O-water | Approx. 1mm | Presence of $^{17}$O after being metabolised into $^{17}$O-water changes the MR signal intensity | Whole body | Expensive |
| **EPR** | 5-10minutes | Yes, spin probe injection | 0.3mm | Measures the relaxation rates of the unpaired electrons on 'spin probes' which change in the presence of oxygen | 5-10cm depth | Not yet ready |
| **What is needed for measuring oxygen from nanobubble delivery?** | *Real time, seconds, or a few minutes is ideal. Delivery peak is 10-20 mins.* | *Ideally no tracer needed* | *Ideally enough to see tumour heterogeneit y in the delivery* | *Need to detect a change in dissolved oxygen levels in the tumour tissues, directly or indirectly* | *Whole body depth needed for clinical tumours* | *Easy fit into clinical workflow necessary* |

## 1.5. Thesis Outline

In summary, oxygen-filled micro and nanobubbles have been investigated as a method of oxygen delivery and have shown promising results at improving therapy response [40], [52]. To continue research of oxygen carriers and hypoxia reduction, consistent methods for measuring changes in tissue oxygenation should be established. The ideal method should be non-invasive and quantitative, allowing tumour oxygen measurements to be obtained before, during, and after treatment. Since MRI is a widely clinically available, non-ionizing, non-invasive imaging technique, it is ideal for determining tissue oxygenation noninvasively. **This thesis aims to examine whether clinically available MRI techniques can be used to detect the change in oxygen caused by the nano-carriers.**

To answer this question, this thesis has used a combination of phantom and preclinical experiments, mathematical modelling, and the analysis of data from two clinical trials.

In **Chapter 2**, the relationship between oxygen and R1 in phantoms and fluids is discussed. The first step in answering this thesis question is to establish the limit of detection of oxygen via our MRI methods, so towards this aim, original results from two phantom MRI experiments measuring the limit of detection in oxygen nanobubble solutions at 3T and 7T are presented. The contributions to knowledge are (1) applying a known technique to a new area and (2) generating a new and original observation, as the limit of detection of oxygen in this nanobubble solution using MRI has not previously been measured or examined.

In **Chapter 3**, the results from three preclinical MRI experiments that aimed to assess whether changes in R1 could be detected from an oxygen nanobubble injection are reported. The contribution to knowledge is generating new observations or results, as this experiment has not previously been performed. Factors such as repeatability, temperature sensitivity, and possible confounds are examined, leading to the conclusion that modelling the expected signal change would be beneficial. The resulting modelling is presented as 3

bodies of work in order of increasing complexity, first modelling the response in simple bodily fluids (**Chapter 4**), then blood (**Chapter 5**), and finally tissues in **Chapter 6**.

In **Chapter 4**, a simplified model for estimating the $r1_{Ox}$ in water, saline, plasma, and vitreous fluids with respect to magnetic field strength and temperature is presented that agrees well with the empirical measurements. The main contribution to knowledge is generating a new and original tool.

**Chapter 5** addresses why this assumption of a linear relationship between oxygen and R1 falls short when experimenting with one of the most important fluids: blood. A general model to estimate the R1 of blood, accounting for haematocrit, oxygen saturation ($SO_2$), the partial pressure of oxygen ($PO_2$), and magnetic field strength, under both normal physiological and hyperoxic conditions, and adjustable for different species is presented. This work builds upon a previous model, and both improves the accuracy of the R1 estimates within the valid range of the previous model and extends its range of validity to include hyperoxic conditions. This model also addresses the request made as 'future work' made in a *Journal of Magnetic Resonance Imaging* June 2020 Editorial [142], stating that "future work could expand the interpretation of the T1 and T2* changes using quantitative models relating total blood oxygen content, $PO_2$ and $SO_2$ to the MRI measures." The results from this model quantify and explain some contradictory R1 changes reported in recent experiments and allow visualizations of the expected R1 changes arising from the relevant factors. The contributions to knowledge are: (1) moving a model or method to a new location, and (2) finding new evidence that sheds light on a current issue, since this model quantitatively clarifies the negative R1 change in blood discussed papers as recently as 2020, where Vatnehol et al. experimented with measure $PO_2$ in blood vessels from an oxygen delivery drink [143].

In **Chapter 6**, a general model to calculate the change in R1 from changes in $PO_2$ is presented. This work expands upon the Chapters 4 and 5 models to contain a tissue

compartment to examine the effect of the gas challenge or nanobubble delivery on R1. Previously reported tissue R1 responses to the gas challenge are discussed and compared to the model estimates. The contributions to knowledge are: (1) generating a new and original observation or result, as to my knowledge, this is the first time quantifying the expected R1 change from micro or nanobubble oxygen delivery; (2) finding new evidence that sheds light on an old issue, since this model quantitatively clarifies the 'contradictory' tissue OE-MRI effect discussed in papers as recent as 2019 [144]; and (3) moving a model or method to a new location, i.e. expanding further on the Chapters 4 and 5 models to be applicable to tissues.

In **Chapter 7**, the major findings from each chapter of this thesis are summarised. Ultimately, successful clinical translation is the end goal for the therapeutic nanobubbles discussed in this thesis. Although it was not possible to perform clinical experiments with nanobubble delivery within the scope of this thesis, the most relevant adjacent research area is clinical OE-MRI, and it was possible to analyse the results from two recently completed clinical OE-MRI studies to shed light on several elements that would be relevant to using this method in a clinical experiment involving nanobubbles, such as the benefits and drawbacks of a chosen T1 mapping method, vulnerability to patient motion, and potential image artefacts. Therefore, in **Chapter 7**, these original research results are used to draw conclusions about the feasibility of using R1 measurements to monitor oxygen delivery from nanobubbles in a clinical MRI setting. Lastly, the broader potential applications of the work produced for this thesis is discussed.

Altogether, using phantom and preclinical experiments, mathematical modelling, and the analysis of data from two clinical trials, this thesis aims to answer the question of whether the delivery of oxygen from the nanobubbles can be detected reliably using clinically available MRI techniques.

# Chapter 2. Oxygen Relaxivity in Nanobubbles

---

*To address the question of whether the change in oxygen caused by the nano-carriers can be detected using clinically available MRI techniques, a first step was to establish the limit of detection of oxygen via the available MRI methods. Towards this aim, this chapter contains original results from two phantom MRI experiments measuring the relaxivity and limit of detection in oxygen nanobubble solutions at 3T and 7T.*

*This chapter includes edited material from the following publication:*

- ***E Bluemke**, L Young, J Owen, S Smart, P Kinchesh, D Bulte, E Stride. Determination of oxygen relaxivity in oxygen nanobubbles at 3 and 7 Tesla. Magnetic Resonance Materials in Physics, Biology and Medicine (MAGMA), 2022. DOI:10.1007/s10334-022-01009-3*

*A subset of these results was presented at the following conferences:*

- ***E Bluemke,** D Bulte, P Kinchesh, S Smart, E Stride. Magnetic Resonance Imaging of Oxygen Micro and Nanobubbles. The 25th European Symposium on Ultrasound Contrast Imaging, Rotterdam Netherlands 2020.*
- ***E Bluemke,** J Owen, E Thompson, P Kinchesh, S Smart, E Stride, D Bulte. Magnetic Resonance Imaging of Oxygen Carriers in Treatment of Hypoxic Tumours. International Society for Magnetic Resonance in Medicine (ISMRM), Montreal Canada 2019.*

---

## 2.1. Introduction

Molecular oxygen is paramagnetic [86], [101], [145]–[150], and it has been demonstrated experimentally repeatedly that the relaxation rate of the imaged material, R1, is linearly proportional to the concentration or partial pressure of oxygen ($PO_2$) [100]–[104], [107], [108], [151]–[156]:

$$R1_{ox} = R1_0 + r1_{Ox} * C \quad \text{(Eq 2.1)}$$

where $R1_{Ox}$ is the relaxation rate with oxygen added, $R1_0$ is the relaxation rate without oxygen, C is the concentration or partial pressure of oxygen, and $r1_{Ox}$ is the relaxivity of oxygen in the imaged material (whose units depend on the oxygen measurement used for C). Since $PO_2$ is a common measurement in biomedicine and clinical applications, in this thesis, C is reported as $PO_2$ in mmHg and $r1_{Ox}$ as $s^{-1}$/mmHg. Conversion factors to other common units such as kPa, Torr, mmol/L, mg/L, and mL/L can be found in Appendix Table A.1.

This linear, reproducible relationship between $PO_2$ and R1 has been used to infer oxygen levels in several bodily fluids and tissues: (1) vitreous fluid as a non-invasive alternative to the highly invasive oxygen electrodes used to measure retinal hypoxia [102]–[105]; (2) bladder urine [105] and urine in the renal pelvis to create a non-invasive detection of renal dysfunction [106]; (3) cerebrospinal fluid [105], [107]; (4) brain tissue [157], [158]; and (5) blood, including foetal blood [108]–[110]. Therefore, it was hypothesized that this method could also be applicable as a non-invasive method for measuring oxygen delivery from these nanocarriers.

However, changes in R1 are not specific to oxygen: the R1 of the material can be affected by the temperature [103], [105], pH [159], protein concentration [104], field strength [160], and numerous other changes in the chemical environment [161]. Therefore, unless the specific $PO_2$-R1 relationship was measured in the material of interest previously (with consistent temperature, scanner protocol, and protein concentration), absolute oxygen levels

cannot be inferred from R1 [105], only a relative change in oxygenation, since the y-intercept of the linear relationship is not known. The nanobubbles used for oxygen-delivery in the studies discussed above are small lipid-based particles, ~100 nm in diameter, within an acidic (pH=2.3) solution. The relaxivity of oxygen in this nanobubble mixture has not yet been measured; however, analogous work by Thompson et al. [162] demonstrated a linear relationship between $PO_2$ and R1 in a phantom containing microbubble solutions of varying $PO_2$ with a relaxivity slope of 0.0003 $s^{-1}$/mmHg at 7T. With a similar objective, Vatnehol et al. measured the relaxivity and limit of detection of oxygen at 3T in “oxygen-enriched” water intended for therapeutic oxygen delivery [143], [156].

In this chapter, two experiments are presented that build upon the experiments by Thompson et al, reproducing the method used towards a similar aim by Vatnehol et al. [156], in order to investigate whether MRI T1 mapping is a suitable technique to examine oxygen delivery from such carriers. Therefore, it was hypothesized that this method could also be applicable as a non-invasive method for measuring oxygen delivery from these nanocarriers and that the additional substances in the nanobubble solution would not interrupt the linear relationship between R1 and $PO_2$ in the solution. To examine this, two separate experiments were performed to find the relaxivity and limit of detection of oxygen in this nanobubble mixture in two experimental scenarios: a preclinical 7T MRI and clinical 3T MRI.

## 2.2. Methods

### 2.2.1. Phantom Design

For the 7T experiment phantom, seven vials containing different solutions were prepared: oxygen-filled nanobubbles, nitrogen-filled nanobubbles, air-filled nanobubbles, water, oxygenated water, and a half oxygen-filled and half nitrogen-filled nanobubble mixture. One 0.5 ml syringe was filled per solution and sealed using Cristaseal wax (ProSciTech Pty Ltd, Australia). A 7-chamber custom-built holder was used to hold seven 0.5 ml syringes in the scanner for the duration of the phantom experiment.

For the 3T experiment phantom, glass vials containing different solutions were prepared: 5 vials of air-filled nanobubbles, 5 vials of oxygen-filled nanobubbles, 5 vials of water, and 5 vials of water sparged with 100% oxygen. All nanobubble and water solutions were prepared according to the method listed in the section below. The vials were placed in a cylindrical vessel with saline solution surrounding them for the duration of the phantom experiment.

Lastly, to examine the effect that temperature may have on the experiment, 3 phantom tubes from a calibration phantom (Eurospin II TO5 phantom, Diagnostic Sonar LTD, Livingston, Scotland) were used in the scanner and a VFA T1 map acquired 5 times while monitoring the temperature. The 3 phantom tubes had nominal T1 values of 830, 1020, and 1350 ms – we selected 3 tubes that were close in T1 and also within the range of typical tissue T1 values [163].

### 2.2.2. Nanobubble Preparation

All nanobubble solutions were prepared according to the following method: lecithin and citric acid were obtained from Special Ingredients (Chesterfield, Derbyshire, UK). Glycyrrhizic acid and glycerol were obtained from Sigma-Aldrich Ltd (Gillingham, Dorset, UK). Oxygen and nitrogen cylinders were obtained from BOC gases (Guildford, Surrey, UK). The nanobubble solutions were prepared according to Owen et al. [40]. To create one 100ml bottle of the solution, glycyrrhizic acid (0.5mg/ml), lecithin (3 mg/ml), citric acid (5 mg/ml) and glycerol (0.0125 ml/ml) were mixed with 100 ml of freshly boiled, filtered deionized water. The solution was then stirred for 30 minutes while it cooled to room temperature. The vial was then immediately sealed and mechanically agitated for 30 s. To produce oxygen-laden nanobubbles, 5 ml of the solution was transferred to a glass vial and sparged with oxygen gas, for 3 minutes. To produce nitrogen or air-laden nanobubbles, the solution was sparged with nitrogen gas or air for 3 minutes. The nanobubble size distribution measurements were ascertained using a nanoparticle tracking analyzer (NTA) (Nanosight NS300, Malvern, PA)

and all size distributions were consistent with results published by Owen et al. [52], where the concentration of the nanobubble solution was $7.0x10^{12}$ particles/ml [52].

### 2.2.3. MRI Acquisition Details

The 7T imaging experiments were performed using a 7.0 T 210 mm horizontal bore VNMRS pre-clinical imaging system equipped with 120 mm small bore gradient insert (Varian Inc. Palo Alto, CA, USA). A variable flip angle T1 map [115] was calculated using non-linear least squares from 3D RF and gradient spoiled gradient echo sequence with 16 flip angles (TR = 3.2 ms, TE = 0.664 ms, matrix = 128×64×64, slice thickness = 2 mm, FA = 1, 1.2, 1.4, 1.6, 1.8, 2, 2.2, 2.4, 2.7, 3.1, 3.7, 4.4, 5.2, 6.1, 7, 8), requiring a scan time of approximately 8 minutes, and B1 correction was applied using Actual Flip Angle method [164]. T1 values were measured and averaged in a region of interest (ROI) placed lengthwise along each syringe to produce a mean T1 value for each syringe.

The 3T imaging experiments were performed using a 3.0 T Siemens Prisma MRI (Erlangen, Germany). T1 maps were calculated from a linear fit of variable flip angle [115] 3D gradient-echo images with 5 different flip angles (TR = 4.1ms, TE = 1.23ms, FA = 3, 6, 9, 12, 15, slice thickness=3mm), Modified Look-Locker Inversion Recovery (MOLLI) [165] T1-mapping sequences (Siemens Myomaps package MOLLI 5(3)3, TR = 3.5 ms, TE = 1.05 ms, 11 inversion times, FA = 35, slice thickness = 8 mm), and Shortened Modified Look-Locker Inversion Recovery (ShMOLLI) [114] (ShMOLLI_192i protocol, TR =371.84 ms, TE = 1.01 s, FA = 35, slice thickness = 8 mm, 7 inversion times TI = 100, 1100, 2100, 3100, 4100, 180, 260 ms, see Figure 1 by Piechnik et al. for MOLLI and ShMOLLI pulse sequences [114]). Each imaging sequence was repeated in the following order: ShMOLLI 1, MOLLI 1, VFA 1, ShMOLLI 2, MOLLI 2, VFA 2, ShMOLLI 3, MOLLI 3. The ShMOLLI T1-mapping method produced the lowest standard deviation within each vial ROI and was therefore used for the relaxivity and limit of detection (LOD) calculations (see Appendix Figure A.1). The ShMOLLI T1 map acquired closest to the time point of the collection of the oxygen measurement

(ShMOLLI 3) was used to calculate the following relaxivity and LOD results. The T1 measurement from each repetition of the 3 ShMOLLI T1-maps was compared in Appendix Figure A.2.

### 2.2.4. Oxygen Measurements

Following the 7T scans, the remaining solution in each of the 7 larger vials was measured using a fibre optic oxygen sensor. All $PO_2$ measurements were carried out using a PreSens OXY Mini fibre-optic oxygen meter in combination with SP-PSt3-NAU oxygen sensor spots inside sealed glass vials (PreSens Precision Sensing GmbH, Regensburg, Germany). All oxygen measurements were calibrated and carried out at room temperature.

Following the 3T scans, the phantom was carefully removed from the scanner, and one by one, each vial was quickly opened and poured into a vial with a PreSens sensor sticker with the PreSens tip recording the $PO_2$ measurement (PreSens OXY Mini fibre-optic oxygen meter). The $PO_2$ was recorded for 30 seconds, recording one measurement per second. All oxygen measurements were calibrated and carried out at room temperature. The oxygenated samples were recorded first, then the non-oxygenated samples, to reduce the time over which the oxygen levels could be decreasing due to exchange with the room air.

### 2.2.5. Calculation of Limit of Detection

The limit of detection of oxygen in the solutions can be calculated by the following equation [166]:

$$LOD = \frac{F x\, SD}{b} \qquad \text{(Eq 2.2)}$$

where b is the slope of the regression line (relaxivity, or $r1_{Ox}$), SD is the standard deviation of the intended in vivo situation, and F is a factor set to 2.2 for LOD calculations with 95% confidence intervals. This method was used by Vatnehol et al. to calculate the limit of detection of dissolved oxygen in water [156].

## 2.3. Results

### 2.3.1. Oxygen Relaxivity

The phantoms and resulting T1 maps can be seen in Figure 2.1. A strong linear relationship ($R^2$=.97 and $R^2$=.97) was measured between $PO_2$ and R1 in the nanobubble solution *in vitro* at 7T and 3T, respectively, shown in Figure 2.2. The relaxivity ($r1_{Ox}$) at 7T and 3T was 0.00024 $s^{-1}$/mmHg and 0.00057 $s^{-1}$/mmHg, respectively, and the corresponding upper and lower confidence intervals and P-values are listed in Table 2.1.

***Table 2.1.*** *The resulting $R^2$, P-value and slope with lower and upper 95% confidence intervals and for each linear regression shown in Figure 2.2.*

| Data | Slope (95% C.I.) [units] | P-value | $R^2$ |
|---|---|---|---|
| R1 vs $PO_2$ at 7T (Fig 2A) | 0.00024 (0.00016, 0.00031) [$s^{-1}$/mmHg] | <0.0001 | 0.97 |
| R1 vs $PO_2$ at 3T (Fig 2B) | 0.00057 (0.00048, 0.00065) [$s^{-1}$/mmHg] | 0.00016 | 0.97 |

### 2.3.2. Limit of Detection

The SD in the LOD equation represents the standard deviation of the method in the intended tissue. Therefore, for the 7T preclinical setting, the mean of 8 reported standard deviation values of R1 from the intended experimental tissue — a preclinical tumour model — was calculated, which was approximately 0.011 $s^{-1}$ [144]. Using the measured relaxivity at 7T (0.000235 $s^{-1}$/mmHg) and Equation 2, the resulting LOD (95% confidence) at 7T in a preclinical tumour model is 103 mmHg. For the 3T clinical setting, the mean of 11 reported standard deviation values of R1 from clinical tumour ROI was calculated, which was approximately 0.029 $s^{-1}$ – the clinical tumour ROI data was published by O'Connor et al. [167]. Using the measured relaxivity at 3T (0.00057 $s^{-1}$/mmHg) and Equation 2, the resulting LOD (95% confidence) at 3T in a clinical tumour is 111 mmHg.

### 2.3.3. Nanobubbles and R1

In comparison to water, the nanobubble solution contains several attributes that may affect R1, in particular, the presence of the lipid-based particles, and the acidity (pH=2.3) of the solution. It was apparent from both the 7T and 3T experiments (Figure 2.3) that the nanobubble solution alone — *without* oxygen added — produced an increase in R1 of 0.03 and 0.07 $s^{-1}$ compared to water; equivalent to increasing the water $PO_2$ by 230 and 130 mmHg (at 7T and 3T, respectively).

The experiment measuring the effect of temperature on R1 showed that the R1 of all 3 tubes decreased as temperature increased, and a linear regression fit strongly ($R^2$=.83, .90, .91). The change in R1 per change in temperature was -0.037, -0.027, and -0.020 $s^{-1}$/°C for the 3 tubes respectively (see Figure 2.4), and a steeper slope corresponded to a higher baseline R1, and vice versa. The corresponding upper and lower confidence intervals and P-values are listed in Table 2.2. This means that from just a 0.5°C fluctuation in temperature, the R1 would change by 0.018 $s^{-1}$, which would correspond to a 32 and 77 mmHg inaccuracy in $PO_2$ estimation, at 3T and 7T, respectively. In terms of T1, a linear regression fit the T1 vs temperature data strongly as well ($R^2$=.83, .90, .91) with a slope of 20, 23, and 29 ms/°C for the 3 tubes respectively. These T1 results are consistent with findings by Zhang *et al.* where the temperature sensitivity increased with baseline T1, following closely a second-order polynomial (see Fig 2 in Zhang et al.) [168].

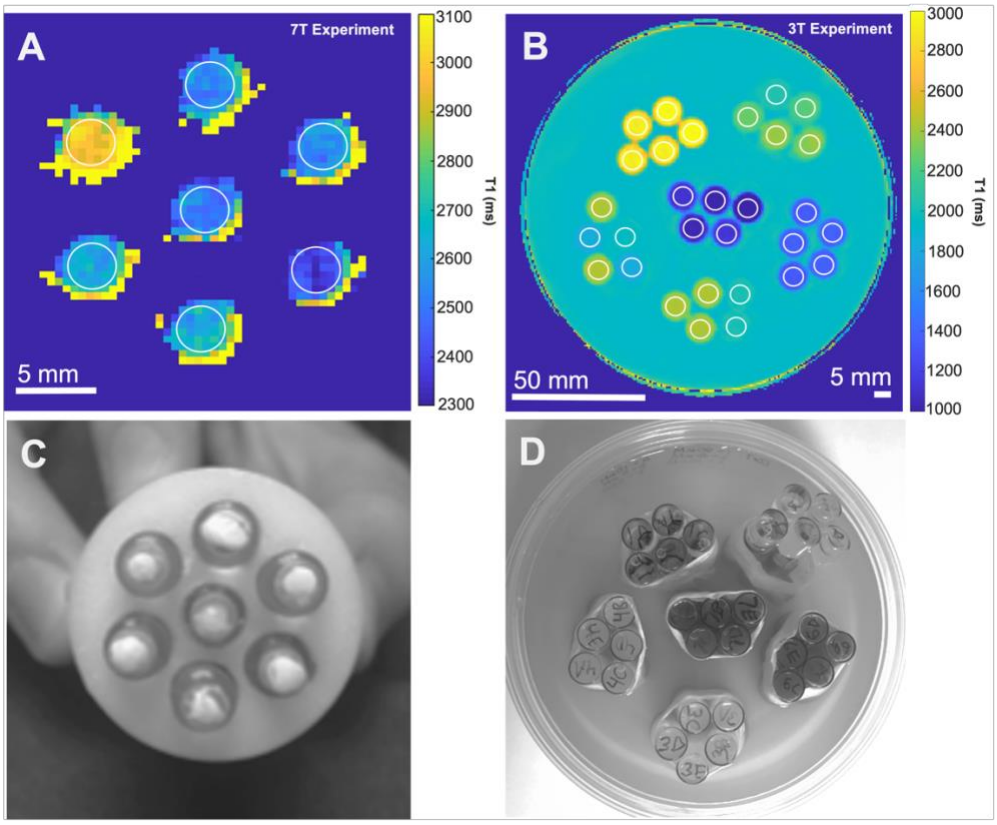


***Figure 2.1. (A-B)*** *Examples of the resulting $T_1$ map with illustrated ROIs through a section of the vials in the* ***(A)*** *7T and* ***(B)*** *3T phantom, with the corresponding photographs of the phantom below (C-D).*

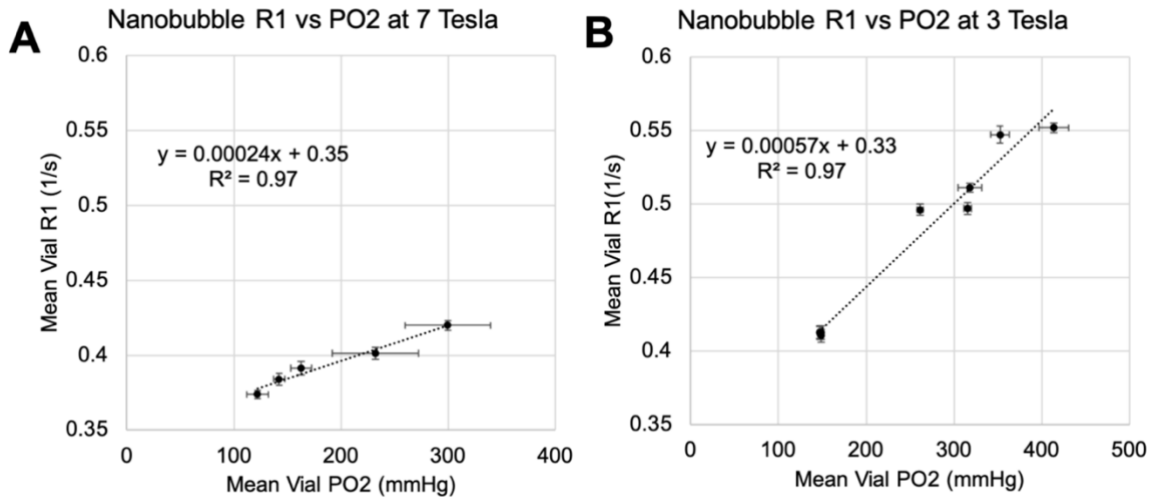


***Figure 2.2.*** *The mean R1 values ($s^{-1}$) and mean $PO_2$ values (mmHg) in the nanobubble solutions at 7T and 3T, plotted with a linear line of best fit ($R^2$=.97 and $R^2$=.97) and relaxivity slope ($r1_{Ox}$) of 0.00024 $s^{-1}$/mmHg and 0.00057 $s^{-1}$/mmHg, respectively. The corresponding upper and lower confidence intervals and P-values are listed in Table 2.1.*

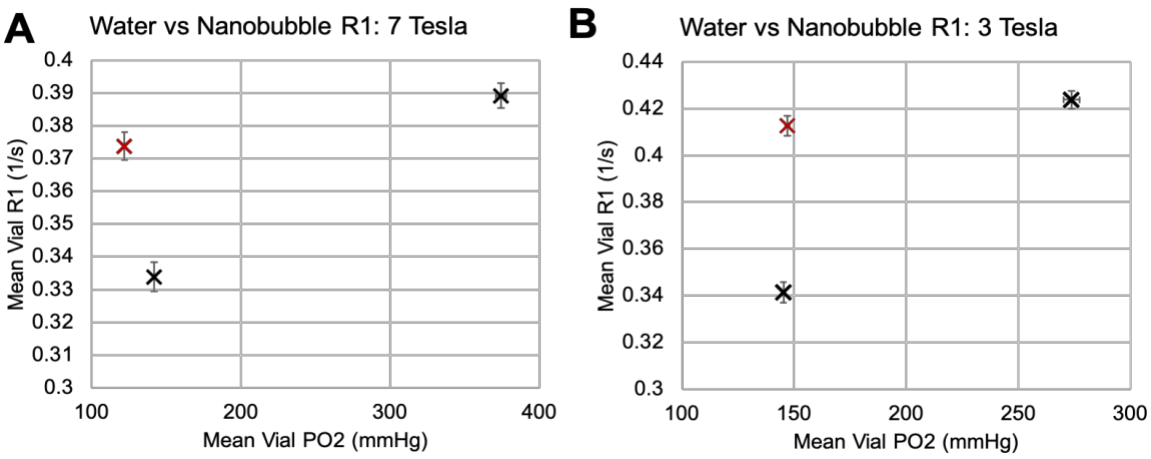


***Figure 2.3.*** *The mean R1 and $PO_2$ values of the vials of water and oxygenated water (black crosses), in comparison to non-oxygenated nanobubbles (red cross), at* ***(A)*** *7T and* ***(B)*** *3T. The contents of the non-oxygenated nanobubble solution resulted in an R1 that was 0.03 and 0.07 $s^{-1}$ higher than water, the equivalent effect as increasing the water $PO_2$ by 230 and 130 mmHg (at 7T and 3T, respectively).*

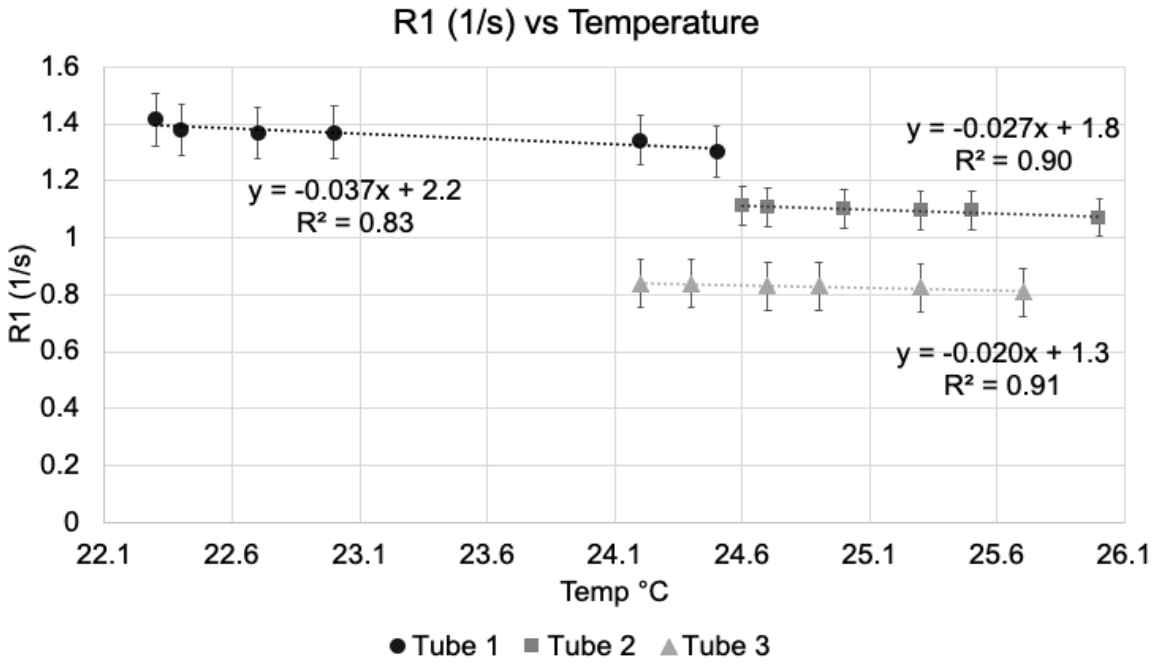


***Figure 2.4.*** *To examine the effect that temperature may have on the experiment, VFA T1 maps of 3 calibration phantom tubes were repeated 5 times while monitoring the temperature. The R1 of all 3 phantom tubes (with a T1 of 830, 1020, and 1350 ms) decreased as temperature increased, and a linear regression fit strongly ($R^2$=.83, .90, .91) with a slope of -0.037, -0.027, and -0.020 $s^{-1}$/°C for the 3 tubes respectively. The corresponding upper and lower confidence intervals and P-values are listed in Table 2.2.*

***Table 2.2.*** *The resulting $R^2$, P-value and slope with lower and upper 95% confidence intervals and for each linear regression shown in Figure 2.4.*

| Data | Slope (95% C.I.) [units] | P-value | $R^2$ |
|---|---|---|---|
| Tube 1 | -0.036 (-0.060, -0.013) [$s^{-1}$/°C] | 0.011 | 0.83 |
| Tube 2 | -0.027 (-0.040, -0.015) [$s^{-1}$/°C] | 0.003 | 0.90 |
| Tube 3 | -0.019 (-0.027, -0.011) [$s^{-1}$/°C] | 0.002 | 0.91 |

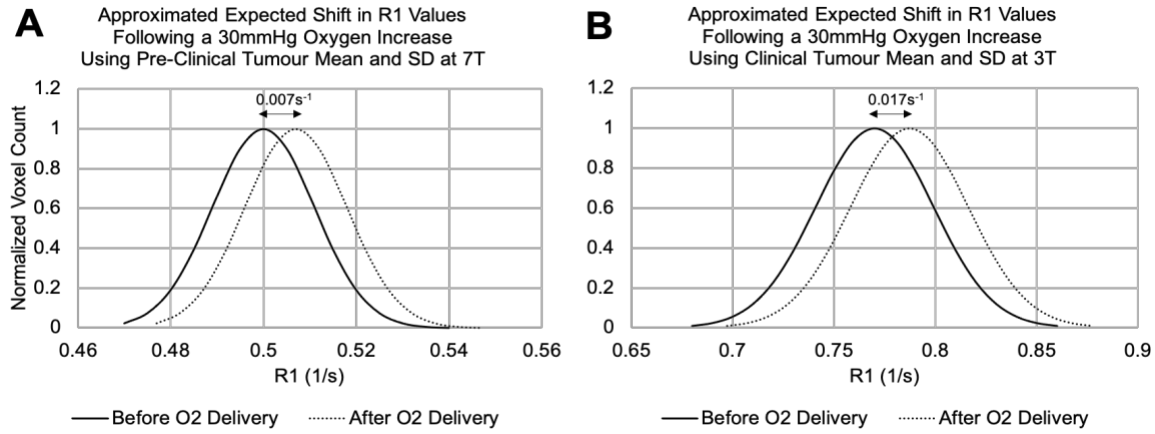


***Figure 2.4.*** *The approximate expected shift in R1 values, based on the relaxivity measured in these experiments, following a hypothetical 30 mmHg oxygen increase in the tumour tissue $PO_2$ as measured by Owen et al.* [52]*. Data published by Yang et al.* [144] *were used to calculate the preclinical tumour mean and standard deviation in* ***(A)****, data published by O'Connor et al.* [167] *were used to calculate the clinical tumour mean and standard deviation in* ***(B)****.*

# 2.4. Discussion

## 2.4.1. Relaxivity

These experiments reproduced the linear R1-$PO_2$ relationship expected ($R^2$=0.97), and showed that the $PO_2$ of the nanobubble solution could be estimated using T1-mapping at 7T and 3T. It was a possibility that the composition of the nanobubble solution would

interrupt this linear R1-$PO_2$ relationship or induce image artefacts. Fortunately, this was not found to be the case.

The $r1_{Ox}$ in the nanobubble solution was 0.00024 $s^{-1}$/mmHg and 0.00057 $s^{-1}$/mmHg at 7T and 3T respectively. In these experiments, the $r1_{Ox}$ was stronger at the lower field strength, which agrees with other reports from phantom measurements of $r1_{Ox}$ being greater at lower field strengths [169]–[171]. The comparable experiments by Thompson et al. [162] measured an $r1_{Ox}$ of 0.0003 $s^{-1}$/mmHg at 7T, which within the upper 95% confidence interval of our measurement performed at 7T (0.00031 $s^{-1}$/mmHg). Therefore, even though the composition of the microbubble solution and nanobubble solutions differ considerably (see Thompson et al. [162] for the microbubble formula), the $r1_{Ox}$ seems to be almost independent of the nano or microbubble composition, which is a notable strength of this method.

### 2.4.2. Limit of Detection

Using our measured $r1_{Ox}$ and published values of the expected standard deviation in R1 within preclinical and clinical tumour tissue, the resulting 95% confidence interval LOD calculated indicates that a 103 mmHg (4.56 mg/L) and 111 mmHg (or 7.04 mg/L) increase in oxygen is required to reliably detect a change in R1 from oxygen delivery (in a preclinical and clinical setting, respectively). These are both slightly lower than the 8.5-12.3 mg/L limit of detection estimated by Vatnehol et al.; however, for their calculations, the authors use the standard deviation in the hepatic portal vein as that is their material of interest [143], [156]. Of course, this raises the most important point of this discussion: these LOD calculations assume that there are no other potential T1 changing effects present other than an increase in oxygen — which, in the body, is an often unrealistic assumption, especially in a voxel containing blood. However, for a voxel that does not contain 100% blood, such as normal tissue, it has been demonstrated that the R1 of the tissue will increase linearly with the level of dissolved oxygen in the tissue. Since the effect from changing deoxyhemoglobin levels

will only pertain to the percent volume in the voxel that is occupied by blood, then the remaining 90-98% of voxel volume will be dominated by R1 change of the tissue. Therefore, while the LOD calculations in this chapter do not account for confounding effects on R1, they are still useful to obtain an estimation of whether the detection of nanobubble oxygen delivery by R1 measurement is feasible.

The expected $PO_2$ change in the tumour tissue following the administration of nanobubbles has been reported to be approximately 30 mmHg, albeit this was measured using a method that was likely underestimating the $PO_2$ [52]. This is much lower than both the LODs calculated in this experiment (103 mmHg and 111 mmHg); however, this LOD calculation is stating that the two peaks of the distributions are separated by 2.2 standard deviations, which is considerable. To examine the degree to which the R1 change expected from 30 mmHg was discernible, the tumour R1 mean and standard deviations published by Yang et al. [144] and O'Connor et al. [167] were used to estimate a normal distribution, and a visually discernible shift in R1 values following a hypothetical 30 mmHg oxygen increase in the tumour tissue $PO_2$ is shown in Figure 2.4. Therefore, although the expected oxygen delivery is below the measured LOD, this could still be a feasible method for detecting the expected change in $PO_2$. In addition, this measurement describes the LOD for a single voxel, which is different from the detection power in a large ROI — due to the repeated number of voxel measures in a large ROI, it would be feasible to detect a much smaller difference between two large ROIs that would otherwise not be realistic in a single voxel.

In addition, the standard deviation within the tumour ROIs used is a combination of both tissue heterogeneity and T1-mapping measurement variability, and as T1-mapping methods continue to improve, it is possible that the standard deviations could decrease significantly, and oxygen detection could be made on a voxel-wise level. Therefore, although the resulting LODs calculated from this experiment are greater than the expected $PO_2$ change, it is possible that as T1 mapping techniques become more stable, assessment of spatial variation of $PO_2$ may then be possible compared to region averaging which is needed

currently, enabling T1 mapping to be a suitable technique to examine oxygen delivery from these nanobubbles.

Lastly, the LOD measurement describes the sensitivity of this technique to detecting $PO_2$ changes in an individual. As a paired measurement in a study across multiple subjects at 3T, however, assuming that a similar standard deviation as previous clinical R1 measurements [167], then a study of 10, 13, or 15 participants would yield 80%, 90%, or 95% power, respectively (alpha 0.05) [172].

### 2.4.3. Additional Confounding Effects

In comparison to water, the lipid content and acidity of the non-oxygenated nanobubble solution resulted in an R1 that was higher than water. The magnitude of this effect was the equivalent of increasing the water $PO_2$ by 230 and 130 mmHg (at 7T and 3T, respectively). Thus, it is likely that increasing the nanobubble concentration in a water or saline phantom solution would increase R1, making it difficult to use that change in signal to infer a change in $PO_2$. This problem is similar to that reported by Vatnehol et al. [143], where the delivery of a dissolved oxygen water drink caused a dilution that changed R1 in both the control drink and the oxygen drink. It is possible that this dilution would be a negligible effect from the nanobubbles once spread out in the circulatory system, however, it could make oxygen nanobubble delivery indistinguishable from non-oxygenated nanobubble delivery. Since the percent volume of nanobubble solution would be far below 10% of the blood volume and the tissue voxel would contain below 10% blood volume, and since the low pH would be neutralized in the bloodstream, it is reasonable to conclude that this confound would not be as substantial as the R1 change from the $PO_2$ change within the tissue dominating 85-98% of the voxel volume, assuming a range of fractional blood volume in tumours of approximately 2-15% [173].

There are additional remaining factors that can affect R1. Experiments using R1 to measure $PO_2$ in vitreous fluid have demonstrated the strong effect of temperature on the R1

measurement [103], [105]. Unfortunately, this is not insignificant — Zaharchuk et al. [105] reported that based on their phantom experiments, there could be a potential error of ±19 mmHg for physiologic temperature fluctuations of ±1°C.

### 2.4.4. Experiment Limitations

The gold-standard T1-mapping method to use would have been inversion recovery, since Look-Locker techniques such as ShMOLLI are known to underestimate the true T1 and VFA will overestimate the true T1 (this has been replicated in phantoms and in vivo) [118]. However, these experiments were intended as preliminary work for preclinical and clinical experiments, and therefore it was more appropriate to use the actual experimental set up and scanning techniques that could be used in mice and human volunteers and/or patients. In comparison to phantoms, scanning live subjects introduces issues such as motion from breathing and limitations to scan time, and therefore faster T1 mapping methods are required than those employed for phantom scanning. Lastly, although the T1 might be over- or under-estimated, the *relative* change in R1 (and therefore $r1_{Ox}$) should remain the same in each method.

An additional limitation is that although the experiments were carried out at room temperature, we did not measure or record the exact temperature of the room. Since temperature can influence R1 and oxygen solubility, future experiments should be sure to measure and record the temperature of any important elements of the experiment, such as the room and the solutions. In addition, this experiment could have been designed to use hypoxic or de-gassed solutions to produce vials with even lower levels of oxygen, however we did not have a robust and reliable workflow available for transferring degassed solutions into the vials. Lastly, although 1.5T is a more common scanner strength in a hospital setting, we used a 3T MRI to represent the clinical environment due to the resources that were available to us at the time.

## 2.5. Conclusion

With the aim of addressing whether the linear relationship between R1 and $PO_2$ would be useful for detecting oxygen delivery from nanobubbles, this chapter has reported the original results of two experiments performed at the two different field strengths and imaging environments of interest for this thesis. This experiment reproduced a strong linear relationship ($R^2$=.97) between $PO_2$ and R1 in the nanobubble solution, measured the relaxivity of oxygen in the nanobubble solution at 7T (0.00024 $s^{-1}$/mmHg), and 3T (0.00057 $s^{-1}$/mmHg), and established that a 103 mmHg and 111 mmHg increase in oxygen is required to detect a change in R1 at 7T and 3T, respectively, with 95% confidence. This suggests that T1 mapping could provide a non-invasive method of measuring oxygen delivery from oxygenated nanobubbles in therapy, depending on the oxygen delivery effect size that is expected and the signal-to-noise ratio of the T1 map acquisition. The results show that T1 mapping could provide a non-invasive method of measuring a >100 mmHg oxygen delivery from oxygenated nanobubbles in therapy, and that as a paired measurement in a study across multiple subjects at 3T, a study of 10-15 participants would be required to yield 80-95% power. In the next chapter, the results of three preclinical pilot experiments for measuring the R1 change in xenograft tumours following nanobubble administration are reported.

# Chapter 3. Pre-Clinical Pilot Experiments

---

*This thesis aims to examine whether the change in oxygen caused by the nano-carriers can be detected using clinically available MRI techniques. Chapter 2 presented the relaxivity and limit of detection of oxygen via measurement of R1, suggesting that it could be a feasible technique to detect oxygen delivery. This chapter presents the results of three pilot preclinical experiments to test whether the oxygen delivery from the nanobubble injection was detectable using R1 measurements.*

*Although the results of these experiments were inconclusive, they inspired investigations that exposed important possible confounding factors such as temperature, and most importantly, these contradictory results were the motivation for the quantitative model presented in the subsequent chapters.*

*This chapter includes material that was presented at the following conference:*

- ***E Bluemke,** J Owen, E Thompson, P Kinchesh, S Smart, E Stride, D Bulte. Magnetic Resonance Imaging of Oxygen Nano-Carriers In Vitro and In Vivo. Postgraduate British Chapter of ISMRM Symposium, Birmingham UK 2019.*

  *Awarded 1st Place Poster Award, 2nd Place Best Power Pitch Award.*

---

# 3.1. Introduction

Although the LOD calculations presented in Chapter 2 erroneously assumed that there would be no other confounding effects on R1, these calculations were still useful to obtain an estimation of whether the detection of nanobubble oxygen delivery by R1 measurement would be feasible. Therefore, in order to examine whether the confounding effects discussed in Chapter 2 would be applicable in a preclinical tumour setting, three separate pilot preclinical experiments were performed, with adjustments and improvements made to the experimental design between each experiment. Therefore, in this chapter, the results of the three pilot preclinical experiments are reported, with the aim of testing whether the oxygen delivery from the nanobubble injection was detectable using R1 measurements.

# 3.2. Methods

## 3.2.1. Experiment Design

Three pilot experiments were carried out on separate days, with adjustments to the experimental design being made in between. Nanobubble solutions were prepared as described in Chapter 2 and sparged with 100% oxygen for 3 minutes. Mice received either a nanobubble injection or control injection, containing either saline or citric acid solution. All injections were administered via tail-vein. An overview of the experiments is shown in Figure 3.1, and the key parameters are summarized in Table 3.1. All animals involved in this study were treated humanely and in accordance with licenced procedures under the UK Animals (Scientific Procedures) Act 1986. Tumour, brain, and thigh muscle ROIs were drawn on the anatomical T2-weighted image and used for further analysis (for tumour type, see Figure 3.1). For the T1-weighted images, the mean Signal Intensity (S.I.) across all slices of the ROI was calculated. The baseline was calculated as the mean signal in the first 5 time points (pre-injection), and the % change in T1-weighted S.I. over time was plotted as a weighted average with 5 time points per period. For the T1 maps, the mean R1 for each 3D ROI was

calculated, and the change pre- and post- injection was statistically evaluated using a two-sample t-test assuming unequal variances (α=0.05).

In all 3 experiments, dynamic T1-weighted images were acquired over a 20–27-minute period. In experiments 2 and 3, T1 mapping was added to the MRI protocol: a VFA T1 map was acquired prior to injection, and a VFA T1 map was acquired at the end of the session.

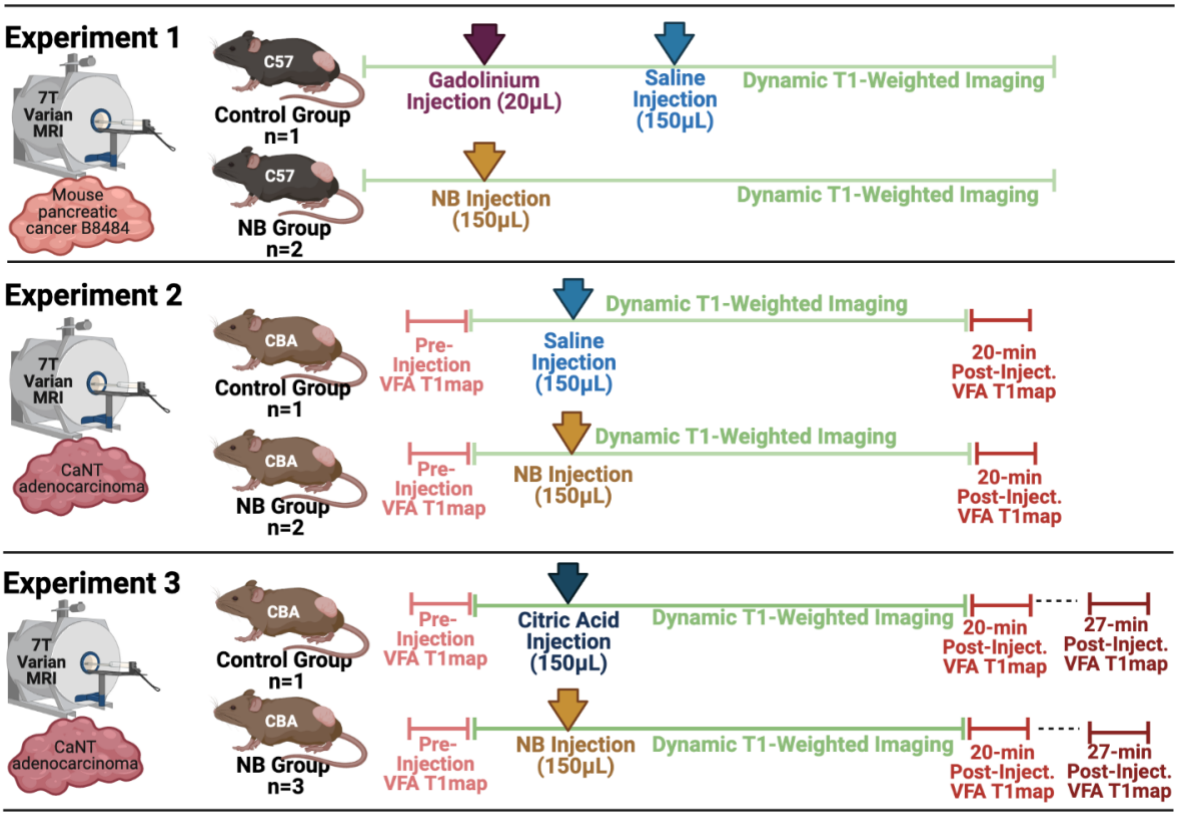


***Figure 3.1.*** *A graphical representation of the design of each of the 3 pilot experiments. Additional details are provided in Table 3.1.*

To examine the effects of the nanobubble injection upon R1 in vivo, other sources of effects on relaxation times must be considered, such as the dilution effect from a 150µl injection (~10% blood volume). Control experiments were performed to control for this dilution effect, as it is known that decreasing haematocrit concentration will decrease R1 [174]. As the nanobubble solution is administered intravenously, it is possible that this effect could counteract the increase in R1 due to increased oxygen present in the tissue. This

dilution effect will be discussed further later in this thesis. In Experiment 1, there was an attempt to measure the dilution effect by first injecting gadolinium then saline, however, the gadolinium signal change would be an order of magnitude greater than any signal change induced by the saline, so this gadolinium step was removed from all future experiments. In Experiment 2, a saline injection was used as a control, and in Experiment 3, the control injection was changed to a citric acid solution to control for the acidity of the nanobubble solution (pH=2.3), since citric acid is one of the main ingredients of the nanobubbles, and an acidic injection could possibly induce haemodynamic or pH changes that could also alter R1.

***Table 3.1.*** *Summary of key parameters and observations influencing the experimental design between the 3 pilot sessions.*

| Details | Experiment 1 | Experiment 2 | Experiment 3 |
|---|---|---|---|
| **Xenograft Details** | C57 mice with mouse pancreatic cancer B8484 | Female CBA mice bearing subcutaneous poorly differentiated corded adenocarcinoma CaNT tumours as a hypoxic tumour model | |
| **Control Injection** | 20 µL of gadolinium and 150 µL saline | 150 µLSaline | 150 µL Citric Acid |
| **Control sample size** | n=1 | n=1 | n=1 |
| **NB sample size** | n=1 | n=2 | n=3 |
| **Timestamp of injection** | Saline/NB injected at repetition 6 | 7 minutes into scan time, lasted 1 min | 7 minutes into scan time, lasted 1 min |
| **Timestamp of VFA 2** | **No VFA** | 20 minutes post-injection | 20 minutes post-injection, + VFA 3 at 27 minutes post-injection |
| **Injection speed** | 72 µL/min | 150 µL/min | 150 µL/min |
| **Date performed** | August 30, 2018 | March 15, 2019 | June 3, 2019 |
| **Issues with the experiment** | In mouse 1, there was gadolinium left in the cannula when the saline was injected. Therefore, although the intention was to see the change in signal from 'dilution', this data will only show the change in signal induced by an additional small injection of gadolinium mixed with saline. For future experiments, the gadolinium injection was removed from the experiment design. | For the post-injection T1 map of mouse 3, there was a large increase in T1 across all voxels in the image, and hence it was excluded from the analysis. | Due to scanner hardware issues during the setting up of the scanner, the nanobubbles injected into the first mouse had a larger delay between oxygen sparging and injection time than the 3 other mice, and hence the resulting oxygen delivery might be less than in mice 2 and 3.<br><br>It is important to note that there were hardware changes made to improve SNR between Experiment 2 and 3. |
| **Corrections made to experimental design** | For future experiments, the gadolinium injection was removed from the experiment design. | Between Experiment 1 to 2, three important changes to the experiment design were made: | Between Experiment 2 to 3, three important changes to the experiment design were made:<br><br>1. First, the control injection was changed to a citric acid solution to |

| | | | |
|---|---|---|---|
| | | 1. A very small signal change was observed in the T1-weighted signal during the 50 timepoint period in Experiment 2, so in Experiment 2, the T1-weighted acquisition period was extended to 100 time points.<br><br>2. The control injection contained only saline - no gadolinium injections were used.<br><br>3. T1 maps were acquired pre- and post-injection as an additional method to measure R1 change, as opposed to only acquiring dynamic T1-weighted images. | control for the acidity of the nanobubble solution (pH=2.3), as citric acid is one of the main ingredients of the nanobubbles, and an acidic injection could induce haemodynamic or pH changes that could also alter R1.<br><br>2. A very variable signal change was observed in the T1-weighted signal during this 100 timepoint acquisition period in Experiment 2, so in Experiment 3, the T1-weighted acquisition period was extended to 120 time points.<br><br>3. From previous experiments measuring oxygen delivery via oxygen probes, it was estimated that 20 minutes would be an appropriate amount of time to observe the change induced from the injections. However, in Experiment 3, an additional post-injection T1-map was acquired at 27 minutes post-injection to check if the R1 change would be different. |

### 3.2.2. MRI Acquisition Details

All imaging experiments were performed using a 7.0T 210 mm horizontal bore VNMRS pre-clinical imaging system equipped with a 120mm bore gradient insert (Varian Inc. Palo Alto, CA, USA). All VFA T1 maps were calculated from SPGR images (TR = 3.2 ms, TE = 0.664 ms, FA = 1, 1.2, 1.4, 1.6, 1.8, 2, 2.2, 2.4, 2.7, 3.1, 3.7, 4.4, 5.2, 6.1, 7, 8). For the dynamic imaging, a T1-weighted image (TR = 1.6ms, TE = 0.656ms) was collected every 12 seconds for the duration noted in the experimental design.

## 3.3. Results

### 3.3.1. Experiment 1 Results

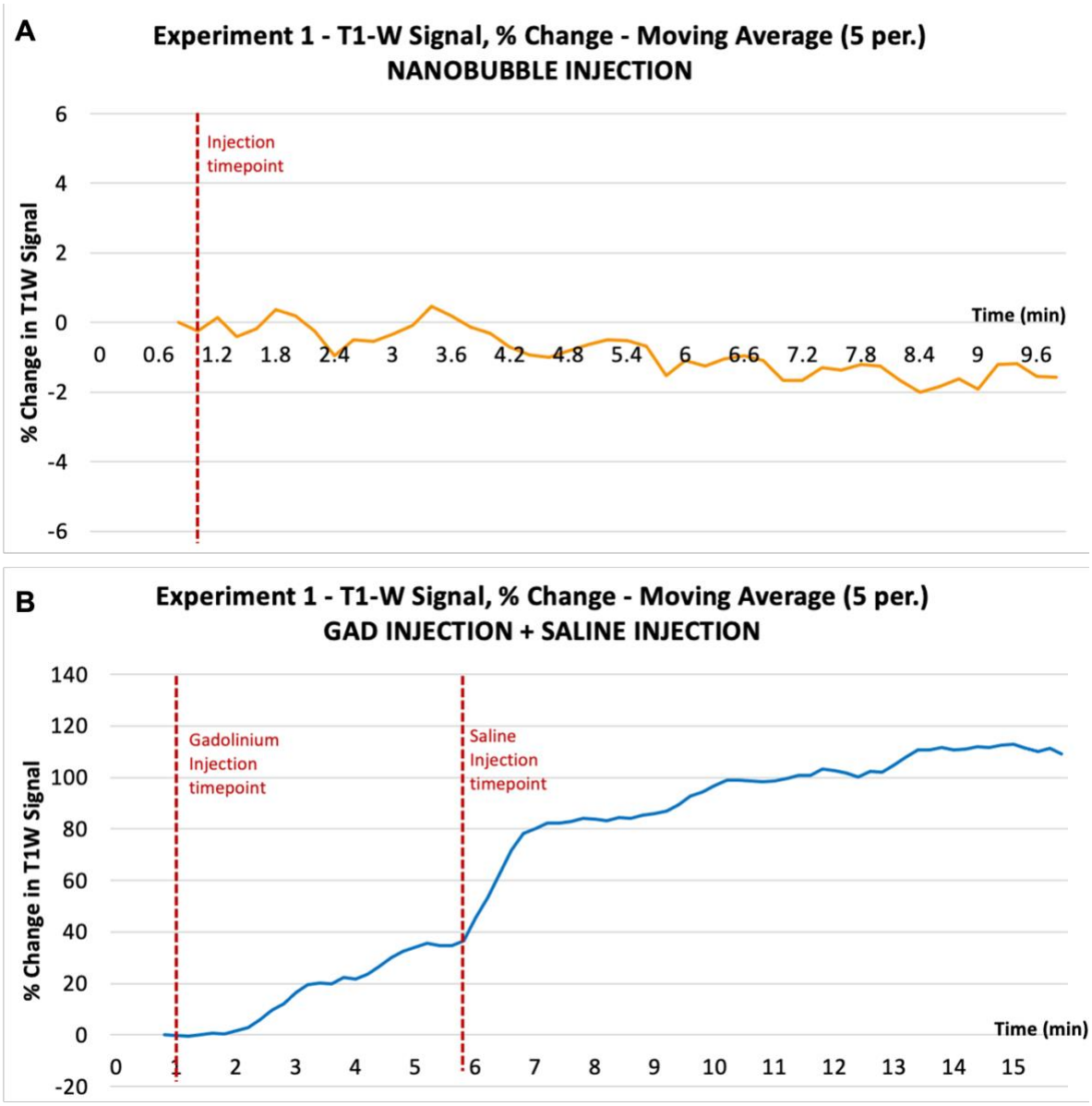


***Figure 3.2.*** *The temporal evolution of MRI T1-weighted % signal change from baseline in the tumour ROI of the mouse receiving the* ***(A)*** *nanobubble injection and* ***(B)*** *control injection in Experiment 1. Baseline was calculated as the mean signal in the first 5 time points (pre-injection), and the plotlines displayed are the moving average (5 timepoints per period). The nanobubble and gadolinium injections occurred at time point 6, the saline injection occurred at timepoint 30.*

The measured T1-weighted signal change is presented in Figure 3.2. The nanobubble injection appeared to cause a gradual negative signal change of ~2%, corresponding to a negative change in R1. In the control mouse, the gadolinium injection

induced a positive signal change of 40%, however, there was gadolinium left in the cannula when the saline injection began, inducing a further signal change due to remaining gadolinium that reached 110% from baseline. The experiment design was then altered, and gadolinium injections were not included in the subsequent experiments.

### 3.3.2. Experiment 2 Results

The R1 change calculated from the T1-maps from each injection is presented in Table 3.2, with the distributions shown as violin plots in Figure 3.3. For the post-injection T1 map for mouse 3, there was a large increase in T1 across all voxels in the image, and hence it was excluded from analysis, and not shown in Figure 3.3. In Mouse 1, receiving the nanobubble injection, a significant increase in R1 was observed in the tumour, thigh, and brain ROIs ($p<0.0001$ in all 3 ROIs). In Mouse 2 receiving the saline control injection, a significant decrease in R1 was observed in the tumour and thigh ROIs ($p<0.0001$ in both ROIs), while no significant change in signal was observed in the brain ROI.

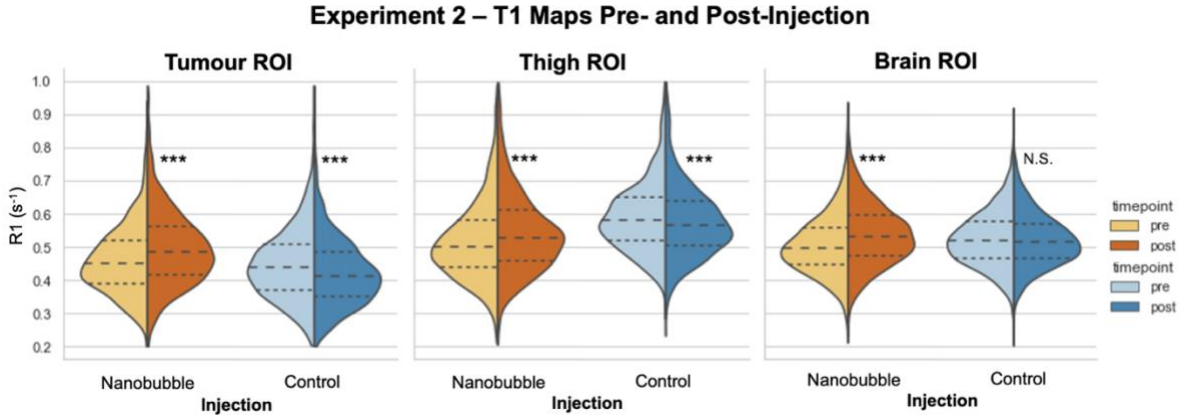


***Figure 3.3.*** *The distribution of R1 measurements extracted from the T1 maps in the tumour, thigh muscle, and brain ROI, pre and post the nanobubble injection (n=1) and control injection (n=1) - mouse 3 is excluded from this plot due to a global image artefact in the post-injection T1 map. R1 values before and after injection were compared statistically using a two-sample t-test assuming unequal variances, the resulting p-values of each change are displayed beside the respective violin plot: No Significance (N.S.), p<0.05 (*), p<0.001 (**), p<0.0001 (***).*

***Table 3.2.*** *A table of the mean R1 measurements extracted from the T1 maps in the tumour, thigh muscle, and brain ROI, pre and post the nanobubble injection (n=2) and control injection (n=1), alongside the resulting ΔR1 ($s^{-1}$) calculated as [post-pre]. R1 values before and after injection were compared statistically using a two-Sample t-test assuming unequal variances, the resulting p-values of each change are displayed beside the respective violin plot: No Significance (N.S.), p<0.05 (*), p<0.001 (**), p<0.0001 (***).*

| Mouse | Injection | T1 Map Data - Tumour ROI R1 ($s^{-1}$) | | | T1 Map Data - Thigh ROI R1 ($s^{-1}$) | | | T1 Map Data - Brain ROI R1 ($s^{-1}$) | | |
|---|---|---|---|---|---|---|---|---|---|---|
| | | Mean R1 (±SD) | | ΔR1 ($s^{-1}$) (post-pre) | Mean R1 (±SD) | | ΔR1 ($s^{-1}$) (post-pre) | Mean R1 (±SD) | | ΔR1 ($s^{-1}$) (post-pre) |
| | | Pre-Inject | Post-Inject 20 min | | Pre-Inject | Post-Inject 20 min | | Pre-Inject | Post-Inject 20 min | |
| 1 | NB | 0.466 (0.1) | 0.501 (0.1) | **+0.034*** ** | 0.527 (0.1) | 0.549 (0.1) | **+0.022*** ** | 0.506 (0.1) | 0.538 (0.1) | **+0.032*** ** |
| 3 | NB | 0.570 (0.2) | 0.422 (0.2) | **-0.15*** ** | 0.562 (0.1) | 0.481 (0.1) | **-0.08*** ** | 0.536 (0.1) | 0.435 (0.1) | **-0.10*** ** |
| 2 | Control | 0.452 (0.1) | 0.430 (0.1) | **-0.021*** ** | 0.601 (0.1) | 0.584 (0.1) | **-0.017*** ** | 0.525 (0.1) | 0.522 (0.1) | **-0.003 N.S.** |

***p<0.0001, **p<0.001, *p<0.05, N.S.=p>0.05

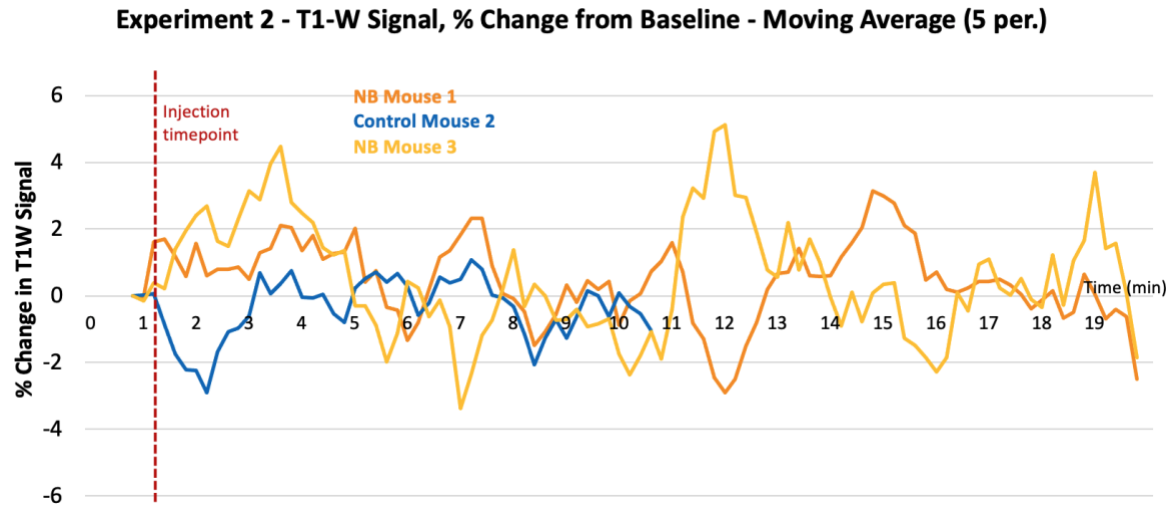


***Figure 3.4.*** *The temporal evolution of MRI T1-weighted % signal change from baseline in the tumour ROI of the three mice in Experiment 2. Baseline was calculated as the mean signal in the first 5 time points (pre-injection), and the plotlines displayed are the moving average (5 time points per period).*

The resulting T1-weighted signal change from each injection is presented in Figure 3.4. The nanobubble injections caused a greater change in signal (-4% to +5%) than in Experiment 1; however, the data varied between positive and negative signal changes, making it difficult to draw conclusions from these scans.

### 3.3.3. Experiment 3 Results

The R1 change calculated from the T1-maps from each injection is presented in Table 3.3. The ΔR1 from baseline at 20 minutes and 27 minutes post-injection for each mouse and ROI is plotted in Figure 3.5, where it can be seen that the largest ΔR1 is observed at 27 minutes rather than 20 minutes. Hence, for the visualization of the R1 distribution pre and post injection Figure 3.6, the 27-minute timepoint is used as the "post-injection" R1 values.

Figure 3.6 shows that in all four mice (including the control), a significant decrease in R1 was observed post-injection in the tumour and thigh ROIs. In the brain ROI of Mouse 1 (receiving the nanobubble injection), a significant increase in R1 was observed, however in the brain ROI of all other 3 mice, a significant decrease in R1 was observed.

Therefore, from the VFA T1 map data alone, it appears the signal change induced from nanobubbles was indistinguishable from the control injection. However, the resulting T1-weighted signal change from each injection is presented in Figure 3.7. Here, it appears that all three nanobubble injections caused a negative T1-weighted signal change of 3-5%, while the control injection caused a mostly positive T1-weighted signal change of ~2%. While a change in R1 of a material should correspond to a change in T1-weighted signal, this is not the case in the results of both Experiments 2 and 3. It is possible that these results could indicate repeatability issues with the T1 mapping method.

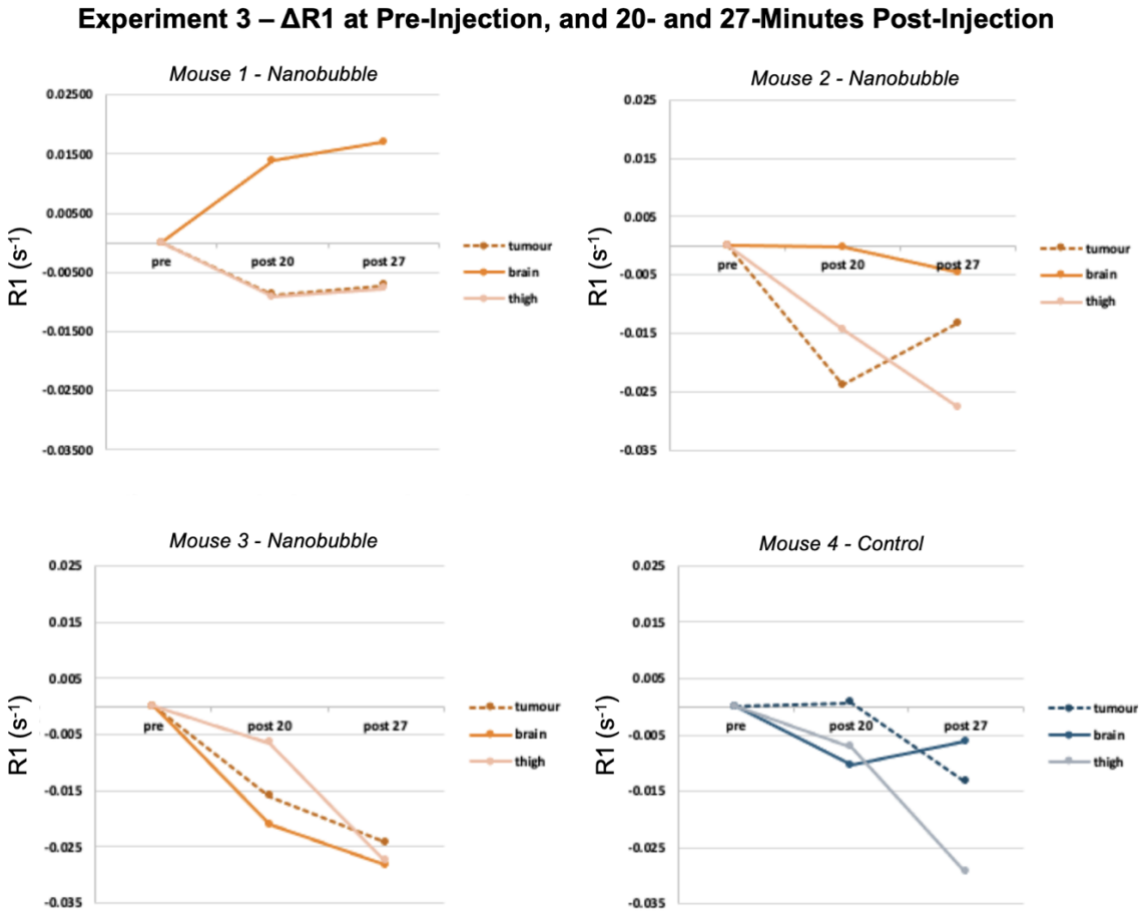


***Figure 3.5***. *The ΔR1 (post-pre injection) of the mean R1 measurements extracted from the three T1 maps timepoints in the tumour, thigh muscle, and brain ROI, in each of the four mice receiving either nanobubble injections (orange) or control injection (blue).*

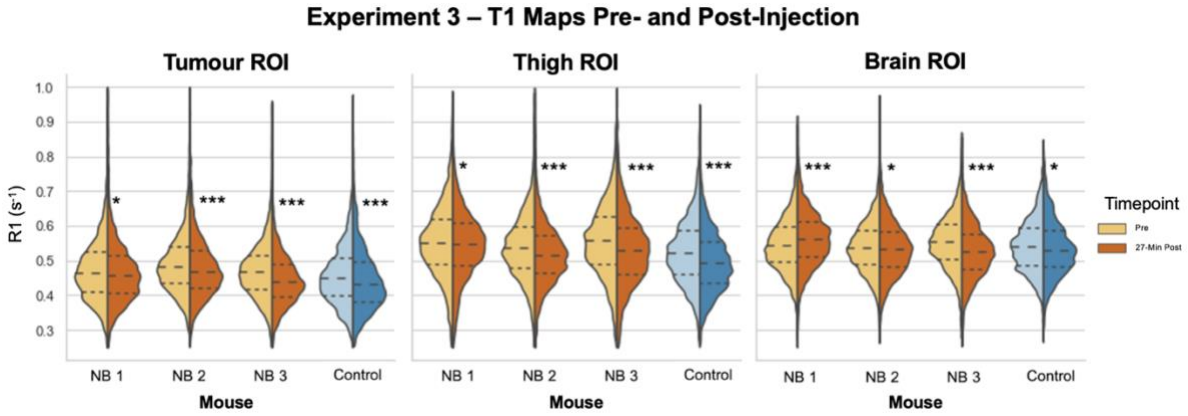


***Figure 3.6.*** *The distribution of R1 measurements extracted from the T1 maps in the tumour, thigh muscle, and brain ROI, pre and post the nanobubble injection (n=3) and control injection (n=1). R1 values before and after injection were compared statistically using a two-sample t-test assuming unequal variances, the resulting p-values of each change are displayed beside the respective violin plot: No Significance (N.S.), p<0.05 (*), p<0.001 (**), p<0.0001 (***).*

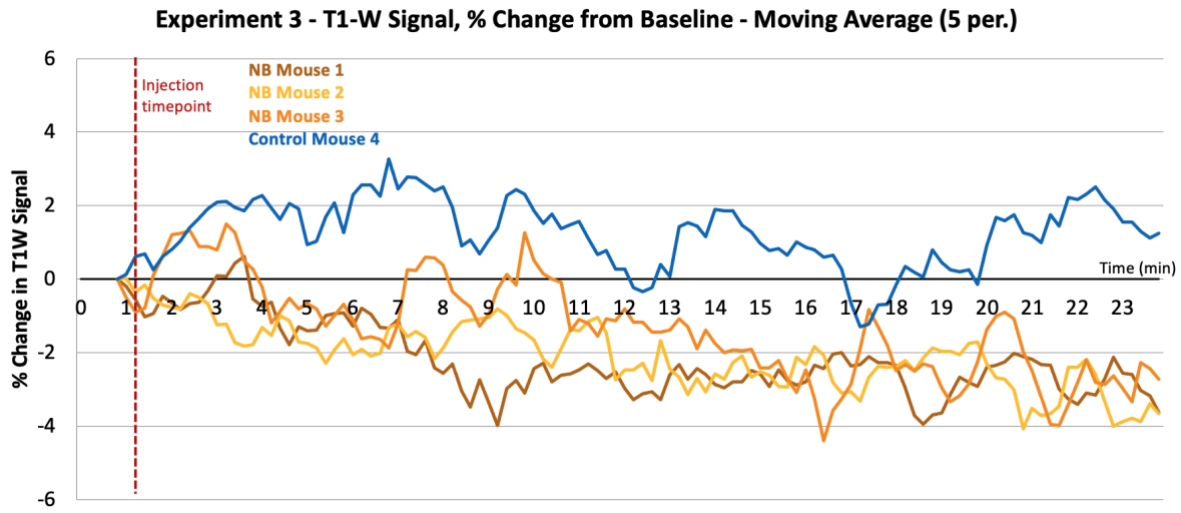


***Figure 3.7.*** *The temporal evolution of MRI T1-weighted % signal change from baseline in the tumour ROI of the four mice in Experiment 3. Baseline was calculated as the mean signal in the first 5 timepoints (pre-injection), and the plotlines displayed are the moving average (5 timepoints per period).*

***Table 3.3.*** *A table of the mean R1 measurements extracted from the T1 maps in the tumour, thigh muscle, and brain ROI, pre and post the nanobubble injection (n=3) and control injection (n=1), alongside the resulting ΔR1 ($s^{-1}$) calculated as [post-pre]. R1 values before and after injection were compared statistically using a two-Sample t-test assuming unequal variances, the resulting p-values of each change are displayed beside the respective violin plot: No Significance (N.S.), p<0.05 (*), p<0.001 (**), p<0.0001 (***).*

| MOUSE | Injection | T1 Map Data - Tumour ROI R1 ($s^{-1}$) | | | | T1 Map Data - Thigh ROI R1 ($s^{-1}$) | | | | T1 Map Data - Brain ROI R1 ($s^{-1}$) | | | |
|---|---|---|---|---|---|---|---|---|---|---|---|---|---|
| | | Mean R1 (±SD) | | | ΔR1 ($s^{-1}$) (post27-pre) | Mean R1 (±SD) | | | ΔR1 ($s^{-1}$) (post27-pre) | Mean R1 (±SD) | | | ΔR1 ($s^{-1}$) (pos27-pre) |
| | | Pre-Inject | Post-Inject 20 min | Post-Inject 27 min | | Pre-Inject | Post-Inject 20 min | Post-Inject 27 min | | Pre-Inject | Post-Inject 20 min | Post-Inject 27 min | |
| 1 | NB | 0.476 (0.1) | 0.467 (0.1) | 0.468 (0.1) | **-0.007*** | 0.556 (0.1) | 0.547 (0.2) | 0.548 (0.1) | **-0.007*** | 0.546 (0.1) | 0.560 (0.1) | 0.563 (0.1) | **+0.017***** |
| 2 | NB | 0.497 (0.1) | 0.473 (0.1) | 0.483 (0.1) | **-0.013***** | 0.549 (0.2) | 0.534 (0.1) | 0.521 (0.1) | **-0.027***** | 0.539 (0.1) | 0.539 (0.1) | 0.534 (0.1) | **-0.005*** |
| 3 | NB | 0.470 (0.1) | 0.454 (0.1) | 0.446 (0.1) | **-0.024***** | 0.563 (0.2) | 0.557 (0.2) | 0.536 (0.2) | **-0.027***** | 0.552 (0.1) | 0.531 (0.1) | 0.524 (0.1) | **-0.028***** |
| 4 | Control | 0.457 (0.1) | 0.458 (0.1) | 0.443 (0.1) | **-0.013***** | 0.527 (0.2) | 0.520 (0.1) | 0.497 (0.1) | **-0.029***** | 0.542 (0.1) | 0.531 (0.1) | 0.536 (0.1) | **-0.006*** |

***p<0.0001, **p<0.001, *p<0.05, N.S.=p>0.05

## 3.4. Discussion

In Chapter 2, the relationship between oxygen and R1 suggested that at 7T, R1 would change by 0.00057 $s^{-1}$/mmHg oxygen delivered. This means that for a change in $PO_2$ of 30 mmHg, a ΔR1 of +0.017 $s^{-1}$ should occur. In this chapter, the results of three pilot

preclinical experiments reported to test whether the oxygen delivery from the nanobubble injection was detectable using R1 measurements.

### 3.4.1. Experiments 1 & 2

The results of Experiment 1 were inconclusive; however they informed the design of Experiment 2. In Experiment 2, no discernible trend in signal change was observed in the T1-weighted signal data (Figure 3.4). However, the nanobubble injection induced a significant positive ΔR1 in the tumour (+0.034 $s^{-1}$), thigh (+0.022 $s^{-1}$), and brain ROIs (+0.032 $s^{-1}$), while the saline control injection induced a significant negative ΔR1 in the tumour and thigh ROIs and no change in the brain ROI (Figure 3.3). The changes in R1 measured in Experiment 2 correspond to the hypothesized signal change of the experiment: a +ΔR1 from nanobubble oxygen delivery, and a -ΔR1 or no change from dilution in the control. In addition, if these results indicate that the dilution from a 150 μL injection results in a ΔR1 of -0.021 $s^{-1}$, the positive R1 change induced by the nanobubble delivery would be large enough to not only cancel out the dilution effect but also induce a positive ΔR1. If the relaxivity slope reported in Chapter 2 is used to estimate oxygen delivery, these results would suggest a $\Delta PO_2$ in the tumour of 59-96 mmHg. However, the sample size in each group is n=1, so the results are inconclusive, and the experiment was altered slightly and repeated for Experiment 3.

### 3.4.2. Experiment 3, Repeatability, & Temperature

It is important to note that there were hardware changes made to improve SNR in between Experiment 2 and 3. No global artifacts were observed in the T1-maps in Experiment 3 (such as what occurred in mouse 3 of Experiment 2). In addition, the T1-weighted signal changes in Experiment 3 showed less variability between timepoints in Experiment 3. For Experiment 3, interestingly, across all 3 nanobubble injections, a negative T1-weighted signal change of 3-5% was seen, while the opposite occurred for the control injection of citric acid. However, the data from the T1 maps indicated negative R1 changes

in all ROIs from both nanobubble and control injections, with the one exception of a +R1 in the Mouse 1 brain ROI. These results did not agree with the results from Experiment 2: all 3 nanobubble-injection mice showed a -R1 instead of the +R1 seen in the Experiment 1 nanobubble injection. In addition, the control showed the opposite response, however that might be expected as citric acid could induce a different R1 change than saline.

A negative R1 change is what would be expected from the dilution effect from both the nanobubble and control injection, however, this consistent R1 decrease which conflicted with the T1-weighted results raised questions about the repeatability issues with the T1 mapping method. To help address this inconsistency, repeatability experiments were performed with phantoms to test our imaging setup (results reported in Chapter 2, see Figure 2.4). These phantom experiments showed that over 6 repeated VFA scans in 3 separate phantoms, the R1 decreased with each repeated scan. The temperature of the phantoms was measured during these scans, and a change in temperature correlated with the change in R1 measurements — the results showed a decrease in R1 at a rate of -0.037 $s^{-1}/°C$ ($R^2$=0.83), -0.028 $s^{-1}/°C$ ($R^2$=0.90), and -0.02 $s^{-1}/°C$ ($R^2$=0.91) (see Figure 2.4).

The mice were in the scanner for 20-27 minutes between the VFA scans, and while their core body temperature might regulate well (unlike the phantom, which continually warmed throughout the duration of the scanning session), it is possible that a tumour xenograft on the outside of the leg could have poorer temperature regulation than the body, either getting cold from the room temperature or warmer from the MRI excitation as heat energy. In addition to temperature, other possible causes of this consistent R1 decrease were investigated, shown in Table 3.4.

### 3.4.3. Post-Experiment Troubleshooting

The possible factors that could induce a change in R1 in these experiments are listed in Table 3.4, and for visualization purposes, the estimated R1 change from each factor is plotted in Figure 3.8. In addition to changes in R1 induced from oxygen delivery, additional

possible confounds in this experiment are the effects of dilution, temperature changes, pH or haemodynamic changes induced from an acidic injection, and even the nanobubble solution itself (without oxygen) which was shown to have a higher R1 than water in Chapter 2 even without oxygen added. In addition, although the hypothesized mechanism for oxygen delivery from these bubbles would be independent of the red blood cells, it is possible that if oxygen saturation is affected by these bubbles, that could induce a change in R1 as well.

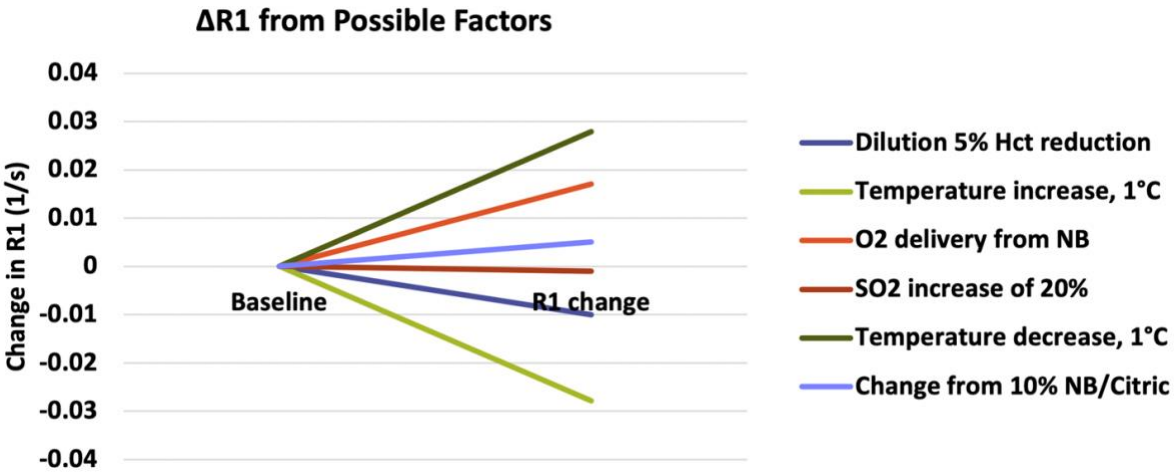


***Figure 3.8.*** *The roughly estimated R1 change from some possible factors that could induce a change in R1 in these pilot experiments. Reasoning behind each estimation is explained in Table 3.4.*

***Table 3.4.*** *The possible factors that could induce a change in R1 in the preclinical pilot experiments performed.*

| Changing Factor | NB | Saline | Citric Acid | R1 change | Reasoning & Estimated Effect Size |
|---|---|---|---|---|---|
| **Dilution from 150uL injection (10% blood volume)** | Yes | Yes | Yes | ⇩ R1 | A 5% Hct reduction would cause 0.2 $s^{-1}$ decrease in pure blood. If blood is 5% of voxel signal, then 0.05x-0.2 $s^{-1}$= -0.01 $s^{-1}$ for a 5%Hct reduction. |
| **Presence of 10% nanobubble solution even without oxygen** | Yes | No | Maybe | ⇧ R1 | In the 7T phantom experiment it's clear that a solution containing 100% non-oxygenated NBs has higher R1 than 100% water, by a 0.05$s^{-1}$ increase. Therefore, a 10% volume of nanobubble could cause a 10%x0.05$s^{-1}$ =+0.005$s^{-1}$ increase. |
| **Temperature change over experiment session** | Maybe | Maybe | Maybe | Temp⇧=⇩R1<br>Temp⇩=⇧R1 | Using the mean slope from experiments in Chapter 2,<br>ΔR1=Tx-0.0279 $s^{-1}$/°C<br>= 1°Cx-0.0279 $s^{-1}$/°C<br>= -0.0279 $s^{-1}$ |
| **Increase in tissue oxygen from delivery** | Yes | No | No | ⇧ R1 | Maximum possible change is ΔR1=r1*c, using r1 slope from Chapter 2 at 3T:<br>= 0.00057$s^{-1}$/mmHg x 30 mmHg<br>= +0.0171$s^{-1}$ |
| **pH decrease from acidic injection** | Maybe | No | Maybe | ⇩ R1 | Brookes [175], showed a 25% decrease in T1 per pH unit increase, but blood should buffer any pH changes so the change should be brief if anything. |
| **Possible blood $SO_2$ increase from oxygen delivery?** | Maybe | No | No | ⇩ R1 | Using relaxivity of deoxyhemoglobin measured by Blockley et al. [96], a 20% increase in $SO_2$ would cause a -0.021$s^{-1}$ change in R1 of pure blood. Assuming 5% blood volume, this could cause a ΔR1=0.05x-0.021$s^{-1}$=-0.00105$s^{-1}$ |

The resulting net ΔR1 from the effects listed in Table 3.4 suggests that both the citric acid and saline controls would be expected to produce a -ΔR1 of maximum -0.01 $s^{-1}$. For a 30 mmHg oxygen delivery to the tumour $PO_2$, the nanobubble solutions (taking dilution and the solution itself into consideration) would produce a +ΔR1 change of maximum 0.013 $s^{-1}$. In conclusion, the saline and nanobubble predictions match the ΔR1 changes seen in Experiment 2 in the T1 maps, however, do not match the ΔR1 changes seen in Experiment 3. In fact, they suggest that the nanobubble solutions in Experiment 3 did not increase the tumour $PO_2$ and instead, that the ΔR1 effects observed in the T1 maps were due to dilution from the injections. It is possible that absence of oxygen delivery is the cause of this — for example, it is possible that there was too much time post-oxygen sparging in the second session. This was a difficult experiment to carry out as there was a long delay (maximum 1.5

hours) between sparging and injection due to the sparging happening in a separate building from the scanning. Future experiments would benefit from planning the experimental set up to make it possible to sparge the solution immediately prior to injection, which would better represent the intended clinical use of these nanobubbles.

However, based on the temperature sensitivity in the phantom measurements reported in Chapter 2, a 1 °C temperature increase, causing a -0.028 $s^{-1}$ ΔR1, would be enough to result in a negative net ΔR1 for all control and nanobubble injections. Hence, it is possible that a temperature increase explains the ΔR1 seen in these experiments.

In addition to the potential temperature confound, the changes in R1 in Experiment 3 are not the first R1-$PO_2$ experiments to be confounded by dilution and R1 decrease effects. Although injections will not cause dilution effects in humans (due to the large volume of a human body), there have been dilution effects observed from drinking water: a very analogous experiment published in 2020 tried using T1 mapping to infer changes in $PO_2$ delivered by an oxygen-delivery drink [143]. In this experiment, the control drink (water) caused a 1.6% increase ($p<0.001$) in T1 in blood of the hepatic portal vein, and the oxygen drink caused an additional 0.7% increase ($p=0.028$) in T1. This *increase in T1* from the addition of oxygen in the drink is contrary to the hypothesis of the R1-$PO_2$ relationship described in Chapter 2. The authors note this unexpected result, and propose one hypothesis that the “high oxygen content increases the absorption rate of water and thereby dilution of HPV blood” [143]. I hypothesize it is more likely that the oxygen drink is affecting the $SO_2$, hence increasing T1. Regardless of whether either hypothesis is true, it is interesting to note this unexpected T1 change from oxygen in these published results.

In conclusion, due to the hardware changes, repeatability issues, temperature sensitivity, and possible confounds, it was decided that further preclinical experiments should be postponed pending further investigation. However, in the Journal of Magnetic Resonance Imaging Editorial for the Vatnehol et al. paper, Desmond et al. suggest that

“future work could expand the interpretation of the T1 and T2* changes using quantitative models relating total blood oxygen content, $PO_2$ and $SO_2$ to the MRI measures… This would improve the specificity of the experiment by facilitating a distinction between hydration and oxygenation effects” [142]. It was this suggestion that motivated the creation of a quantitative model to better understand the expected T1/R1 changes induced from oxygen delivery, which is presented in the following chapters of this thesis.

## 3.5. Conclusion

In this chapter, the results of three pilot preclinical experiments are reported, the aim of which was to test whether the oxygen delivery from the nanobubble injection was detectable using R1 measurement. The results of the three experiments were not consistent with the simple R1-$PO_2$ relationship described in Chapter 2. They did, however, inspire investigations that exposed important possible confounding factors such as temperature. In addition, some of the findings were consistent with those reported for a similar experiment reported by Vatnehol et al. [143] of a contrary R1 response to increased oxygen. The contrary R1 responses obtained were the motivation for the quantitative model presented in the subsequent chapters.

# Chapter 4. A Model of Oxygen Relaxivity in Bodily Fluids

---

*In order to model the expected R1 response from nanobubble oxygen delivery, a value for the $r1_{Ox}$ in bodily fluids must be known. In this chapter, all reported $r1_{Ox}$ values from the literature in phantoms, saline and water solutions, and vitreous fluid are consolidated, which showed a large variability in values of $r1_{Ox}$. Therefore, a simplified model is proposed for estimating $r1_{Ox}$ in these fluids based with respect to the magnetic field and temperature, which is able to explain the majority of the variance in $r1_{Ox}$ values.*

*This chapter includes edited material from the following publication:*

- ***E Bluemke,** E Stride, D Bulte. A simplified empirical model to estimate oxygen relaxivity at different magnetic fields. NMR in Biomedicine, 2021. DOI:10.1002/nbm.4625*

---

## 4.1. Introduction

Many researchers have investigated using the paramagnetic relaxivity effect of oxygen on longitudinal relaxation as a means of inferring oxygenation levels for applications ranging from cancer therapy to seawater analysis [103], [106], [143], [146], [176]. For example, measurements of the longitudinal relaxation rate R1 (1/T1) have been used to infer oxygen levels in vitreous fluid as a non-invasive alternative to the highly invasive oxygen electrodes used to measure retinal hypoxia [102]–[104], bladder urine [105] and urine in the renal pelvis to create a non-invasive detection of renal dysfunction [106], and cerebrospinal fluid [105], [107], and this relationship between $PO_2$ and R1 is also the basis for oxygen-enhanced MRI techniques [177]–[179]. In the linear relationship between $PO_2$ and R1, the slope represents the relaxivity of oxygen, or $r1_{Ox}$, in that material. Unfortunately, however, there is considerable variability in the values reported for $r1_{Ox}$ from empirical measurements, and consequently, reliable quantification of $PO_2$ from R1 measurements presents a challenge.

This paper provides a summary of the empirical measurements reported in the literature, investigating the relationship between R1 and the partial pressure of oxygen in phantoms, saline and water solutions, and vitreous fluid. These experiments have been performed using different equipment and field strengths and reported with a variety of units. For consistency, therefore, all T1 values will be reported in [ms], R1 in [$s^{-1}$], and relaxivity in [$s^{-1}$/mmHg oxygen] with the corresponding field strength, temperature and material specified where these data are available. Next, a simplified empirical model is proposed for estimating $r1_{Ox}$ in water, saline, plasma, and vitreous fluids based on these reported literature values and report the resulting model parameters. The aim is to provide a useful review and tool for researchers seeking to quantify $PO_2$ in simple fluids, such as water and saline phantoms, or bodily fluids such as vitreous fluids, cerebrospinal fluids, and amniotic fluids. This model does not represent the $r1_{Ox}$ in blood or tissue, due to the addition of proteins, structure, cells,

lipids, and deoxyhaemoglobin that will affect the R1-$PO_2$ relationship, which will be addressed in Chapter 5.

## 4.2. Methods

### 4.2.1. Model Theory

The T1 (measured in ms), and its inverse, R1 (typically reported in $s^{-1}$), have both been used in the literature when reporting the relaxivity effect of oxygen. R1 is linearly dependent on the concentration of paramagnetic particles [101], [145], in this case, dissolved molecular oxygen in the solution, described by Equation 2.1 (in Chapter 2), where $R1_{Ox}$ is the relaxation rate in the solution with oxygen added, $R1_0$ is the relaxation rate in the solution without oxygen, C is the concentration or partial pressure of oxygen, and $r1_{Ox}$ is the relaxivity of oxygen in that solution (whose units depend on the oxygen measurement used in the constant C) (shown in Figure 4.1). Since the partial pressure of oxygen ($PO_2$) is a common measurement in biomedicine and clinical applications, in this thesis, C is reported as $PO_2$ in mmHg and $r1_{Ox}$ as $s^{-1}$/mmHg.

Both changes in T1 and R1 have been used to report changes in $PO_2$ in the past [152]. However, although an increase in oxygen could still qualitatively roughly be inferred from a shortening of T1, it is important to note that the linear relationship exists between 1/T1 (R1) – not T1 – and therefore the change in T1 caused by oxygen will be dependent on the original T1 (shown in Figure 4.2). Therefore, for a quantitative inference of $PO_2$ change it is necessary to discuss changes with respect to R1.

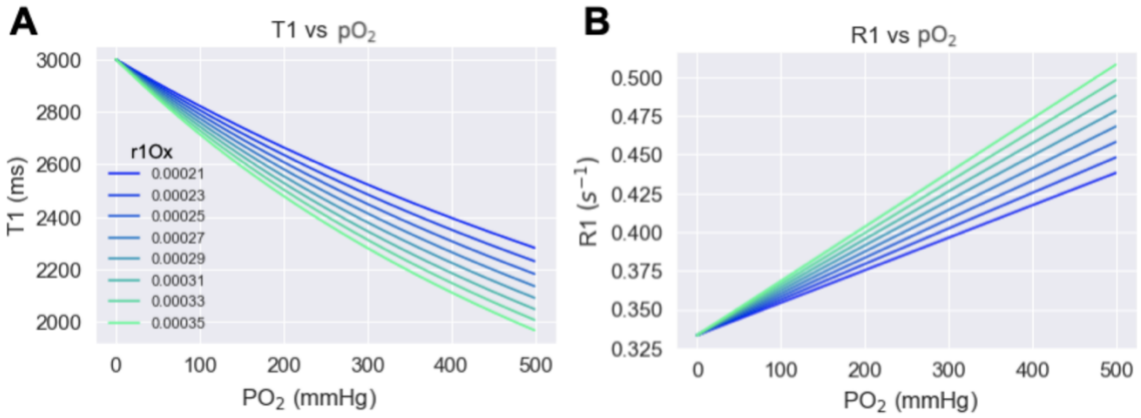


***Figure 4.1.*** *The relationship between* ***(A)*** *T1 vs $PO_2$ and* ***(B)*** *R1 vs $PO_2$ in a solution, with the initial T1 of 3000ms. The values are calculated using a range of $r1_{Ox}$ (relaxivity) reported in the literature at 1.5T, in units $s^{-1}$/mmHg oxygen.*

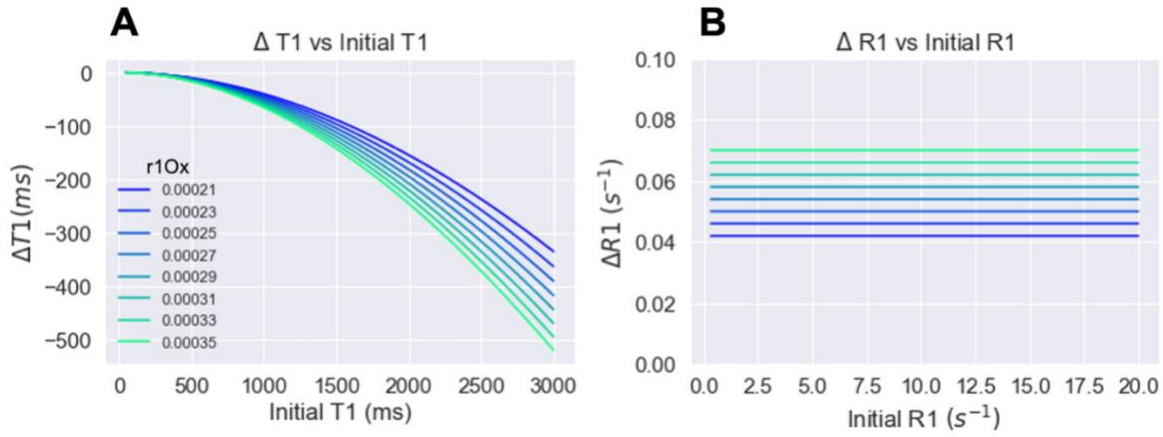


***Figure 4.2.*** *The relationship between* ***(A)*** *ΔT1 vs Initial T1 and* ***(B)*** *ΔR1 vs Initial R1, for a $\Delta PO_2$ of 200 mmHg. The values are calculated using a range of $r1_{Ox}$ (relaxivity) reported in the literature at 1.5T, in units $s^{-1}$/mmHg oxygen.*

The $r1_{Ox}$, or relaxivity of oxygen is affected by various experimental factors, including field strength. Equations already exist to determine the relationship between field strength and R1; in 2001, Teng et al. [171] measured the proton spin-lattice relaxation rate in water as a function of magnetic field strength at 1 atm of oxygen (approximately 760 mmHg) and found that the magnetic relaxation dispersion due to the paramagnetic contribution from

molecular oxygen is well approximated by a Lorentzian shape, for which they proposed the following equation:

$$\frac{1}{T1_{Ox}} = A\frac{\tau}{1+\tau^2{\omega_s}^2} + B \quad \text{(Eq 4.1)}$$

Where A and B are constants, $\omega_S$ is the electron Larmor frequency, and t is the correlation time for the electron-nuclear coupling (empirically measured to be 6.8±0.5 ps in water) [171]. One variable of particular interest for medical imaging research is field strength, which can be related to the electron Larmor frequency above ($\omega_S$) by the electron gyromagnetic ratio ($\gamma_e$= 1.76x$10^{11}$ rad $s^{-1}$ $T^{-1}$) and Larmor equation $\omega_s = \gamma_e B0$. By substituting $\omega_s = \gamma_e B0$ into Equation 4.1, the following equation is obtained:

$$\frac{1}{T1_{Ox}} = A\frac{\tau}{1+\tau^2{\gamma_e}^2B0^2} + B \quad \text{(Eq 4.2)}$$

From Equation 2.1, it is known that $1/T1_{Ox}$ is proportional to the relaxivity ($r1_{Ox}$), and from Teng et al. [171], it is known that the Lorentzian magnetic relaxation dispersion is due to the paramagnetic contribution from molecular oxygen. Therefore, the relationship between $r1_{Ox}$ and field strength will be well approximated by a similar Lorentzian equation with new constants:

$$r1_{Ox} = \frac{C_1}{1+C_2B0^2} + C_3 \quad \text{(Eq 4.3)}$$

Where $C_1$, $C_2$, and $C_3$ are new constants, and B0 is the magnetic field strength (T). It is worth noting that in Equation 4.3, $C_1$ will not be equal to A×t as it is in Equation 4.2, since Equation 4.2 is calculating R1 and Equation 4.3 is calculating $r1_{Ox}$ — while R1 and $r1_{Ox}$ should be proportional, there are additional multiplying or dividing factors that will be encompassed by $C_1$.

Lastly, the relaxivity of oxygen is also reported to be affected by temperature, as seen in the varied relaxivity measurements reported by Muir et al. [103]. To account for this,

a fourth constant ($C_{Temp}$) was added which represents the linear slope of relaxivity change due to temperature, resulting in the final Equation 4.4:

$$r1_{Ox} = \frac{C_1}{1 + C_2 B0^2} + C_3 + C_{Temp} * T \quad \text{(Eq 4.4)}$$

### 4.2.2. Data Collection and Analysis

The 28 reported values for oxygen relaxivity were collected from the literature, and all units were converted to $s^{-1}$/mmHg oxygen, shown in Table 4.1 alongside the field strength and material used in each experiment. If data extraction from graphs was necessary, a digital plot analyzer was used to reliably extract values [180].

The SciPy *optimize* function for nonlinear least-squares fitting was used [181]. Equation 4.4 was fitted using a randomized subset of 90% of the 28 literature data points in Table 4.1, fitting with the B0 and temperature values simultaneously. The dataset was split into randomized subsets for fitting using the sklearn *train_test_fit* function with shuffling [182]. This process was iterated 1000 times, and the median and 95% confidence interval of the distribution of fitted values for each parameter were used as the final parameters (listed in Table 4.2). Violin plots showing the distribution of parameter estimates from each iteration are shown in Appendix Figure B.1. Following the model fitting, all 4 final parameter values were substituted into Equation 4.4, and the accuracy of the model's predicted $r1_{Ox}$ was compared against the 'true' $r1_{Ox}$ values, shown in Figure 4.3.

## 4.3. Results

As shown in Table 4.1, 28 total measurements of $r1_{Ox}$ were found: 7 measured in saline solutions [100], [104], [105], [152], [155], 18 in water [103], [105], [108], [153], [156], [176], [183], 1 in vitreous fluid [104], and 2 in plasma (*ex vivo*) [152], [154]. The measurements were collected at field strengths ranging from 0.011-8.45T and temperatures ranging from 21-40°C. 12 additional values of $r1_{Ox}$, measured in blood (*ex vivo* [110], [152], [154] and *in vivo* [108], [184]) and tissues (lung [170] and brain [157]), were also found

(provided in Appendix Table B.1), however these were not included in the model fitting because blood and tissues will contain factors not accounted for in this model (see Discussion).

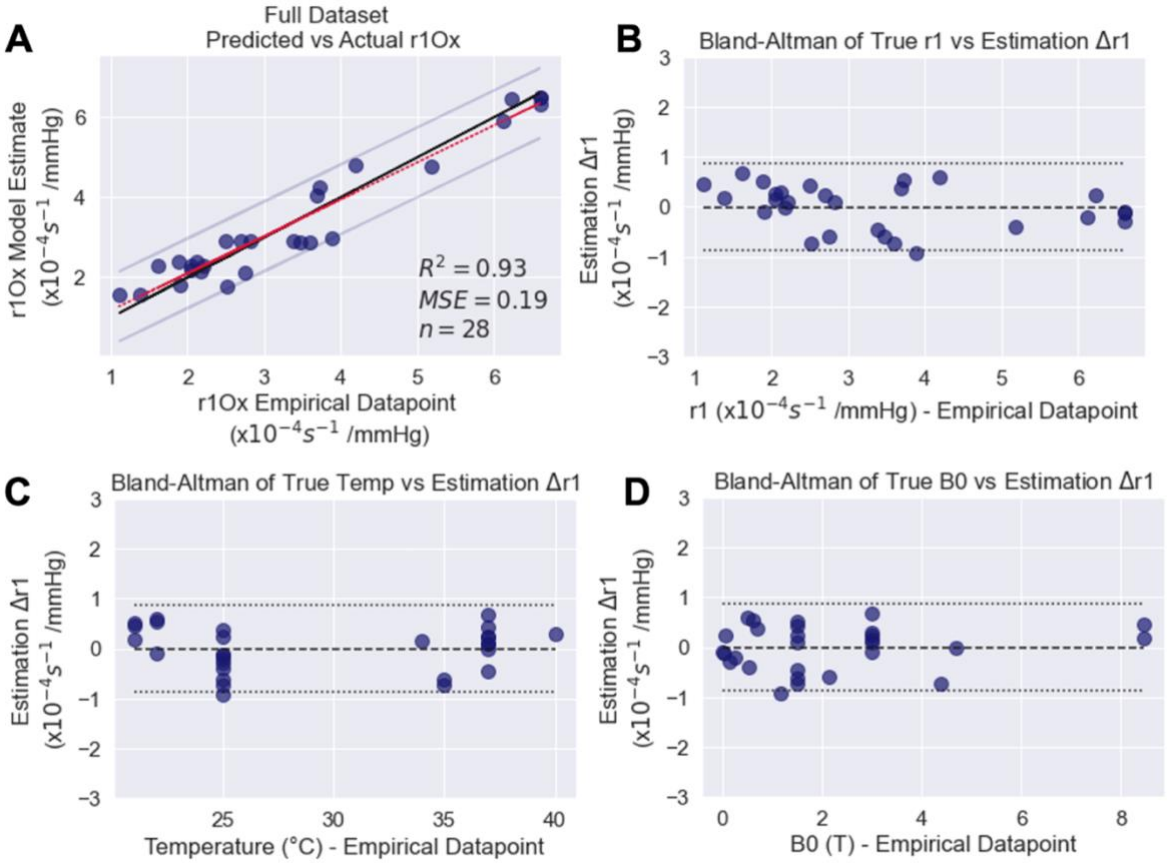


***Figure 4.3. (A)*** *The modelled vs measured $r1_{Ox}$ values, plotted against the line of equality (solid black line) and a linear regression (red dotted line, $R^2$=0.93).* ***(B)*** *A Bland-Altman plot showing the difference between the modelled and measured values of $r1_{Ox}$. The horizontal long-dashed lines show the mean value of $\Delta r1_{Ox}$ (-0.005 $s^{-1}x10^{-4}$/mmHg), and the horizontal dotted lines show the limits of agreement (long dashes, calculated by mean($\Delta r1_{Ox}$) ± (1.96xSD($\Delta r1_{Ox}$)). Bland-Altman plots for the error in modelled $r1_{Ox}$ against* ***(C)*** *temperature, and* ***(D)*** *field strength are also shown to examine bias in the model.*

The final values for the 4 parameters $C_1$, $C_2$, $C_3$, and $C_{Temp}$ (with lower and upper 95% confidence intervals) are listed in Table 4.2. The predicted versus true $r1_{Ox}$ values are plotted against the line of equality (solid black line) and a linear regression (dotted line, $R^2$=0.93) in Figure 4.3A, with a final mean squared error (MSE) of 0.19x$10^{-4}$ ($s^{-1}$/mmHg)$^2$. To examine bias in the model with respect to $r1_{Ox}$, B0, and temperature variables, Bland-Altman

plots are provided in Figure 4.3B-D. The performance of the model on the subset of water measurements only ($R^2$=0.94) and saline measurements only ($R^2$=0.73) are provided in Appendix Figure B.3.

The modelled vs measured $r1_{Ox}$ values from the randomized unseen test set of each iteration is plotted in Appendix Figure B.2A alongside the line of equality and the linear regression ($R^2$=0.90, MSE=0.26 ($x10^{-4}$ $s^{-1}$/mmHg)$^2$). The difference between the modelled and measured $r1_{Ox}$ values from the randomized unseen test set of each iteration is illustrated as Bland-Altman plots in Appendix Figure B.2(B-D).

To understand the behaviour of the resulting model, the effect of varying field strength on $r1_{Ox}$ is illustrated using synthetic data under varying temperatures (Figure 4.4), and the linear effect of varying temperature on $r1_{Ox}$ is illustrated using synthetic data under varying field strengths (Appendix Figure B.4). The resulting model prediction is also shown over a scatterplot of the $r1_{Ox}$ of the 28 literature points in Figure 4.5.

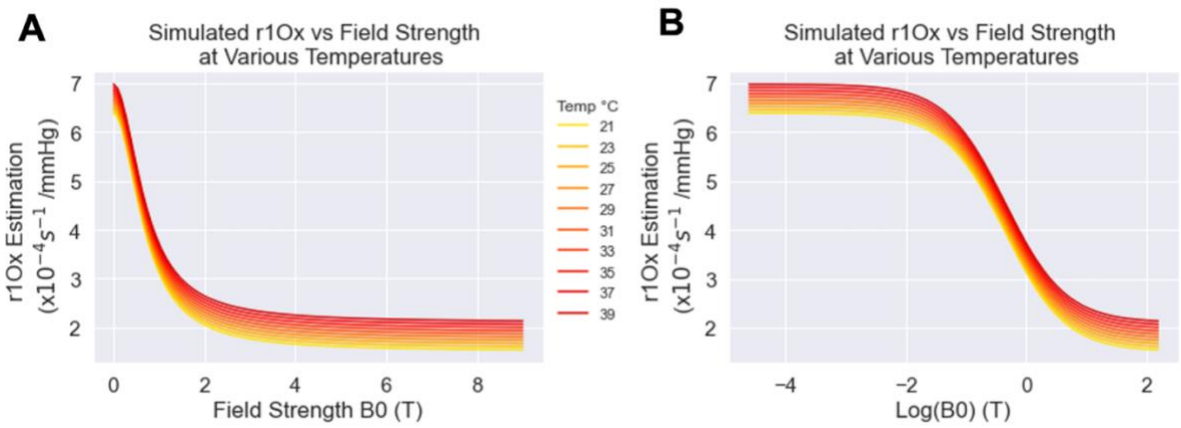


***Figure 4.4.*** *Plots with simulated data to illustrate the behaviour of Equation 4.5 (with the fit parameter values) with respect to* ***(A)*** *B0 and* ***(B)*** *log(B0) for a variety of temperatures.*

***Table 4.1.*** *A collection of 28 reported values for oxygen relaxivity from the literature with all units to [$s^{-1}$/mmHg oxygen] alongside the field strength and material used in each experiment. Temperature is indicated where it was reported. The MRI acquisition details from each experiment are listed in Appendix Table B.3. *Temperature not reported, assumed 37°C*

| Reference | $r1_{Ox}$ ($s^{-1}$/mmHg) x$10^{-4}$ | Field strength (T) | Temp (°C) | Material |
|---|---|---|---|---|
| Matsumoto et al., 2006 | 2.17 | 4.7 | 37 | Saline |
| Zaharchuk et al., 2005 | 2.7 | 1.5 | 37 | Saline |
| d'Othée et al., 2003 | 1.38 | 8.45 | 21 | Saline |
| d'Othée et al., 2003 | 1.90 | 1.5 | 21 | Saline |
| Kramer et al., 2013 | 2.82 | 1.5 | 37* | Saline |
| Kramer et al., 2013 | 2.21 | 3 | 37* | Saline |
| Simpson et al., 2013 | 3.6 | 1.5 | 35 | Saline |
| Pilkinton et al., 2012 | 1.61 | 3 | 37 | Water |
| Vatnehol et al., 2020 | 1.9 | 3 | 22 | Water |
| Nestle et al., 2003 | 4.2 | 0.5 | 22 | Water |
| Hausser and Noack, 1965 | 3.72 | 0.63 | 22 | Water |
| Zaharchuk et al., 2006 | 2.49 | 1.5 | 37 | Water |
| Graf et al., 1980 | 6.60 | 0.011 | 25 | Water |
| Graf et al., 1980 | 6.60 | 0.031 | 25 | Water |
| Graf et al., 1980 | 6.23 | 0.051 | 25 | Water |
| Graf et al., 1980 | 6.60 | 0.137 | 25 | Water |
| Graf et al., 1980 | 6.13 | 0.259 | 25 | Water |
| Graf et al., 1980 | 5.18 | 0.525 | 25 | Water |
| Graf et al., 1980 | 3.68 | 0.713 | 25 | Water |
| Graf et al., 1980 | 3.89 | 0.159 | 25 | Water |
| Graf et al., 1980 | 2.74 | 2.139 | 25 | Water |
| Graf et al., 1980 | 2.51 | 4.387 | 25 | Water |
| Muir et al., 2013 | 2.04 | 3 | 34 | Water |
| Muir et al., 2013 | 2.05 | 3 | 37 | Water |
| Muir et al., 2013 | 2.11 | 3 | 40 | Water |
| Simpson et al., 2013 | 3.47 | 1.5 | 35 | Vitreous fluid |
| d'Othée et al., 2003 | 1.11 | 8.45 | 21 | Plasma (*ex vivo*) |
| Hueckel et al, 2000 | 3.38 | 1.5 | 37 | Plasma (*ex vivo*) |

***Table 4.2.*** *A summary of the final 4 parameter estimates from the model fitting. Multiply the final model $r1_{Ox}$ result by $10^4$ to get a relaxivity in units of $s^{-1}$/mmHg. * If using temperature in Kelvin, subtract 273.15 to convert your temperature to °C.*

| Parameter Name | Resulting Value from Fit (95% lower and upper confidence intervals) | Units* |
|---|---|---|
| $C_1$ | 4.87 (4.70, 5.04) | $x10^{-4}\ s^{-1}$/mmHg |
| $C_2$ | 1.99 (1.59, 2.38) | $T^{-2}$ |
| $C_3$ | 0.844 (0.452,1.24) | $x10^{-4}\ s^{-1}$/mmHg |
| $C_{Temp}$ | 0.0323 (0.0211, 0.0434) | $x10^{-4}\ s^{-1}$/mmHg /°C * |

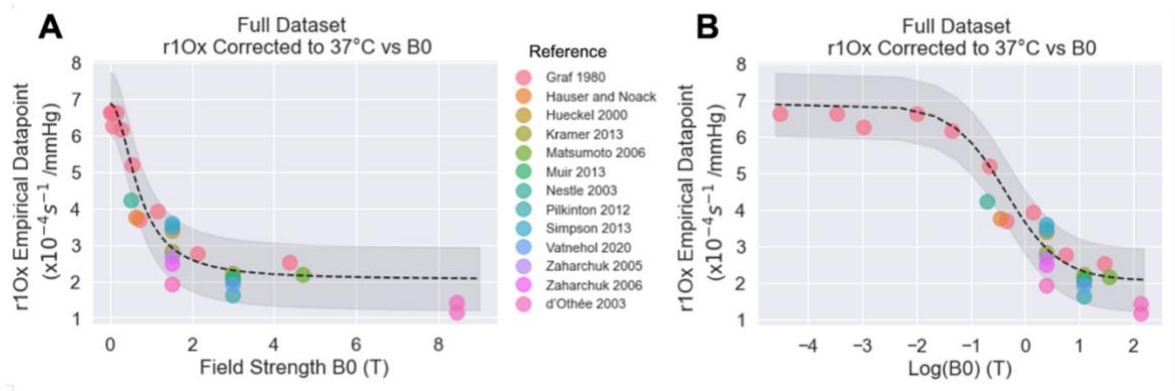


***Figure 4.5.*** *The $r1_{Ox}$ of the 28 literature points, plotted against **(A)** B0 and **(B)** log(B0) alongside the $r1_{Ox}$ estimated using the new model (black dashed line) at the appropriate B0, and 37°C with the 95% confidence interval shown in grey. For this plot only, each literature value has been linearly corrected to 37°C using the $C_{Temp}$ parameter.*

Since Equation 4.4 contains 4 parameters, the fitting process was repeated for all combinations of fewer parameters (e.g., removing $C_{Temp}$) and the Akaike Information Criterion (AIC) was calculated for each version of the model — the best-fit model according to the AIC is the model that explains the greatest amount of variation using the fewest possible independent variables [185]. The AIC score, $R^2$, and MSE results of the different models tested are listed in Appendix Table B.2. The model with all 4 parameters scored the highest according to the AIC and was therefore used in this thesis. Removing only $C_3$ produced the second-highest AIC score and removing only $C_{Temp}$ produced the third highest AIC score. The resulting predicted versus true $r1_{Ox}$ values and parameter distributions from each model are shown in Appendix Figure B.5.

## 4.4. Discussion

I have compiled empirical measurements of the relaxivity of oxygen over 50 years of MRI research in phantoms, saline and water solutions, plasma, and vitreous fluid, ranging from 0.011-8.45T and 21-40°C. While the reported relaxivity of oxygen varied greatly, it was found that in the solutions of water, saline, vitreous fluid, and plasma, the variance could largely be explained by the differences in field strength and temperature, and that this variation was well approximated by a Lorentzian function and linear relationship with temperature. Therefore, while the table of reported $r1_{Ox}$ empirical measurements can be referred to for future oxygen-MRI experiments, the $r1_{Ox}$ can also be estimated using the proposed simplified model for estimating the $r1_{Ox}$ in water, saline, plasma, and vitreous fluids that agrees well with the empirical measurements. This will provide a useful resource for researchers seeking to quantify $PO_2$ in simple fluids, such as water and saline phantoms, or bodily fluids such as vitreous fluids, cerebrospinal fluids, and amniotic fluids.

The relationship between longitudinal relaxation and the paramagnetism of oxygen has a long history in NMR, and there is a large body of both theoretical and empirical work [86], [101], [145]–[150]. For materials containing paramagnetic contrast agents, there can be complex relationships between R1 and field strength, and these relationships are affected by various factors inherent to the contrast agent [186]. This relationship between contrast agent relaxivity and the magnetic field is important, as it can obscure the reproducibility of MRI-oxygen experiments if performed at different field strengths and temperatures.

The physical mechanisms that explain the relationship between field strength and relaxivity are complex, and although there are sophisticated explanations for specific contrast agents [187]–[190], much of the modelling of this relaxivity relies on empirical measurements [191]. While there has been previous evidence for modelling relaxivity-B0 relationships as linear [192] or logarithmic [193], one major limitation is that the majority of relaxivity measurements of contrast agents are performed at only two field strengths (1.5T

and 3T), which makes it difficult to properly describe the true relationship from empirical results. Interestingly, to address this issue, an experiment by Chou et al. measured the relaxivity of a gadolinium-based contrast agent at a large range of field strengths 0-12T, revealing a curve that peaks around 1-2T and drops off (in a Lorentzian shape) as field strength increases [187]. While these data are from a gadolinium-based contrast agent rather than oxygen, it suggests that the relationship of oxygen relaxivity and magnetic field strength may also follow a more complex curve than simply linear, or logarithmic. Therefore, for any modelling of relaxivity, it is important to state the range of field strengths over which the model is valid. The lowest field strength used to fit this model was 0.011 T, and below this field strength, it is likely that the $r1_{Ox}$ curves back down to zero as field strengths approaches zero, in a similar manner to the pattern seen by Chou et al. [187], which has been reproduced in Appendix Figure B.6.

### 4.4.1. Limitations

The relaxivity values collected were from experiments performed over a timespan of five decades with a huge variation in experimental equipment and temperature measurement techniques. Experimental measurement of $r1_{Ox}$ can be difficult even within a relatively simple system such as water, because the measurement accuracy depends on the proper selection of acquisition protocols and parameters (i.e. repetition and inversion times). For convenience, acquisition details from each experiment used in developing the present model are listed in Appendix Table B.3. MRI technology has advanced significantly since the measurements made in the 1980s, which account for the measurements made below 0.5 T, and low-field systems usually also suffer from poor signal to noise ratio. In addition, the values have often been extracted from original plots, some hand-drawn, which is a source of error, and converted from the various original units to $s^{-1}$/mmHg, which can be another source of error. Lastly, one experiment did not report the temperature of the solution during the experiment, and it was assumed to be at 37°C. These limitations inevitably represent a large source of potential error in the accuracy of this model. It is hoped, however, that this

can be addressed as the NMR community produces new measurements of $r1_{Ox}$ at a range of field strengths and temperatures. As a future direction of this work, the open-source model code and current $r1_{Ox}$ measurements have been hosted publicly on GitHub (github.com/BulteGroup/OxygenRelaxivityModel), making it possible for the NMR community to share new $r1_{Ox}$ measurement results and refit the model to improve accuracy and enhance the utility of the model.

Furthermore, for the fitting of this model, $r1_{Ox}$ values from water, saline, plasma, and vitreous fluids were combined. In reality, there are factors that would cause the relaxivity in these solutions to differ, even amongst saline solutions with different compositions and concentrations. The decision to combine them was due to a lack of sufficient data points at a range of field strengths and temperatures in each solution, however this is a considerable limitation, as it seems to fit more accurately to the water samples ($R^2$=.94) than saline samples ($R^2$=.73) alone (Appendix Figure B.3). Most importantly, values from the vitreous fluid and plasma would ideally be fit with separate models, as there are extra proteins in the plasma and vitreous fluid that have been shown to decrease the relaxivity slightly [104], [152], [154]. However, this simply was not possible due to a lack of available data points in the literature. As above, is it possible that this issue will be addressed as new data are acquired by future researchers.

### 4.4.2. Implications for Measurement of Nanobubble Oxygen Delivery

From this model, combined with the results from Chapter 2, it can be concluded that oxygen relaxivity will be stronger at lower field strengths. Thus, for $PO_2$-R1 experiments, it could be most effective to perform them at lower field strengths to take advantage of the larger signal change. In particular, this model shows that oxygen has a very large effect on R1 at low fields, especially below 1.5T. Although 1.5T has been the most common scanner strength used clinically for decades, there are exciting possibilities of low-field MRI (defined as 1-199mT [194]) increasing in popularity in the future due to its low cost, low foot-print, and

better accessibility for patients [195]. Therefore, since the effect of oxygen on R1 will be roughly 3 times stronger at 1-199mT compared to 1.5T, it is possible that future low-field scanners will provide a more sensitive method for detecting changes in $PO_2$ from R1.

However, while the relaxation rate of a contrast agent can vary with field strength, the native T1 ($T1_0$) does as well [196]. Thus, in order to calculate the change in contrast per change in field strength, the change in T1 may also be a relevant factor. This brings up an important point about contrast. For a T1-weighted image, the resulting contrast, or percent change in tissue relaxation from the contrast agent can be calculated using the equation [197], [198]:

$$\%\Delta\frac{1}{T1} = \frac{\frac{1}{T1_{Ox}} - \frac{1}{T1_0}}{\frac{1}{T1_0}} = T1_0 r1_{Ox}[C]*100\% \quad \text{(Eq 4.5)}$$

Where $T1_0$ is the baseline T1 and $T1_{Ox}$ is the T1 following the administration of oxygen (or a contrast agent). In this T1-weighted example (Equation 4.5), for a contrast agent with constant relaxivity at two fields, the actual T1 change would be greater at the higher field because the baseline T1 ($T1_0$) is higher.

However, if one is using T1 mapping and only measuring the ΔR1 or Δ(1/T1) to try to infer [*C*], then:

$$\Delta\frac{1}{T1} = \frac{1}{T1_{Ox}} - \frac{1}{T1_0} = r1_{Ox}[C] \quad \text{(Eq 4.6)}$$

In this T1 mapping example (Equation 4.6), a greater $r1_{Ox}$ would result in a greater Δ1/T1 for the same change in contrast agent concentration. In summary, this model suggests that field strength dependency should be considered when planning future experiments using R1 to infer $PO_2$ changes. Most importantly, however, in order to create a model estimating ΔR1 in tissues following oxygen delivery, the value of $r1_{Ox}$ in tissues must be known, a problem that will be addressed in Chapter 6.

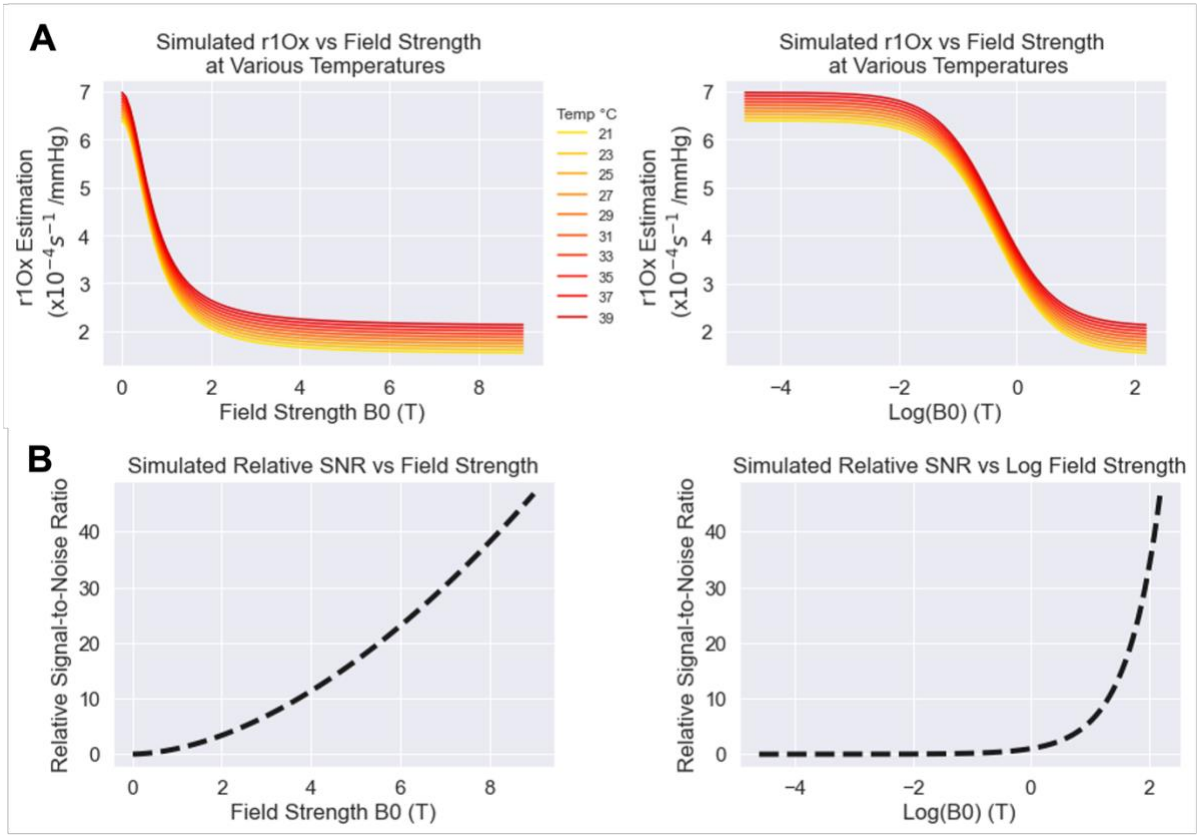


***Figure 4.6.*** *Plots with simulated data to illustrate the behaviour of* ***(A )*** *$r1_{ox}$ and* ***(B)*** *relative signal to noise ratio (SNR) with respect to B0 and log(B0).*

In addition, this model suggests that a 1.5T scanner may be preferred over a higher field MRI in future experiments for detecting the change in oxygen caused by nanobubbles. While the oxygen relaxivity would be even stronger below 1.5T, for extremely low fields, main challenges for low-field MRI is the loss in SNR: a generally accepted assumption is that SNR scales with the static magnetic field $B0^{7/4}$ above 0.11T [195]. A simple simulation of this scaling is shown in Figure 4.6 alongside the corresponding increase in $r1_{Ox}$ as B0 increases. With further work, it may be possible to use this information to pinpoint what field strength provides the best trade-off between keeping high enough SNR while exploiting the stronger relaxivity of oxygen. However, it is possible that with a combination of high performance acquisition techniques and detectors and future image processing techniques, low-field MRI will continue to improve image quality despite SNR challenges at lower field strengths [194], [195].

## 4.5. Conclusion

In order to model the expected R1 response from nanobubble oxygen delivery, a value for the $r1_{Ox}$ in bodily fluids must first be known. Therefore, in this chapter, an overview of the literature reporting a relationship between longitudinal relaxation and oxygen in phantoms, saline and water solutions, and vitreous fluid is provided. In addition, a simplified model for estimating the $r1_{Ox}$ in water, saline, plasma, and vitreous fluids that agrees well with the empirical measurements ranging from 0.011-8.45T and 21-40°C was created. This model does not represent the $r1_{Ox}$ in blood and tissues, where the addition of proteins, lipids, and deoxyhaemoglobin will affect the R1-$PO_2$ relationship. Therefore, in Chapter 5, a separate general model to calculate the R1 of blood is presented, accounting for haematocrit, oxygen saturation, oxygen partial pressure, and magnetic field strength under hyperoxic conditions.

# Chapter 5. A Model of Blood R1 in Response to Hyperoxia

---

*In order to model the expected R1 response from nanobubble oxygen delivery, the expected R1 change in blood following an increase in oxygen must be known. Therefore, in this chapter, a general model to calculate the R1 of blood is presented, accounting for haematocrit, oxygen saturation, oxygen partial pressure, and magnetic field strength under hyperoxic conditions.*

*This chapter includes edited material from the following publication:*

- ***E Bluemke**, E Stride, D Bulte. A general model to calculate the spin-lattice relaxation rate (R1) of blood, accounting for hematocrit, oxygen saturation, oxygen partial pressure, and magnetic field strength under hyperoxic conditions. Journal of Magnetic Resonance Imaging, 2021. DOI:10.1002/jmri.27938*

*A subset of these results was presented at the following conference:*

1. ***E Bluemke,** E Stride, D Bulte. A general model to calculate the spin-lattice relaxation rate (R1) of blood, accounting for hematocrit, oxygen saturation, oxygen partial pressure, and magnetic field strength under hyperoxic conditions. British Chapter of International Society for Magnetic Resonance in Medicine MR-Fest, 2021. Digital Poster.*

   *Awarded 1st Place Poster Award in "Body MR" Category.*

---

## 5.1. Introduction

This thesis aims to examine whether the change in oxygen caused by the nano-carriers can be detected using clinically available MRI techniques. This chapter examines why this assumption of a linear relationship between oxygen and R1 falls short when experimenting with one of the most important fluids in medicine: blood.

Under normal physiological conditions, the relaxation rate in blood is influenced by many factors, including haematocrit, field strength, temperature, protein concentrations, and the weak paramagnetic effects of deoxyhaemoglobin and dissolved oxygen in the plasma [96], [110]. In addition, evolving techniques such as oxygen-enhanced MRI require high fractions of inspired oxygen to induce hyperoxia, which complicates the R1 signal further [100], [144], [178], [199]–[201]. Whilst a linear increase in R1 with oxygen partial pressure has been reported in phantom experiments, measurements in blood have produced contradictory effects, in some cases showing an unexpected decrease in R1 following an delivery of oxygen [143].

In response to these contradictory results, a recent Journal of Magnetic Resonance Imaging Editorial by Desmond et al. suggests that “future work could expand the interpretation of the T1 and T2* changes using quantitative models relating total blood oxygen content, $PO_2$ and $SO_2$ to the MRI measures” [142]. Existing models for predicting R1 in blood can account for $SO_2$, haematocrit, and magnetic field strength, but are not applicable under conditions of artificially increased $PO_2$, or hyperoxic experiments [192]. Therefore, our aim was to establish a general model that could estimate the R1 of blood, accounting for haematocrit, $SO_2$, $PO_2$, and magnetic field strength under both normal physiological and hyperoxic conditions.

## 5.2. Methods

### 5.2.1. Background Theory

The relationship between longitudinal relaxation and the paramagnetism of oxygen in blood has a long history in MRI, beginning when Young et al. [86] and Tripathi et al. [184] found that increasing inspired oxygen fractions led to a small but definite increase in the R1 of blood in the left ventricle (i.e., oxygenated blood), but no change in R1 in the right ventricle (i.e., deoxygenated blood). To identify the physiology underlying these contrast changes, experiments using the vitreous fluid of the eye [102] and *ex vivo* blood samples at varying levels of oxygenation led to the hypothesis that the paramagnetic dissolved oxygen in the plasma provides the contrast during hyperoxia [151]. This hypothesis was confirmed in *ex vivo* blood samples by d'Othee et al. [152], where measurements of the *bound* and *dissolved* oxygen plotted alongside the measured R1 (reproduced in Appendix Figure C.1) showed that following full oxygen saturation, the R1 of blood increases linearly with increasing dissolved oxygen, while the bound oxygen remains constant. Prior to full oxygen saturation, however, experiments by Silvennoinen et al. [110] showed that the main source of contrast change is caused by changing levels of paramagnetic deoxyhaemoglobin, where R1 decreased linearly as $SO_2$ increased (i.e., with decreasing deoxyhaemoglobin concentration).

In 2016, Hales et al. published a general model to calculate the spin-lattice relaxation time constant (T1) of blood, accounting for haematocrit, $SO_2$ and magnetic field strength [192]. The model built upon a two-compartment model proposed by Grgac et al. [202], in which a fast-exchange model [203] was used to describe blood R1 because the water exchange rate between the plasma and cytoplasm is faster than the difference in R1 between these two compartments [132], [202], [204], given by:

$$R1_b(SO_2) = f_e R1_e SO_2 + (1 - f_e) R1_p \quad \text{(Eq 5.1)}$$

where $R1_b$ is the relaxation rate of whole blood, $SO_2$ is the oxygen saturation fraction (0-1), $R1_p$ is the longitudinal relaxation rate of plasma ($s^{-1}$), and $R1_e$ is the longitudinal relaxation rate of erythrocytes ($s^{-1}$).

The variable $f_e$ is the fraction of water in whole blood that resides in erythrocytes (0-1), which is described by the equation:

$$f_e(Hct) = \frac{W_{RBC}\ Hct}{W_{RBC}Hct + W_{plasma}(1-Hct)} \quad \text{(Eq 5.2)}$$

where Hct is the haematocrit (range of 0-1), $W_{RBC}$ is the volume fraction of water within the erythrocyte (typically valued at 0.70 due to haemoglobin occupying approximately 30% of the erythrocyte volume) and $W_{plasma}$ is the volume fraction of water within the plasma (typically valued at 0.95, where the other 5% volume is occupied by plasma proteins such as albumin) [204].

Hales et al. extended this model to account for the effect that deoxyhaemoglobin has on $R1_e$, as a paramagnetic contrast agent, expressing $R1_e$ as a function of $SO_2$:

$$R1_e(SO_2) = R1_{eox} + r1_{dHb}[Hb](1 - SO_2) \quad \text{(Eq 5.3)}$$

where $R1_{eox}$ is the relaxation rate of erythrocytes when $SO_2$=100%, [Hb] is the mean corpuscular haemoglobin concentration (5.15 mmol Hb tetramer/L plasma), and $r1_{dHb}$ is the molar relaxivity of deoxyhaemoglobin (in $s^{-1}$ L plasma in erythrocyte/mmol Hb tetramer). Combining Equations 5.1-5.3 results in the following model for calculating R1 of blood (Equation 5.4):

$$R1_b(SO_2) = f_e\big(R1_{eox} + r1_{dHb}[Hb](1 - SO_2)\big) + (1 - f_e)R1_p \quad \text{(Eq 5.4)}$$

In addition, Hales et al. modelled $R1_{eox}$, $R1_p$, and $r1_{dHb}$ to have a linear dependence on B0 (where $\beta_0$ and $\beta_1$ are the y-intercept and slope for the linear fit):

$$R1_{eox}(B0) = \beta_{0,R1_{eox}} + \beta_{1,R1_{eox}}B0 \quad \text{(Eq 5.5)}$$

$$R1_p(B0) = \beta_{0,R1_p} + \beta_{1,R1_p} B0 \quad \text{(Eq 5.6)}$$

$$r1_{dHb}(B0) = \beta_{0,r1_{dHb}} + \beta_{1,r1_{dHb}} B0 \quad \text{(Eq 5.7)}$$

Hales et al. fit this model to 42 data points from the literature with R1 measured at various Hct, $SO_2$, and B0 (1.5-7T). If the data were not acquired at 37°C or in vivo, the T1 values were increased to account for the shift in R1 caused by the difference in temperature (by 12% for a shift from 22°C to 37°C). From this model and subset of data, Hales et al. obtained values for the five parameters $\beta_{0,R1eox}$, $\beta_{1,R1eox}$, $\beta_{0,r1dHb}$, $\beta_{0,R1p}$, and $\beta_{1,R1p}$. In the fitting process performed by Hales et al., $\beta_{1,r1dHb}$ was found to be almost zero and it was concluded that $r1_{dHb}$ was not dependent on field strength [192].

## 5.2.2. New Model

The fitted value for $r1_{dHb}$ of 0.033 ($s^{-1}$ L plasma in erythrocyte/mmol Hb tetramer) from Hales et al. lies between the mean fitted values of 0.052 and 0.012 ($s^{-1}$ L plasma in erythrocyte/mmol Hb tetramer) estimated previously [96], [202]. However, these estimates do not agree with empirical results from Silvennoinen et al. [110], who from their data, estimated that the R1 in erythrocytes decreased with oxygenation level linearly with the equation 1.46 $s^{-1}$ – 0.60 $s^{-1}$ $SO_2$. When divided by 5.15 (mmol Hb tetramer/L plasma), the $r1_{deoxyHb}$ is -0.117 $s^{-1}$ L plasma in erythrocyte/mmol Hb tetramer, which is a greater effect on R1 than the $r1_{dHb}$ estimated by Hales et al. This disagreement is likely explained by a key limitation of Equation 5.4, i.e., that there is no parameter accounting for the change in plasma R1 caused by increasing partial pressure of oxygen due to changing $SO_2$.

To address this limitation, I defined a new parameter, $r1_{pox}$, the relaxivity of dissolved oxygen in the plasma in $s^{-1}$ /mmHg oxygen (Equation 5.8), which was modelled as having a linear dependence on field strength (Equation 5.9) in the same manner as Hales et al. have for $r1_{dHb}$, $R1_{eox}$, and $R1_p$ (Equations 5.5-5.7):

$$R1_b(SO_2, PO_2) = f_e\left(R1_{eox} + r1_{dHb}[Hb](1 - SO_2)\right) + (1 - f_e)(R1_p + r1_{pOx}PO_2) \quad \text{(Eq 5.8)}$$

$$r1_{pOx}(B0) = \beta_{0,r1_{pOx}} + \beta_{1,r1_{pOxB0}} B0 \quad \text{(Eq 5.9)}$$

Although Equations 5.5-5.7 and 5.9 have been modelled as linear, the true relationship between field strength and both R1 and the relaxivity (r1) is nonlinear and depends on the material [160], [186], [187], [191]. For R1, protons in highly mobile molecules such as water or plasma will be less affected by changing field strength, whereas in materials such as biological tissues the R1 has been empirically shown to decrease as field strength increases by approximately $B0^{-⅓}$ (see Figure 5.1A-B) [160]. However, when examined from the range of 1.5-7T, measurements by Rooney et al. (provided in Figure 5.1B) suggest that using a linear model for $R1_{eox}(B0)$ (Equation 5.5) and $R1_{p}(B0)$ (Equation 5.6) is appropriate in the field strength range of this model (1.5-8.45T). Similarly, an experiment by Chou et al. [187] measured the relaxivity (r1) of paramagnetic contrast agents over a large range of field strengths (0-12 T), revealing a Lorentzian shape (reproduced in Figure 5.1C-D). However, when only examined between the range of 1.5-8.45T, the measurements by Chou et al. [187] suggest that using a linear model for $r1_{dHb}(B0)$ (Equation 5.7) and $r1_{Ox}(B0)$ (Equation 5.9) is appropriate in the field strength range used in this model (1.5-8.45T). Therefore, a linear model has been chosen for Equations 5.5-5.7 and 5.9.

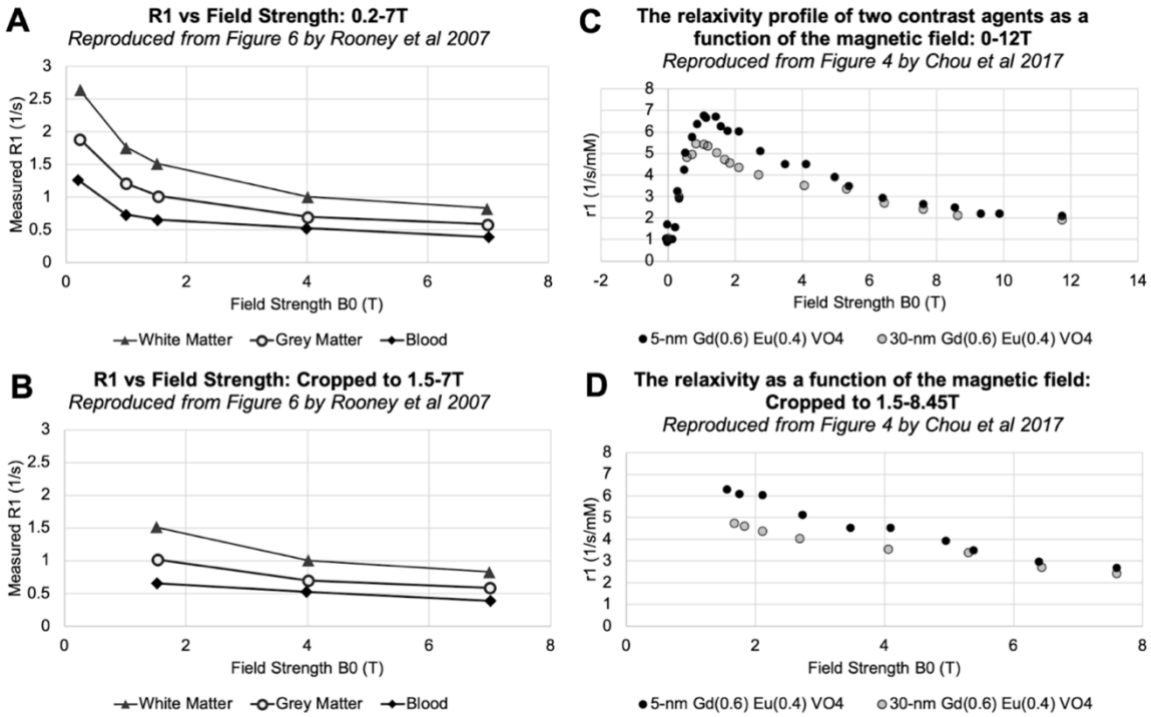


***Figure 5.1. (A-B)*** *Reproduced data Figure 6 of Rooney et al.* [160]*, showing the measured R1 of white matter, grey matter, and blood measured at* ***(C)*** *a range of field strengths 0.2-7T and* ***(D)*** *cropped to only show 1.5-7T.* ***(C-D)*** *Reproduced from Figure 4 from Chou et al.* [187]*, showing the relaxivity profiles of 5-nm and 30-nm gadolinium vanadate nanoparticles with and without Eu-ion doping are presented as a function of the magnetic field.*

Equation 5.8 is a function of both $SO_2$ and $PO_2$, which can be related by the invertible form of the haemoglobin-oxygen dissociation curve (the Hill equation) [205]:

$$SO_2(PO_2) = \frac{PO2^n}{PO2^n + P50^n} \quad \text{(Eq 5.10)}$$

where P50 is the half-saturation $PO_2$ and n is the Hill exponent for haemoglobin (typically 2.7) [205]. P50 will vary by species and can be set to match the species of interest by using values obtained experimentally [206]. By substituting Equation 5.10 into Equation 5.8, Equation 5.11 can be obtained for calculating the R1 of blood that is no longer limited to normal physiological oxygen ranges. Thus Equation 5.11 can be used to calculate R1 even when the partial pressure of oxygen in the plasma reaches normobaric hyperoxic levels.

$$R1_b(PO_2) = f_e\left(R1_{eox} + r1_{dHb}[Hb]\left(1 - \frac{{PO_2}^n}{{PO_2}^n + P50^n}\right)\right) + (1 - f_e)(R1_p + r1_{pOx}PO_2) \quad \text{(Eq 5.11)}$$

In addition, it is known that many paramagnetic contrast agents interact with macromolecules and exhibit a higher relaxivity at higher macromolecule concentrations [207]. This is also true for molecular oxygen, and blood with artificially high levels of haematocrit (Hct=0.6) has been shown to have a higher relaxivity than blood at regular haematocrit levels [154]. To account for this haematocrit sensitivity, the effect of adding an extra term, $\beta_{1,r1pOxHct}$, to Equation 5.9 was also tested, assuming a linear dependence on haematocrit.

### 5.2.3. Data Analysis

In order to estimate values for the parameters in the new model, 126 data points for R1 in blood were collected from the literature with measured or estimated Hct, $SO_2$, and $PO_2$ at a range of field strengths (1.5-9 T) and under normoxic and hyperoxic conditions (Table 5.1) [96], [108], [152], [154], [174], [202], [208]–[210]. Data was extracted either from tables, manuscript text or graphs, and if data extraction from graphs was necessary, a digital plot analyser was used to reliably extract values [180]. The distribution of the resulting data is shown in Appendix Figure C.2. An accurate measurement of T1 depends on the selection of acquisition protocols and parameters (such as repetition and inversion times), and therefore the acquisition details from each experiment are listed in Appendix Table C.1.

The T1 values from Stefanovic and Pike [210] and d'Othée et al. [152] were increased by 12% to account for the shift in T1 between 22°C and 37°C. If not reported, $PO_2$ values were calculated from the reported $SO_2$ values using Equation 5.10. Since the value of P50 (half-saturation $PO_2$) can differ greatly between species, a P50 of 25 mmHg was used for all human data points, and a P50 of 44 mmHg was used for the bovine and rat, based on the P50 values found experimentally in human, bovine, and rat blood samples [206].

For model fitting, the SciPy *optimize* function for nonlinear least-squares fitting was used [181]. Equation 5.11 was fitted using a randomized subset of 95% of the 126 data points, fitting with the R1, B0, P50, Hct and $PO_2$ values simultaneously, and testing on the

remaining 5%. The dataset was split for fitting and testing using the SciKitLearn *train_test_fit* function with shuffling [182]. This process was iterated 10000 times, and the mean and 95% confidence interval of the distribution of fitted values for each of the parameters were recorded (listed in Table 5.2).

### 5.2.4. Statistical Analysis

Since Equation 5.11 contains 8 fitting parameters, the fitting process was repeated for all combinations of fewer parameters (i.e., removing the dependence of $R1_p$ on B0) and the Akaike Information Criterion (AIC) was calculated for each version of the model — the best-fit model according to the AIC is the model that explains the greatest amount of variation using the fewest possible independent variables. The model that scored the highest according to the AIC was therefore selected as the best model and used in further investigation. The $R^2$ coefficient of determination and mean squared error (MSE) were also calculated for each model, and Bland-Altman analysis was used to examine the model bias with haematocrit, B0, $SO_2$ and $PO_2$.

## 5.3. Results

### 5.3.1. Akaike Information Criterion

The AIC score, $R^2$, and MSE results of the 4 highest AIC-scoring models tested are listed in Appendix Table C.2, and results are plotted in Appendix Figure C.3. The version of the model with $\beta_{1,R1p}$ set to 0 (i.e. with Equation 6 set to $R1_p=\beta_{0,R1p}$, hence 7 total parameters) resulted in the highest AIC score, and was therefore used in this thesis.

The version of the model with the extra fitting parameter $\beta_{1,r1pOxHct}$ in Equation 9 resulted in a similar fit ($R^2$=0.927 vs $R^2$=0.926), but the best-fit model according to the AIC was the model without this extra parameter (see Appendix Table C.2). Therefore, the best model was the 7-parameter model which did not include this dependency on haematocrit.

### 5.3.2. Model Fitting

The modelled vs measured $R1_b$ values from the randomized unseen test set of each iteration is plotted in Appendix Figure C.4 alongside the line of equality and the linear regression ($R^2$=0.91). The difference between the modelled and measured $R1_b$ values from the randomized unseen test set of each iteration is illustrated as Bland-Altman plots in Appendix Figure C.4(B-F) with the resulting mean error of $R1_{blood}$ as $1x10^{-4}$ $s^{-1}$ and the limits of agreement of -0.078 and 0.078$s^{-1}$. Violin plots showing the distribution of parameter estimates from each iteration are shown in Appendix Figure C.5.

The median parameter values for the final optimal 7 parameters $\beta_{0,R1eox}$, $\beta_{1,R1eox}$, $\beta_{0,r1dHb}$, $\beta_{1,r1dHb}$, $\beta_{0,R1p}$, $\beta_{0,r1pOx}$, and $\beta_{1,r1pOx}$ (with lower and upper 95% confidence intervals) are listed in Table 5.2. The accuracy of the final model's predicted R1 compared against the 'true' $R1_b$ values is shown in Figure 5.2(A). The predicted versus true $R1_b$ values are plotted against the line of equality (solid black line) and a linear regression (dotted line, $R^2$=0.93) in Figure 5.2(A), with a final MSE of 0.0013 $s^{-2}$. To examine bias in the model with respect to $SO_2$, $PO_2$, B0, Hct, or R1 variables, Bland-Altman plots are provided in Figure 5.2(B-F), with the resulting mean error of $R1_b$ as $6x10^{-6}$ $s^{-1}$ and the limits of agreement of -0.071 $s^{-1}$ and 0.071 $s^{-1}$. A systematic trend in the error distribution by R1 (Figure 5.2B) indicated that the model did not entirely explain the non-noise variance in the data, and possible causes of this were further examined by viewing the data points according to the original source (provided in Appendix Figure C.6).

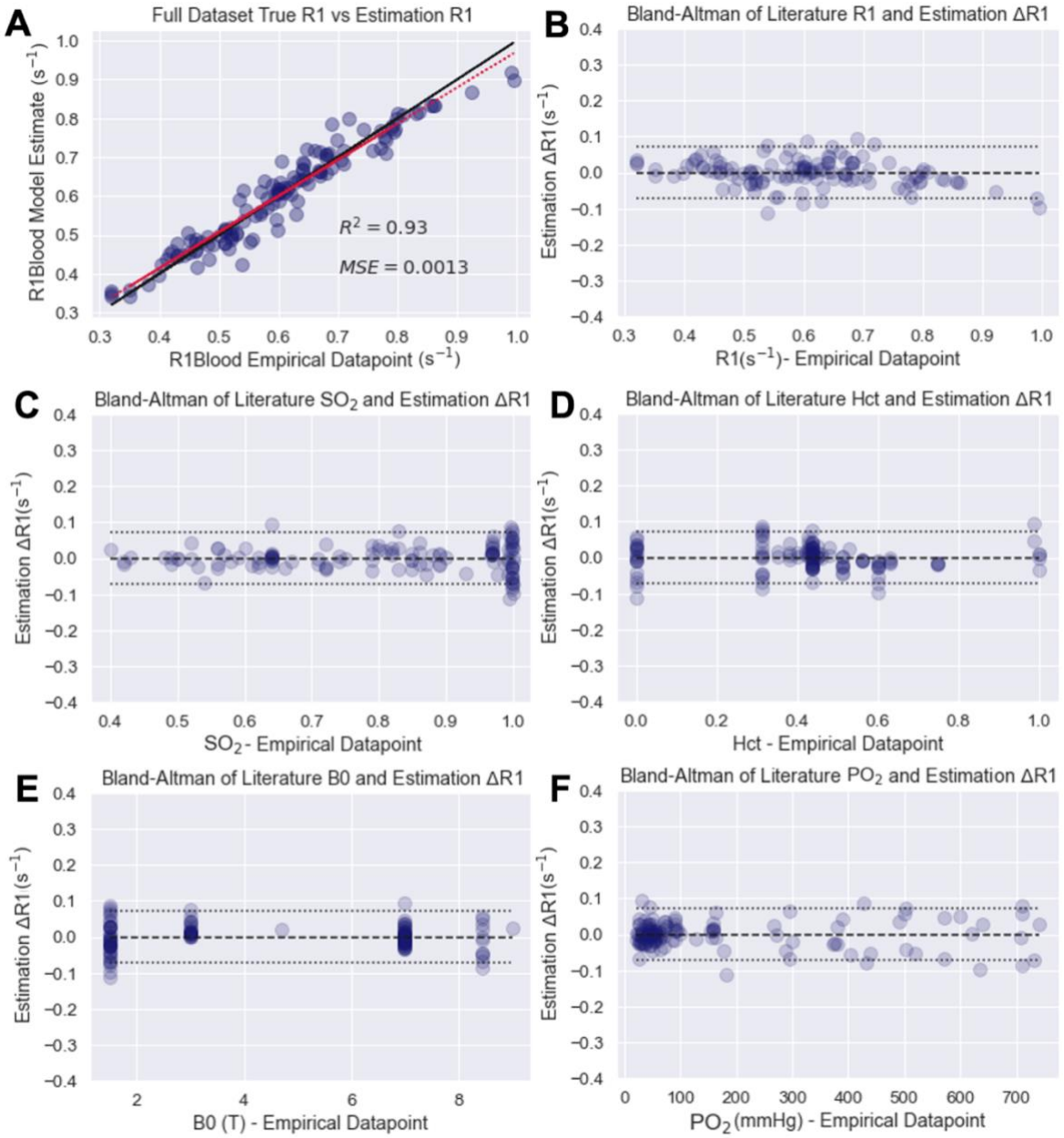


***Figure 5.2. (A)*** *The modelled vs measured $R1_b$ values, plotted against the line of equality (solid black line) and a linear regression (red dotted line, $R^2$=0.93), number of datapoints n=126.* ***(B)*** *A Bland-Altman plot showing the difference between the modelled and measured values of $R1_b$. The horizontal long-dashed lines show the mean value of $\Delta R1_b$ ($6x10^{-6}$ $s^{-1}$), and the horizontal dotted lines show the limits of agreement (long dashes, calculated by mean($\Delta R1_b$) ± (1.96xSD($\Delta R1_b$)). Bland-Altman plots for the error in modelled $R1_b$ against* ***(C)*** *$SO_2$,* ***(D)*** *hematocrit, (E) B0, and (F) $PO_2$ levels are also shown to examine bias in the model.*

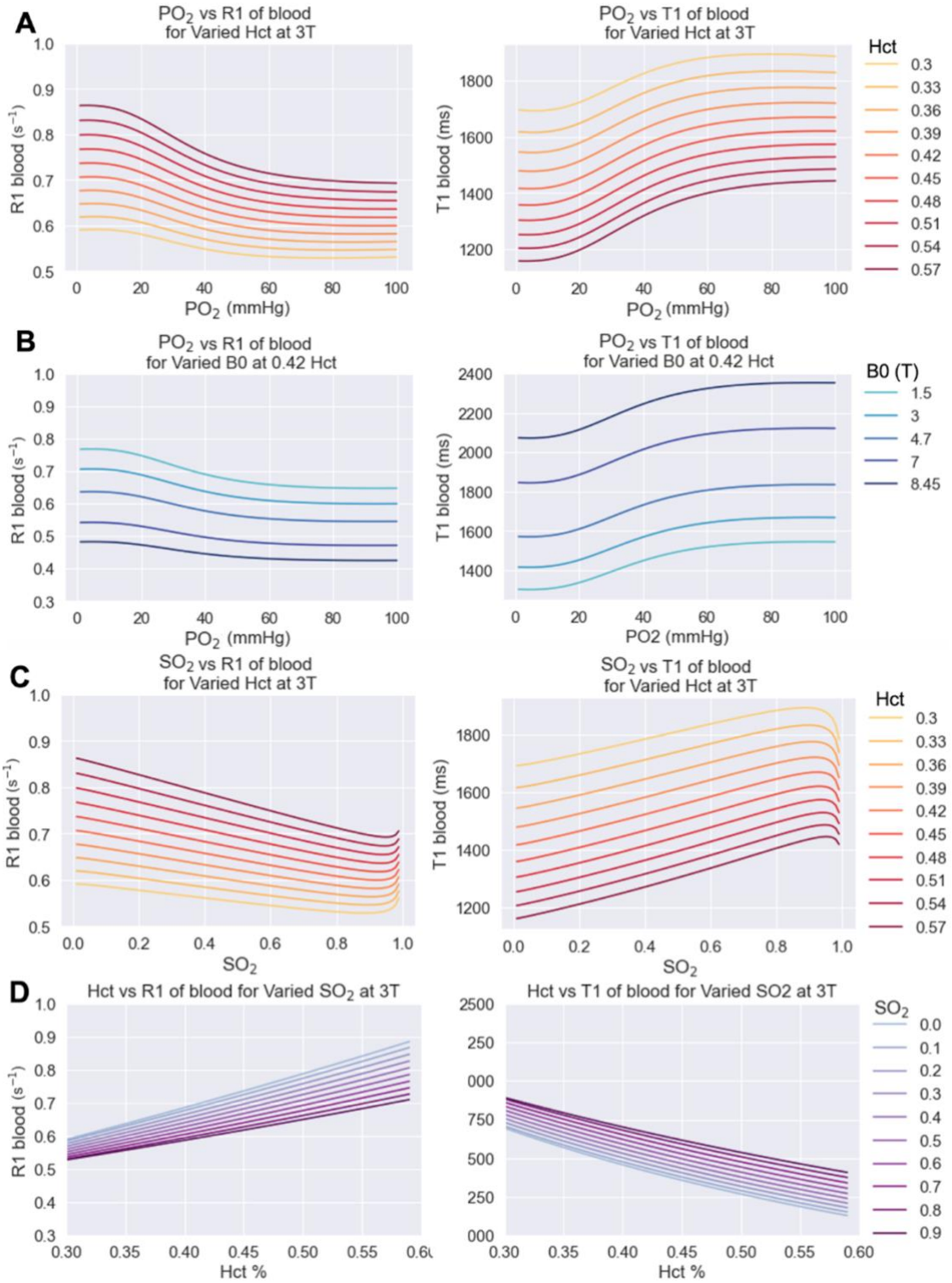


***Figure 5.3.*** *Plots with simulated data to illustrate the behaviour of the model (with parameters fit from all data) under non-hyperoxic conditions ($SO_2$<99%).* ***(A)*** *$PO_2$ vs $R1_b$ and $T1_b$ and* ***(B)*** *$SO_2$ vs $R1_b$ and $T1_b$ for a range of hematocrit values (0.3-0.57) at 3T.* ***(C)*** *$PO_2$ vs $R1_b$ and $T1_b$ at a range of field strengths (1.5-7T) with Hct=0.42.* ***(D)*** *Hematocrit vs $R1_b$ and $T1_b$ for a range of $SO_2$ values (0-90%) at 3T.*

### 5.3.3. Model Behaviour

To understand the behaviour of the resulting model, the effect of varying $PO_2$, $SO_2$, field strength and haematocrit on R1 is illustrated using synthetic data from 0 to the upper level of normal oxygen levels (Figure 5.3) and extending to hyperoxic conditions (Figure 5.4).

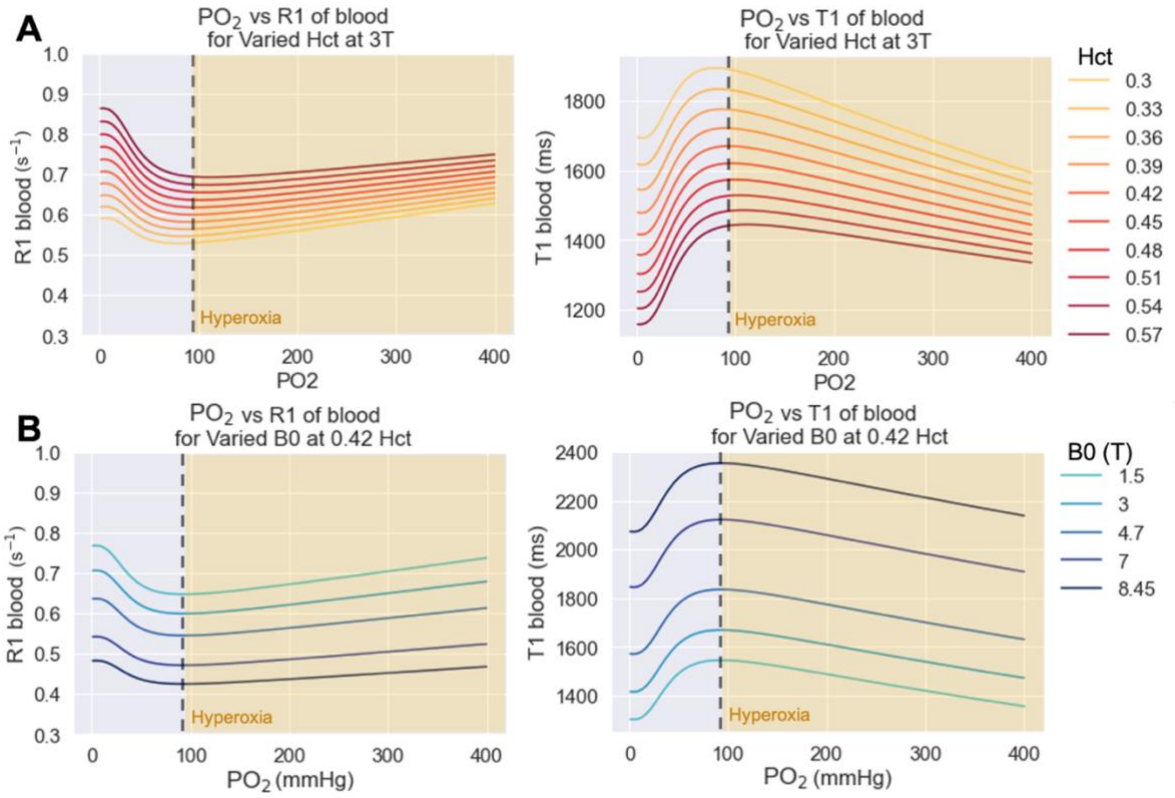


***Figure 5.4.*** *Plots with simulated data to illustrate the behaviour of the model extending to hyperoxic conditions.* ***(A)*** *$PO_2$ vs $R1_b$ and $T1_b$ for a range of hematocrit values (0.3-0.57) at 3T.* ***(B)*** *$PO_2$ vs $R1_b$ and $T1_b$ for a range of field strengths (1.5-8.45T) at 0.42 Hct.*

As shown in Figure 5.5, the ability of the new model to predict blood R1 was compared with the model and parameter values estimated by Hales et al., on a subset of data points (n=128) from non-hyperoxic blood i.e., within the range that the Hales model is stated to be valid ($SO_2$=0.4-0.99). Within this range, the model agreed well with the Hales model estimates of R1 ($R^2$=0.96), and showed slightly closer agreement with the literature values ($R^2$=0.93 vs 0.92, MSE=0.00096 vs 0.00011 $s^{-2}$ for Hales vs new model, respectively). In addition, the new model was preferred slightly over the Hales model by the

AIC criterion, achieving an AIC score of -547 vs -551 for Hales vs new model, respectively. The divergence of the predictions of the Hales model versus the new model as oxygen levels become hyperoxic is shown in Appendix Figure C.7.

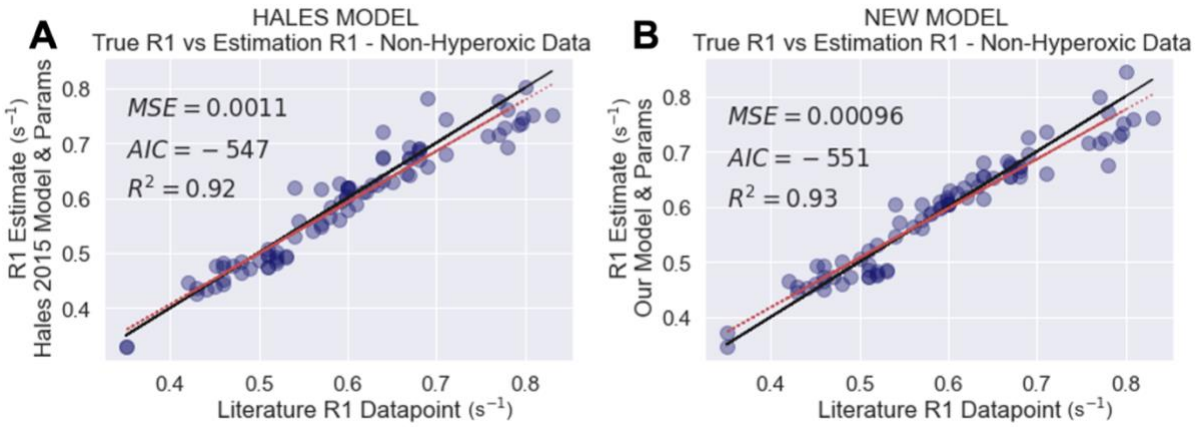


***Figure 5.5.*** *Scatterplots of a subset of 82 literature data points from non-hyperoxic blood ($SO_2$<99%) and the performance of* ***(A)*** *the model and parameters estimated by Hales et al. ($R^2$=0.92, MSE=0.0011 $s^{-2}$, AIC=-547) and* ***(B)*** *the new model and parameters ($R^2$=0.93, MSE=0.00096 $s^{-2}$, AIC=-551), plotted against the line of equality (solid black line).*

The behaviour of the erythrocyte and plasma components of the model is shown in Figure 5.6, where the model showed that as oxygen levels increased in the blood, the R1 decreased due to the paramagnetic effect of the deoxyhaemoglobin fraction, and once full saturation was reached, the predominant remaining effect was the increase in R1 due to the paramagnetic dissolved oxygen in the plasma.

The predicted changes in R1 that would be induced by an increase in oxygen levels are illustrated in Figure 5.7(A-B), which shows the so-called 'contradictory' negative ΔR1 that has been observed by oxygen-enhanced MRI researchers in hypoxic tumours [100], [144], [178], [199]–[201]. As can be seen in Figure 5.7(C), when starting from a low saturation, the R1 first decreases until full saturation is reached, and then increases linearly with $PO_2$. Shown in Figure 5.7(D), the model showed that a change in $PO_2$ from 39 to 48 mmHg (such as in venous blood) induced a negative ΔR1, while a change (such as in arterial blood) from 98 to 600 mmHg induced a large positive ΔR1.

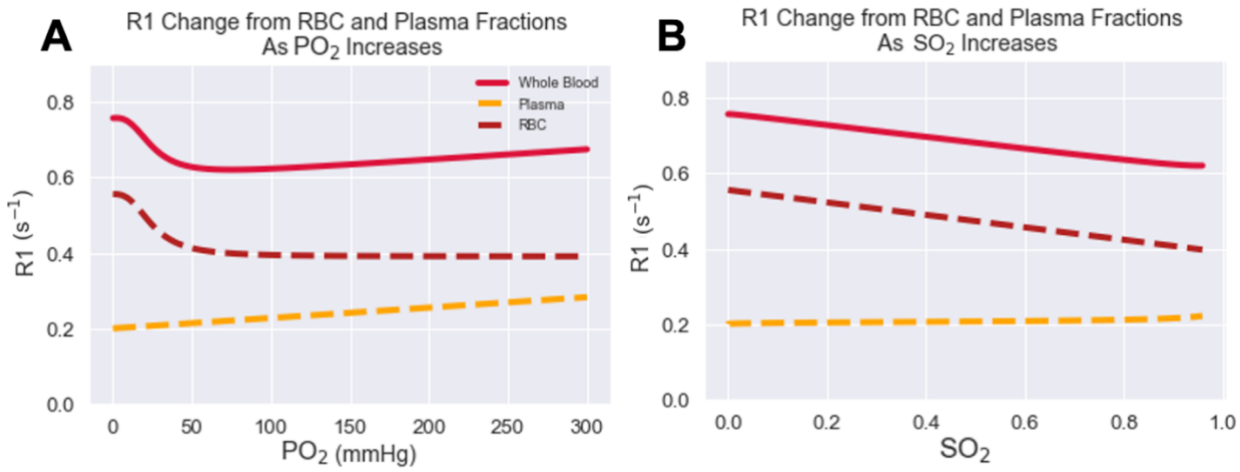


***Figure 5.6.*** *Plots with simulated data to illustrate the behaviour of the two compartments of the model, the plasma fraction (yellow) and erythrocyte fraction (maroon), as* ***(A)*** *$PO_2$ increases and* ***(B)*** *$SO_2$ increases. B0=3T, Hct=0.42.*

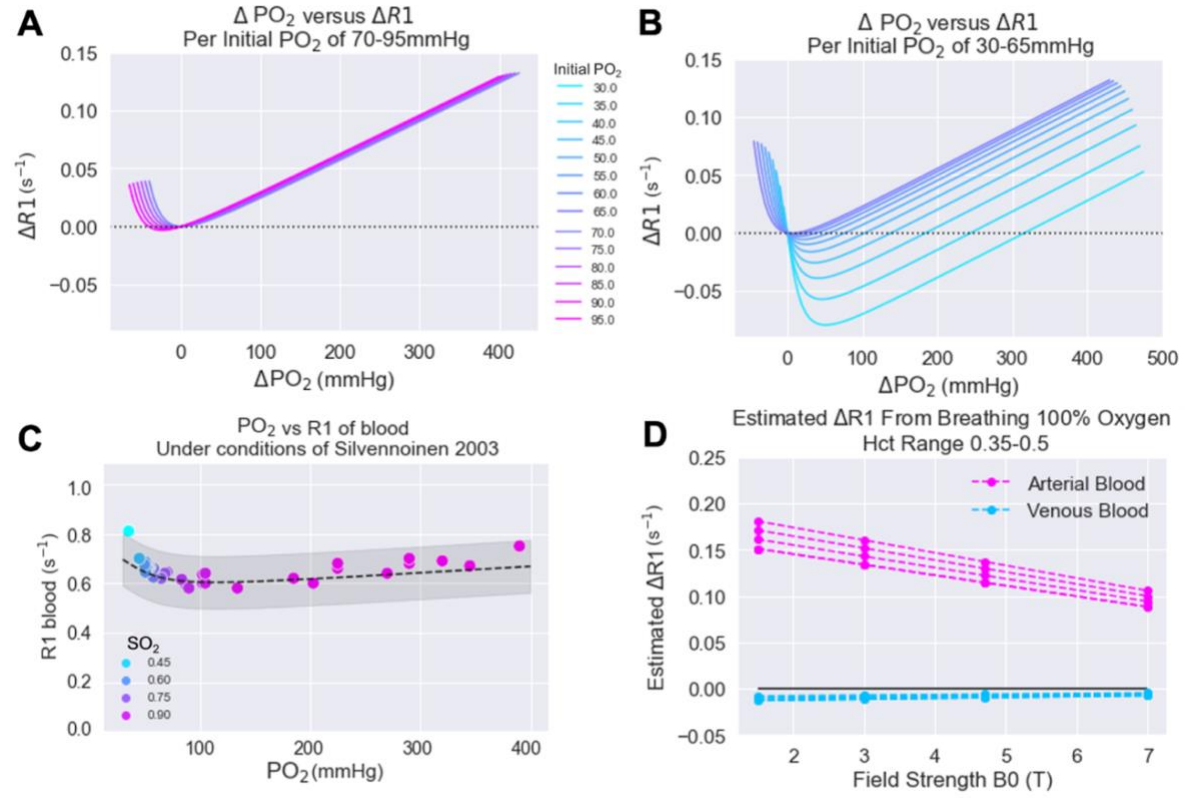


***Figure 5.7.*** *Estimated $\Delta R1_b$ as a function of $\Delta PO_2$ (at 3T and Hct=0.42) for various initial $PO_2$ levels of* ***(A)*** *70-95 mmHg and* ***(B)*** *20-70 mmHg. The ΔR1 trends match the data shown in* ***(C)****, which shows the $PO_2$ vs $R1_b$ data from Silvennoinen et al. (2003) (blue-pink scale is $SO_2$ level), plotted alongside the $R1_b$ estimated using the new model at the appropriate B0, Hct, $PO_2$, and $SO_2$ (dashed line) with the 95% confidence interval shown in grey.* ***(D)*** *The estimated $R1_b$ in venous and arterial blood after breathing 100% oxygen, based on empirical $PO_2$ measurements.*

***Table 5.1.*** *Summary of the literature sources for the data used to parameterize the new model. The distribution of the data points is plotted in Appendix Figure C.2. The MRI acquisition details from each experiment are listed in Appendix Table C.1.*

| Reference | B0(T) | n | Blood Source | Hematocrit | $SO_2$(%) | $PO_2$(mmHg) | Temp(°C) | Normal or Hyperoxic |
|---|---|---|---|---|---|---|---|---|
| **Lu 2004** | 3 | 9 | Bovine blood ex vivo | Measured | Measured | Calculated | 37 | Normal |
| **Grgac 2013** | 7 | 20 | | Measured | Measured | Calculated | 37 | Normal |
| **Dobre 2007** | 4.7 | 1 | | Measured | Measured | Calculated | 37 | Normal |
| | 7 | 1 | | | | | | |
| | 9 | 1 | | | | | | |
| **d'Othée 2003** | 8.45 | 11 | | Measured | Measured | Measured | 22 | Hyperoxic |
| | 3 | 7 | | | | | | |
| **Pilkinton 2012** | 3 | 5 | Rat blood in vivo | Estimated | Calculated | Measured | In vivo | Hyperoxic |
| **Blockley 2008** | 1.5 | 11 | Human Blood ex vivo | Measured | Measured | Calculated | 37 | Normal |
| | 3 | 7 | | | | | | |
| | 7 | 11 | | | | | | |
| **Hueckel 2000** | 1.5 | 17 | | Measured | Calculated | Measured | 37 | Hyperoxic |
| **Stefanovic 2004** | 1.5 | 8 | | Measured | Measured | Calculated | 22 | Normal |
| **Rane 2013** | 7 | 10 | | Measured | Measured | Calculated | 37 | Normal |
| **Summary: Total Data Range** | 1.5-9 | Total data points n=126 | Human n=64, Bovine n=58, Rat n=5 | Total Hct range of 0-1 | Total $SO_2$ range of 42-100% | Total $PO_2$ range of 33-739 mmHg | All R1 values corrected to 37°C | 86 data points normal, 40 hyperoxic |

***Table 5.2.*** *A summary of the final parameter estimates from the model fitting.*

| Parameter Meaning | Parameter Name | Mean Parameter Value (95% lower and upper confidence intervals) | | Units |
|---|---|---|---|---|
| | | Hales 2016 Parameters | New Model Parameters | |
| The Y-intercept of the linear dependence on B0 for the $R1_{eox}$, the relaxation rate of erythrocytes when $SO_2$=100% | $\beta_{0,R1eox}$ | 1.10 (0.97, 1.28) | 1.237 (1.221, 1.252) | $s^{-1}$ |
| The slope of the linear dependence on B0 for the $R1_{eox}$, the relaxation rate of erythrocytes when $SO_2$=100% | $\beta_{1,R1eox}$ | −0.058 (−0.085, −0.038) | -0.0825 (-0.0854, -0.0796) | $s^{-1}T^{-1}$ |
| The Y-intercept of the linear dependence on B0 for the $r1_{dHb}$, which is the molar relaxivity of deoxyhemoglobin | $\beta_{0,r1dHb}$ | 0.033 ($1.8 \times 10^{-9}$, 0.056) | 0.102 (0.093, 0.110) | $s^{-1}$ L plasma in erythrocyte / mmol Hb tetramer |
| The slope of the linear dependence on B0 for the $r1_{dHb}$, which is the molar relaxivity of deoxyhemoglobin | $\beta_{1,r1dHb}$ | Not used - set to 0 | -0.00688 (-0.00853, -0.00523) | $s^{-1}$ $T^{-1}$ L plasma in erythrocyte / mmol Hb tetramer |
| The Y-intercept of the linear dependence on B0 for $R1_p$, the longitudinal relaxation rate of plasma | $\beta_{0,R1p}$ | 0.49 (0.40, 0.57) | 0.332 (0.326,0.337) | $s^{-1}$ |
| The slope of the linear dependence on B0 for $R1_p$, the longitudinal relaxation rate of plasma | $\beta_{1,R1p}$ | −0.023 (−0.035, −0.0079) | Not used - set to 0 | $s^{-1}$ $T^{-1}$ |
| The Y-intercept of the linear dependence on B0 for $r1_{pOx}$, the relaxivity of dissolved oxygen in the plasma | $\beta_{0,r1pOx}$ | Not tested | $5.70x10^{-4}$ ($5.87x10^{-4}$,$8.95x10^{-5}$) | $s^{-1}$/mmHg |
| The slope of the linear dependence on B0 for $r1_{pOx}$, the relaxivity of dissolved oxygen in the plasma | $\beta_{1,r1pOxB0}$ | Not tested | $-3.86x10^{-5}$ ($-4.27x10^{-5}$, $-3.56x10^{-5}$) | $s^{-1}$ $T^{-1}$ /mmHg |

## 5.4. Discussion

This chapter has presented a general model to estimate the R1 of blood, accounting for hematocrit, oxygen saturation ($SO_2$), the partial pressure of oxygen ($PO_2$), and magnetic field strength under both normal physiological and hyperoxic conditions. The model was valid for the following parameter ranges: B0=1.5-8.45T, $SO_2$=0.40-1, $PO_2$=30-700 mmHg, and adjustable for different species by adjusting the P50 constant appropriately. The model estimates agreed well with literature values ($R^2$=0.93, MSE=0.0013 $s^{-2}$) and the model performance was consistent across R1, $SO_2$, $PO_2$, B0 and Hct levels.

The new model builds upon a previous model for R1 or T1 of blood [192], accounting for hematocrit, field strength and $SO_2$, valid between 1.5-7T and $SO_2$ of 40-99% (non-hyperoxic conditions). The new model showed improved accuracy and preference within the valid range of the previous model, likely due to the four parameters added which better reflected the true behaviour, and also due to a 3x increase in data points available for model fitting. The new model was also valid over a slightly larger range of field strengths (1.5-8.45T). The main improvement of the new model, however, was that it could account for changes in $PO_2$ under hyperoxic conditions.

Our model showed that there are two competing effects on blood R1 that arise from increasing oxygen levels (paramagnetic oxygen and paramagnetic deoxyhemoglobin), and that the effect on R1 due to deoxyhemoglobin dominates during lower oxygen levels. O'Connor et al. [211] reported that when breathing 100% oxygen, there is a small increase in the venous $PO_2$ from 39 mmHg to 48 mmHg, while the arterial $PO_2$ shows a high increase from 98 mmHg to 600 mmHg. By modelling these hyperoxic conditions, it was possible to quantify the expected ΔR1 in venous and arterial blood after breathing 100% oxygen.

By modelling venous and arterial conditions, this model also provided an explanation for the unexpected additional *increase* in T1 (decrease in R1) from the oxygen-enhanced drink versus the control drink reported by Vatnehol et al. in the hepatic portal vein, where the

authors expected an increase in R1 from increased oxygenation [143]. The authors hypothesized that this contradictory result was due to oxygen increasing the amount of water absorbed into the bloodstream from the beverage and hence increasing the dilution effect [143]. However, according to our model, if the drink increased the oxygen saturation levels in the vein, then a decrease in R1 should be expected — which is consistent with their observations.

As mentioned in the background theory, the R1 of protons in highly mobile molecules such as plasma will be less affected by changing field strength, whereas in low mobility materials (such as protons in biological tissues) the R1 has been empirically shown to decrease as field strength increases [160]. The resulting slope of the field-strength dependence for $R1_p$ (plasma) and $R1_{eox}$ (erythrocytes) agreed well with this theory — the resulting slope for $R1_P$ (i.e., $\beta_{1,R1p}$) was almost 0. In fact, the version of the model with $\beta_{1,R1p}$ set to 0 (i.e., with Equation 5.6 set to $R1_p=\beta_{0,R1p}$, hence 7 total parameters) resulted in the highest AIC score and was therefore used in this thesis In addition, the removal of the dependence of $R1_{eox}$ produced an extremely low AIC score, therefore suggesting that the R1 of the protons within the erythrocytes was more affected by changing field strength than the R1 of the protons within the plasma, which was consistent with this background theory.

For the purpose of this model, the values used for $W_{RBC}$ and $W_{plasma}$ were 0.70 and 0.95, even though in reality these can range from $W_{RBC}$=54-78% and $W_{plasma}$=94-96%. When testing the effect of the full range of these variables on R1, it resulted in a maximum difference of 0.07 $s^{-1}$ and standard deviation of 0.02 $s^{-1}$ between any combination of $W_{RBC}$ and $W_{plasma}$ values and set hematocrit, suggesting that deviation from the chosen population average values of 0.70 and 0.95 could account for the remaining variance in the R1 estimates.

### 5.4.1. Limitations

The R1 values collected were from experiments performed over a timespan of two decades with variation in the experimental equipment and T1-mapping technique used. An accurate measurement of T1 in blood samples or in vivo can be difficult and the measurement accuracy depends on the proper selection of acquisition protocols and parameters (such as repetition and inversion times). Of note, some of the R1 data points collected from Stefanovic et al. were underestimated by the model — these were the only data points collected by a Look-Locker T1 mapping method, which are known to overestimate R1 [118].

It is important to note that the values of blood R1 have often been extracted from original plots, some hand-drawn, which is a source of error, and converted from the various original units to $s^{-1}$/mmHg, which can be another source of error. The hematocrit, $SO_2$ and $PO_2$ measurements collected from the literature also have several limitations — for example, it was apparent that researchers tended to report certain rounded values more often than others and to different levels of precision. In addition, data acquired in vivo was assumed to be 37°C, however as discussed in Chapters 2-4, a change in temperature of just ±0.5°C could alter the R1 by ±0.018 $s^{-1}$. Altogether, these limitations are a large source of potential error in the accuracy of this model. As a future direction of this work, the open-source model code and current $R1_b$ measurements have been hosted publicly on GitHub (github.com/BulteGroup/R1BloodModel), making it possible for the MRI community to share more modern measurements of blood R1 at a range of field strengths, hematocrit, $SO_2$, and $PO_2$, both *in vivo* and *ex vivo* and refit the model to improve accuracy.

Finally, it should be noted that there are other factors that will influence R1 in blood not included in the model. Plasma proteins that are relevant from an MRI perspective due to either diamagnetism or paramagnetism are albumin, Immunoglobulin G and fibrinogen, transferrin, and ceruloplasmin, and the concentrations of these can differ by age and sex,

resulting in a varied plasma R1 [207], [212]. It is possible that some of the variability in the literature data could be accounted for if these concentrations were also measured and reported. In fact, Li et al. have proposed a highly specific model of the R1 of blood accounting for haemoglobin saturation, methaemoglobin and albumin under non-hyperoxic conditions [204]. These data were not available in the literature used for the model, but if these were recorded in future studies alongside new R1 measurements they could be utilized for refitting.

### 5.4.2. Implications for Measurement of Nanobubble Oxygen Delivery

By confirming that the deoxyhemoglobin effect can dominate the R1 changes prior to full oxygen saturation levels, the results from this model can shed some light on the unexpected negative ΔR1 measured in the preclinical experiments of Chapter 3. For example, it is possible that in the hypoxic xenografts, the delivery of oxygen-laden nanobubbles provided excess dissolved oxygen for the tissue to extract, resulting in less oxygen being extracted from the red blood cells, and therefore resulting in lower deoxyhemoglobin levels in the venous blood post-injection compared to pre-injection levels. While this reasoning certainly explains the negative ΔR1 measured by Vatnehol in voxels containing 100% blood following their oxygen delivery drink experiment [143], our preclinical measurements were from voxels containing tumour tissue. For a voxel that does not contain 100% blood, such as a normal tissue voxel, the effect from changing deoxyhemoglobin levels will only pertain to the percent volume in the voxel that is occupied by blood, and the remaining voxel volume will be dominated by R1 change of the tissue. Therefore, in order to estimate the changes expected in a tumour tissue voxel, in Chapter 6, a model to estimate changes in tissue R1 in response to changing oxygen levels is presented.

## 5.5. Conclusion

In this work, a general model is presented for estimating the R1 of blood, accounting for hematocrit, magnetic field strength, $SO_2$, and $PO_2$, under both normal physiological and

hyperoxic conditions, and adjustable for different species. This work was built upon a previous model, and it has both improved the accuracy of the R1 estimates within the valid range of the previous model and extended its range of validity to include hyperoxic conditions. Using the predictions of this model, it was possible to quantify and explain contradictory oxygen-induced R1 changes reported in the literature and characterized the expected R1 changes arising from the relevant physiological factors.

However, for a voxel that does not contain 100% blood, such as normal tissue, the effect from changing deoxyhemoglobin levels will only pertain to the percent volume in the voxel that is occupied by blood, and the remaining voxel volume will be dominated by R1 change of the tissue. Therefore, in Chapter 6, a model to estimate changes in tissue R1 in response to changing oxygen levels is presented.

# Chapter 6. A Model of Tissue R1 Response to Oxygen Delivery

---

*Although the model in Chapter 5 accurately describes the expected R1 change in blood, the aim of this thesis is to detect the oxygen delivery from these nanobubbles in tissue. Therefore, in this chapter, a 3-compartment model is proposed for estimating the changes in R1 that could be expected in tissues depending on field strength, blood oxygen saturation, blood volume, hematocrit, oxygen extraction fraction, and changes in the partial pressure of oxygen.*

*This chapter includes edited material from the following manuscripts:*

- ***E Bluemke,** E Stride, D Bulte. Modelling the effect of hyperoxia on the spin-lattice relaxation rate R1 of tissues. Magnetic Resonance in Medicine, 2022. DOI:10.1002/mrm.29315*
- ***E Bluemke,** E Stride, D Bulte. The effect of oxygen on longitudinal relaxation: a review of oxygen-enhanced MRI. In preparation.*

---

## 6.1. Introduction

The model presented in Chapter 5 successfully describes the changes that would occur in the R1 of blood from hyperoxia or oxygen delivery. However, for a voxel that does not contain 100% blood, the size of the effect from changing deoxyhemoglobin levels and dissolved oxygen will depend on the proportion of the voxel volume that is occupied by blood. In most cases it will also be necessary to consider the change in R1 in the tissue surrounding the blood vessels. Therefore, in this chapter, a 3-compartment model is proposed for estimating the changes in R1 that could be expected in tumour tissues depending on field strength, blood $SO_2$, blood volume, hematocrit, oxygen extraction fraction, and changes in $PO_2$ in both the blood and tissue. This model has been developed with the aim of estimating the expected ΔR1 induced from the oxygen delivery by nanobubbles in a voxel containing tumour tissue.

Since modelling tissue oxygen diffusion and consumption is a broad, active research area with many different approaches, this model has been designed to make it possible for users to easily substitute their preferred model for tissue oxygen diffusion and consumption and hence tailor it to their tissue of interest. For the purposes of demonstration, in this thesis the classic Krogh tissue cylinder model for oxygen diffusion is used, with the Michaelis-Menten equation for oxygen consumption.

For the models presented in Chapters 4-5, it was possible to evaluate their accuracy quantitatively by comparing the simulated data with empirical measurements from the literature. For this tissue model, unfortunately no empirical data yet exist for nanobubble oxygen delivery. Analogous data are however available from the OE-MRI literature and evaluation was therefore carried out by simulating the ΔR1 response to a hyperoxic gas challenge. Since this model contains variables that were not measured at the time of OE-MRI data collection (i.e., hematocrit, changes in arterial $PO_2$, tumour blood volume) it is not possible to quantitatively compare the model ΔR1 predictions to the measured ΔR1 with

metrics such as $R^2$ and MSE. Instead, the ΔR1 responses from different tumour tissue types from the OE-MRI literature have been categorized to allow comparisons to be made between trends seen from this model and trends seen empirically. In addition, for a select few OE-MRI studies that did report either measured or estimated $PaO_2$ changes, the model is used to simulate the corresponding ΔR1 to that B0 and $PaO_2$ levels, making a semi-quantitative assessment of the model's accuracy possible.

After assessing the accuracy of the model in comparison with OE-MRI literature, the model was used to simulate the expected R1 changes following oxygen delivery from nanobubbles. The results from both the evaluation and simulations of nanobubble delivery are presented in this chapter.

## 6.2. Theory and Methods

### 6.2.1. Model Background and Overview

There have been two previous attempts at modelling the changes in tissue R1 following increased oxygen: both arise from the research field of OE-MRI [207], [213]. In 2013, Holliday [213] used a 2-compartment model of blood to estimate the ΔR1 in a capillary given a change in capillary $PO_2$ (Equation 6.1), and used a Krogh tissue cylinder model to estimate the corresponding tissue $\Delta PO_2$ ($\Delta PO_{2\,T}$), allowing the ΔR1 in tissue to be calculated by Equation 6.2.

$$\Delta R1_{capillary} = \Delta PO_2 * r1_{Ox} + \Delta(1 - SO_2) * r1_{dHb} \quad \text{(Eq 6.1)}$$

$$\Delta R1_{tis} = \Delta PO_{2\,tis} * r1_{Ox} \quad \text{(Eq 6.2)}$$

Holliday used the $r1_{dHb}$ at 1.5T reported by Blockley et al. (0.11 $s^{-1}$) [96]. The main insight provided by Holliday's approach is the benefit of using a Krogh tissue cylinder in order to better estimate the resulting $\Delta PO_{2\,T}$, since it will be less than the $\Delta PO_2$ induced in the arterial blood. The main limitation of Holliday's approach is that the resulting model contains many independently adjustable variables, such as the blood flow velocity, oxygen consumption

rate, vessel geometry, and length of capillary. In practice, these variables are often impossible to measure in tissues.

In 2018, Kindvall [207] proposed a much simpler equation to estimate the expected R1 change in pulmonary OE-MRI, in which the total ΔR1 is separated into the expected ΔR1 of the oxygenated blood ($\Delta R1_{B,Ox}$), deoxygenated blood ($\Delta R1_{B,deOx}$), and tissue $\Delta R1_T$, and divided by 3 to yield an average ΔR1:

$$\Delta R1 = \frac{\Delta R1_{B,Ox} + \Delta R1_{B,deOx} + \Delta R1_T}{3} \quad \text{(Eq 6.3)}$$

Kindvall then used empirical measurements from previous experiments to estimate the ΔR1 at a set magnetic field strength (4.7T): the $\Delta R1_{B,Ox}$ and $\Delta R1_T$ were set to be the same values (0.2 $s^{-1}$), and the $\Delta R1_{B,deOx}$ was estimated to be -0.05 $s^{-1}$ based on the relaxivity of deoxyhemoglobin ($r1_{dHb}$) reported by Silvennoinen et al. (0.35 $s^{-1}$) and a rough estimate of the expected change in venous deoxyhemoglobin levels [110]. The main insight provided by Kindvall's approach was the benefit of separating the R1 changes in oxygenated blood and deoxygenated blood to observe the negative ΔR1 induced in deoxygenated blood, as opposed to Holliday's approach of estimating the ΔR1 of the capillary blood. However, the division by 3 assumes a 66% blood volume fraction in the voxel, which is too high of a blood volume fraction for most tissue voxels.

Lastly, a substantial limitation to both of these approaches is that the equations used to calculate the blood ΔR1 were of unknown accuracy and were not compared with literature values (the issues with the values for $r1_{dHb}$ from Blockley and Silvennoinen are discussed in Chapter 5), did not take into account the blood hematocrit levels, and is not adjustable for magnetic field strength, which has considerable effect on the relaxivity values included (as discussed in Chapters 4-5).

Therefore, this new model builds upon the strengths from each model and propose a 3-compartment model that calculates the expected ΔR1 of the oxygenated blood or arterial

($\Delta R1_{B,A}$), deoxygenated or venous blood ($\Delta R1_{B,V}$), and tissue $\Delta R1_T$ as separate compartments, and uses a Krogh tissue cylinder model to estimate the corresponding tissue $\Delta PO_2$ ($\Delta PO_{2\,T}$). The model takes into account the magnetic field strength (B0), blood $SO_2$, blood volume fraction (BV), hematocrit (Hct), oxygen extraction fraction of the tissue (OEF), and changes in $PO_2$ in both the blood and tissue. Lastly, the model uses the blood volume fraction (BV) to calculate the resulting ΔR1 of the voxel ($\Delta R1_{voxel}$).

An overview of the model is illustrated in Figure 6.1. The model can be conceptually separated into 4 steps:

**Step 1. Calculate $PO_2$ along the capillary.** The $\Delta R1_{B,deOx}$ and $\Delta R1_T$ and $\Delta R1_{B,Ox}$ are all related by a calculation of the $SO_2$ or $PO_2$ along the capillary length, which is determined by the arterial $PO_2$ and the OEF of the tissue.

**Step 2. Calculate $\Delta PO_2$ of each compartment.** Knowing the $PO_2$ along the capillary allows the $\Delta PO_2$ from oxygen administration to be calculated in the blood and tissue compartments, using the Krogh tissue cylinder to model the oxygen diffusion into the tissue, and the set OEF is related to the tissue oxygen consumption rate. The Krogh tissue cylinder radius is calculated from the set blood volume.

**Step 3. Calculate ΔR1 of each compartment.** Knowing the $\Delta PO_2$ in each compartment allows the $\Delta R1_T$ to be calculated simply using the relaxivity of oxygen, and the ΔR1 of each blood compartment to be calculated using the Blood R1 model presented in Chapter 5.

**Step 4. Calculate ΔR1 of voxel.** Once the ΔR1 in each compartment is calculated, the set blood volume fraction (BV) is used to calculate the resulting ΔR1 of the voxel ($\Delta R1_{voxel}$).

The theory and reasoning behind each part of this model is provided in the following sections. The model is provided as a public code repository, and a graphical overview of the inputs and outputs of each function created to implement this model is provided Figure 6.2.

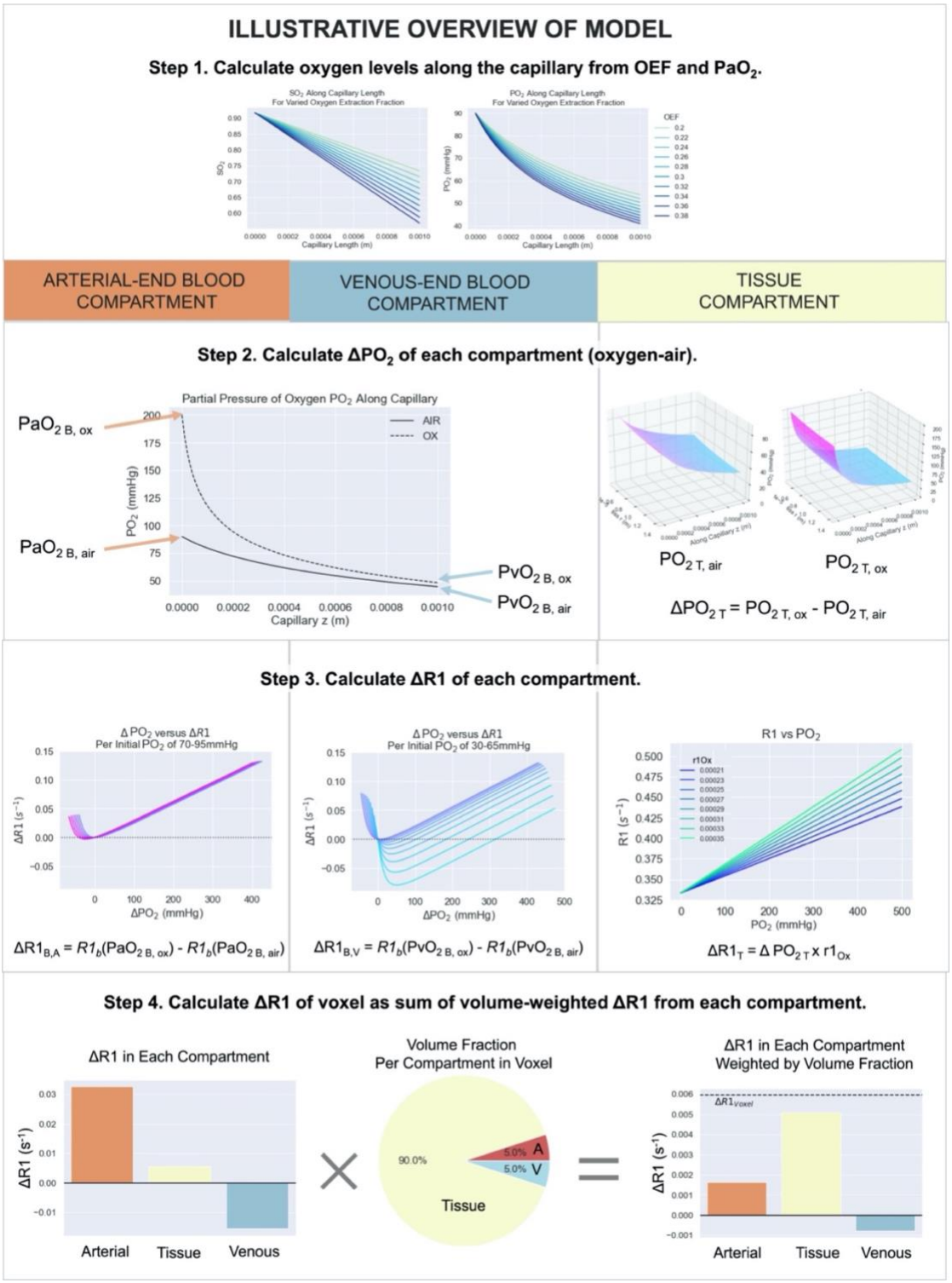


***Figure 6.1.*** *An illustrative overview of the 3-compartment model, which can be separated conceptually into 4 steps as shown. The inputs and outputs of the functions used in each step are shown in Figure 6.2.*

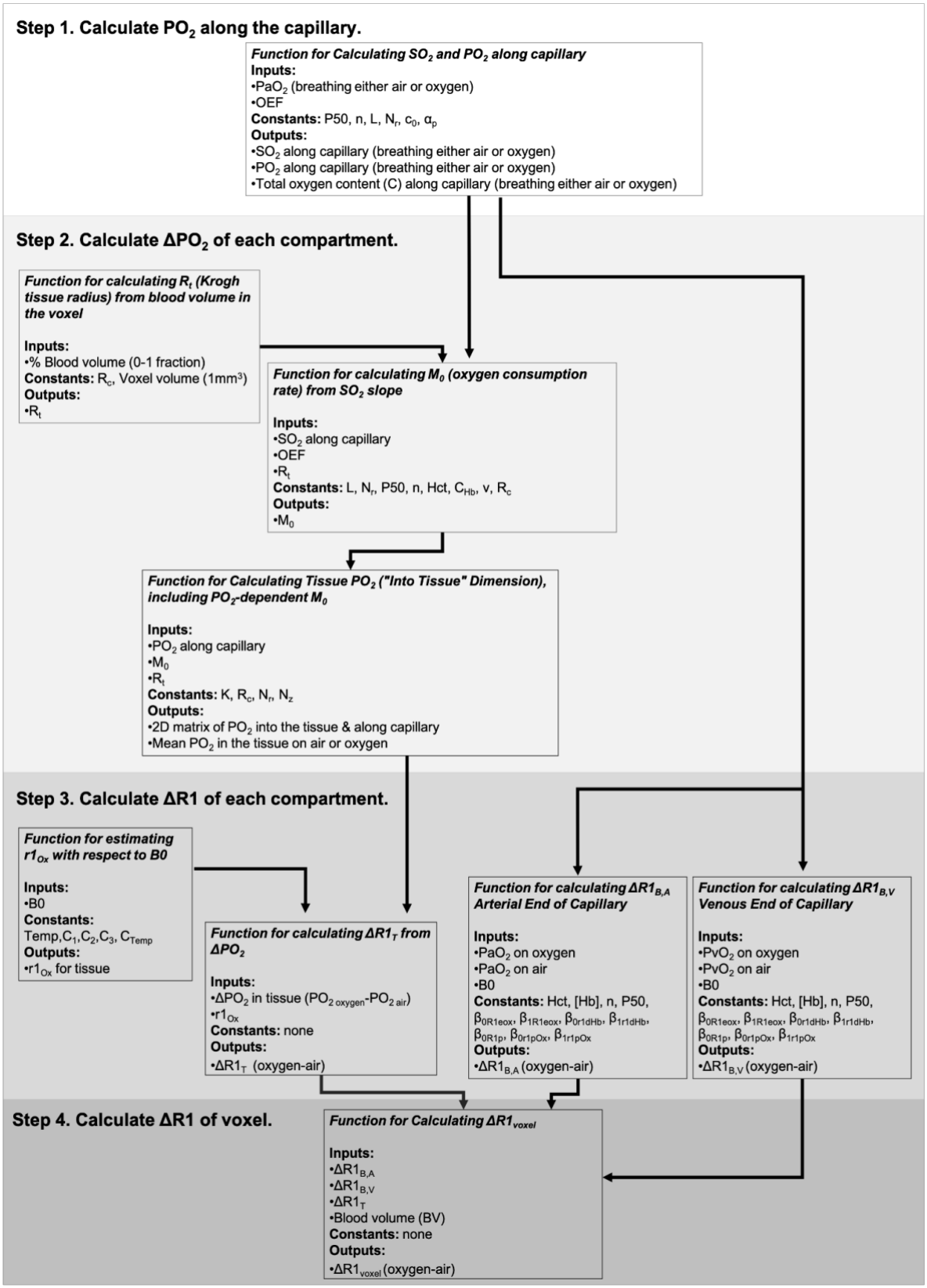


***Figure 6.2.*** *The inputs and outputs of each resulting function used in this model.*

### 6.2.2. Step 1: Calculating $PO_2$ Along Capillary Length

In this step, the $PO_2$ along the capillary is calculated using the inputs of arterial oxygen content and oxygen extraction fraction. The output of this step is the known $SO_2$ and $PO_2$ along the capillary, which can be calculated before and after the oxygen delivery or hyperoxic gas challenge.

The total concentration of oxygen (c) in the blood is the sum of the concentrations of bound and dissolved oxygen [214]:

$$c = c_{dissolved} + c_{bound} = \alpha_p * PO_2 + Hct * c_0 * SO_2 \quad \text{(Eq 6.4)}$$

Where c is the total blood oxygen concentration, and $c_0$ is the concentration of oxygen per unit volume of RBCs at maximal saturation. The total concentration (c) can also be referred to as the arterial oxygen content ($C_aO_2$) and venous oxygen content ($C_vO_2$). The following relationship between $C_aO_2$ and $C_vO_2$ defines the oxygen extraction fraction (OEF), which is the ratio of blood oxygen that a tissue takes from the blood flow (Rasmussen et al., 2010):

$$OEF = \frac{C_aO_2 - C_vO_2}{C_aO_2} \quad \text{(Eq 6.5)}$$

Using developed formalism from Gjedde et al. [215] and Rasmussen et al. [216], assuming that the total oxygen extraction rises linearly with distance along the capillary, as established by Kety et al. [217], the mean $SO_2$ in the capillary ($S_{cap,mean}$) can be defined in relation to OEF as [218]:

$$S_{cap,mean} = SaO_2 \left(1 - \frac{OEF}{2}\right) \quad \text{(Eq 6.6)}$$

The total oxygen content along the capillary can therefore be calculated for any given OEF (Figure 6.3) and initial $SO_2$, $PO_2$, or $CaO_2$ value, and find the resulting $PO_2$ and $SO_2$ along the capillary length by using Equation 6.6 and the Hill equation (Equation 5.10). In addition, we can repeat these calculations on both air ($PO_2$=100 mmHg) and supplemental oxygen

($PO_2$=400 mmHg), and find the resulting $PO_2$ and $SO_2$ along the capillary length by using Equation 6.6 and the Hill equation (Equation 5.10).

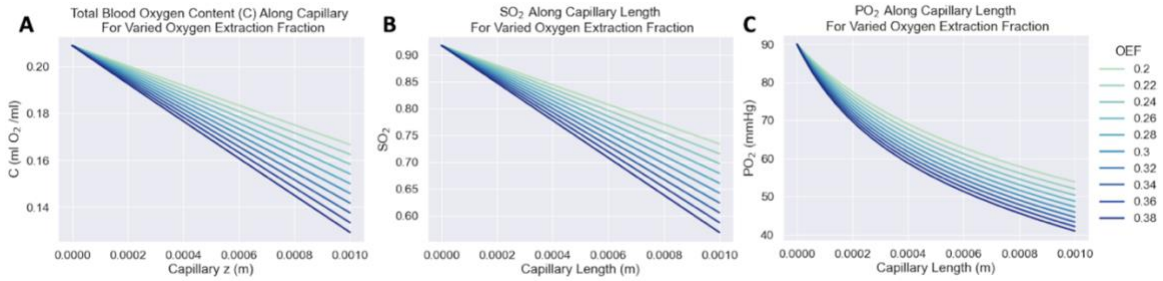


***Figure 6.3.*** *The **(A)** total oxygen content ($CaO_2$), **(B)** $SO_2$, and **(C)** $PO_2$ along the capillary for OEF ranging from 0.2-0.4.*

## 6.2.3. Step 2: Estimating ΔPO2 in the 3 Compartments

### *6.2.3.1. Blood Compartments*

In this model, the arterial $PO_2$ levels are chosen by the user. The arterial $PO_2$ following a hyperoxic gas challenge such as is used in OE-MRI is estimated to increase from 90mmHg to 600mmHg based on empirical measurements [211], and therefore this is used for the duration of this chapter. The corresponding change in venous $PO_2$ will depend on the OEF and is therefore calculated by the $PO_2$ values at the venous end of the capillary at baseline or with oxygen added.

### *6.2.3.2. Tissue Compartment - Oxygen Diffusion*

A wide variety of models for tissue oxygen diffusion and metabolism have been established, accounting for differing capillary networks, geometry, and other special features. For the purpose of this chapter, we use the classic Krogh tissue cylinder model and common Michaelis-Menten equation for oxygen consumption rate, however any preferred tissue model can be substituted to calculate the resulting change in tissue oxygen levels ($\Delta PO_{2\,T}$) from hyperoxia to use in Step 3. The Krogh-Erlang solution has the following assumptions, paraphrased from Goldman et al., [205]: (1) tissue oxygen consumption is constant and uniform; (2) tissue oxygen at the capillary wall equals average capillary $PO_2$; (3) tissue oxygen solubility and diffusivity are uniform (4) axial (or longitudinal) diffusion of

oxygen is not significant; (5) all important microvascular oxygen transport phenomena are steady-state; (6) all capillaries are parallel, unbranched, and equally spaced; (7) all capillaries receive equal convective oxygen supply; (8) capillaries are the only microvessels that play a role in oxygen transport to tissue.

For steady state $PO_2$ in the tissue cylinder and a given capillary $PO_2$, the Krogh-Erlang solution is:

$$PO_2(r) = P_{cap} + \frac{M_0}{4K}\left(r^2 - {R_c}^2\right) - \frac{M_0 {R_t}^2}{2K} ln(\frac{r}{R_c}) \quad \text{(Eq 6.7)}$$

Where $PO_2(r)$ is the $PO_2$ at r in the tissue, $R_c$ is capillary radius, $R_t$ is the Krogh tissue radius, $P=P_{cap}$ at $R=R_c$, r is the radial coordinate, $M_0$ is the maximum tissue oxygen consumption rate, and K is the Krogh diffusion constant $K=Da_T$, where D is the tissue oxygen diffusivity and $a_T$ is the tissue oxygen solubility [205]. The behaviour of Equation 6.7 for different levels of $P_{cap}$ is shown in Figure Figure 6.4A.

### *6.2.3.3. Tissue Compartment - Oxygen Consumption*

As discussed by Goldman et al. [205], one important modification commonly made to the Krogh cylinder model is the addition of $PO_2$-dependent tissue oxygen consumption. The most common model, Michaelis-Menten, calculates the oxygen consumption rate by the following equation:

$$M(PO_2) = \frac{M_0 PO_2}{PO_2 + P_{crit}} \quad \text{(Eq 6.8)}$$

where tissue oxygen consumption rate $M(PO_2)$ is found to be approximately constant for tissue $PO_2$ above a certain value ($P_{crit}$), and below this value the oxygen consumption drops off sharply to zero [205]. The behaviour of Equation 6.8, and the effect of varying $P_{crit}$, is shown in Figure 6.4A, and the effect of varying $M_0$ on the behaviour of Equation 6.7 is shown in Figure 6.4B. Therefore, this manuscript, the $M_0$ constant in Equation 6.7 has been replaced with the function $M(PO_2)$ (Equation 6.8).

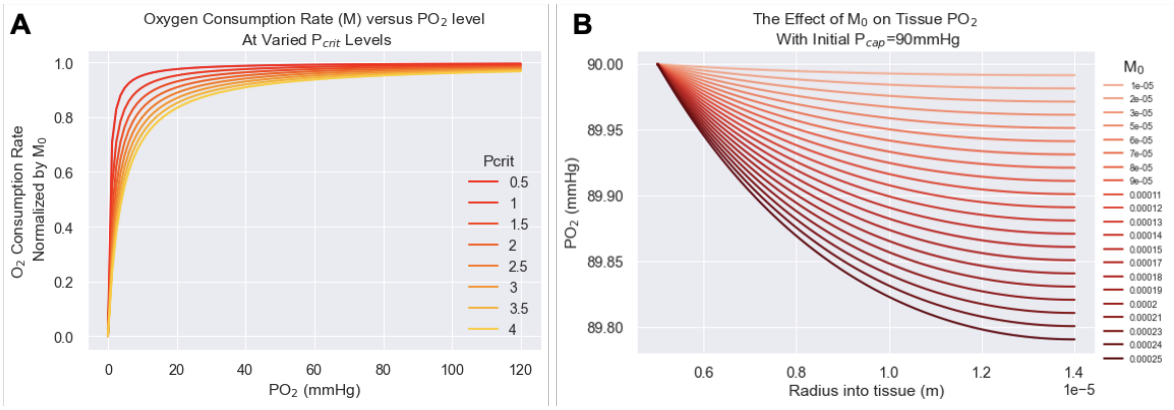


***Figure 6.4.*** *(A) The behaviour of the oxygen consumption rate (M) as described by the Michaelis-Menten model (Equation 6.8) for a range of values chosen for $P_{crit}$ (0.5-4 mmHg). (B) The behaviour of $PO_2$ into the tissue radius as described by the Krogh-Erlang solution (Equation 6.7), is shown for a range of $M_0$ to illustrate the effect of different rates of $M_0$ on $PO_2$ (with constant $P_{cap}$= 90 mmHg).*

### *6.2.3.4. Tissue Compartment - Estimating $R_t$ from Blood Volume*

Equation 6.7 requires knowledge of the Krogh tissue radius ($R_t$), which can be estimated as follows in accordance with the chosen blood volume (BV). Based on the Krogh assumptions above, we can model the capillaries as cylinders that are parallel, unbranched, and equally spaced throughout the 3D voxel (illustrated in Figure 6.5). Capillary length can range from 0.5-1.5 mm so for simplicity in modelling a $1mm^3$ voxel, we will assume a capillary length of 1mm. The volume of one cylindrical capillary is:

$$V_{cap} = \pi {R_c}^2 L \qquad \text{(Eq 6.9)}$$

The estimated blood volume can be related to the capillary density in the voxel through the following equation from which $N_{cap}$ can be calculated (assuming a constant $R_c$ and L):

$$BV = \frac{N_{cap} x V_{cap}}{V_{voxel}} \qquad \text{(Eq 6.10)}$$

In a cross section, based on the 6th assumption from the Krogh-Erlang solution, the number of capillaries ($N_{cap}$) are spaced evenly across the width and length of the voxel cross-section. Therefore, $R_t$ can be found by using the following equation:

$$Voxel_{width} = 2R_t * \sqrt{N_{cap}} \qquad \text{(Eq 6.11)}$$

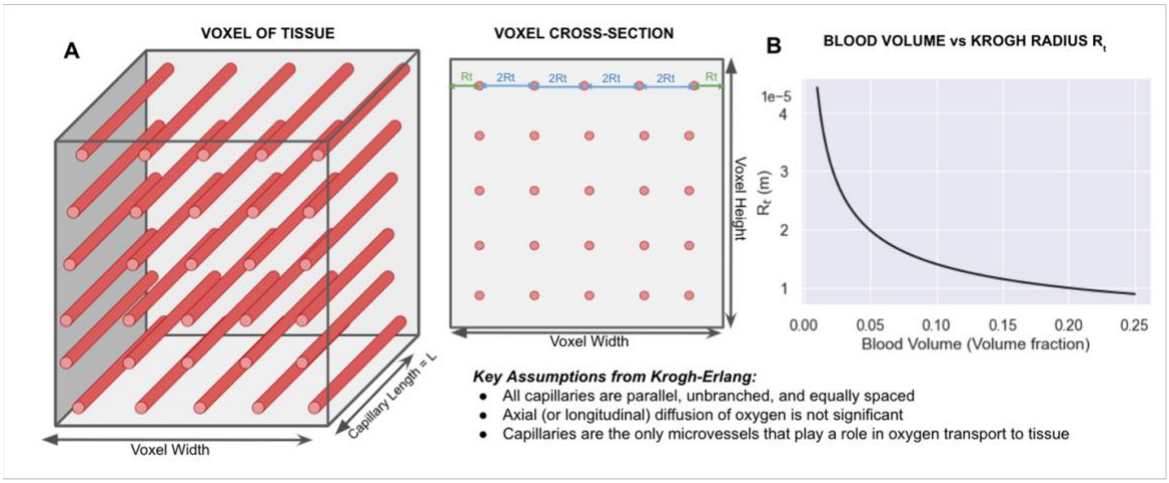


***Figure 6.5. (A)*** *An illustration of a 3D voxel of tissue with capillaries as cylinders that are parallel, unbranched, and equally spaced throughout the voxel.* ***(B)*** *The inverse relationship between blood volume and the Krogh Radius $R_t$ resulting from following this method.*

### *6.2.3.5. Tissue Compartment - Estimating Oxygen Consumption*

Using the Krogh-Erlang solution (Equation 6.7) also requires knowledge of the maximum tissue oxygen consumption rate, $M_0$. Once $R_t$ is found, we can derive $M_0$ from the OEF using the following logic and assumptions. It is important to note that in order for the assumptions of the following equations to be valid, $M_0$ must be calculated in the pre-oxygen state (i.e. the patient is breathing air, or the nanobubbles are not yet delivered). Under this assumption, the $SO_2$ along the capillary can be calculated using the linear equation [205]:

$$SO_2(z) = SaO_2 - \frac{(R_t{}^2 - R_c{}^2)\, M_0}{Hct\ C_{Hb}\ v} * z \qquad \text{(Eq 6.12)}$$

Using Equation 6.6 which relates mean $SO_2$ to the OEF, we can create a linear equation of $SO_2$ along z, the mean $SO_2$ in the capillary ($S_{cap,\,mean}$) will be equal to the linear Equation 6.12 at 0.5L. Therefore, $M_0$ can be related to OEF using the following steps:

$$S_{cap,mean} = SaO_2 * \left(1 - \frac{OEF}{2}\right) = SO_2(0.5L) = SaO_2 - \frac{(R_t{}^2 - R_c{}^2)\, M_0}{Hct\ C_{Hb}\ v} * 0.5L \qquad \text{(Eq 6.13)}$$

Which can be rearranged to calculate $M_0$:

$$M_0 = \frac{SaO_2\ OEF\ Hct\ C_{Hb}\ v}{(R_t{}^2 - R_c{}^2)\, L} \qquad \text{(Eq 6.14)}$$

Finally, with $M_0$ and $R_t$ estimated from the OEF and blood volume, the tissue $PO_2$ (into-tissue axis) can be calculated. Since the $PO_2$ along the capillary ($P_{cap}$) on air and oxygen breathing is known from Step 1, the $PO_2$ throughout the Krogh cylinder can be calculated, for both air and oxygen breathing situations (shown in Figure 6.6).

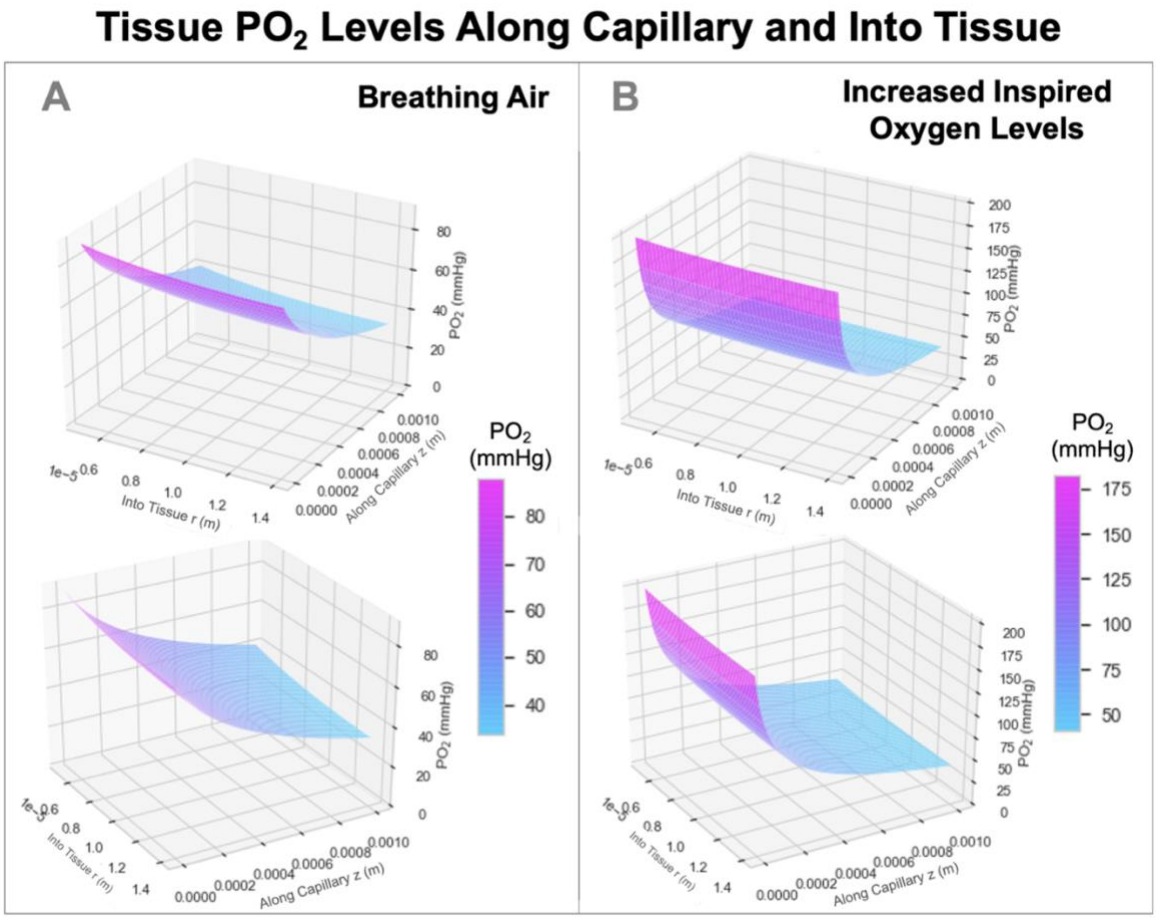


***Figure 6.6.*** *Example 3D surface plots (shown from two viewing angles) of the $PO_2$ into the tissue radius and along the capillary, on* ***(A)*** *air and* ***(B)*** *oxygen breathing, assuming a post-oxygen arterial $PO_2$ change from 90 mmHg to 200 mmHg.*

## 6.2.4. Step 3. Calculating ΔR1 in the 3 Compartments

### *6.2.4.1. Blood Compartments*

Using the model presented in Chapter 5, the ΔR1 induced from supplemental oxygen in the arterial ($\Delta R1_{B,A}$) and venous ($\Delta R1_{B,V}$) blood compartments can both be calculated from the following equation:

$$\Delta R1_B = R1_b(PO_{2,ox}) - R1_b(PO_{2,air}) \quad \text{(Eq 6.15)}$$

Where $R1_b(PO_2)$ is Equation 5.11 from Chapter 5. Recall that this equation accounts for hematocrit, B0, $SO_2$, and $PO_2$, and is adjustable for different species (i.e., rat or human) by changing the P50 value.

### *6.2.4.2. Tissue Compartment*

Between the air and oxygen states, the only paramagnetic factor changing in the tissue compartment is the concentration of oxygen dissolved either intracellularly or interstitially (see Figure 1.3 in Chapter 1). Therefore, the $\Delta PO_{2\,T}$ calculated in Step 2 can be used to calculate the $\Delta R1_T$ using the following equation:

$$\Delta R1_T = r1_{Ox} * \Delta PO_{2\,T} \quad \text{(Eq 6.16)}$$

Where the relaxivity of oxygen, $r1_{Ox}$, is dependent on field strength, and calculated using the model presented in Chapter 4 (Equation 4.4). In the context of this tissue model, temperature is assumed to be 37°C.

## 6.2.5. Step 4. Calculating Weighted Voxel ΔR1

Lastly, the model uses the blood volume fraction (BV) to calculate the resulting ΔR1 of the voxel ($\Delta R1_{voxel}$), assuming equal fractions of oxygenated and deoxygenated blood are present in the voxel, using the following equation:

$$\Delta R1_{voxel} = (\frac{BV}{2})\Delta R1_{B,A} + (1 - BV)\Delta R1_T + (\frac{BV}{2})\Delta R1_{B,V} \quad \text{(Eq 6.17)}$$

By keeping the arterial and venous changes separate, the +ΔR1 in oxygenated blood will be accounted for in the "arterial end" compartment and the -ΔR1 in the less oxygenated blood will be accounted for in the "venous end" section. Ultimately, the large volume fraction of tissue contributes the most to the final $\Delta R1_{voxel}$ (see schematic in Figure 6.7).

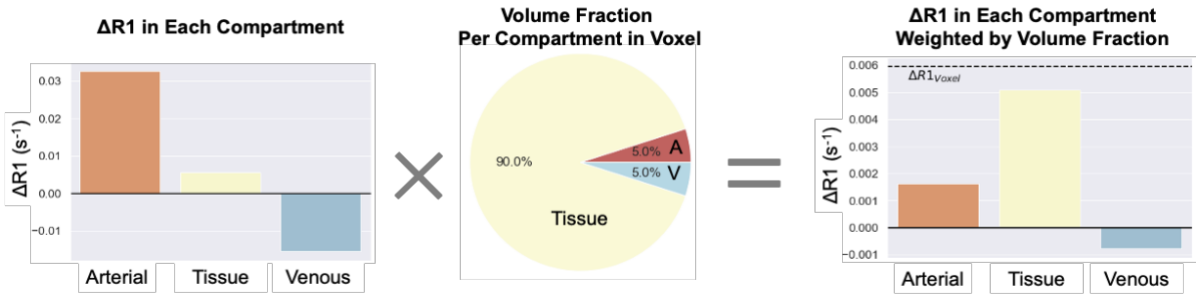


***Figure 6.7.*** *A schematic of Step 4, where the ΔR1 from each compartment is weighted by the volume fraction of each compartment within the voxel. The final* $\Delta R1_{voxel}$ *is the sum of the weighted components*.

## 6.2.6. Applying Model to Simulate ΔR1 from OE-MRI

### *6.2.6.1. Model Variables and Constants*

To demonstrate the application of this model for the purpose of this chapter, the 5 independent variables that vary between different types of tumour tissues, patients and experiments were: the magnetic field B0, hematocrit, oxygen extraction fraction, blood volume in the voxel, and $P_{crit}$ — the ranges of these values used to produce the results in this chapter are listed in Table 6.1. Next, there are 4 dependent variables that are calculated from the independent variables: (1) the fraction of erythrocytes in whole blood $f_e$ is calculated from hematocrit, (2) the $r1_{Ox}$ is calculated from B0, (3) the Krogh tissue radius $R_t$ is calculated from OEF and blood volume, and the tissue oxygen consumption rate is calculated from OEF, $R_t$, and $P_{crit}$ (shown in Table 6.2). Lastly, the constants used for the remaining parameters are listed in Table 6.3.

The chosen "tissue types" to simulate were: healthy brain tissue, and tumour regions of "vascular periphery", "necrotic tissue", "tissue with high metabolism" to simulate hypoxic

regions (split into “more hypoxic” and “less hypoxic” by higher and lower blood volume ranges, and “tissue with normal metabolism” to simulate the regions of the tumour which are not hypoxic. To select ranges for OEF, $P_{crit}$, and blood volume that have already been approved in peer-review were used, such as the values published in a computational model for tumour oxygenation by Welter et al. were used [214], or published values that were measured experimentally. For OEF: Welter et al. [214] report an OEF in healthy breast tissue of 0.11±0.09, and breast tumour tissue of 0.34±0.1; Cho et al. [219] report an OEF in healthy brain tissue of 34.2 ± 2.6%; and necrotic tissue was assumed to be very low, between 0.02-0.05. For blood volume: Leenders et al. [220] measured the blood volume in healthy brain tissue to be 5.2±1.4% and 2.7±0.6% for grey and white matter, respectively; Welter et al. [214] report that using MRI and a brain tumour animal model, BV of tumour tissue was 5.3±0.6% which is used as the “low blood volume range”, and Qi et al. [173] measured 13±4.1% blood volume in VX2 squamous cell tumours which is used as the “high blood volume” range; for necrotic tissue, a 0.01% blood volume is used, i.e. almost no blood compartment is present. Lastly, Welter et al. [214] report that literature values of $P_{crit}$ range from 1-4 mmHg, and Welter et al. lowered $P_{crit}$ for tumour tissue by ½ due to resistance to hypoxia; this corresponds with reports from Honig and Gayeski [221] who report tumour $P_{crit}$ as 0.5 mmHg.

For the dependent variables, the resulting range of $R_t$ calculated from the range of BV values chosen in Table 6.1 is 1.07-4.43x$10^{-5}$ m, which is similar to ranges reported such as 4x$10^{-5}$ m [222] and 2.5x$10^{-5}$ [223]. The resulting range of $M_0$ calculated from the range of OEF chosen in Table 2 is 1.2x$10^{-5}$ - 3.5x$10^{-4}$ $mlO_2$/mL/s, which is consistent with the reported $M_0$ values of 6x$10^{-5}$ and 2.4x$10^{-4}$ $mlO_2$/mL/s for normal tissue and tumour tissue, respectively, used by Welter et al. [214]. Lastly, simulations were run using varying blood velocity (0.0001-0.001 m/s,), capillary length (0.0015-0.0005 m), and capillary radius (2-5x$10^{-6}$m) while maintaining constant values for all other variables. These alterations resulted in a negligible effect of just 0.00003% to 0.00007% of the $\Delta R1_{voxel}$ estimates.

***Table 6.1.*** *A table of the 5 independent variables that vary between different types of tumour tissues, patients, and experiments. The chosen ranges of these values used to produce the simulated results in this chapter are listed.*

| **Variable** | **Value or Range Used** | | | | | **Units** |
|---|---|---|---|---|---|---|
| | **Healthy Brain Tissue** | **Tumour Vascular Periphery** *No Tissue Compartment* | **Tumour Tissue with High Metabolism i.e. Hypoxic** *2 types: Low BV and High BV* | **Tumour Tissue with Normal Metabolism** | **Tumour Necrotic Tissue** *No Blood Compartments* | |
| Main magnetic field of MRI (B0) | 1.5, 3, 4.7, 7 | | | | | T |
| Hematocrit (Hct) | Total range: 0.36-0.50<br>Female range: 0.36-0.48<br>Male range: 0.41-0.50 | | | | | 0-1 Volume fraction |
| Oxygen extraction fraction (OEF) | 0.31-0.37 | 0.24-0.44 | | 0.02-0.2 | 0.02-0.05 | 0-1 Fraction |
| Blood volume in voxel (BV) | 2-7% | 100% blood volume, no tissue compartment | Low BV range= 4.7-5.9%<br><br>High BV range = 9-17% | 4.7-5.9% | 0.01% blood volume, i.e., no blood compartments | 0-1 Volume fraction |
| The $PO_2$ value above which the tissue oxygen consumption rate is relatively constant ($P_{crit}$) | 1-4 mmHg | N/A | 0.5-2 mmHg | | | mmHg |

***Table 6.2.*** *A table of the 4 dependent variables that are calculated from the independent variables listed in Table 6.1.*

| **Parameter Meaning** | **Parameter Name** | **Value or Range Used** | **Units** |
|---|---|---|---|
| Fraction of erythrocytes in whole blood | $f_e$ | Calculated by Equation 5.2 as a function of Hct, $W_{RBC}$ and $W_{plasma}$ | 0-1 Volume fraction |
| Relaxivity of oxygen | $r1_{Ox}$ | Calculated by Equation 4.4 as a function of B0 and temperature (set to 37°C for tissue model) | $s^{-1}$ $mmHg^{-1}$ |
| Krogh tissue radius | $R_t$ | Determined by the blood volume | m |
| Tissue oxygen consumption | $M_0$ | Determined by the OEF and the $R_t$ | $mlO_2$ $ml^{-1}$ $s^{-1}$ |

***Table 6.3.*** *The constants used for the remaining parameters of the model.*

| Constant Meaning | Name | Value Used (Units) | Source |
|---|---|---|---|
| The oxygen tension when haemoglobin is 50% saturated with oxygen | P50 | 37 (mmHg) | [205], [224] |
| Hill coefficient | n | 2.7 (unitless) | [205], [224] |
| Plasma $O_2$ solubility | $a_p$ | $3.1x10^{-5}$ ($ml O_2$ $ml^{-1}$ $mmHg^{-1}$)<br>**Assuming 22.4L/mol under normal conditions* | [214], [225] |
| Haemoglobin binding capacity (Hüffner factor) | $C_{Hb}$ | 1.36 ($ml O_2$ $g^{-1}$) | [214] |
| The concentration of oxygen per unit volume of RBCs at maximal saturation: calculated as the product of the haemoglobin binding capacity $C_{Hb}$ and the mean corpuscular haemoglobin concentration [Hb] | $c_0$ | Calculated from<br>$c_0 = C_{Hb}$ x [Hb]<br>=1.36 $ml O_2$/g x 0.43g/ml<br>=0.5 ($ml O_2$ $ml^{-1}$) | |
| Tissue $O_2$ solubility | $a_T$ | $2.8x10^{-5}$ ($ml O_2$ $ml^{-1}$ $mmHg^{-1}$) | [214], [225] |
| Tissue $O_2$ diffusivity | $D_T$ | $2.41x10^{-9}$ ($m^2 s^{-1}$) | [214], [225] |
| Capillary length | L | 0.001 (m) | [226] |
| Capillary radius | $R_c$ | $3.5x10^{-6}$ (m) | [226] |
| Capillary velocity | v | 0.00079 (m $s^{-1}$) | [227] |

### *6.2.6.2. Comparison with Empirical OE-MRI Results*

Empirical OE-MRI measurements by Winter et al. [228], Bhogal et al. [229], O'Connor et al. [167], and Little et al. [178], were used for comparison because they either estimated or measured the $PaO_2$ change induced by their hyperoxic gas challenge. Altogether, these studies provided measurements in "healthy brain tissue", "vascular periphery", "tumour core", "necrotic tissue", and whole tumour ROI measurements from clinical patient data by O'Connor et al. [167], and Little et al. [178]. As it is not possible to know the composition of the whole tumour ROIs reported, the simulated ΔR1 for each possible tumour tissue type is calculated for comparison, and it is assumed that the empirical whole tumour ROI should fall within that range of ΔR1.

### 6.2.7. Applying Model to Simulate ΔR1 from Nanobubble Delivery

For simulating the possible R1 change following oxygen delivery from nanobubbles in tissue, a different approach was taken. Since the $\Delta PO_2$ in tumour tissue produced by nanobubbles has been measured to be approximately 30 mmHg [52], the relationship between $\Delta PO_2$ in the tissue compartment and $\Delta R1_{voxel}$ resulting from any set of OEF, blood volume, $P_{crit}$, and $PaO_2$ change can be established. The $\Delta R1_{voxel}$ corresponding to a $\Delta PO_2$ of 30 mmHg was therefore calculated and the mean and standard deviation of expected $\Delta R1_{voxe}$ determined.

## 6.3. Results

### 6.3.1. Model Behaviour

To visualize the relationship between the independent variables, dependent variables, and ΔR1, the following plots were produced. The effect of all combinations of blood volume and OEF on the baseline tissue $PO_2$ (mean and minimum) and maximum oxygen consumption rate is shown in Appendix Figure D.1. The effect of OEF on the ΔR1 of the venous, arterial, and tissue compartments individually, for varied $PaO_2$ changes induced from oxygen, is shown in Figure 6.8A-C, and the resulting ΔR1 for the voxel is shown in Figure 6.8D-E. In this model, there is an inverse relationship between blood volume and the Krogh Radius $R_t$ (shown in Figure 6.5), and therefore blood volume influences the $M_0$ (see Appendix Figure D.1C), and also the final $\Delta R1_{voxel}$ (see Figure 6.8D-E). In this model, the OEF chosen has a large effect on $\Delta R1_{voxel}$, which can be seen clearly in Figure 6.8. Lastly, the relationship between $\Delta PO_2$ in the tissue compartment and $\Delta R1_{voxel}$ is shown in Figure 6.9.

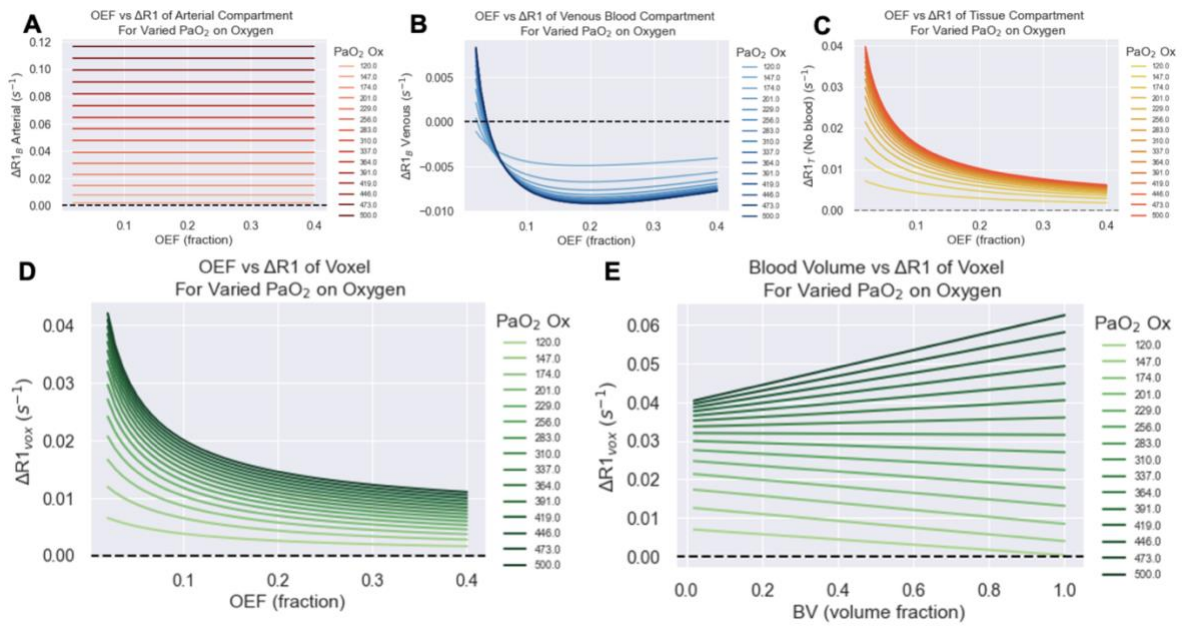


***Figure 6.8.*** *Simulated data showing the effect of OEF on the ΔR1 of the* ***(A)*** *arterial blood,* ***(B)*** *venous blood, and* ***(C)*** *tissue compartments individually, and* ***(D)*** *total voxel ΔR1 for varied $PaO_2$ changes induced from increased oxygen breathing, with blood volume set to 10%. The corresponding effect of varying blood volume with a set OEF (OEF=0.2) is shown in* ***(E)****.*

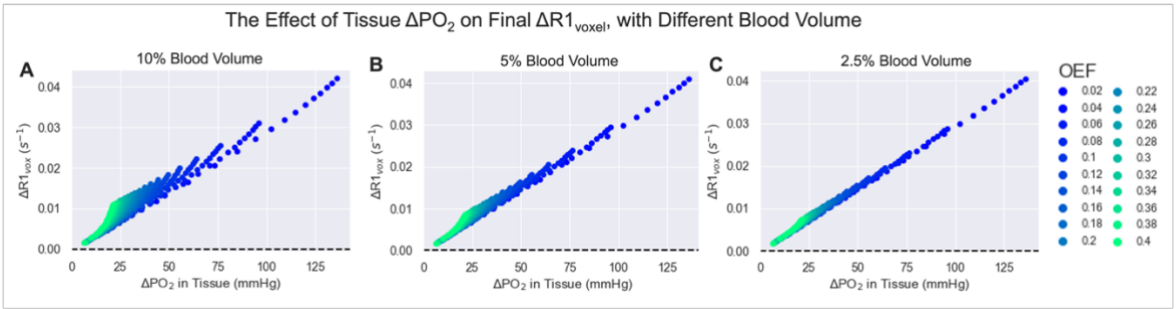


***Figure 6.9.*** *Simulated data showing the relationship between $\Delta PO_2$ in the tissue compartment and $\Delta R1_{voxel}$, for* ***(A)*** *10%,* ***(B)*** *5%, and* ***(C)*** *2.5% blood volume. The data points are coloured by the OEF (0.02-0.40) used in that $\Delta R1_{voxel}$ calculation (see OEF legend).*

## 6.3.2. Applying Model to Simulate ΔR1 from OE-MRI

The resulting ΔR1 calculated from this model is plotted in Figure 6.10, calculated using different field strengths, and using all combinations of the chosen range of Hct, OEF, BV, $P_{crit}$ listed in Table 6.1 for each respective tissue type, and calculated using the female and male ranges for hematocrit, separately, to examine the expected difference in ΔR1. In

this simulation, the largest difference in ΔR1 between the sexes was 0.0045 $s^{-1}$, which occurred in the vascular periphery due to containing the highest percentage of blood component and therefore most affected by differences in hematocrit. The difference in ΔR1 between the sexes was negligible in the other simulated tissue types.

Unlike the models in Chapters 4 and 5, It is difficult to quantitatively compare the simulations from this model to empirical ΔR1 measurements, because although B0 is reported, the variables of OEF, hematocrit, and $P_{crit}$ are never measured or reported, and the $PaO_2$ on air or oxygen is only sometimes reported, either as a measurement or an estimation. However, the following section uses a variety of reported ΔR1 from OE-MRI literature to gain a rough estimation of the accuracy of this model.

First, the qualitative ΔR1 responses, categorized by different tumour tissue types by the authors of the OE-MRI literature, are listed in Table 6.4. Overall, the simulated ΔR1 for each tissue type shown in Figure 6.10 does correspond with observations from OE-MRI literature: as seen in experiments by Winter et al. [228], the “vascular periphery” shows greater +ΔR1 than the “tumour core” and “necrotic” regions, and the “necrotic” regions show a greater +ΔR1 than the “tumour core” but less than “vascular periphery”. As observed in experiments by Burrell et al. [97], the “less hypoxic” tumour type shows greater +ΔR1 than the “more hypoxic” tumour type. Lastly, in these simulations, the healthy brain tissue is predicted to show a very small ΔR1 that might end up ‘not detectable’, as observed by Bhogal et al. [229].

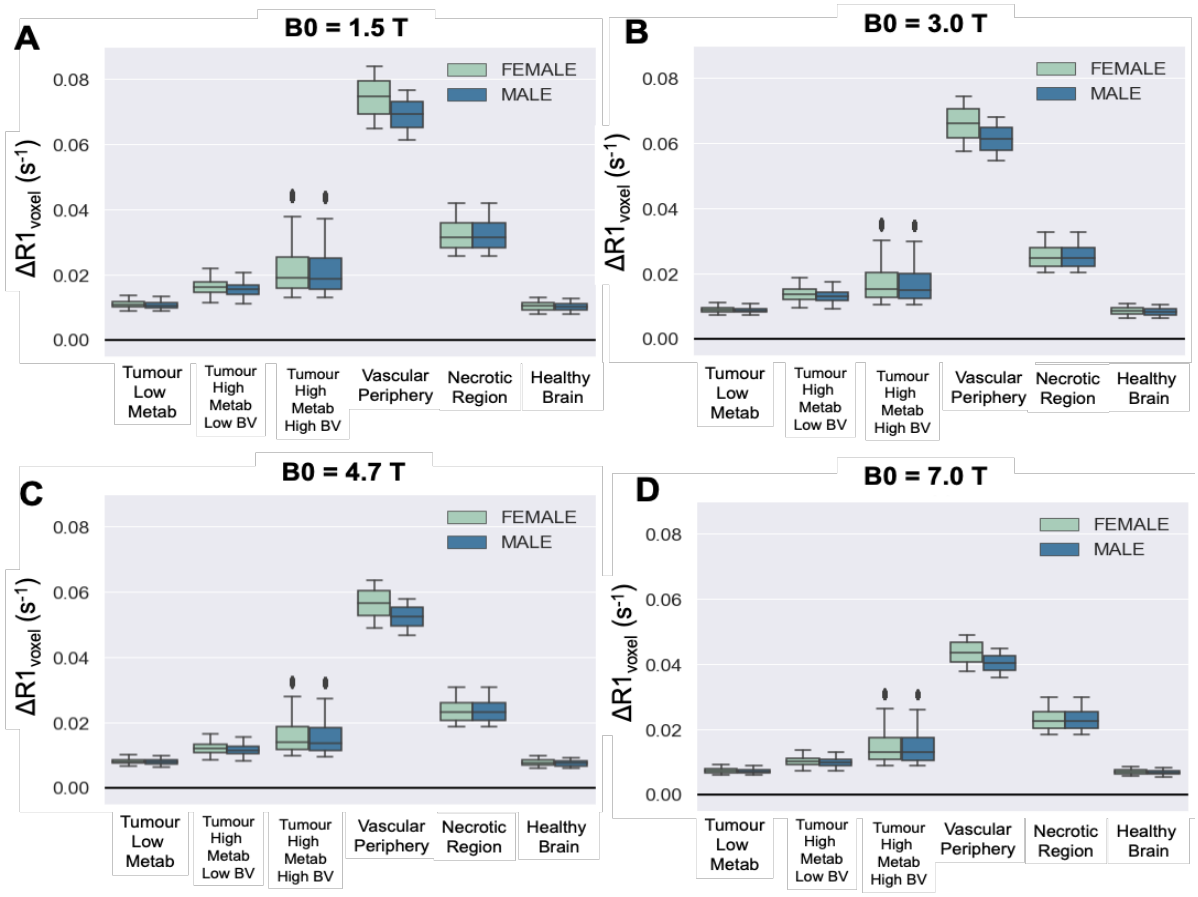


***Figure 6.10.*** *The resulting ΔR1 from a hyperoxic gas challenge calculated from this model, calculated using all combinations of the chosen range of Hct, OEF, BV, $P_{crit}$ listed in Table 6.1, for each respective tissue type, using the female and male ranges for hematocrit separately, with B0 set to* ***(A)*** *1.5T,* ***(B)*** *3T,* ***(C)*** *4.7T,* ***(D)*** *7T.*

***Table 6.4.*** *The OE-MRI response in different tissue types identified by various studies.*

| Generalized Tumour Tissue Type | Empirical ΔR1 Response to 100% O2 |
|---|---|
| Well-perfused tissues, vascular rim tissue, or called "Vascular Periphery" | • Positive ΔR1 (1.5T) [167]<br>• Positive ΔR1 (1.5T) [228] |
| Tumour core, possibly hypoxic, but is perfused, or hypoxic region that consumes the $O_2$ | • Mostly positive ΔR1 (1 small negative ΔR1) (1.5T) [228]<br>• Low or absent ΔR1, but moderate perfusion from IAUC60 (1.5T) [167]<br>• More hypoxic tumour type showed smaller positive ΔR1, less hypoxic tumour type showed larger positive ΔR1* (7T) [97] (*Used carbogen)<br>• Strong negative ΔR1 seen in the contrast enhancing areas of the glioblastoma and metastasis (1.5T) [201] |
| Necrotic/avascular tissue that has little perfusion | • Positive ΔR1 (1.5T) [228]<br>• Moderate positive ΔR1 in peritumoral edema and necrotic areas (1.5T) [201]<br>• Low or absent ΔR1 (1.5T) [167] |

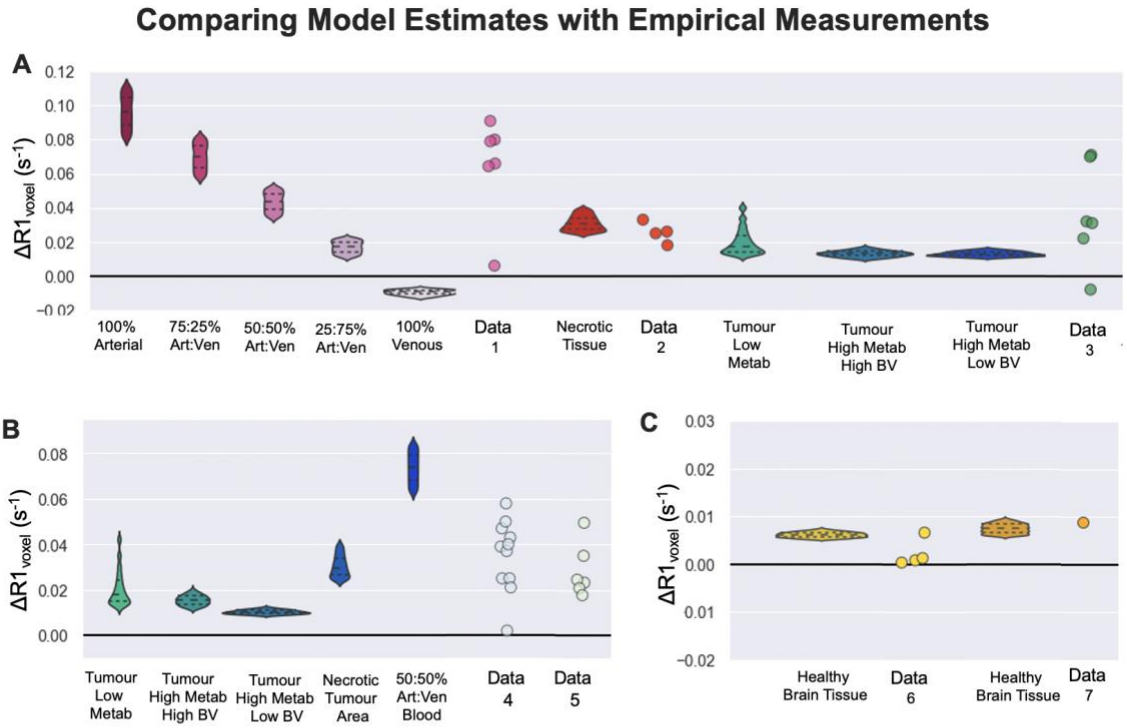


| Source of Empirical Measurements | | |
|---|---|---|
| Label | Reference | Details |
| Data 1 | Winter et al. 2011 | "Vascular Periphery" of rabbit VX2 carcinoma tumours, 1.5T; $PaO_{2,air}$= 83 mmHg; $PaO_{2,ox}$= 428 mmHg |
| Data 2 | | "Necrotic" region of rabbit VX2 carcinoma tumours, 1.5T; $PaO_{2,air}$= 83 mmHg; $PaO_{2,ox}$= 428 mmHg |
| Data 3 | | "Tumour core" region of rabbit VX2 carcinoma tumours, 1.5T; $PaO_{2,air}$= 83 mmHg; $PaO_{2,ox}$= 428 mmHg |
| Data 4 | O'Connor et al. 2009 | Whole tumour ROI of patients with advanced cancer of the abdomen and pelvis, 1.5T; $PaO_{2,air}$= 98 mmHg; $PaO_{2,ox}$= 600 mmHg |
| Data 5 | Little et al. 2018 | Whole tumour ROI of patients with renal cell carcinoma, 1.5T; $PaO_{2,air}$= 98 mmHg; $PaO_{2,ox}$= 600 mmHg |
| Data 6 | Bhogal et al. 2017 | Healthy human brain ROI, 7T, $PaO_{2,air}$= 109 mmHg; $PaO_{2,ox}$= 500 mmHg |
| Data 7 | Muir et al. 2016 | Healthy human brain ROI, 7T, $PaO_{2,air}$= 98 mmHg; $PaO_{2,ox}$= 750 mmHg |

***Figure 6.11.*** *Plots containing 7 sets of empirical ΔR1 measurements, alongside the respective simulated ΔR1 according to the B0, $PaO_2$ and tissue type.*

For a rough quantitative comparison, empirical ΔR1 measurements from 6 tissue types, alongside the respective simulated ΔR1 according to the B0, $PaO_2$ and tissue type, are shown in Figure 6.11. It is not possible to know the composition of the whole tumour ROIs reported by O'Connor et al. [167] and Little et al. [178], or the "tumour core" reported by Winter et al. [228], however, each datapoint for empirical tumour ΔR1 falls within the range of ΔR1 simulated for each possible tumour tissue type, therefore these whole tumour ROIs could reasonably be the sum of a composition of these different tumour tissue types. There is one notable exception to this, which is one "tumour core" datapoint reported by Winter et al. [228], which reaches a negative ΔR1 close to that of pure venous blood.

### 6.3.3. Applying Model to Simulate ΔR1 from Nanobubble Delivery

The $\Delta PO_2$ in the tissue from the nanobubbles has been measured to be approximately 30 mmHg [52], and the relationship between $\Delta PO_2$ in the tissue compartment and $\Delta R1_{voxel}$ resulting from any set of OEF, blood volume, $P_{crit}$, and $PaO_2$ change is shown in Figure 6.9. The $\Delta R1_{voxel}$ corresponding to a $\Delta PO_2$ of 30 mmHg was 0.012 ± 0.0014 $s^{-1}$, the effect size illustrated in Figure 6.12. Therefore, using the same power calculation method as performed in Chapter 2, as a paired measurement in a study across multiple subjects at 1.5T, a study of 14, 17, and 21 participants would yield 80%, 90%, or 95% power, respectively (two-tailed, alpha=0.05).

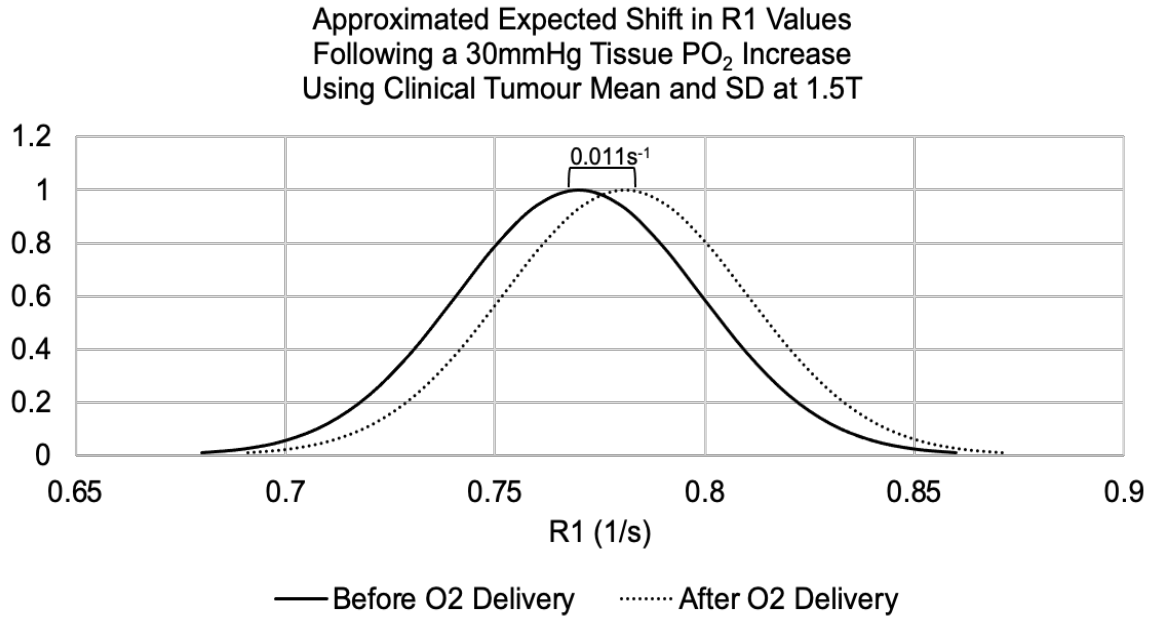


***Figure 6.12.*** *A simulation of the expected shift in tumour R1 values, following a hypothetical 30 mmHg oxygen increase in the tumour tissue $PO_2$ as measured by Owen et al.* [52]. *Data published by O'Connor et al.* [167] *were used to calculate the clinical tumour mean and standard deviation.*

## 6.4. Discussion

### 6.4.1. Model Design and Behaviour

In this chapter, a 3-compartment model has been proposed for estimating the changes in R1 that could be expected in tumour tissues depending on field strength, blood

$SO_2$, blood volume, hematocrit, oxygen extraction fraction, and changes in $PO_2$ in both the blood and tissue. This model has been developed with the aim of estimating the expected ΔR1 induced by the oxygen delivery from nanobubbles in a voxel containing tumour tissue, however it is generally applicable to OE-MRI research as well, and has been designed to make it possible for a researcher to easily substitute their preferred model for tissue oxygen diffusion and consumption and make this model tailored to their tissue of interest, for example, lung or liver. The model has been hosted open-source at GitHub.com/BulteGroup/TissueR1Model for other researchers to adopt, adapt and improve.

Although this model still includes some constants and variables that cannot be measured in individual patients, a strength of this model is that it has been designed so that the independent variables are either known (B0), or can be measured via a non-imaging method (i.e., arterial $PO_2$, hematocrit), or through another imaging method (i.e., measuring blood volume or OEF). For example, initial $SO_2$ of venous system could be measured using MR sequences such as T2-Relaxation-Under-Spin-Tagging [230] or Quantitative Susceptibility Mapping based methods [231]. Testing whether it would be possible to use $SO_2$, OEF or blood volume measurements from another imaging modality is beyond the scope of this thesis, however, in the future, as methods for these factors continue to advance, this connection could prove useful in future work.

Interestingly, the relationship between $\Delta PO_2$ in the tissue compartment and $\Delta R1_{voxel}$ (Figure 6.9) shows that the linear relationship between $\Delta PO_2$ and $\Delta R1_{voxel}$ seen in phantoms almost holds true in tissue voxels containing lower blood volume; however, in voxels containing higher blood volume, the ΔR1 contribution from the blood compartment interrupts the linear relationship. This suggests that despite the influence of deoxyhemoglobin changes, measuring ΔR1 does provide an indication of the final change in $PO_2$ in the tissue.

### 6.4.2. Applying Model to Simulate ΔR1 from OE-MRI

The $r1_{Ox}$ model and R1 Blood model both agree well with empirical measurements ($R^2$=0.93 and 0.93); however, since the tissue compartment of this model contains variables that were not measured at the time of OE-MRI data collection (i.e., hematocrit, changes in arterial $PO_2$, tumour blood volume), it is not possible to quantitatively compare the model ΔR1 predictions to the measured ΔR1 with metrics such as $R^2$ and MSE. However, for a select few OE-MRI studies that did report either measured or estimated $PaO_2$ changes, the simulated ΔR1 from the model did result in ΔR1 values that were in good agreement with the empirical data (Figure 6.11). The values for brain tissue and necrotic tissue were particularly accurate, and although it is not possible to know the composition of the whole tumour ROIs, "vascular periphery", or "tumour core", each datapoint for empirical tumour ΔR1 fell within the range of ΔR1 simulated for each possible tumour tissue type, and therefore the empirical ΔR1 could reasonably be the sum of a composition of these different tumour tissue types.

This model may be useful for OE-MRI researchers looking to predict the effect of certain factors, such as hematocrit. It is interesting that hematocrit differences in the male and female populations did have a slight effect on ΔR1 when the voxel contained larger blood volumes. In fact, this predicted difference has been empirically observed in lung tissue — where blood volume is approximately 33-36% [232] — by Kindvall et al. [212] reported that age and sex were all predictors of ΔR1 in lung tissue, likely due to the hematocrit differences.

### 6.4.3. Limitations

It is currently difficult to quantify the agreement of this model with the empirical data, and the model still includes some constants and variables that cannot be measured in individual patients. Testing whether it would be possible to use OEF or blood volume measurements from another imaging modality is beyond the scope of this paper; however, in the future, as methods for measuring blood volume or OEF continue to advance, this

connection could prove useful in future work. In addition, there may be unpublished raw datasets from former OE-MRI studies held by other research groups where arterial $PO_2$ was measured but perhaps not reported. We welcome other researchers to test the predictions of this model against a larger sample size of data — this would greatly improve confidence in this model before it is applied in oxygen-enhanced MRI studies.

Another limitation is that in this current model, the arterial blood volume has been set to be equal to the venous blood volume — this will not be true for all voxels. Since the open-source code for the model has been provided, future researchers are welcome to adjust this parameter if they have more information about the ratio of arterial and venous blood in their voxels of interest.

In addition, this model sets only one value for haematocrit in the system, however the Fåhræus–Lindqvist effect suggests that capillary haematocrit will be lower than the systemic haematocrit [233]. It has not yet been determined how much the average hematocrit level is reduced from this [234], however at the scale of a 1 $mm^3$ voxel or greater, this effect is unlikely to have a large effect on the accuracy of the R1 estimates. Across 1 $mm^3$, the voxel would contain tissue, larger vessels, and smaller vessels, and therefore the contribution from the smaller vessels is multiplied by a smaller volume fraction than the tissue compartment, which remains the largest contributor to ΔR1 in the voxel.

The parameters for the $r1_{Ox}$ model presented in Chapter 4 were created by compiling empirical measurements of the relaxivity of oxygen over 50 years of MRI research in phantoms, saline and water solutions, vitreous fluid, and plasma, and fitting this data to a Lorentzian equation which fit $R^2$=0.93. Of course, the $r1_{Ox}$ in these solutions may be slightly different than the $r1_{Ox}$ in tissues, and indeed, the $r1_{Ox}$ may vary between tissues as well. However, we believe the $r1_{Ox}$ derived from this empirically-driven model will better represent the $r1_{Ox}$ in tissue than using any single $r1_{Ox}$ datapoint measured in saline or water, as has

been common practice in previously published manuscripts [85], [100], [103], [106], [157], [207], [213].

Lastly, this model contains fewer independent variables than the model by Holliday et al. [213], but considerably more variables than the simple equation proposed by Kindvall et al. [207]. Ideally, the outputs of these three models could be compared; however, since they are so different and contain such different parameters, it is difficult to choose the variable 'settings' at which to compare them. For example, this new model adjusts all field-dependent parameters according to field strength, while both of the previous models are only applicable at one field strength. Similarly, neither of the previous models account for hematocrit differences, which *do* affect the resulting ΔR1, as we have now demonstrated in this manuscript and as was actually measured in human lung tissue by Kindvall et al. [212]. Therefore, although it is not possible to provide a robust comparison of this model to the previous two models, we are confident that this model brings significant improvements for two main reasons: first, the utility of this model surpasses the previous models simply by the fact that the previous models only apply to a single field strength [207]. OE-MRI research occurs at a variety of field strengths, and therefore the model must account for the effect of B0 on each of the relevant variables. This field-strength consideration is an extremely useful feature that will allow data acquired at different field strengths to be compared. Second, one previous model incorrectly combines values from different field strengths into one single model (using $r1_{dHb}$ from Silvennoinnen et al. [110] at 4.7T alongside $r1_{Ox}$ from Pilkinton et al. [108] at 1.5T), which suggests it will be produce slightly incorrect results at any field strength [213].

### 6.4.4. Implications for Measurement of Nanobubble Oxygen Delivery

The $\Delta R1_{voxel}$ corresponding to a $\Delta PO_2$ of 30 mmHg was 0.012 ± 0.0014 $s^{-1}$, the effect size illustrated in Figure 6.12. Therefore, using the same power calculation method as employed in Chapter 2, as a paired measurement in a study across multiple subjects at

1.5T, a study of 14, 17, and 21 participants would yield 80%, 90%, or 95% power, when detecting a 30 mmHg change in $PO_2$, respectively (two-tailed, alpha=0.05) [172]. Overall, despite hypothesizing that the paramagnetism of deoxyhemoglobin could greatly interrupt ΔR1, this expected ΔR1 is only slightly smaller from the ΔR1 predicted from the phantom experiments in Chapter 2. The resulting relationship between $\Delta PO_2$ in the tissue and ΔR1 of the voxel suggests that despite the influence of deoxyhemoglobin changes, when blood volume is below 10%, the $\Delta R1_{voxel}$ does retain a linear relationship with the $\Delta PO_2$ in the tissue. Of course, however, it does not measure the *total delivery of oxygen to the tissue*, since some regions will consume the oxygen and thus induce no change in ΔR1.

The original motivation for creating this model was to understand results observed in the preclinical experiments seen in Chapter 3. Interestingly, this model does not predict that nanobubbles should induce a negative ΔR1 in tissues, unless the voxel contains almost entirely venous blood. Therefore, it is likely that the negative ΔR1 following nanobubble delivery measured in Chapter 3 is more likely due to temperature fluctuations, which could induce a change in R1 of -0.0279 $s^{-1}/°C$.

### 6.4.5. Optional expansion: Inclusion of a Capillary Compartment

If a researcher preferred to consider the capillary bed as a separate fourth compartment of this model, the following additional steps are required:

1. Using the value of the mean capillary $SO_2$ ($S_{cap,\ mean}$) on air and on oxygen and the Hill Equation (Equation 5.10) to calculate mean capillary $PO_2$.
2. Use the mean capillary $PO_2$ and Equation 5.11 to calculate the R1 of the capillary compartment on air then on oxygen.
3. Calculate the ΔR1 of the capillary compartment using Equation 6.15 and the calculated R1 on air and on oxygen.

4. Calculate $\Delta R1_{voxel}$ by altering Equation 6.17 to include a fourth compartment ($\Delta R1_{b,cap}$) and set the relative blood volume fractions in accordance with the desired tissue type.

## 6.5. Conclusion

In this chapter, a 3-compartment model has been presented for estimating the changes in R1 that could be expected in healthy, hypoxic and necrotic tumour tissues depending on field strength B0, $SO_2$, blood volume (BV), hematocrit, oxygen extraction fraction (OEF), and changes in blood and tissue $PO_2$. This model has been designed to be easy for researchers to tailor to their tissue of interest by substituting their preferred model for tissue oxygen diffusion and consumption. In a demonstration of the model, the resulting ΔR1 are consistent with reported literature OE-MRI results in a variety of tissue types, and predicted differences due to factors, such as sex, agree with empirical observations from human lungs. Lastly, when using the model to estimate R1 changes from nanobubble delivery, the model shows that as a paired measurement in a study across multiple subjects at 1.5T, a study of 14-21 participants would be required to yield 80-95% power when detecting a 30 mmHg change in $PO_2$.

# Chapter 7. Conclusions, Clinical Translation, and Future Work

---

*In this chapter, the major findings from each chapter of this thesis are summarised. These estimates are, however, based on theoretical calculations, and ultimately, successful clinical translation is the end goal for the therapeutic nanobubbles discussed in this thesis. Although it was not possible to perform clinical experiments with nanobubble delivery within the scope of this thesis, the most relevant adjacent research area is clinical OE-MRI, and it was possible to analyse the results from two recently completed clinical OE-MRI studies. These results are useful for shedding light on several elements that would be relevant to using this method in a clinical experiment involving nanobubbles, such as the benefits and drawbacks of a chosen T1 mapping method, vulnerability to patient motion, and potential image artefacts.*

*Therefore, in this chapter, these original research results are used to draw conclusions about the feasibility of using R1 measurements to monitor oxygen delivery from nanobubbles in a clinical MRI setting. Lastly, the broader potential applications of the work produced for this thesis is discussed.*

*This chapter includes edited material from the following manuscripts:*

- ***E Bluemke**, A Bertrand, K Chu, A Murchison, T Greenhalgh, B Burns, N Taylor, K Shah, F Gleeson, D Bulte. Using Variable Flip Angle (VFA) and Modified Look Locker Inversion Recovery (MOLLI) T1 Mapping in Clinical OE-MRI. Magnetic Resonance Imaging, 2022. DOI:10.1016/j.mri.2022.03.001*
- ***E Bluemke**, A Bertrand, K Chu, A Murchison, T Greenhalgh, B Burns, N Taylor, K Shah, F Gleeson, D Bulte. Oxygen-enhanced MRI and radiotherapy in patients with oropharyngeal squamous cell carcinoma. Under review.*
- ***E Bluemke**, D Bulte, A Bertrand, P Ferencz, B George, R Cooke, K Chu, L Durrant, V Goh, C Jacobs, SM Ng, VY Strauss, MA Hawkins, and R Muirhead. Oxygen-enhanced MRI and chemoradiotherapy in patients with anal squamous cell carcinoma. In preparation.*
- ***E Bluemke***, D Bulte*, A Bertrand, B George, R Booke, K Chu, L Durrant, V Goh, C Jacobs, S Ng, V Strauss, M Hawkins, R Muirhead; Oxygen-Enhanced MRI MOLLI T1 Mapping during Chemoradiotherapy in Anal Squamous Cell Carcinoma. Clinical and Translational Radiation Oncology, 2020. DOI:10.1016/j.ctro.2020.03.001*

---

## 7.1. Main Findings

In previous work, oxygen-filled nanobubbles have been investigated as a method of oxygen delivery and have shown promising results in improving therapeutic response to ultrasound mediated drug delivery in a mouse model of pancreatic cancer [40], [52]. The aim of this thesis was to examine whether clinically available MRI techniques can be used to detect the change in oxygen levels produced by these nanobubbles. To answer this question, a combination of phantom and preclinical experiments, mathematical modelling, and the analysis of data from two clinical trials has been used. The major findings from each chapter of this thesis are summarised below.

The literature review provided in **Chapter 1** led to the conclusion that out of several clinically available MRI techniques, quantitative T1 measurements were the most promising for the purpose of measuring oxygen delivery from nanobubbles.

The experiments in **Chapter 2** showed that the presence of nanobubbles does not interrupt the linear relationship between $PO_2$ and R1, and that T1 mapping could provide a non-invasive method of measuring a >100 mmHg whole voxel oxygen delivery from nanobubbles. This measurement describes the LOD for a single voxel, which is different from the detection power in a large ROI — due to the repeated number of voxel measures in a large ROI, it would be feasible to detect a smaller difference between two large ROIs that would otherwise not be realistic in a single voxel. As a paired measurement in a study across multiple subjects at 3T, a study of 10-15 participants would be required to yield 80-95% power.

The experiments in **Chapter 3** showed that the administration of nanobubbles did not induce the positive change in R1 in xenograft tumours that was expected, and that this technique is vulnerable to fluctuations in temperature. These preclinical pilot experiments produced unexpected results which motivated the creation of the models that are presented in Chapters 4-6.

The model presented in **Chapter 4** shows that the relaxivity of oxygen in water, saline, plasma and vitreous fluids can be accurately estimated as a function of the magnetic field strength and temperature. In addition, this model shows that relaxivity decreases with increasing magnetic field strength in a Lorentzian shape, with oxygen having a very strong effect on R1 at field strengths below 2 T. Not only is this a relevant finding for low-field MRI research, but it also suggests that a 1.5T scanner may be preferred over a higher field MRI in future experiments for detecting the change in oxygen caused by nanobubbles. While the oxygen relaxivity would be even stronger below 1.5T, for extremely low fields, main challenges for low-field MRI is the loss in SNR, and it is possible that between 0.5-2T would provide the best trade-off between keeping high enough SNR while exploiting the stronger relaxivity of oxygen. However, it is possible that with a combination of high performance acquisition techniques and detectors and future image processing techniques, low-field MRI will continue to improve image quality despite SNR challenges at lower field strengths [194], [195].

The model presented in **Chapter 5** shows that the R1 of blood can be estimated as a function of the haematocrit, $SO_2$, $PO_2$, and magnetic field strength, under both normal physiological and hyperoxic conditions. This model was able to predict and hence explain the apparently contradictory negative changes in blood R1 following oxygen delivery or hyperoxic breathing in previously reported experiments [143]. This model also addresses the suggestion made in a *Journal of Magnetic Resonance Imaging* June 2020 Editorial, that "future work could expand the interpretation of the T1 and T2* changes using quantitative models relating total blood oxygen content, $PO_2$ and $SO_2$ to the MRI measures" [142].

The model presented in **Chapter 6** shows that the change in R1 in tissues in response to increased oxygen levels can be estimated according to the oxygen extraction fraction, blood volume haematocrit, magnetic field strength, and other factors. When using the model to estimate OE-MRI response in tissues, the resulting ΔR1 are consistent with reported literature OE-MRI results in a variety of tissue types, and predicted differences due

to factors such as sex agree with empirical observations from human lungs. When using the model to estimate R1 changes from nanobubble delivery, the model shows that as a paired measurement in a study across multiple subjects at 1.5T, a study of 14-21 participants would be required to yield 80-95% power when detecting a 30 mmHg change in $PO_2$.

## 7.2. Clinical Translation

### 7.2.1. Background

Thus far, the phantom and modelling work presented estimate that measuring R1 could provide a non-invasive method of measuring a >100 mmHg whole voxel oxygen delivery from oxygenated nanobubbles in a single patient setting with 95% confidence, and that as a paired measurement in a study across multiple subjects at 1.5T, a study of 14-21 participants would be required to yield 80-95% power when detecting a 30 mmHg change in $PO_2$. These estimates are, however, based on theoretical calculations. As any biomedical researcher knows, although testing a method using phantoms and modelling is useful, the reality of applying that method successfully in human patients can present a whole new set of challenges. Ultimately, however, successful clinical translation is the end goal for most biomedical research applications, including the therapeutic nanobubbles discussed in this thesis. Therefore, a final important aspect of this thesis is to gauge what practical challenges would be faced if this sort of experiment were attempted.

Although it was not possible to perform clinical experiments with nanobubble delivery within the timeframe of this thesis, the most relevant adjacent research area is clinical OE-MRI, and it was possible to analyse the results from two recently completed clinical OE-MRI studies: (1) "*ART: Anal Squamous Cell Carcinoma: Investigation of Functional Imaging During chemoRadioTherapy*" (ClinicalTrials.gov no.: NCT02145416) and (2) "*BIOPIC: Biological Magnetic Resonance Imaging Parameters in oropharyngeal squamous cell carcinoma*" (ISRCTN12676704). The main focus of the OE-MRI branch of the ART and BIOPIC studies — i.e., whether tumour OE-MRI response related to patient outcome — is

tangential to the scope of this thesis and therefore are not included in this chapter, however the data acquired for the study shed light on several elements that would be relevant to using this method in a clinical experiment involving nanobubbles, such as the benefits and drawbacks of a chosen T1 mapping method, vulnerability to patient motion, and potential image artefacts.

Over the years, OE-MRI studies have used a variety of methods to detect oxygen-enhanced changes in R1 — some have used semi-quantitative signal intensity changes in T1-weighted imaging [92], [98], [235]–[237], and some have used quantitative T1 mapping methods such as Inversion Recovery [104], [107], [200], [238]–[240], Saturation Recovery [241], Variable Flip Angle (VFA) [167], [199], [211], [228], [237], [242], [243], or Look-Locker variants such as Modified Look-Locker Inversion Recovery (MOLLI) [103], [156], [201], [212], [244]. There are trade-offs between T1 estimation accuracy and acquisition time between each of these methods, and some are known to over- or under-estimate T1 [118]. Although using these techniques for OE-MRI has shown success in pre-clinical work, applying these techniques to a clinical trial workflow heightens the relevance of two factors: acquisition time and patient motion.

Therefore, observations on 3 elements from the BIOPIC trial data were reported: (1) the difference in estimated T1 from each method used (MOLLI and VFA), (2) the standard deviation within the tumour ROIs, and (3) the OE-MRI response resulting from either method. These original research results are used to draw conclusions about the feasibility of using R1 measurements to monitor oxygen delivery from nanobubbles in a clinical MRI setting. In addition, the artefacts and practical difficulties encountered in the BIOPIC and ART studies were discussed. Lastly, the MRI acquisition details from over 45 relevant manuscripts has been collated as a convenient reference for researchers planning future studies. The change in R1 from the OE-MRI response is fully reported in the resulting individual manuscripts and has not been included in this thesis, however it is worth noting

that the changes in R1 observed were consistent with the underlying theory of R1 changes listed in Appendix Table E.3.

### 7.2.2. Discussion of Relevant Results

The data acquired for the ART and BIOPIC studies shed light on several elements that would be relevant to using this method in a clinical experiment involving nanobubbles, such as the benefits and drawbacks of a chosen T1 mapping method, vulnerability to patient motion, and potential image artefacts. These results do not serve as a rigorous comparison of T1-mapping methods, but instead serve as a report on the practical challenges faced, with the aim that sharing this is helpful to researchers planning future studies. There are tradeoffs between T1 estimation accuracy and acquisition time between each of these methods, and some are known to over- or under-estimate T1 [118], which was also observed in the BIOPIC study when using both VFA and MOLLI T1 mapping: when comparing respective slices of the tumour ROI, the VFA T1 estimation was higher than the MOLLI estimation by 27% on average (Min -1%, Max 73%). These results are consistent with the discrepancy shown by Stikov et al. [118], where the peaks from VFA, IR and Look-Locker methods varied by as much as 30%. There was no significant difference in the standard deviation seen within the tumour ROIs from the VFA method versus MOLLI (paired t-test, alpha=0.05, two-tailed p=0.95).

In these studies, the VFA T1 mapping method was able to generate a 3D image and therefore OE-MRI information is captured from the entire tumour using this method, while the single-slice MOLLI method only captured OE-MRI response in one slice. In this respect, the VFA data was more useful for gaining information about the tumour as a whole (and hence patient outcome or response); however VFA was also a more robust method when considering the potential of patient motion: patient motion in the z-plane (occurring in 7/12 patients) resulted in the MOLLI scan capturing a different area of the tumour, rendering it unusable for OE-MRI analysis. In addition, the data gathered by VFA included 10x as many

voxels, and additionally would not result in the same ΔR1 as the data collected by the MOLLI method.

Recent OE-MRI research has shown that categorizing the *fraction* of voxels that do or do not show oxygen-enhancement is a better technique for capturing the overall oxygen R1 response due to tissue heterogeneity in tumours [178], [200], [243], [245], [246]. Successfully obtaining a voxel-wise or fractionated measurement from OE-MRI requires very good alignment of voxels between the air and oxygen images and other modalities (such as R2* maps or DCE-MRI), which can be difficult to achieve: patients must breathe during the gas challenge (or nanobubble delivery), images are acquired minutes apart and the patient may voluntarily or involuntarily move throughout the session, and artefacts such as susceptibility artefacts can cause poor alignment between different modalities (examples shown in Appendix Figure E.1). Aside from bulk patient motion, internal organs can move during the session as well, due to motion in the bowels (relevant for anorectal tumours in ART) [244] or tongue position (relevant for oropharyngeal cancers in BIOPIC), causing relative motion within the body frame which can be more difficult to correct reliably with registration than bulk motion. Patient motion is especially detrimental if the original region of interest moves out of the imaging field-of-view, which has occurred in studies using 2D rather than 3D imaging techniques [244], [247]. In the BIOPIC study, patient motion was a nontrivial concern: patient motion in the z-plane occurred in 7/12 patients, resulting in the MOLLI T1 map capturing a different section of the tumour, rendering it unusable for OE-MRI analysis. Therefore, although MOLLI provides a rapid, accurate method for T1 mapping that is appropriate for applications such as cardiac imaging, future OE-MRI researchers who require comparison between timepoints should perhaps prioritize 3D T1 mapping techniques. In addition, 3D imaging captures information from the entire tumour or lung region of interest, which provides important information from throughout a heterogeneous tumour.

In addition, several practical challenges were encountered in both studies: (1) acquisition settings were sometimes changed by well-meaning radiographers, leading to inconsistent FOV and resolution between subjects, visits, and modalities, as well as some artefacts such as phase wrap-around, a dark band near the sinuses seen on the MOLLI T1 maps, sometimes accompanied by a corresponding bright band (shown in Appendix Figure E.4A). Fortunately, the artefacts did not occlude any tumour ROI, however these challenges remain a potential source of data corruption. In the ART study, internal patient motion, such as motion from the bowels (shown in Appendix Figure E.4B), resulted in tumour ROI occlusion and the exclusion of those patients from the final dataset.

An additional non-technical challenge that was observed was time in the scanner: as the study progressed, some patients needed shorter scan time and some images were removed from the protocol in order to satisfy this. In some appointments, the acquisition of a B1 map was removed from the protocol. There can be errors between the intended versus actual flip angle applied, and B1 maps can be used to correct for this in the VFA T1 calculation. In the BIOPIC study, B1 maps were one of the image types that were removed from the protocol when the scan time became too long for a patient, which made it impossible to use B1 correction in the VFA T1 calculation, resulting in less accurate T1 measurements. Depending on the method chosen, acquiring a B1 map can be performed in as little as 2 minutes [248], and being able to perform B1 correction in the VFA calculation would have improved the accuracy of T1 estimates from the VFA. Therefore, clear communication of the relevance of each part of the scanner protocol, and researchers may find it useful to have a plan in place for which scans may be removed from protocol — while having the least effect on the clinical study results — if a patient is in need of reduced scan time.

Lastly, as a useful resource, the MRI acquisition details and scanning parameters (i.e. inversion and repetition times) from over 45 relevant manuscripts are provided in Appendix Table E.1 [85], [92], [97], [98], [100], [103]–[107], [143], [144], [158], [167], [199]–

[201], [211], [212], [228], [229], [236]–[240], [242]–[247], [249]–[257]. This table serves as a useful resource for future researchers because the inversion time, flip angles, and repetition times can affect the contrast to noise ratio of oxygen-enhancement for a particular tissue [213], [252], [255].

### 7.2.3. Implications for Measurement of Nanobubble Oxygen Delivery

The analysis of this clinical data suggests that if a clinical trial were to use R1 to measure oxygen delivery, the technique would likely be very vulnerable to patient motion, and that 3D T1 mapping techniques would be more useful in the application of measuring changes in tumour oxygen levels. In addition, achieving very good alignment between images would be necessary to obtain voxel-wise ΔR1 measurements, which may be a more sensitive method to track $PO_2$ changes from nanobubble delivery in comparison to whole-tumour-mean ΔR1 measurements.

## 7.3. Future Work and Broader Applications

In the process of answering the core question regarding the feasibility of detecting the effect of oxygen nanobubbles in vivo, three separate mathematical models were generated for predicting changes in R1 in tissue. This section discusses some broader potential applications of these models and plans for future studies.

Based on the literature review in **Chapter 1**, EPR would also appear to be a promising method for measuring oxygen delivery from nanobubbles; although it has not yet been developed for clinical use. A benefit of using EPR over water proton R1 is that the EPR signal is specific to dissolved oxygen, and would therefore not be affected by the deoxyhemoglobin levels which ended up being a consequential obstruction to measuring the R1 signal changes. Therefore, a promising future experiment may be to repeat the phantom experiments in **Chapter 2** using EPR measurements instead of water proton R1 measurements, and perform experiments similar to those in **Chapter 3** with an appropriate control arm for EPR experiments.

The phantom results in **Chapter 2** showed that R1 could be used to reliably infer $PO_2$ within nanobubble solutions in phantoms, which may be of interest as a non-invasive $PO_2$ measurement in manufacturing, quality control, or chemical engineering applications, however, there may be more convenient industrial methods than NMR to use for this purpose.

In future research, the oxygen relaxivity model in **Chapter 4** could be refitted specifically with urine, CSF, or vitreous data only to provide better accuracy for measurement in specific bodily fluids.

The model presented in **Chapter 4** showed that oxygen has a very large effect on T1 at low fields, especially below 1.5T. Although 1.5T has been the most common scanner strength used clinically for decades, there are exciting possibilities of low-field MRI (defined as 1-199mT [194]) increasing in popularity in the future due to its low cost, low foot-print, and better accessibility for patients [195]. According to the model in **Chapter 4**, if any supplemental oxygen is administered to the patient being scanned, the effect of supplemental oxygen on T1 will be roughly 3 times stronger at 1-199mT compared to 1.5T. If radiologists are unaware of this effect, it could result in an incorrect abnormal findings, which has occurred previously in history: in the early 2000s, clinicians reported that patients under general anaesthesia showed an increase in T1-weighted signal intensity in their cerebrospinal fluid due to the supplemental oxygen [258]–[262], and a warning had to be issued to radiologists to avoid mistakenly interpreting this as an abnormal finding, such as haemorrhage or elevated protein content. This particular history with CSF misdiagnosis is especially important, since Marques et al. [194] have stated that some of the most promising applications for low-field MRI is point-of-care diagnostics and detecting congenital and neonatal hydrocephalus, which is characterized by cerebrospinal fluid (CSF) accumulation. Therefore, it is important to communicate the findings of the Chapter 4 model to radiologists working with low-field MRI, because point-of-care patients and neonatal situations will commonly involve supplemental oxygen or anaesthesia. This information is also highly

relevant for researchers developing quantitative imaging metrics for low-field diagnostics, since patients receiving anaesthesia (and hence supplemental oxygen) will have different T1 values than expected in some regions, and therefore this could lead to a misdiagnosis if people are unaware of this effect.

In future research, the blood model presented in **Chapter 5** could be refitted with additional, more accurate measurements of R1, hematocrit, $SO_2$, and $PO_2$. In addition, future work could incorporate a model by Li et al. which describes the effect of plasma proteins such as albumin and methaemoglobin on R1 [204]. Although its development was motivated by the narrow aim of this thesis, the blood model presented in Chapter 5 is a very general-use model with broad applications for MRI researchers, including oxygen-enhanced MRI, or the use of noninvasively measuring oxygen levels in blood-rich regions such as the umbilical cord — indeed, this new blood model would likely improve the accuracy of the work on the umbilical cord research published by Portnoy et al. [109]. In order to use the model in this way, however, future research is needed in order to determine the effects of pulsatile flow on blood R1.

The blood model presented in **Chapter 5** is also relevant to research that does not study oxygen nor hyperoxia: for example, an accurate estimate of R1 in blood is important for several other research techniques such as arterial spin labelling [263] and black blood imaging [264]. In addition, quantitative MRI is a rapidly growing field [265], and this model can help with the research that is working on the interpretation of T1 values — for example, differences in haematocrit levels due to sex or age could be controlled for using this model.

The tissue model presented in **Chapter 6** has been designed to be easy for researchers to tailor to their tissue of interest by substituting their preferred model for tissue oxygen diffusion and consumption, and could therefore be useful for broader applications studying hyperoxia and tissues (including OE-MRI for the study of pulmonary diseases). In particular, this model may be useful for OE-MRI researchers looking to predict the effect of

certain factors, such as hematocrit, and the sex hematocrit differences did have a slight effect on ΔR1 when the voxel contained larger blood volumes, matching what has been empirically observed in lung tissue [212].

The model in **Chapter 6** could also be extended to include multi-modality information, such as R2* changes. A 2019 review by O'Connor et al [179] includes a figure (Figure 8 in review) that illustrates an estimation of the corresponding R2* and R1 changes for hypoxic, perfused, and necrotic tumour tissues. O'Connor et al. [179] also discuss that the contribution of blood deoxyhaemoglobin to the R2* of each voxel is not simple, and will depend on voxel dimensions, vascular geometry, vascular volume, change in blood oxygenation and the change in tissue deoxyhaemoglobin concentration caused by hyperoxia. Although this is beyond the scope of this thesis, as an aid for future researchers, the reported ΔR1 and ΔR2* for different tumour tissue types have been collated and displayed in Appendix Table E.2, with the hypothesis of the underlying causes of each OE-MRI response listed in Appendix Table E.3. For easier viewing, this information has also been displayed as an illustration in Appendix Figure E.2, from which it is clear that although a detailed quantitative model of R2* response may not be feasible, it may be possible to simply use positive versus negative changes in R2* to distinguish between tissue types. For example, although both necrotic and well-perfused regions will show a positive ΔR1, necrotic tissue shows a positive ΔR2* and well perfused tissue shows a negative ΔR2*, allowing them to be differentiated from each other. In addition, including measurements of native R1 and native R2* may provide an additional 2 dimensions to allow these tissue types to be sufficiently differentiated in a multidimensional space using various data-driven classification methods.

There are some emerging data-driven OE-MRI analysis techniques that may find the predictions from this to be model useful. For example, since data-driven clustering methods showed promise in locating tumour sub-regions in other tumour imaging techniques [43], [266]–[271], Featherstone et al. [199] recently examined the use of principal component

analysis and clustering using Gaussian mixture modelling for OE-MRI analysis. Similarly, Moosvi et al. [272] used independent component analysis to increase the sensitivity of the OE-MRI analysis to the very small changes in R1 that arise from the dissolved oxygen. Instead of acquiring data pre-and post-gas challenge, Moosvi et al. [272] used a cycling gas challenge and acquired dynamic T1-weighted images, using ICA to separate the gas-challenge response into 3 clusters: "$O_2$ positive", "$O_2$ negative", and voxels that showed a weak or no response. Altogether, it is possible that ICA and other clustering methods provide a promising strategy for increasing sensitivity and reducing scan-time in OE-MRI, and it is possible that the OE-MRI model presented in **Chapter 6** could provide additional information on classifying or identifying these clustered responses. In addition, incorporating values obtained from other modalities such as R2* or DCE-MRI response could allow tissues with a similar ΔR1 to be separated along another dimension (such as ΔR2* response) in a classification model such as a support-vector network [273].

The analysis of the clinical trial data discussed in **Chapter 7** was performed to shed light on future possible nanobubble clinical experiments, however it is ultimately most helpful to researchers planning future studies of clinical OE-MRI. When any research technique is being developed, it is important for researchers to communicate about the practical challenges experienced. If we all only report on our achievements, we will inevitably waste time repeating each other's mistakes. OE-MRI has attracted considerable interest after showing promising results in preclinical experiments, however, some clinical studies have unfortunately faced difficulties with patient motion, image registration, and the limitations of imaging methods. As clinical studies begin to assess feasibility of using OE-MRI in patients, it is very important for researchers to communicate about the practical challenges experienced when using OE-MRI on patients to help the technique advance. These results serve that purpose. In addition, **Chapter 7** contains a useful collation of the MRI acquisition details from over 45 relevant manuscripts as a convenient reference for researchers planning future studies.

## 7.4. Thesis Conclusion

The aim of this thesis was to examine whether clinically available MRI techniques can be used to detect the change in oxygen caused by nanobubbles. The results from both the experimental and theoretical work indicates that clinically available sequences for T1 mapping could be used to detect the change in oxygen caused by nanobubbles, however the following important elements should be considered: (1) the relaxivity of oxygen will be much stronger when using a lower field scanner (i.e. ≤ 1.5T), and if the SNR is sufficient, would allow the study to be much more sensitive to changes in $PO_2$; (2) in an individual patient, an oxygen delivery of >100 mmHg would be detectable with 95% confidence, however it would be feasible to detect a much smaller difference between two large ROIs that would otherwise not be realistic in a single voxel due to the repeated number of voxel measures across a large ROI; (3) in order to measure a 30 mmHg change in tissue $PO_2$ from nanobubble delivery as a paired measurement in a study across multiple subjects at 1.5T, a study of 14-21 participants would be required to yield 80-95% power; (4) regions containing high levels of deoxygenated blood may impede the expected linear R1 change due to the paramagnetism of deoxyhemoglobin, and thus a voxel-wise ΔR1 rather than tumour-mean ΔR1 measurement may be most useful; and (5) the success of this technique will be highly vulnerable to patient motion, and therefore for this particular use case, the use of a 3D volumetric T1 map should be prioritized over a single-slice T1 mapping sequence with a shorter scan time to prevent data loss from subject motion along the z-plane.

In the process of answering this thesis question focusing on nanobubble delivery, this work produced three separate mathematical models that are useful for areas of research beyond the focus of this thesis, especially low-field MRI, quantitative MRI, and oxygen-enhanced MRI. The open-source code for each model has been hosted publicly on GitHub for future researchers to use, adapt, and improve upon easily.

# Appendices

## Appendix A

### A.1. Figures

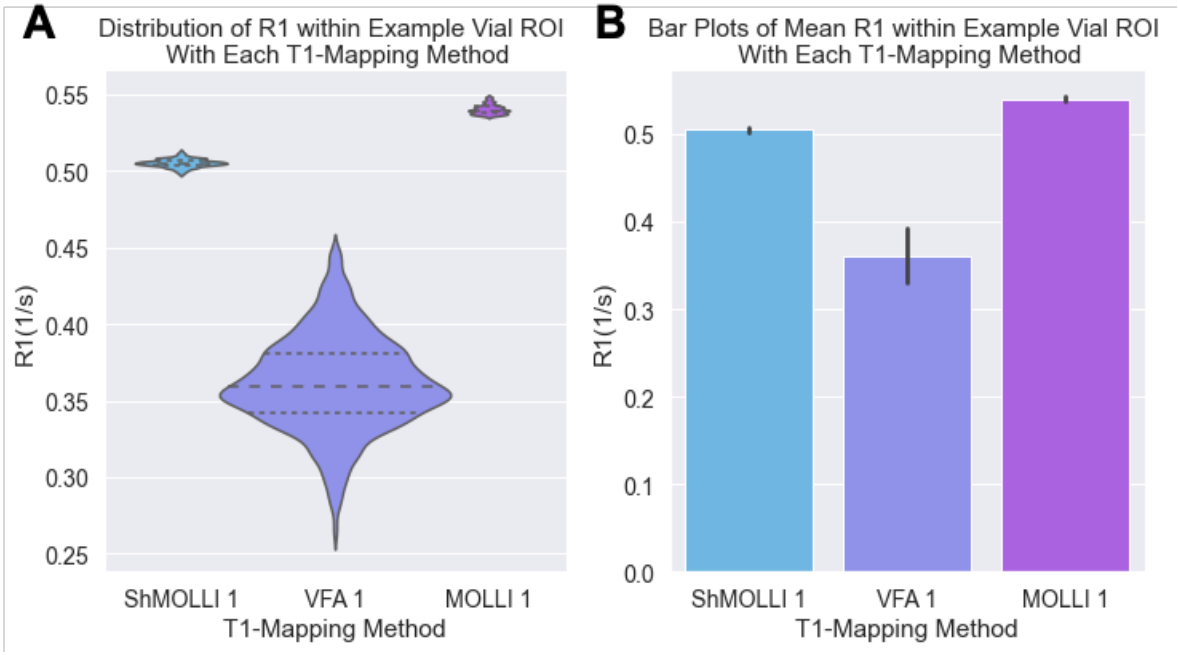


***Appendix Figure A.1. (A)*** *Violin plots of the distribution and* ***(B)*** *bar plots of the R1 within a representative example vial ROI collected from each T1 mapping method (Mean±SD): ShMOLLI (0.50±0.0027), VFA (0.36±0.031), and MOLLI (0.54±0.0031). The ShMOLLI T1-maps resulted in the lowest standard deviation and normal distribution within the ROIs and were therefore used for the relaxivity and LOD calculations. The vial contained the oxygenated nanobubble solution.*

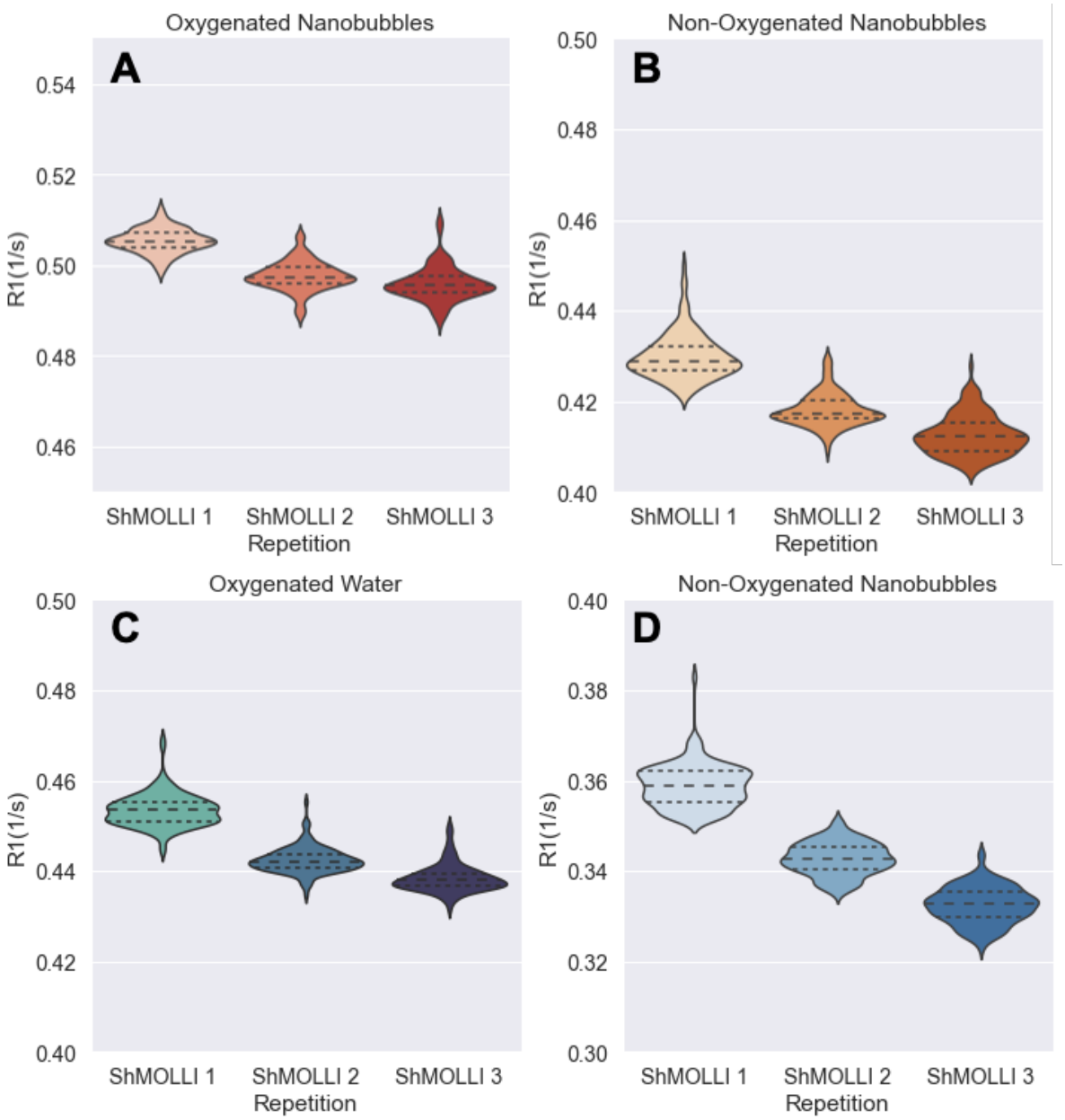


***Appendix Figure A.2.*** *Violin plots of the distribution of the R1 within a representative example vial ROI collected from each repetition of the 3 ShMOLLI T1-maps in* ***(A)*** *oxygenated nanobubbles,* ***(B)*** *non-oxygenated nanobubbles,* ***(C)*** *oxygenated water, and* ***(D)*** *non-oxygenated nanobubbles.*

## A.2. Tables

***Appendix Table A.1.*** *Conversion factors from $s^{-1}$/mmHg to other commonly used oxygen units. Converted using Loligo Systems Online Oxygen Converter (loligosystems.com/convert-oxygen-units).*

| Commonly used Oxygen Unit | Conversion Factor from 1 mmHg Oxygen | |
|---|---|---|
| | *Body Temp: 37°C<br>Salinity=0%<br>Atm. Pressure = 1 atm* | *Room Temp: 20°C<br>Salinity=0%<br>Atm. Pressure = 1 atm* |
| **[kPa]** | 1 mmHg = 0.13332 kPa | 1 mmHg = 0.13332 kPa |
| **[Torr]** | 1 mmHg = 1.00000 Torr | 1 mmHg = 1.00000 Torr |
| **[mmol/L]** | 1 mmHg = 0.00140 mmol/L | 1 mmHg = 0.00183 mmol/L |
| **[mg/L]** | 1 mmHg = 0.04470 mg/L | 1 mmHg = 0.05857 mg/L |
| **[mL/L]** | 1 mmHg = 0.03555 mL/L | 1 mmHg = 0.04403 mL/L |

# Appendix B

## B.1. Figures

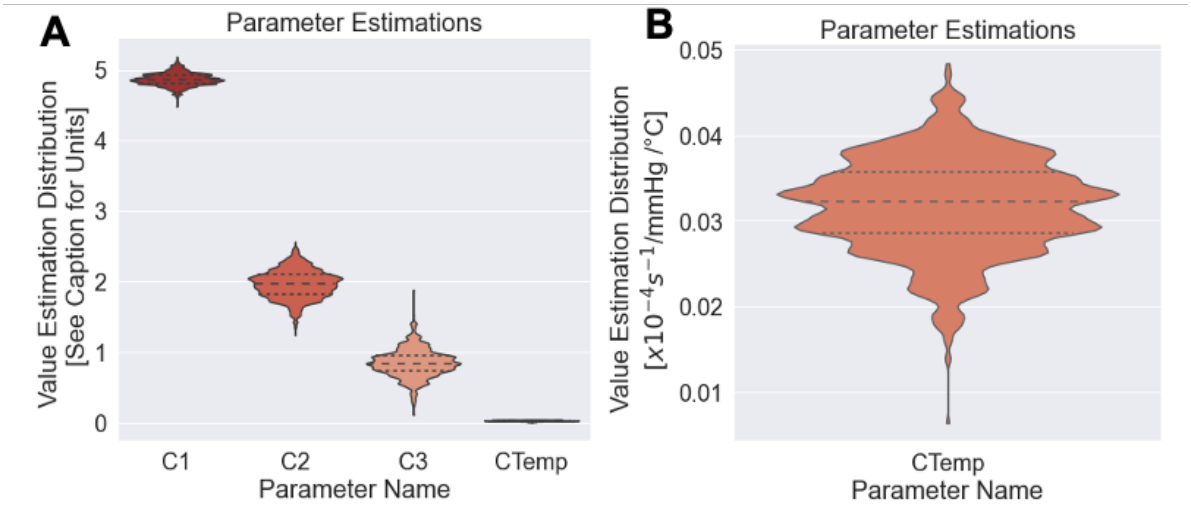


***Appendix Figure B.1. (A)*** *Violin plots showing the distribution of parameter estimates from each iteration. Y axis units per parameter:* $C_1$ *[x10*$^{-4}$ *s*$^{-1}$*/mmHg],* $C_2$ *[T*$^{-2}$*],* $C_3$ *[x10*$^{-4}$ *s*$^{-1}$*/mmHg], and* $C_{Temp}$ *[x10*$^{-4}$ *s*$^{-1}$*/mmHg /°C].* ***(B)*** $C_{Temp}$ *displayed separately for better visualization of the distribution.*

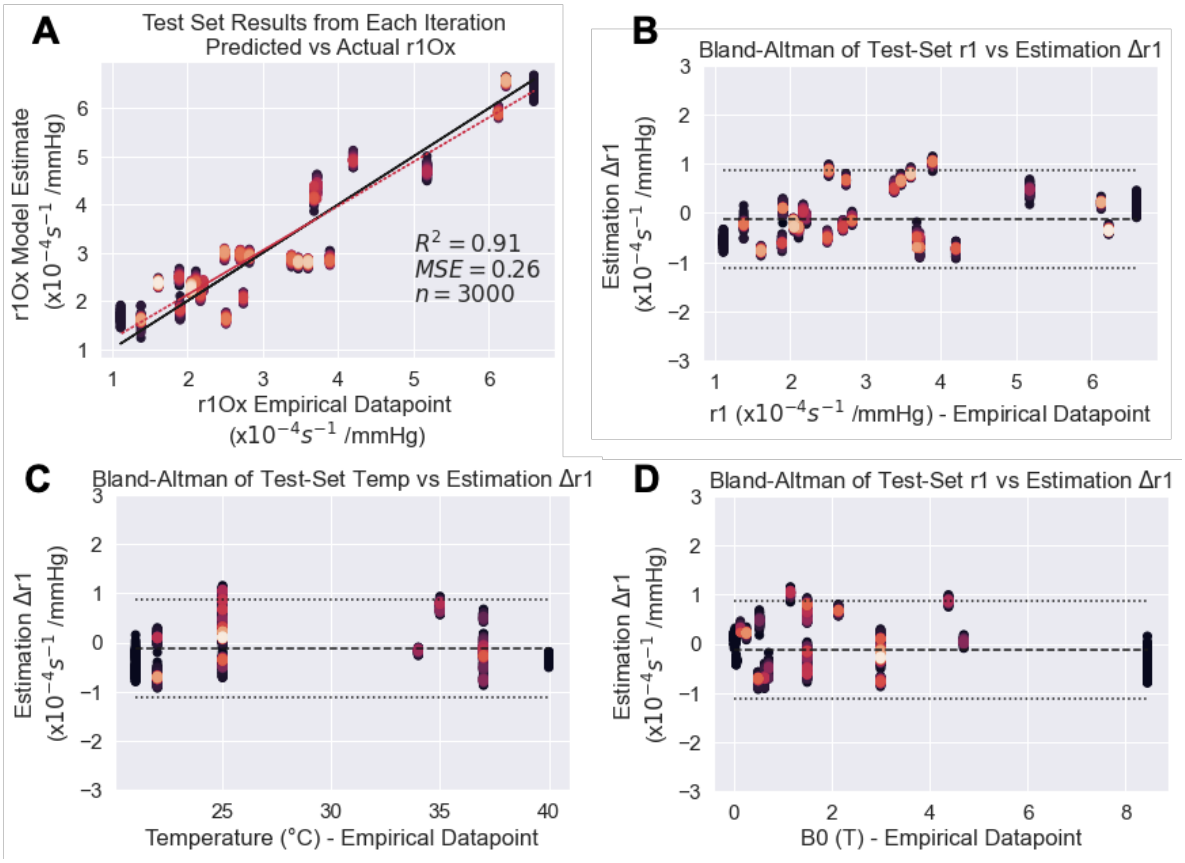


***Appendix Figure B.2. (A)*** *The modelled vs measured $r1_{Ox}$ values from the randomized unseen test set of each iteration, plotted against the line of equality (solid black line) and a linear regression (red dotted line, $R^2$=0.91).* ***(B)*** *A Bland-Altman plot showing the difference between the modelled and measured values of $r1_{Ox}$. The horizontal long-dashed lines show the mean value of $\Delta r1_{Ox}$ (-0.005 x10$^{-4}$ s$^{-1}$/mmHg), and the horizontal dotted lines show the limits of agreement (long dashes, calculated by mean($\Delta r1_{Ox}$) ± (1.96xSD($\Delta r1_{Ox}$)). Bland-Altman plots for the error in modelled $r1_{Ox}$ against* ***(C)*** *temperature, and* ***(D)*** *field strength are also shown to examine bias in the model.*

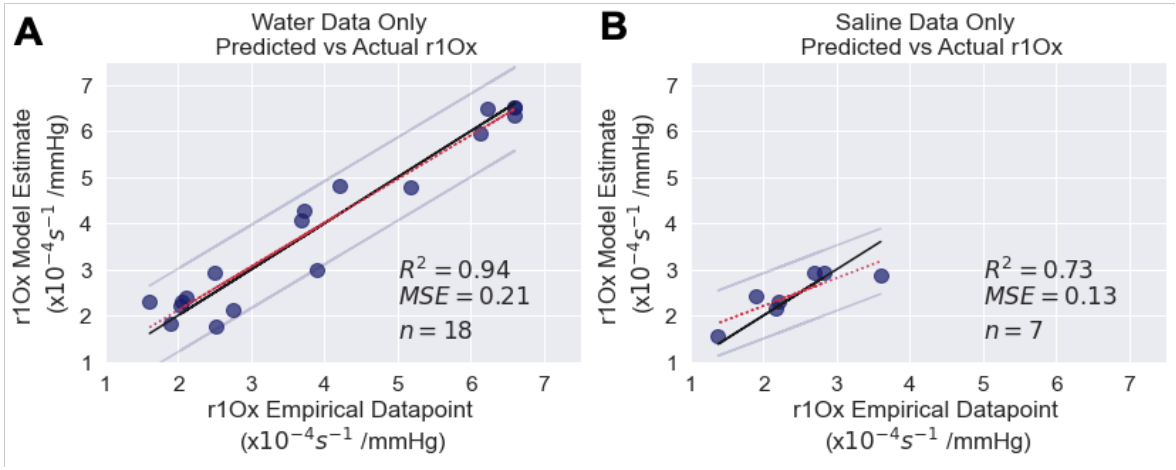


***Appendix Figure B.3.*** *The modelled vs measured $r1_{Ox}$ values, plotted against the line of equality (solid black line) and a linear regression (red dotted line, $R^2$=0.93) for the subset of data from water samples only* ***(A)*** *and saline samples only* ***(B)****. Note the smaller range of values available from saline.*

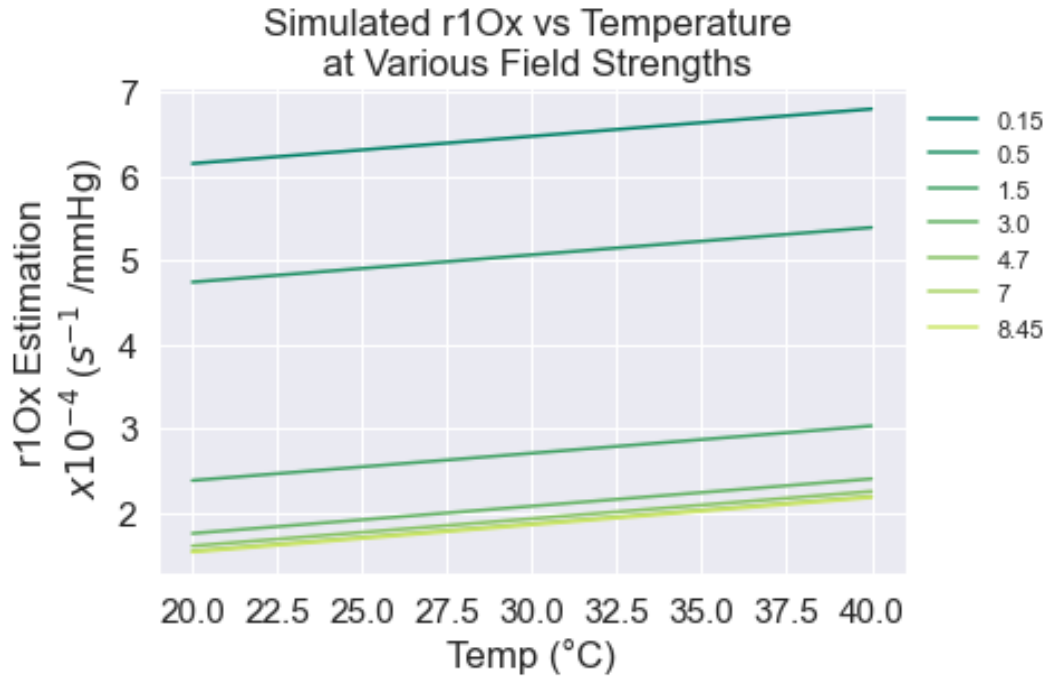


***Appendix Figure B.4.*** *A plot with simulated data to illustrate the behaviour of Equation 5 (with the fit parameter values) with respect to temperature and for a variety of magnetic field strengths.*

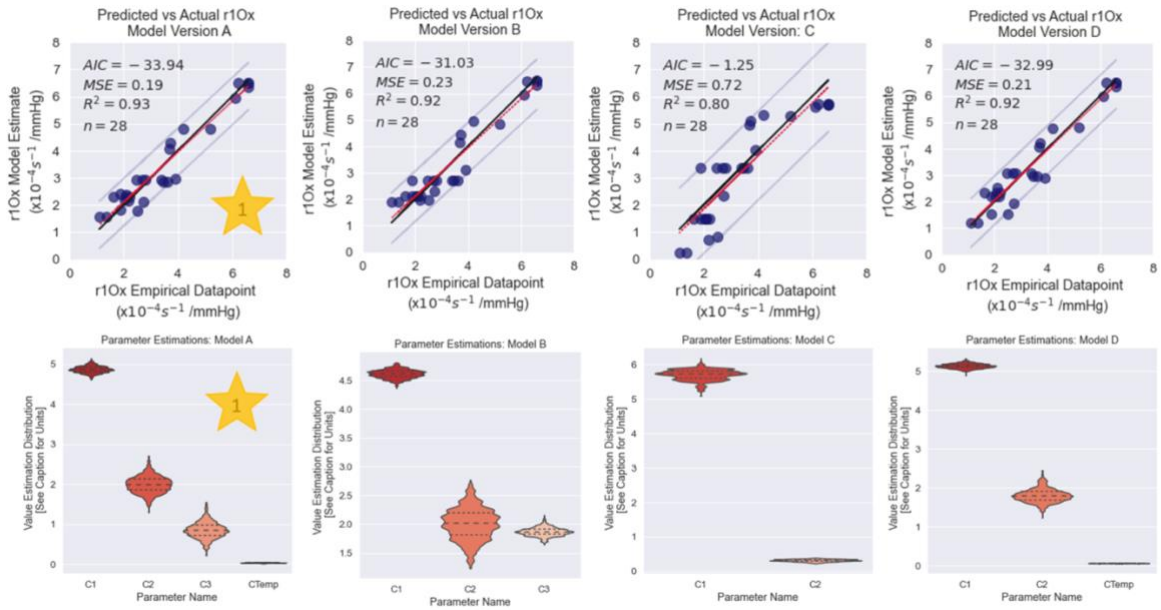


***Appendix Figure B.5.*** *The fitting process was repeated for all combinations of fewer parameters, and the Akaike Information Criterion (AIC), $R^2$, and MSE was calculated for each version of the model. These are the resulting modelled vs measured $r1_{Ox}$ values, plotted against the line of equality (solid black line) and a linear regression (red dotted line) for each model, and violin plots showing the distribution of parameter estimates from each iteration. Y axis units per parameter: $C_1$ [x10$^{-4}$ s$^{-1}$/mmHg], $C_2$ [T$^{-2}$], $C_3$ [x10$^{-4}$ s$^{-1}$/mmHg], and $C_{Temp}$ [x10$^{-4}$ s$^{-1}$/mmHg /°C]. The model with all 4 parameters (Model A - see yellow star) scored the highest according to the AIC, and was therefore used in this thesis. For the AIC, $R^2$, and MSE values in table form, please see Appendix Table B.2.*

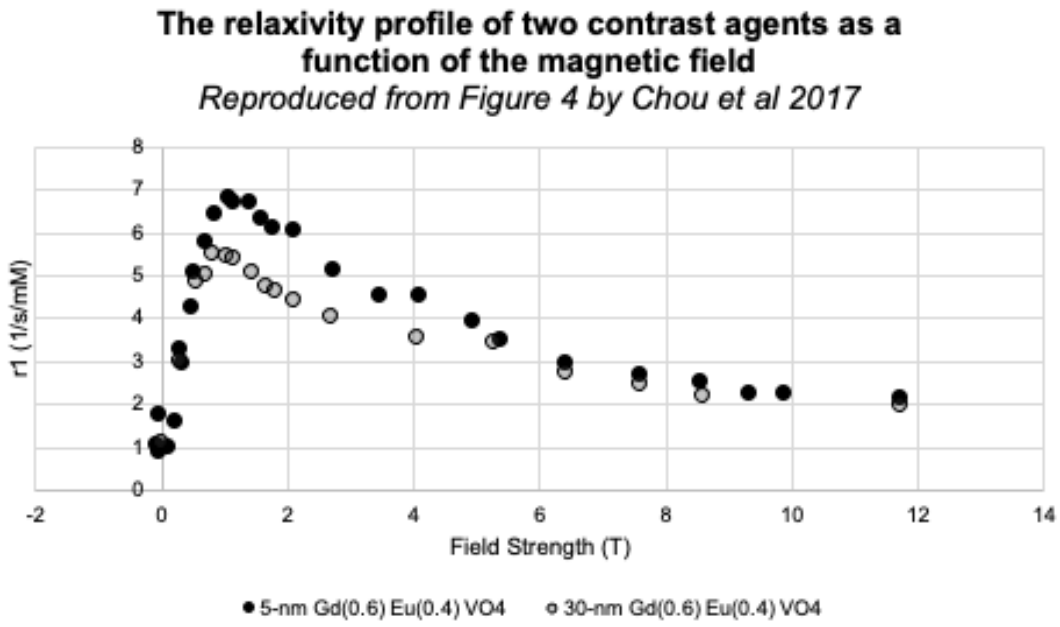


***Appendix Figure B.6.*** *Reproduced data Figure 4 of Chou et al.* [187]*. The relaxivity profiles of 5-nm and 30-nm gadolinium vanadate nanoparticles with and without Eu-ion doping are presented as a function of the magnetic field*.

## B.2. Tables

***Appendix Table B.1.*** *A collection of 12 additional reported values for oxygen relaxivity in blood and tissues from the literature with all units to [$s^{-1}$/mmHg oxygen] alongside the field strength and material used in each experiment. Temperature is indicated where it was reported. For experiments performed in vivo, an average body temperature could be assumed.*

| Reference | r1Ox ($s^{-1}$/mmHg) x$10^{-4}$ | Field strength (T) | Temp (°C) | Material |
|---|---|---|---|---|
| **BLOOD** | | | | |
| d'Othée et al., 2003 | 2.5 | 8.45 | 21 | Blood (*ex vivo*) |
| d'Othée et al., 2003 | 3.5 | 1.5 | 21 | Blood (*ex vivo*) |
| Tripathi et al., 1984 - Dog 2 | 2.9 | 0.15 | *In vivo* | Blood (left ventricle) |
| Tripathi et al., 1984 - Dog 3 | 3.8 | 0.15 | *In vivo* | Blood (left ventricle) |
| Tripathi et al., 1984 - Dog 4 | 2.5 | 0.15 | *In vivo* | Blood (left ventricle) |
| Tripathi et al., 1984 - Dog 5 | 9.2 | 0.15 | *In vivo* | Blood (left ventricle) |
| Silvennoinen et al., 2003 | 4.1 | 4.7 | 37 | Blood (*ex vivo*) |
| Hueckel et al, 2000 | 4.38 | 1.5 | 37 | Erythrocyte-enriched blood (*ex vivo*) |
| Pilkinton et al., 2012 | 1.44 | 3 | *In vivo* | Blood |
| **TISSUES** | | | | |
| Campbell-Washburn et al., 2019 | 4.7 | 0.55 | *In vivo* | Lung tissue |
| Campbell-Washburn et al., 2019 | 3.1 | 1.5 | *In vivo* | Lung tissue |
| Beeman et al., 2016 | 9.0 | 4.7 | *In vivo* | Brain tissue |

***Appendix Table B.2.*** *The fitting process was repeated for all combinations of fewer parameters, and the Akaike Information Criterion (AIC), $R^2$, and MSE was calculated for each version of the model. The best-fit model according to the AIC is the model that explains the greatest amount of variation using the fewest possible independent variables. The model with all 4 parameters (Model A) scored the highest according to the AIC, and was therefore used in this thesis. Removing only $C_3$ produced the second-best AIC score, and removing only $C_{Temp}$ produced the third best AIC score. For the resulting plots from each model, please see Appendix Figure B.5.*

| | Equation | Variables included | Rank (AIC) | AIC Score | $R^2$ | MSE |
|---|---|---|---|---|---|---|
| **A** | $r1_{Ox} = \frac{C_1}{1 + C_2 B0^2} + C_3 + C_{Temp} * T$ | $C_1$, $C_2$, $C_3$, $C_{Temp}$ | 1 | -33.94 | 0.93 | 0.19 |
| **B** | $r1_{Ox} = \frac{C_1}{1 + C_2 B0^2} + C_3$ | $C_1$, $C_2$, $C_3$ | 3 | -31.04 | 0.92 | 0.23 |
| **C** | $r1_{Ox} = \frac{C_1}{1 + C_2 B0^2}$ | $C_1$, $C_2$ | 4 | -1.25 | 0.80 | 0.72 |
| **D** | $r1_{Ox} = \frac{C_1}{1 + C_2 B0^2} + C_{Temp} * T$ | $C_1$, $C_2$, $C_{Temp}$ | 2 | -32.99 | 0.92 | 0.215 |

***Appendix Table B.3.*** *The acquisition details from each experiment listed in Table 4.1.*

| Reference | MRI Acquisition Details (Relevant Section) |
|---|---|
| **Matsumoto 2006** | For T1 and T2 mapping, spin-echo images were obtained using a multislice multiecho (MSME) sequence with two different TRs (4000 and 800 ms) and a 16-echo train with TE=15 ms. The scantime for the T1 and T2 mapping image set (NEX=1) by the MSME sequence was 10 min. **SPGR (also referred to as gradient-echo fast imaging (GEFI); TR=75 ms, TE=3 ms,FA=45°, NEX=8) was employed to observe the T1 effect.** |
| **Zaharchuk 2005** | Based on a compromise between spatial and temporal resolution established during pilot studies, we chose to **measure T1 using a two-point 3D modified fast inversion recovery (MFIR) method** (TR/TE/TI=11 s/140 ms/[3.2 s,none], fast spin-echo [FSE] readout). Additionally, to test the validity of the two-point method, more complete sampling of the IR curve was performed with 10 different TIs (TR/TE/TI = 11s/140 ms/[0.4, 0.8, 1.2, 1.6, 2.0, 2.4, 2.8, 3.2, 4.0, 5.0 s]). T1 was measured using a least-squares, three-parameter fitting method. |
| **d'Othée 2003** | With the 8.45-Tesla magnet, calculations of T1 were based on the evolution of the signal intensity (SI) over time (T1 relaxation curve) after stimulation by a **T1-weighted inversion recovery (IR) sequence** using multiple inversion times (TIs). Nine different TIs were chosen:0.008, 0.05, 0.25, 0.5, 0.8, 1.0, 4.0, 7.0, and 12.0 seconds. A standard broadband probe with a 20-mm diameter radiofrequency coil was used for all measurements. The experimental conditions were such that the temporal resolution was under 3 minutes per T1 measurement. The following parameters were applied: one average, sweep width of 4,990 Hz, matrix size 8,192, and the duration of the 180°pulse was 110 microseconds. The signal intensity values were fitted on MATLAB software according to the equation: $I_{(t)}=I_{(0)}(1–2e^{(-TI/T1)})$.<br><br>On the 1.5-Tesla MRI, we used an **inversion recovery sequence** with multiple TIs of 0.2, 0.4, 0.8, 1, 2, 4, 5, and 6 seconds. Acquisition parameters were as follows: repetition time=8 seconds, flip angle=8 degrees, slice thickness=8 mm, matrix=64x128, field of view=150x150 mm. |
| **Kramer 2013** | An **inversion recovery sequence** with 20 different inversion times (100 ms-15 s) was used to determine the T1 time, and a spin-echo sequence with a total of 9 different echo times (10 ms-2 s) was used to determine the T2 time. The measured T1 and T2 times made it possible to calculate the relaxivity of oxygen. |
| **Simpson 2013** | The scanning protocol used **an inversion recovery (IR) true fast imaging with steady-state precession (TrueFISP) imaging sequence that was repeated using 17 inversion times** (TI) in the range 0.7 to 30 seconds. The order of the inversion times was initially randomized to mitigate potential drift effects in the scanner. Other TrueFISP parameters were: repetition time =(20 þ TI) seconds, echo time = 1.52 ms, flip angle = 808, matrix =256 x 256, and voxel dimensions = 0.9 x0.9 x 4 $mm^3$. |
| **Pilkinton 2012** | An **inversion-prepared single-shot FSE sequence** was used with 10 inversion times (90, 200, 400, 800,1200, 1600, 2400, 4000, 6000, 1000 ms) with a TR=20 s. |
| **Vatnehol 2020** | Based on a previous study on in vivo stability [9], **two MOLLI schemes** of 10(5)5 and 5(3)3 were selected. Table 1 shows selected sequence parameters for both sequences. Parameters relevant for contrast were flip angle=20, TR/TE shortest (2.4/1.07 ms and 2.6/1.2 ms), and minimum TI 178.3 and 196.1 ms for the MOLI 10(5)5 and 5(3)3, respectively. A simulated ECG signal was used for image triggering at a rate of 60 beats per minute. Following localizer images, the sequences for quantitative estimation of T1 were acquired six times for each sequence. |
| **Nestle 2003** | The NMR studies were performed in a simple **NMR relaxometer** MRS 6 (JSI, Ljubljana, Slovenia). |
| **Hausser and Noack 1965** | Used an **NMR relaxometer**. The manuscript is in German, please refer to the original manuscript for NMR details. |

| | |
|---|---|
| **Zaharchuk 2006** | **R1 was determined by the Iterative R1 Measurement Using a Dual-Shot SSFSE Sequence, using five iterations**. Images were acquired using the following parameters: $T_{SR1}$ =10 seconds, $T_{SR2}$=3 seconds, TE =200 milliseconds, field of view=20 cm, matrix 320x256, slice thickness =8 mm, receiver bandwidth =31.25 kHz, and echo train length 136. |
| **Graf 1980** | Used an **NMR relaxometer**. Please refer to the original manuscript for NMR details. |
| **Muir 2013** | **R1 measurements were made by using a Look-Locker sequence with a spoiled gradient-echo readout**, in which data at 26 inversion times were acquired after a single inversion pulse with minimum inversion time of 103 msec; the equal spacing between inversion times was 264 msec. Images were acquired in two shots with the following parameters: repetition time msec/echo time msec, 6.6/3.2; field of view, 100x100 mm; matrix, 100x100; partial Fourier factor, 0.8; a single 6-mm section; flip angle, 4°; six to nine repetitions; and 20 seconds between repetitions of the inversion pulse. |
| **Hueckel 2000** | **TI relaxation times were measured by use of an inversion recovery single shot turbo spin echo sequence (RARE).** The imaging parameters were as follows: TE,s = 4.2 ms, inter-echo time = 4.2 ms, slice thickness = 10 mm, FOV = 240 mm x 240 mm. The inversion time (TI) was adjusted to 16 different values in the range between 50 ms and 9000 ms for each TI measurement.<br>Calculation of the TI values was done by a three- parameter-fit corresponding to the following equation: Si (TI) = a + b exp(-TI/TI). This fit compensates for the influence of imperfect inversion pulses on the calculated TI values. |

# Appendix C

## C.1. Figures

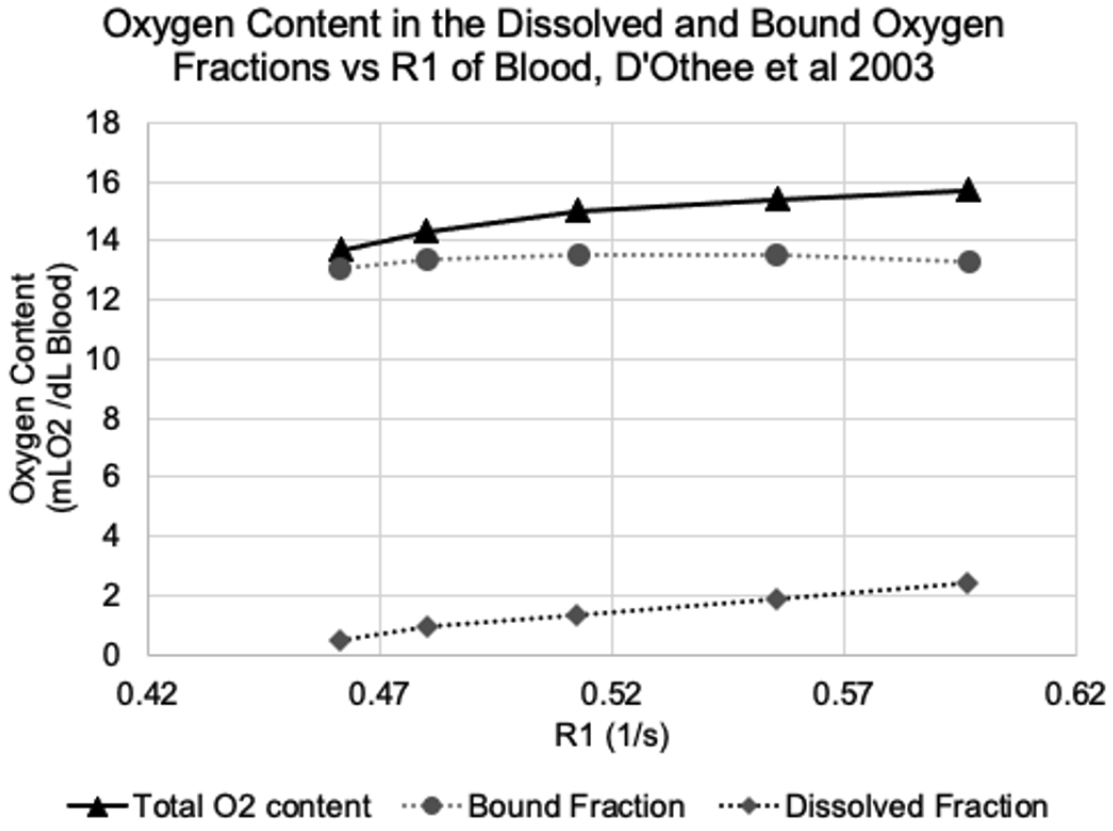


***Appendix Figure C.1.*** *Reproduced from Figure 4 from d'Othee et al* [152].

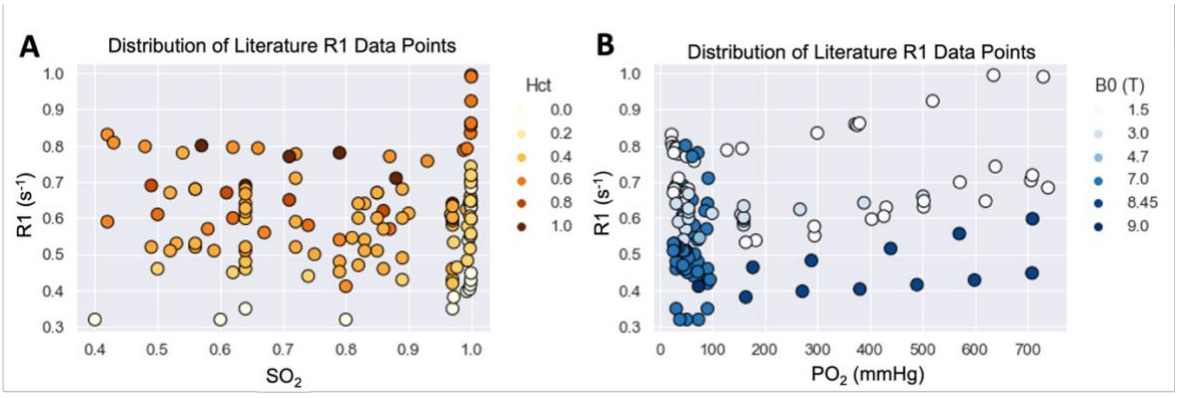


***Appendix Figure C.2.*** *The distribution of the literature data points, plotted against* ***(A)*** $SO_2$ *and coloured by hematocrit levels (oranges) and* ***(B)*** $PO_2$ *and coloured by B0 levels (blues).*

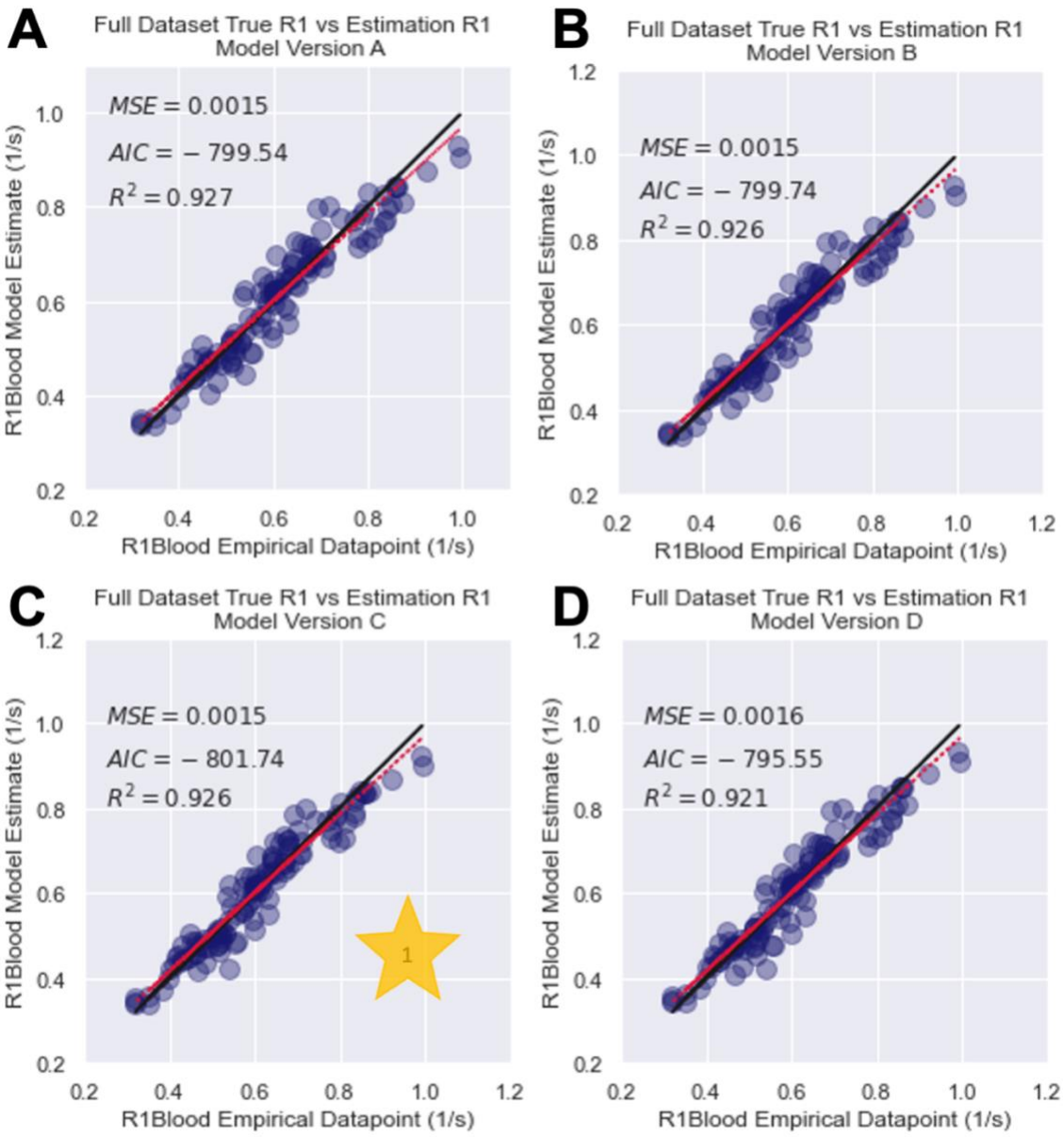


***Appendix Figure C.3.*** *The model fitting process was repeated for all combinations of fewer parameters and the Akaike Information Criterion (AIC) was calculated for each version of the model. The resulting modelled vs measured $R1_b$ values are plotted against the line of equality (solid black line) and a linear regression (red dotted line) for each model. Model C (marked with yellow star), with 7 parameters total, scored the highest according to the AIC (-801.74), and was therefore used in this thesis. For the AIC, $R^2$, and MSE values in table form, please see Appendix Table C.2.*

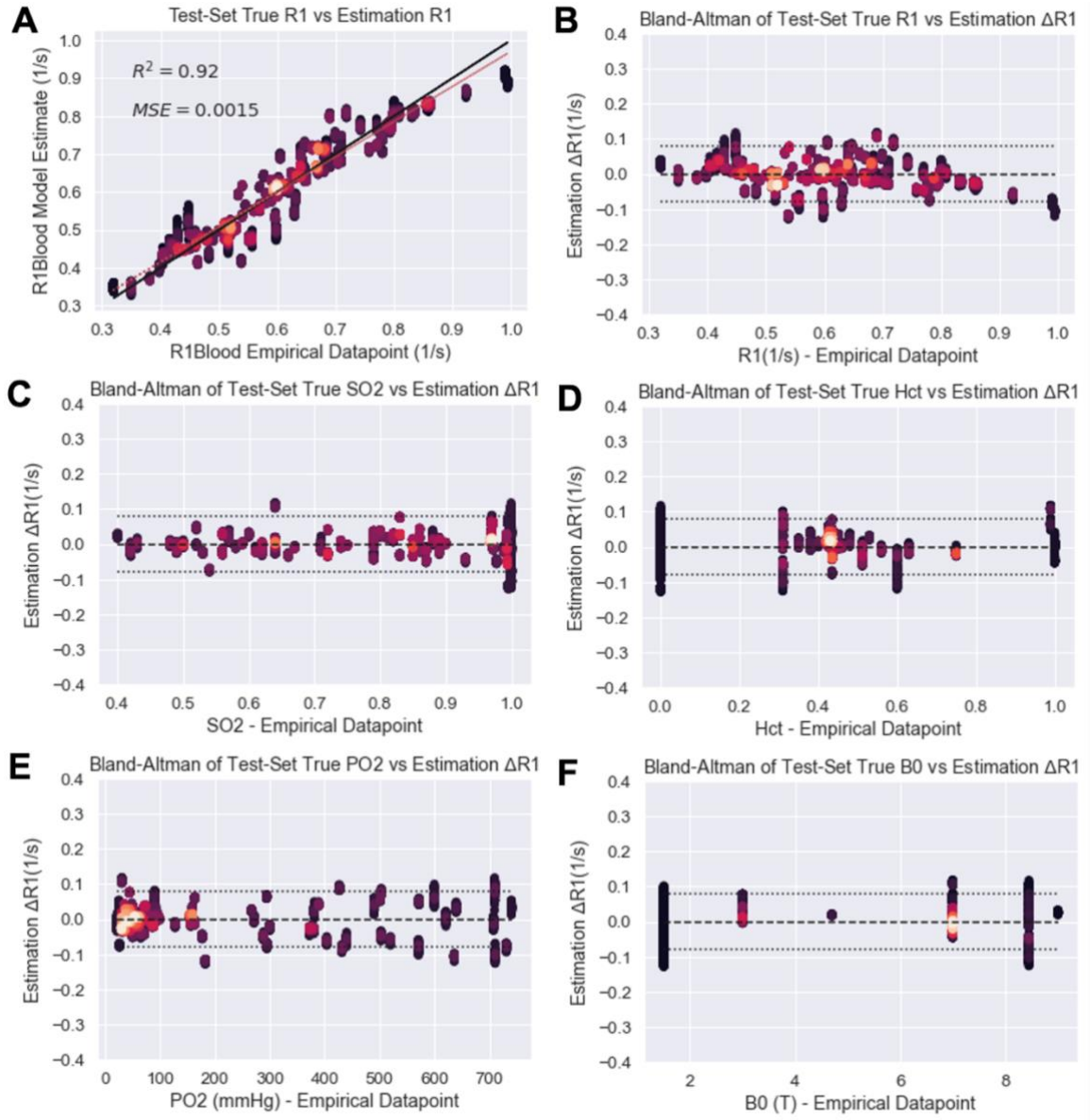


***Appendix Figure C.4. (A)*** *The modelled vs measured $R1_{blood}$ values from the randomized unseen test set of each iteration, plotted against the line of equality (solid black line) and a linear regression ($R^2$=0.92, red dotted line). The scatter plot points are coloured by density (bright=more dense), number of datapoints n=70,000.* ***(B)*** *A Bland-Altman plots showing the difference between the modelled and measured values of $R1_b$ from the randomized unseen test set of each iteration. The horizontal long-dashed line show the mean value of $\Delta R1_{blood}(1x10^{-4}\ s^{-1})$, and the horizontal dotted lines show the limits of agreement of -0.078 and 0.078 $s^{-1}$ (long dashes, calculated by mean($\Delta R1_b$) ± (1.96xSD($\Delta R1_b$)). The Bland-Altman plots for the error in modelled $R1_b$ against* ***(C)*** *$SO_2$,* ***(D)*** *hematocrit,* ***(E)*** *field strength, and* ***(F)*** *$PO_2$ levels are also shown to examine bias in the model.*

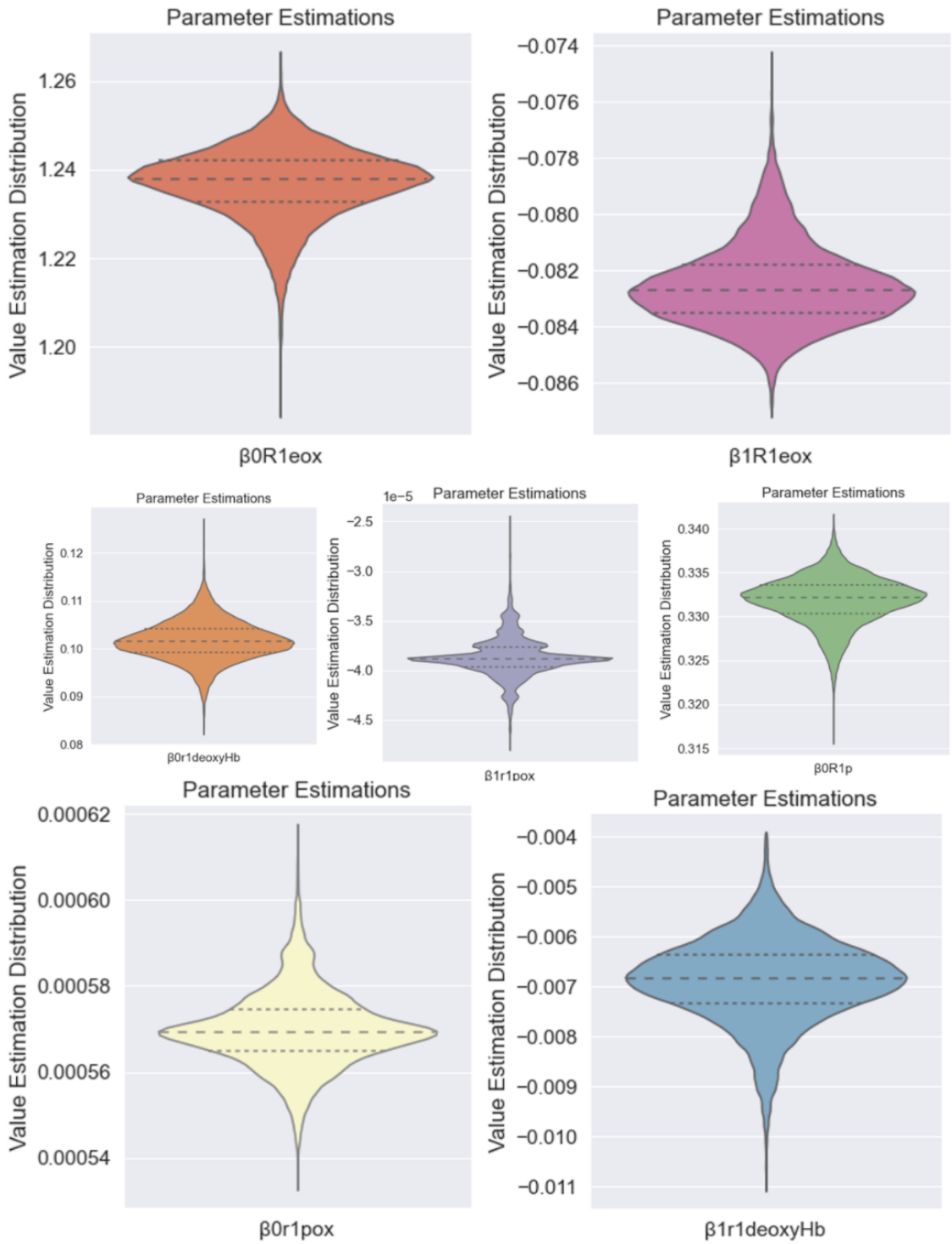


***Appendix Figure C.5.*** *Violin plots showing the distribution of parameter estimates from each iteration. Y axis units per parameter: $\beta_{0,R1eox}$ [$s^{-1}$], $\beta_{1,R1eox}$ [$s^{-1}T^{-1}$], $\beta_{0,r1dHb}$ [$s^{-1}$ L plasma in erythrocyte / mmol Hb tetramer], $\beta_{1,r1dHb}$ [$s^{-1}$ $T^{-1}$ L plasma in erythrocyte / mmol Hb tetramer], $\beta_{0,R1p}$ [$s^{-1}$], $\beta_{0,r1pOx}$ [$s^{-1}$/mmHg], and $\beta_{1,r1pOx}$ [$s^{-1}$ $T^{-1}$/mmHg].*

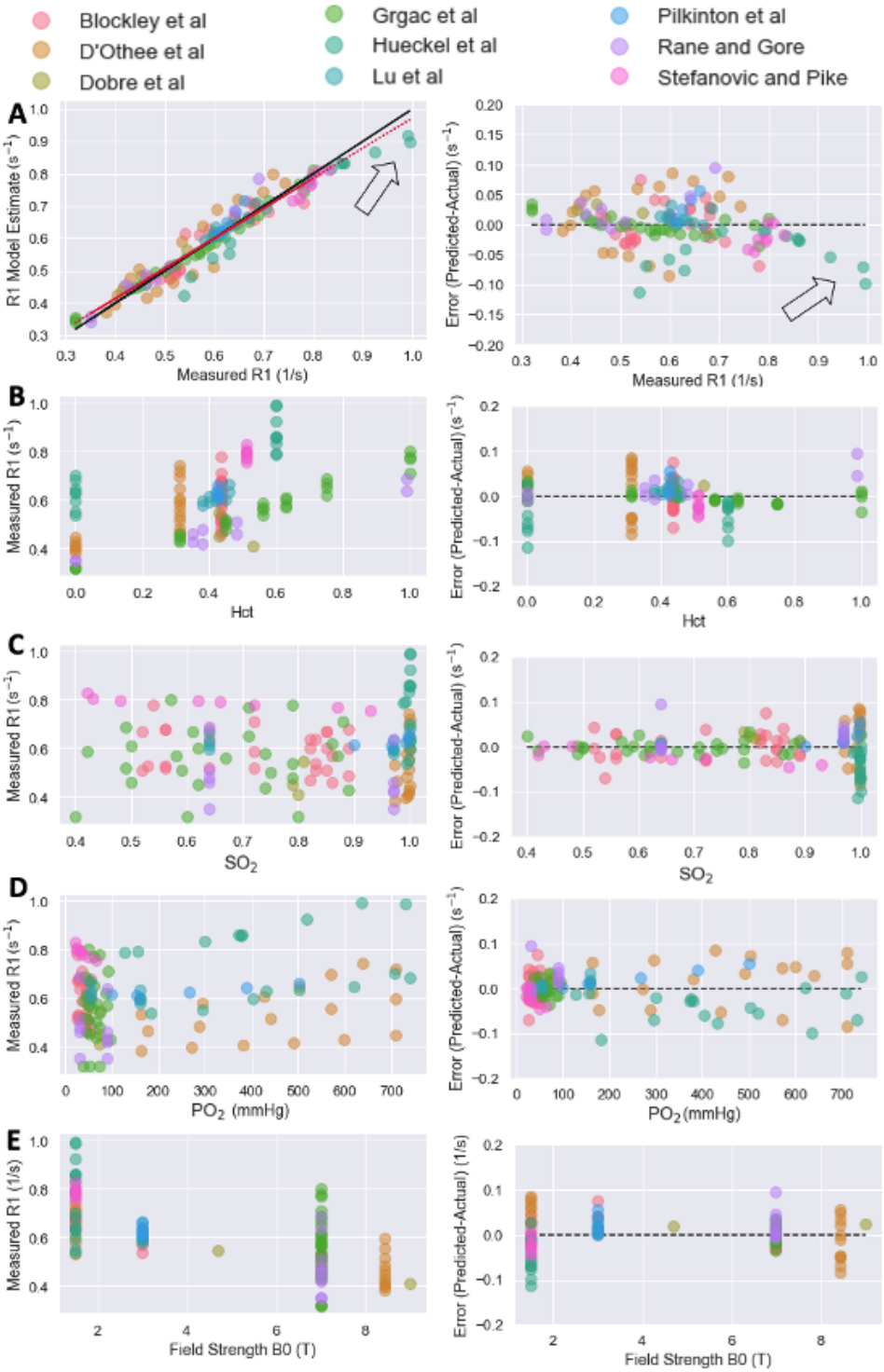


***Appendix Figure C.6. (A)*** *A slight systematic trend in the error distribution by R1 (see arrows) indicated that the model does not entirely explain the non-noise variance in the data. Possible causes of this were further examined by viewing the error sorted according to the original source. One literature source (Hueckel et al. 2000) was consistently under-estimated in R1 in a way that was not explained by categorizing by* ***(B)*** *Hct,* ***(C)*** *$SO_2$,* ***(D)*** *$PO_2$ or* ***(E)*** *B0 values, and some data points collected from Stefanovic 2004 were underestimated by the model.*

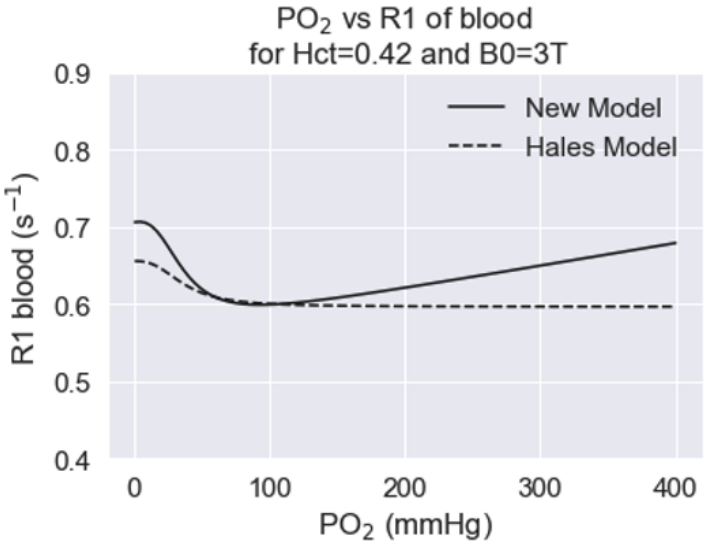


***Appendix Figure C.7.*** *Simulated data showing the divergence of the predictions of the Hales model versus the new model as the $PO_2$ levels become hyperoxic (Hct=0.42 and B0=3T).*

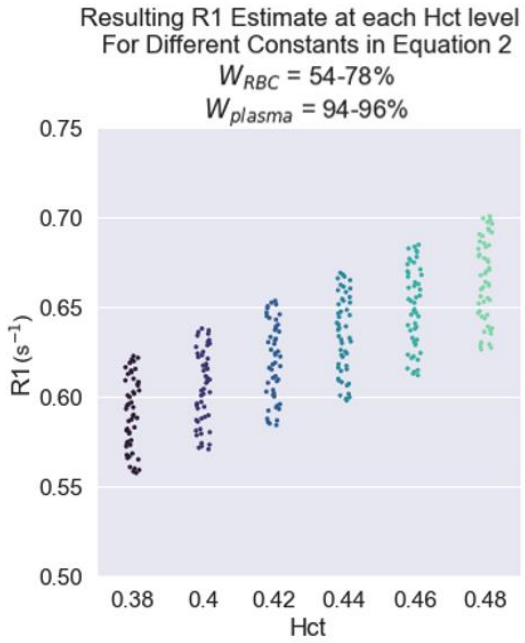


***Appendix Figure C.8.*** *To examine the effect of the range of possible values for $W_{RBC}$ and $W_{plasma}$ on the final R1, R1 was calculated for all combinations of $W_{RBC}$=54-78% and $W_{plasma}$=94-96%, and Hct=0.38-0.48. The distribution of resulting R1 values is plotted — the maximum difference in R1 maximum difference is 0.07 $s^{-1}$ and standard deviation is 0.02 $s^{-1}$ between any combination of $W_{RBC}$ and $W_{plasma}$ values and set hematocrit.*

## C.2. Tables

***Appendix Table C.1.*** *Acquisition details from each experiment in Table I.*

| Reference | MRI Acquisition Details (Relevant Section) |
|---|---|
| **Lu 2004** | **An inversion recovery imaging sequence was used for T1 measurements.** TI values of 10, 50,100, 250, 500, 1000, 2000, 3000, 5000, and 10000 ms were acquired in randomized order, with a constant recovery time of 9s (5 T1) and the following parameters: TE =13 ms, FOV = 100 x 100 $mm^2$, matrix = 32 x 32, single-shot EPI, non-slice-selective sinc RF inversion pulse, and total scan time = 2.5 min. A single slice (10 mm thick) next to the tip of the thermosensor was imaged. After the desired blood conditions (e.g., Hct, temperature, and oxygenation) were achieved, several scans (range = 2– 8, mean ± SD = 4.1 ± 2.1) were made consecutively and the results were averaged to provide one point in the graphs. Data for different Hct values were usually acquired indifferent experiments (i.e., on different days). Arterial T1's at Hct values of 0.38 and 0.46 were each measured twice indifferent blood samples, and T1's at the other Hct values were each measured once |
| **Grgac 2013** | **Conventional inversion recovery sequence was performed for T1 measurement using a non-selective adiabatic inversion pulse** (hyperbolic secant pulse, length 8.6 ms, peak power 15 mT, and bandwidth 1500 Hz). A total of 10 inversion delay times (TI = [100, 400, 700, 1000, 1400, 1900, 2500, 4000, 6000, 9000] ms) were sampled. To minimize possible radiation damping effects, a small dephasing gradient (0.6 mT/m) was applied continuously during the inversion delay time. Axial slice-selective excitation pulse (slice thickness = 10 mm) was utilized to only obtain signals from a central region of the tubing where relatively homogeneous B0 field and B1 field were expected. A local volume covering the slice of interest was shimmed. |
| **Dobre 2007** | **An inversion recovery sequence, followed by slice selection based on Localization by Adiabatic SElective Refocusing (LASER), was used for T1 measurements**. Square pulses were used for inversion (pi =170 As) and subsequent excitation (pi/2=85 As), and two adiabatic full passage pulses were used to localize a 5-mm thick slice at 4.7 and 9.4 T and a 7.5-mm-thick slice at 7 T perpendicular to the long axis of a measurement tube positioned vertically in horizontal bore magnets. Measurements with delay time tI (in ms) were acquired at each field strength (one scan per tI): 10, 100, 200, 400, 800, 1000, 1200, 1400, 1800, 2000, 2400, 2600, 2800, 3000, 5000, 10,000 and 20,000. TR=21 s and TE= 6.36 ms (at 4.7 T), 9.36 ms (at 7 T) and 7.36 ms (at 9.4 T) were used. |
| **Silvennoinen 2003** | **R1 was determined using an inversion recovery sequence** (adiabatic inversion, pulse angle optimized to imaging slice, six inversion times of 100, 500, 1000, 1500, 2000, and 2500 ms), pulse repetition time 10 sec, two dummy scans, two averages), followed by a Hahn single spin echo (echo time 12 ms) profile acquisition (164, FOV 25 mm, 5 mm slice perpendicular to the tube). From the profiles, points with intensity higher than 50% of the maximum were summed and T1 was determined from a three-parameter fit. |
| **d'Othee 2003** | See Appendix Table B.3 |
| **Pilkinton 2012** | See Appendix Table B.3 |
| **Blockley 2008** | **T1 was measured using a single slice inversion recovery sequence** with EPI image acquisition (IR-EPI) which cycled through a range of inversion delay times (TI) sepa-rated by a repetition time TR. Inversion was achieved using a nonselective hyperbolic secant pulse. Data were acquired for 10 TIs in the range 50 ms to 7000 ms, tailored to the field strength and contrast agent concentration. Images were acquired on a 6419 matrix with in-plane resolution of 1 mm2and slice thickness of 3.3 mm. The shortest attainable EPI echo time (TE) was used (5.4, 4.7,and 4.9 ms at 1.5, 3.0, and 7.0T, respectively) to minimize susceptibility induced distortions and to increase signal-to-noise ratio. A TR of 10 s was used for the samples with varying oxygenation, but this was reduced to 6 s for samples containing contrast agent due to their much-reducedT1. Total scan duration was 101 s for data with TR of 10 s and 61 s for data with TR of 6 s. |

| | |
|---|---|
| **Hueckel 2000** | See Appendix Table B.3 |
| **Stefanovic 2004** | The spin-lattice time constant of blood was quantified by means of a single-slice Look-Locker sequence (27) with a segmented EPI readout (2.3 x 2.3 x 5 mm). A composite 90°x -180°y -90°x pulse was used for nonselective inversion, with inversion time (TI) set to 15 ms. Each of the four 20° excitation pulses, applied every 495 ms, was followed by a readout with a TE of 10 ms. The readout bandwidth was set to 140 Hz/pixel, with a 150-mm readout FOV, 75%phase FOV, and 4-s TR. The total scan time per set of four blood samples was approximately 80 min. In each case, the imaging slice was 5 mm thick, perpendicular to the long axes of the vacutainers, and positioned at the center of the 20-mm-long, blood-filled compartment. Localized Shimming was done on the imaging slice at the beginning of the experimental protocol. The Look-Locker data, obtained from the same set of blood samples (Hct= 51.2% ± 0.4%, mean ± standard error), were fitted to a monoexponential recovery model via the nonlinear least-squares minimization. The dependence of the resulting T1 Estimates on Y was obtained by linear fitting of the spin-lattice relaxation rates |
| **Rane 2013** | Voxel size=2×2×3mm3 (in vivo, 1 slice), 2.5×2.5×3mm3 (samples, 5 slices), TR/TE=7000/5.3ms, TI=300, 500 700, 900,1100, 1500, 1900, 2100, 2300 and 3400ms. Temperature was maintained at 37°C using a water bath. An adiabatic non-selective inversion pulse was used in this protocol. Data at very long TI were not acquired due to the long acquisition time of this experiment, sedimentation of the red blood cells and deterioration of the sample over time. However, we believe that this does not affect the calculated T1 value significantly. The imaging slice was chosen in the middle of the samples to minimize the effect of sedimentation at the top and bottom of the tubes. The samples were inspected visually for obvious sedimentation effects. |

***Appendix Table C.2.*** *The fitting process was repeated for all combinations of fewer parameters (i.e. removing the dependence of $r1_{dHb}$ on B0) and the Akaike Information Criterion (AIC) was calculated for each version of the model — the best-fit model according to the AIC is the model that explains the greatest amount of variation using the fewest possible independent variables. The AIC score, $R^2$, and MSE results of the 4 highest AIC-scoring models tested are listed below. The model that scored the highest according to the AIC (Model B) was used in this thesis.*

| Version of Equation | | Rank | AIC | $R^2$ | MSE ($s^{-2}$) |
|---|---|---|---|---|---|
| A | 9 parameter model, using a version of Equation 9 with Hct dependency added: $$r1_{pOx}(B0, Hct) = \beta_{0,r1_{pOx}} + \beta_{1,r1_{pOxB0}} B0 + \beta_{1,r1_{pOxHct}} Hct$$ | 3 | -799.54 | 0.927 | 0.0015 |
| B | 8 parameter model, using standard version of Equation 9 without Hct dependency: $$r1_{pOx}(B0, Hct) = \beta_{0,r1_{pOx}} + \beta_{1,r1_{pOxB0}} B0$$ | 2 | -799.74 | 0.926 | 0.0015 |
| C | 7 parameter model, using standard version of Equation 9 without Hct dependency: $$r1_{pOx}(B0, Hct) = \beta_{0,r1_{pOx}} + \beta_{1,r1_{pOxB0}} B0$$ and Equation 6 without the B0 dependency: $$R1_p(B0) = \beta_{0,R1_p}$$ | 1 | -801.74 | 0.926 | 0.0015 |
| D | 6 parameter model, using standard version of Equation 9 without Hct dependency: $$r1_{pOx}(B0, Hct) = \beta_{0,r1_{pOx}} + \beta_{1,r1_{pOxB0}} B0$$ and Equation 6 without the B0 dependency: $R1_p(B0) = \beta_{0,R1_p}$ And Equation 7 without the B0 dependency: $r1_{dHb}(B0) = \beta_{0,r1_{dHb}}$ | 4 | -795.56 | 0.9207 | 0.0016 |

# Appendix D

## D.1. Figures

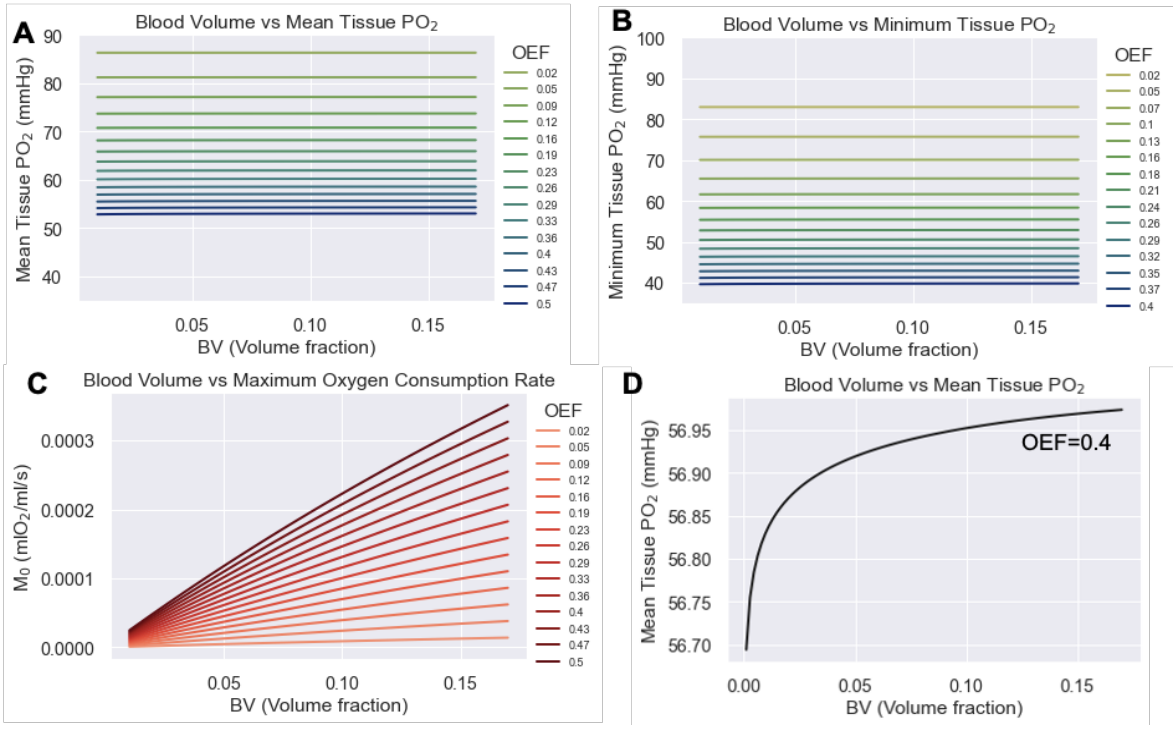


***Appendix Figure D.1.*** *Simulated data showing the resulting* ***(A)*** *mean tissue $PO_2$,* ***(B)*** *minimum tissue $PO_2$, and* ***(C)*** *maximum oxygen consumption rate resulting from all combinations of the ranges of blood volume and OEF used.* ***(D)*** *The blood volume vs. mean tissue $PO_2$ is shown for just OEF=0.4, to show the subtle curve not visible in plots A-B due to the scale of the y-axis. All plots use $PaO_2$=90 mmHg.*

# Appendix E

## E.1. Figures

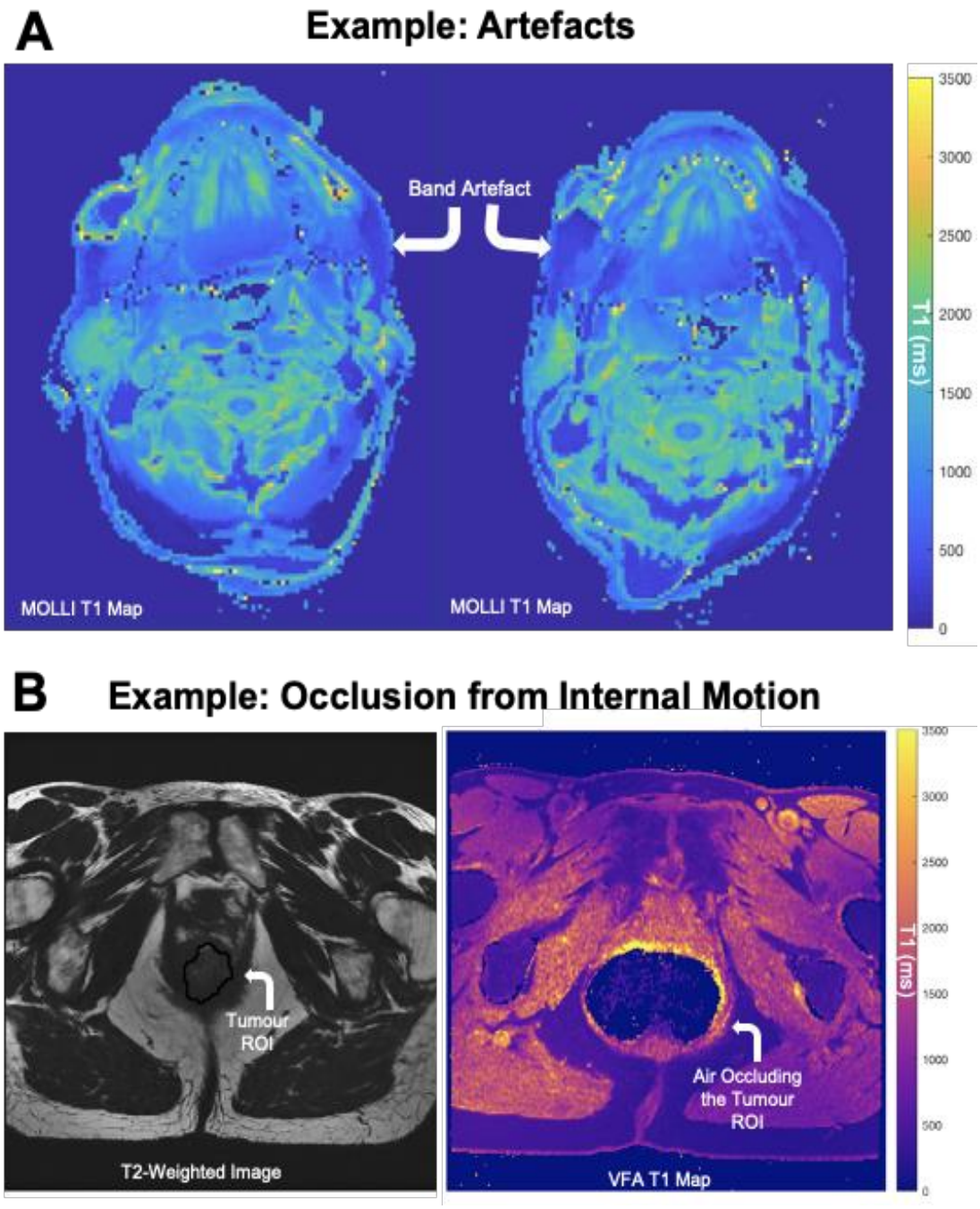


***Appendix Figure E.1.*** *Examples of artefacts seen in the BIOPIC and ART studies, such as* ***(A)*** *a dark band near the sinuses seen on the MOLLI T1 maps (shown here in two separate patients), which was an intentionally placed saturation band, which should not affect the analyzed R1 values but still adds variability, and* ***(B)*** *internal patient motion, such as motion from the bowels which resulted in tumour ROI occlusion and the exclusion of those patients from the final dataset.*

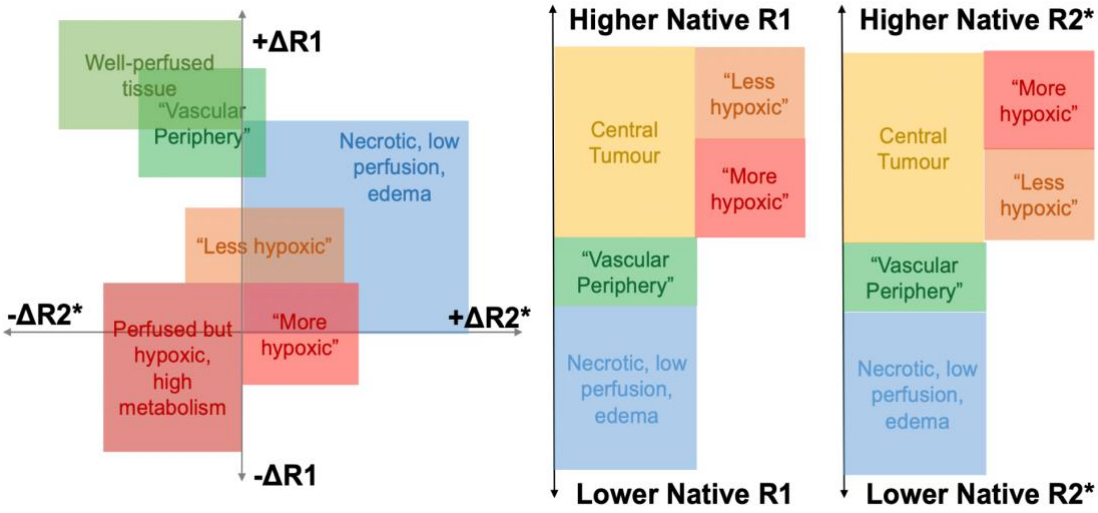


***Appendix Figure E.2.*** *An illustration of the OE-MRI response in different tissue types identified by various studies, as listed in Appendix Table E.2. The hypothesis of the underlying causes of each response are shown in Appendix Table E.3.*

## E.2 Tables

***Appendix Table E.1.*** *The acquisition details from example experiments measuring hyperoxia-induced changes in T1 in in vivo body fluids and tissues.*

| Reference | MRI Acquisition Details (Relevant Section) |
|---|---|
| Edelman 1996 | **TI -weighted images are acquired using a HASTE (half Fourier acquisition single-shot turbo spin-echo) pulse sequence.** For a 128 x 256 matrix, 72 phase-encoding steps are acquired including 8 steps for a phase correction. The inter-echo spacing is very short (4.2 ms). The short inter-echo spacing minimizes the sensitivity to static field inhomogeneities within the lung tissue and, in conjunction with the half-Fourier acquisition, shortens the duration of the data collection (approximately 300 ms for a 128 x 256 matrix; that is, 72 phase-encoding steps x 4.2 ms/echo). The effective echo time (TE) is 25 ms, section thickness is 6-20 mm, field of view is 45 cm x 45 cm, and the duration of the truncated sine waveform is 1 ms for the 90° excitation and 180° refocusing pulses. The refocusing pulses are spatially nonselective in order to reduce signal loss from excited spins washing out of the section during the echo train. The inversion time (TI) of 720 ms was selected based on initial volunteer studies to null the magnetization of the lung parenchyma in room air (21% $O_2$). Images were acquired every three seconds over a period of 2 to 4 min for each series. |
| Tadamura 1997 | **Images used for T1 calculations were obtained using an IR-HASTE sequence**. Images were acquired with at least nine different TIs ranging from 200 to 2,500 msec after a nonselective inversion pulse. Six images were acquired at each TI value for averaging during diastole with electrocardiogram (EKG)-gating.The trigger delay after R wave was varied in such a way as to maintain the acquisition at the same cardiac phase when TI was changed. The data acquisition window for each image was 302 msec. Sequence parameters were: TE/echo spacing = 25 msec/ 4.2 msec, readout bandwidth of 488 Hz/pixel, 12- to 20mm section thickness, 128 X 256 acquisition matrix, 30 to 40-cm field of view, 1-msec duration truncated sinc waveform for the 90° excitation and 180° refocusing pulses. |
| Loffler 2000 | **Sixteen inversion recovery single-shot turbo SE images were acquired with increasing inversion times** (10 msec to 5000 msec) during breathing room air and 100%$O_2$. The sequence parameters were: echo time 4.2 msec, repetition time 7.5 sec, TI 1300 msec, receiver pixel bandwidth 651Hz, slice thickness 8 mm, field of view 400 mm, and matrix size 128x256 (phase encoding x readout direction).The sequence was centrically reordered. The time delay between two images was 7.5 sec to allow complete recovery of longitudinal magnetization. |
| Kinoshita 2000 | The oxygen-enhanced MR images were acquired using an **inversion recovery-preparation fast low angle shot (IR-FLASH) sequence**.The acquisition parameters for the IR-FLASH sequence were as follows: repetition time (TR), 30 ms; echo time (TE), 8 ms; flip angle, 30; field of view, 80 x80 mm; matrix, 128 x128;one excitation; slice thickness, 2.0 mm. The inversion time was 1000 ms to sensitize the acquisition to the paramagnetic effects of molecular oxygen. |
| Hatabu 2001 | Ten images were acquired in the same coronal plane containing pulmonary hila using an **inversion recovery pulse sequence with a single-shot, half-Fourier, turboSE acquisition for each inversion recovery time** before and after inhalation of the oxygen. The acquisition time for each single image was 302 ms (not including the IR pulses), and images were obtained every 3 s while breathing quietly. Sequence parameters were — TR/TE/echo spacing = 3000 ms/25 ms/4.2 ms, readout bandwidth of 488 Hz/pixel, 20 mm section thickness, 128×256 acquisition matrix, 60×60 cm field of view, 1 ms duration truncated sinc waveform for the 90° excitation and 180° refocusing pulses. The acquisition is preceded by a 180° radiofrequency pulse with various inversion recovery times including 200, 400, 600, 700, 800, 1000, 1200, 1400, 2000 and 2500 ms. A 1 ms duration spatially non-selective 180° radiofrequency pulse was applied for the inversion, followed by a 3 ms spoiler gradient of 8 milliTesla/m amplitude. |
| Ohno 2001 | T1-weighted images were obtained with a respiratory synchronized **inversion recovery half-Fourier acquisition single-shot turbo spin-echo inversion recovery (HASTE) pulse sequence**. For a 128 × 128 matrix, 68 phase-encoding steps were obtained, including three steps for phase correction. The interecho spacing was 4.0 msec. The effective TE was 16 msec, section thickness was 10 mm, field of view was 450 × 450 mm with an inversion time of 720 msec. |
| Jones 2002 | For the T1 measurements an **inversion prepared, segmented, half Fourier TSE sequence** (FOV=420x400, TR=4.5 sec, inter echo interval=6 msec, ETL=28, number of shots=3, band-width per pixel=543 Hz, nominal resolution of 1.6x2.5x10 mm) was used to acquire coronal images of a single slice with inversion times (TIs) of 100, 200, 350, 700, and 1300 msec, with each image (TI) being acquired in a separate breathhold. |
| **2004: Messroghli published MOLLI Technique 10.1002/mrm.20110** | |
| Zaharchuk 2005 | See Appendix B.3. |

| | |
|---|---|
| Zaharchuk 2006 | See Appendix B.3. |
| Matsumoto 2006 | See Appendix Table B.3. |
| | **2006: Cheng and Wright publish VFA T1-mapping technique 10.1002/mrm.20791** |
| Uematsu 2007 | **For T1, single-section spin-echo (SE) images were obtained at increasing repetition times** (0.3, 0.6, 1, 1.5, 2, and 5 seconds; echo time, 6.6 milliseconds; number of excitations, 1; field of view, 22 cm; matrix, 6464; and slice thickness, 1 mm). Regions of interest were visually placed on the cerebral cortex in the frontal lobe and pituitary gland in all images by the consensus decision of 2 investigators referring to anatomical SE images, and noise-corrected signal intensities were then fitted to an exponential to calculate T1 and T2 values. |
| O'Connor 2007 | **Series of 3D T1-weighted fast field echo images were acquired over a 9.9-cm volume slab through the upper abdomen to allow estimation of tissue T1 relaxation times** (TR=3.5 ms, TE=0.9 ms,FA=2°/8°/17°, 3 averages, bandwidth=500 Hz, FOV=384 mm, matrix size=128x128, slice thickness=3 mm). Data were processed in three stages using a voxel-by-voxel fitting process with in-house software. **T1 maps at each time point were generated using the variable flip angle method.** |
| Wang 2008 | Used the same method as Zaharchuk 2006. |
| McGrath 2008 | **T1 relaxation time was measured using a half Fourier single-shot turbo spin-echo (HASTE) sequence** with 68 phase encoding steps and inter-echo spacing of 4 ms, effective echo time=16 ms, 128×128 matrix with field of view (FOV)=450×450 $mm^2$, coronal section with slice thickness=10 mm. **T1 measurements were performed using a saturation recovery (SR) HASTE sequence** with saturation times (TSAT) of 100, 200, 400, 800, 1200, 1700, 2300, 3000, 3500 ms, and with a nonselective saturation pulse. Five images were collected for each saturation time to enable averaging over the cardiac cycle. Saturation recovery was chosen in preference to inversion recovery (IR) to reduce the total imaging time. |
| O'Connor 2009 | Series of **3D T1-weighted fast field echo images were acquired** (TR=3.5 ms,TE0.9 ms,a=2/8/17, FOV 375 mm, matrix 128128) to estimate tissue T1.. **R1 maps were generated using the variable flip angle method** at each of the 96 time points and median R1 was calculated for each timepoint. |
| Kershaw 2010 | This volume was imaged using an **inversion-recovery turbo field echo sequence** (TR/TE=2.2/1.0 ms, flip angle=5, acquisition matrix=64x128 zero filled to 256x256) **to acquire images throughout recovery from an initial nonselective inversion pulse** (25 inversion times were used, shortest74 ms with intervals of 143 ms), **permitting a measurement of T1**. The mean signal intensity for the ROI was extracted for each image in the dynamic series, and **dynamic measurements of T1 were extracted by fitting the Look-Locker signal equation** for each set of 25 images corresponding to a T1 measurement time point. |
| Winter 2011 | **Quantitative R1 values were measured using a series of 3D fast spoiled gradient recalled (FSPGR) echo scans with three different flip angles (FA)**. Imaging parameters included repetition time (TR) = 6.55 ms, echo time (TE) = 2.7 ms, FA = 2◦, 10◦ and 21◦, field of view (FOV) = 120 mm, matrix = 192 × 160, slice thickness (SLTH) = 3 mm, slice spacing (SLSP) = 0 mm, number of slices (NSL) = 10, number of averages (NAVG) = 4. R1 parameter maps were generated using the signal equation for the SPGR steady state magnetization with analytical-based FA correction using B1 field maps acquired separately. |
| Simpson 2013 | See Appendix Table B.3. |
| Remmele 2013 | **R1 with Look Locker:** 2D (center slice), a=10°, TR=7 ms, TE=2.0 ms, period between two inversion pulses TRIR=8 s, 34 LL phases, spacing of LL phases $\Delta T_{LL}$ =70 ms, Δx=1.8 mm, Δz=10 mm, FOV=250x250 $mm^2$. Performed at each time point and used as reference and as baseline $R_{1,0}$scan. |
| Burrell 2013 | **Inversion recovery True-FISP image**s (TE=1.2 ms, TR=2.4 ms, 25 inversion times spaced 155 ms apart, initial inversion time of 109 ms, total scan TR=10 s, a=60°, 8 averages, AQ of 8 min) were acquired from 3 contiguous 1 mm slices over a 33 cm field of view and 128x128 matrix, whilst the host breathed air. For each slice, R2* and R1 were determined from a region-of-interest (ROI) encompassing the whole tumour but excluding the surrounding skin/muscle. Data were fitted using a Bayesian maximum a posteriori approach. This approach takes into account the data's Rician distribution, which was used in the calculation of a log-likelihood function which incorporated the Rice probability density function. |
| Haddock 2013 | **A saturation recovery gradient recalled sequence was used for T1-weighted dynamic imaging**. After a saturation time delay of 612 ms, echoes were read out following RF flip angles of 30°, a TR of 3.8 ms, and a TE of 2.1 ms. To alleviate inflow effects a non-selective saturation pulse and centric phase encoding was chosen along with a SENSE factor of 2. The field of view (FOV) was 240×192 mm and 8 slices of 6 mm thickness were obtained. Images were acquired with a matrix of 80×64 resulting in a spatial resolution of 3×3×6 $mm^3$. Temporal resolution was 6.0 s per frame |
| Muir 2013 | See Appendix Table C.1. |

| | |
|---|---|
| Morgan 2014 | **Static T1 mapping scans were performed using an inversion-recovery turbo spin echo (IR-TSE) sequence with repetition time** (TR) = 6000 ms, echo time (TE) = 3.2 ms, FOV= 450 × 450 mm2, matrix size = 128 × 128 and slice thickness = 10 mm, with inversion times (TI) of 60, 300, 1100, 2000 and 5000 ms with 5 repeats acquired at each TI. **Dynamic OE-MRI data were acquired using the same sequence as described for static acquisition with TI = 1100 ms.**<br>To correct for breathing motion, images were registered to end expiration using a previously described method. T1 maps were calculated on a voxelwise basis from static IR-TSE data by fitting the equation:<br>$SI = S0(1-2fe^{-TI/T1} - (1-2f)\, e^{-(TR-ETL\times TE)/T1})$<br>Dynamic T1 maps were calculated using the baseline T1 on air and S0 calculated from the mean of the first 15 images in the dynamic series. |
| Hallac 2014 | **TOLD images were acquired using a gradient echo sequence**: TR/TE=30/5ms, flip angle=45°, acquisition time=3 s. The two sequences were interleaved in an automated fashion to obtain BOLD and TOLD MR images using the same field-of-view, matrix size and imaging plane, as for the high resolution T2W images to allow effective co-registration. |
| Linnik 2014 | This was followed by a **series of slice selective inversion recovery (IR) prepared FLASH acquisitions in order to measure pre-oxygen R1** with the following parameters: TR/TE=21 ms/2.2ms; a=20°; 1 average, acquisition matrix=128x64; inversion slice thickness=20 mm; FOV=40 mmx40mm; four 2-mm-thick axial slices; inversion times of 0.01, 0.25, 0.5, 0.75, 1, 2, 5, 7, 9, and 12 s. |
| Zhao 2015 | Following shimming on tissue water signal to a typical linewidth of 50 Hz, **a spin echo multiple slice (SEMS) sequence was applied to acquire R1 maps** under air breathing (baseline) with the following acquisition parameters: repetition time (TR) arrayed as nine values from 100 ms to 3.5 s, echo time (TE) = 20 ms, field of view = 40×40 $mm^2$, matrix = 64×64 and three adjacent slices each 1.5 mm thick and separated by 1 mm space in 10½ min. Then five T1-weighted (TR = 30 ms, TE = 5 ms, flip angle = 45°; acquisition time = 3 s, matrix = 128×128) and T2*-weighted (TR = 150 ms, TE = 20 ms, flip angle = 20°, acquisition time = 19 s, matrix= 128×128) **spoiled gradient-echo (SPGRE) images were acquired in an interleaved fashion, as baseline**. SI in the initial five T1- or T2*-weighted images (during air breathing) was averaged to obtain mean baseline images, and relative changes in SI with respect to CB challenge were calculated on a voxel by voxel basis. R1 values for a given voxel were obtained by fitting the signal intensities corresponding to nine delay values to a three-parameter least squares curve, using a Levenberg–Marquardt algorithm. |
| Zhang 2015 | Baseline lung T1 measurements were made using a set of **T1 weighted centric ordered inversion-recovery single-shot turbo spin echo sequence (IR-TSE), using a non-selective adiabatic inversion pulse**, with 5 inversion times (TI = 60/300/1100/2000/5000 ms). There were 5 repetitions for each TI to average over the cardiac and respiratory cycles. Other scanning parameters included: repetition time (TR) 6000 ms, effective echo time (TE) 3.2 ms, matrix 128×128 (full k-space sampling) and pixel size 3.52 mm×3.52 mm. No breath-holding, respiratory or cardiac triggering was used. |
| Muir 2016 | **T1 was measured using inversion-recovery gradient-echo echo planar imaging** with field of view = 25.6 × 25.6 $mm^2$, matrix = 96×96, seven 1.5 mm thick slices, 2/3 partial Fourier acquisition, echo time = 9.9 ms, and repetition time = 12 s. Data acquired in both groups with hyperbaric conditions used ten inversion times from 23 to 3623 ms equally spaced by 400 ms and 3 signal averages. The data of the NBO group were acquired using the same parameters, except that six inversion times (25, 500, 1000, 2000, 4000, and 8000 ms) and 4 signal averages were used. |
| Cao-Pham 2016 | **The segmented IR-FISP sequence (SSFP-FID mode) was used for R1 acquisition** with the following parameters: TR/TE/FA/BW/FOV/matrix size/slice thickness Z=4 ms/ 1.35 ms/10°/100 kHz/55x30 mm/100x85/1 mm, 4 segments, 100 TI from 13 ms to 8329 ms every 84 ms, and a total acquisition time of 20 minutes. |
| White 2016 | Interleaved dynamic blood-oxygenation level dependent (BOLD or R2*) and **tissue-oxygenation level dependent (TOLD or T1- weighted) measurements were performed** for about 10 minutes for baseline air and during a hyperoxic oxygen breathing challenge. Using in-house algorithms developed in Matlab, voxel-by-voxel %ΔSI in BOLD and TOLD responses with respect to inhaling oxygen was calculated from the whole tumor region-of-interest. BOLD images were selected at a single echo time (TE = 20 ms) for analysis. Voxel-by-voxel R2* maps were generated from BOLD images by **fitting the multi-echo data to the echo time (TE) in a nonlinear least squares equation** and quantitative ΔR2* values were calculated. Likewise, **R1 with respect to the repetition times (TR).** |
| O'Connor 2016 | OE-MRI: **Inversion recovery (IR) True-FISP images were usedto calculate R1**(TR=2.4ms; scan TR=10 seconds,48 inversion times spaced 38.8 ms apart with initial inversion time of 106.2ms; TE=1.2 ms; a=60°). **Dynamic images were used to quantify the temporal onset of R1 changes induced** by switching between air and 100% oxygen. The dynamic images required 2 signal averages and took 2 minutes and 40 seconds to perform. |
| Cao-Pham 2017 | **The segmented inversion-recovery fast imaging with steady state precession (IR-FISP) sequence (SSFP-FID or Steady State Free Precession Free Induction Decay mode) was used for R1 acquisition** with the following parameters: TR/TE/flip angle (FA)/band-width (BW)/FOV/matrix size/slice thickness = 4 ms/1.35 ms/10°/100 kHz/55 × 30 mm2/100 × 85/1 mm, four segments, 100 TI from 13 ms to 8329 ms every 84 ms, and a total acquisition time of 20 min. The resonance frequency for excitation of the R1 sequence was on resonance for water. |

| | |
|---|---|
| Fan 2017 | **A dynamic OE-MRI series with an IR-TSE sequence** (TE/ TR, 48/9575 ms; inversion time, 1915 ms; FOV, 80×80 mm; matrix, 192×96; half-Fourier, 6/8; one 2-mm-thick axial slice) was acquired. |
| Kindvall 2018 | **All T1 measurements were made with the Snaps FLASH pulse sequence which is based on the Look and Locker sequence.** Following spin inversion, several gradient echo images were collected during magnetization recovery. Imaging parameters were as follows: matrix=128x64,zero filled to 256x256; 450mm square field of view; 1.5cm slice thickness; TE= 0.67ms; TR= 3.0ms; and flip angle= 7˚.A non-selective hyperbolic secant pulse was used for spin inversion and Hanning-windowed sinc pulses with 1.6 side lobes were used for image acquisition. |
| Bhogal 2017 | Prior to T1 mapping, a B0 map was acquired (3D gradient-echo, TR/TE: 4/1.54 ms, scan duration: 11.4 s, reconstructed resolution: 3.75 mm3 , slices: 29, FOV: 240 112.5 180 mm3 , flip angle: 10°). This map was used to perform third-order image-based B0 shimming. **T1 maps were acquired using a non-slice selective adiabatic inversion pulse,** which served to minimize inflow effects relating to limited transmit coil volume, followed by sequential acquisition of slices at increasing inversion times along the T1 recovery curve. This process was repeated over 23 scans. For each repetition, the acquired slice order was shifted such that each slices were acquired at 23 distinct inversion times – for details see Polders et al. Scan parameters were as follows: **multi-slice single-shot echo planar imaging (EPI)**, inversion time range: 132.2–5074.4 ms, inversion time spacing: 224.6 ms, TR/TE: 10,000/9.42 ms, scan duration: 4 min, reconstructed resolution: 1x1x1.5 $mm^3$ , slices: 46, FOV: 224x224x91.5 $mm^3$ , flip angle: 150°, SENSE factor: 3.6 (AP), Half Scan factor: 0.61. Post processing was done using an IDL tool whereby slices were re-ordered and temporally consistent image volumes were reconstructed. **From here, a voxel-wise T1 fit was performed assuming complete inversion (i.e. a two parameter fit)** to generate whole brain, high-resolution T1 maps. |
| Featherstone 2017 | **A variable flip angle method was carried out to measure tissue baseline T1(45) using 3D modified driven equilibriumFourier transform sequences**: TR=30.00 ms; TE=1.44ms; a=5°,10°,20°; five averages; matrix=64x64; field of view=32mmx32mm; 161mm thick coronal slices. **This was followed by 42 dynamic acquisitions** (acquisition details as above but a=20° only) at a temporal resolution of one image volume every 28.80 s. |
| Moosvi 2018 | **Dynamic oxygen enhanced MRI (dOE-MRI) scans were acquired with a 2D multi-slice FLASH-based sequence** with TE/TR = 2.67 ms/66.7 ms, α = 40◦, temporal resolution of 4.3s with 198 repetitions. |
| Little 2018 | **Inversion recovery half-Fourier rapid acquisition with relaxation enhancement images to calculate R1 at baseline and dynamically throughout the gas challenge. Dynamic images were used to quantify the temporal onset of R1 changes** induced by switching between air and 100% oxygen (switch performed after nine baseline measurements). |
| Zhou 2019 | **R1 maps were acquired using T1 fast field echo (FFE) with variable flip angles (five flip angles from 2◦ to 14◦ ),** FOV = 240–260 mm, in-plane resolution 0.94 mm, slice thickness = 3 mm. R1 maps were obtained through curve fitting with multiple flip angles. |
| Yang 2019 | **R1 measurements used the modified fast inversion-recovery (MFIR) method integrated with a slice-selective inversion pulse and a segmented turbo FLASH acquisition**. The scan parameters were: inversion-recovery TR = 6s, TI = 0.01, 0.35, 1.4, 3.1, 5.5s (quadratically spaced), 4 averages, and scan time of 8 min. During each inversion-recovery TR, 16 k-space lines were acquired with the following parameters: 10° flip angle, acquisition TR =10ms, TE =5 ms. BOLD and TOLD measurements were interleaved, with 20 acquisitions during baseline and 20 accompanying challenge gas. **TOLD measurements were acquired as T1-weighted images using a gradient-echo sequence with transverse-magnetization spoiling** (TR = 30 ms, TE = 5 ms, 45° flip angle, 8 averages, 20 dummy scans, and scan time of 16 s). |
| Salem 2019 | Preclinical: OE-MRI consisted of a **variable flip angle (VFA) spoiled gradient echo (SPGR) acquisition** to calculate native tissue R1 (TR=30ms; TE=1.44 ms; a=5°/10°/20°). This was followed by 42 **dynamic T1-weighted spoiled gradient recalled acquisitions in the steady state** (SPGR; TR=30ms; TE=1.44ms; a=20°; temporal resolution=28.8s).<br>Clinical: **R1 was calculated using a series of coronal 3D single-shot inversion recovery–prepared SPGR acquisitions** (TR=2.1 ms; TE=0.50 ms; a=6°, number of excitations=5, TI= 10, 50, 300, 1,100, 2,000, 5,000 ms). |
| Qian 2020 | **R1 maps were acquired using T1 fast field echo (FFE) with variable flip angles** (flip angles = 7°,16°,37°), TR/TE= 32/2ms, FOV= 240mm×240mm, in-plane resolution=1.88mm, slice thickness = 5mm. We chose greater flip angles to minimize transmit RF field imperfection induced incorrect flip angles according to previous studies. |
| Bluemke 2020 | **Modified Look-Locker Inversion Recovery (MOLLI) T1-mapping** sequences (FIESTA sequence, slice thick-ness 5.0mm, resolution 1.7mmx1.7mm, FOV = 380mm, 11 inversion times, flip angle = 35°, TR = 3000ms, TE = 120ms) were acquired in a single transverse slice through the tumour volume. |
| Vatnehol 2020 | A **modified Look–Locker inversion recovery (MOLLI)** with a 10(5)5 scheme and a multi fast field echo (mFFE) was used to acquire T1- and T2*- weighted images used for T1 and T2* relaxation time measurements. Selected sequence parameters for the sequences are given in Table 1 (of Vatnehol Manuscript). |

***Appendix Table E.2.*** *The OE-MRI response in different tissue types identified by various studies. These responses are displayed as an illustration in Appendix Figure E.2. The hypothesis of the underlying causes of each response are shown in Appendix Table E.3.*

| Generalized Tumour tissue type/situation | Observations | | | | |
|---|---|---|---|---|---|
| | **Native R1** | **ΔR1 Response to 100% O2** | **Native R2 or R2*** | **ΔR2* Response to 100% O2** | **DCE-MRI measures** |
| **Well-perfused tissues, vascular rim tissue, or called "Vascular Periphery"** | Higher native R1 than necrotic, but lower than central tumour (1.5T) [228] | Positive ΔR1 (1.5T) [167]<br><br>Positive ΔR1 (1.5T) [228] | Higher R2* than necrotic, but lower than central tumour (1.5T) [228] | Mostly negative ΔR2* (1.5T) [228] | High perfusion as measured by IAUC60 [167] (1.5T) |
| **Tumour core, possibly hypoxic, but is perfused, or hypoxic region that consumes the $O_2$** | Higher native R1 than both vascular periphery and necrotic (1.5T) [228]<br><br>More hypoxic has lower native R1 than less hypoxic (7T) [97] | More hypoxic showed smaller positive ΔR1, less hypoxic showed larger positive ΔR1 (7T) [97]<br><br>Mostly positive ΔR1 (1 small negative) (1.5T) [228]<br><br>Strong negative ΔR1 seen in the contrast enhancing areas of the glioblastoma and metastasis (1.5) [201]<br><br>Low or absent ΔR1, but moderate perfusion from IAUC60 (1.5T) [167] | Higher native R2* than both vascular periphery and necrotic (1.5T) [228]<br><br>More hypoxic has higher native R2* than less hypoxic (7T) [97] | More hypoxic showed only positive ΔR2*, less hypoxic showed heterogeneity in direction of ΔR2* but overall trend toward positive ΔR2* (7T) [97]<br><br>All negative ΔR2* (1.5T) [228]<br><br>Strong negative ΔR2* seen in the contrast enhancing areas of the glioblastoma and metastasis (1.5) [201] | Does contrast-enhance with DCE-MRI (1.5) [201]<br><br>Moderate perfusion as measured by IAUC60 (1.5T) [167] |
| **Necrotic/avascular tissue that has little perfusion** | Lower native R1 than both vascular periphery and central tumour (1.5T) [228] | Positive ΔR1 (1.5T) [228]<br><br>Moderate positive ΔR1 in peritumoral oedema and necrotic areas (1.5) [201]<br><br>Low or absent ΔR1 (1.5T) [167] | Lower native R2* than both vascular periphery and central tumour (1.5T) [228] | Positive ΔR2* (1.5T) [228]<br><br>Moderate positive ΔR2* in peritumoral oedema and necrotic areas (1.5) [201] | Low or absent perfusion as measured by IAUC60 (1.5T) [167] |

***Appendix Table E.3.*** *The hypothesis of the underlying causes of each OE-MRI response in different tissue types listed in Appendix Table E.2. These responses are displayed as an illustration in Appendix Figure E.2.*

| Metric | Interpretations |
|---|---|
| **Native R1** | Overall, native R1 does not seem to be a reliable indicator of tissue $PO_2$, however a general observation has been that faster median R1 values corresponded to a more well oxygenated tissue [250]. |
| **Positive ΔR1** | Following a hyperoxic challenge, an increase in R1 is most likely due to an increase in dissolved oxygen levels.<br>Since a hyperoxic challenge should increase arterial $PO_2$, an increase in oxygen (and hence increase in R1) would be expected in healthy, normal tissues that are supplied from those arteries. A positive ΔR1 in healthy, normal tissues would be expected to be paired with a negative ΔR2* (see "Negative ΔR2*" below).<br>However, healthy normal tissues are not the only situation where an increase in R1 has been observed — when paired with a positive ΔR2*, a positive ΔR1 has been found in tissues with high fluid content such as oedema, necrotic areas and CSF [201], [228]. Remmele et al. [201] hypothesized that this is due to perfusion with a greatly reduced number of erythrocytes (hence no decrease in R2* as expected from decrease in deoxyHb), therefore resulting in dissolved oxygen being the dominant effect. |
| **Negative ΔR1** | Following a hyperoxic challenge, a decrease in R1 could occur from an increase in oxygen saturation within that ROI, and hence a lower concentration of paramagnetic deoxyhemoglobin.<br>A negative ΔR1 has been interpreted as a sign of hypoxic tissue, since hypoxic tissue will have a high concentration of deoxyhemoglobin at baseline and will then have a large increase in $SO_2$ without much change in dissolved oxygen [97], [200].<br>It has also been hypothesized that a negative ΔR1 could arise from "vascular steal", an effect where blood is redistributed away from the tumour by the systemic vasculature, leading to an overall reduction in tumour oxygenation [274], [275]. Cao-Pham et al. [249] have hypothesized that vascular steal would be paired with a positive ΔR2*. |
| **Native R2*** | Overall, native R2* has been shown to *not* correlate exactly with tissue $PO_2$ [91], a *general trend* has been reported that tumours with higher native R2* were more likely to be hypoxic [89], [90]. This is hypothesized to be because hypoxic tumour tissue will contain higher levels of deoxyhemoglobin than highly-oxygenated tissues, and therefore higher R2*. |
| **Negative ΔR2*** | Following a hyperoxic challenge, the arterial $SO_2$ may increase slightly to full saturation, and the levels of dissolved oxygen in the plasma will increase to as much as 600 mmHg [211]. This will result in less oxygen being extracted from the erythrocytes as it passes through tissues, and therefore there will be a higher remaining $SO_2$ on the venous end, and therefore a decreased concentration in deoxyhemoglobin, corresponding to a decreased R2* [228].<br>A negative ΔR2* has been observed in the vascular periphery, a well-perfused, vascular tissue of the tumour [228], as well as areas of the tumour which also showed a positive ΔR1, suggesting a well-perfused region [201]. |
| **Positive ΔR2*** | The interpretations of an *increase* in R2* following a hyperoxic challenge are more complex, depending on the gas challenge. Following a carbogen challenge, an increased R2* has been hypothesized to be due to a vasodilatation-mediated *increase* in blood volume — which may increase the concentration of deoxyhemoglobin within the voxel and thus increase R2* [167]. Cao-Pham et al. [250] have hypothesized that since tumour vasculature comprises both mature and unstable, immature blood vessels, and only the mature blood vessels are believed to be 'responsive' to carbogen breathing, therefore inducing an increase in blood volume where vessels are mature (+ΔR2*), and a decrease in blood volume where vessels were immature (-ΔR2*).<br>Following a 100% oxygen challenge, Breuer et al. [87] hypothesized that since inhalation of pure oxygen may induce vasoconstriction in tumour vessels, which may cause the concentration of deoxyhemoglobin to decrease and therefore increase R2*. Voxels with *both* a positive ΔR2* and ΔR1 have been found tissues with high fluid content such as oedema, necrotic areas, and CSF [201]. |

# References


[1] N. Chaudary and R. P. Hill, 'Hypoxia and Metastasis', *Clin. Cancer Res.*, vol. 13, no. 7, pp. 1947–1949, Apr. 2007, doi: 10.1158/1078-0432.CCR-06-2971.

[2] M. Milosevic *et al.*, 'Tumor hypoxia predicts biochemical failure following radiotherapy for clinically localized prostate cancer', *Clin. Cancer Res. Off. J. Am. Assoc. Cancer Res.*, vol. 18, no. 7, pp. 2108–2114, Apr. 2012, doi: 10.1158/1078-0432.CCR-11-2711.

[3] G. D. Stewart, J. A. Ross, D. B. McLaren, C. C. Parker, F. K. Habib, and A. C. P. Riddick, 'The relevance of a hypoxic tumour microenvironment in prostate cancer', *BJU Int.*, vol. 105, no. 1, pp. 8–13, 2010, doi: 10.1111/j.1464-410X.2009.08921.x.

[4] A. Yuen and B. Díaz, 'The impact of hypoxia in pancreatic cancer invasion and metastasis', *Hypoxia Auckl. NZ*, vol. 2, pp. 91–106, 2014, doi: 10.2147/HP.S52636.

[5] K. L. Eales, K. E. R. Hollinshead, and D. A. Tennant, 'Hypoxia and metabolic adaptation of cancer cells', *Oncogenesis*, vol. 5, no. 1, pp. e190–e190, Jan. 2016, doi: 10.1038/oncsis.2015.50.

[6] H. Maeda, J. Wu, T. Sawa, Y. Matsumura, and K. Hori, 'Tumor vascular permeability and the EPR effect in macromolecular therapeutics: a review', *J. Control. Release Off. J. Control. Release Soc.*, vol. 65, no. 1–2, pp. 271–284, Mar. 2000, doi: 10.1016/s0168-3659(99)00248-5.

[7] P. Carmeliet and R. K. Jain, 'Angiogenesis in cancer and other diseases', *Nature*, vol. 407, no. 6801, pp. 249–257, Sep. 2000, doi: 10.1038/35025220.

[8] Y. Boucher, M. Leunig, and R. K. Jain, 'Tumor angiogenesis and interstitial hypertension', *Cancer Res.*, vol. 56, no. 18, pp. 4264–4266, Sep. 1996.

[9] J. W. Nichols and Y. H. Bae, 'EPR: Evidence and fallacy', *J. Control. Release Off. J. Control. Release Soc.*, vol. 190, pp. 451–464, Sep. 2014, doi: 10.1016/j.jconrel.2014.03.057.

[10] M. Horsman, L. Mortensen, and P.-J. reviews Clinical …, 'Imaging hypoxia to improve radiotherapy outcome', 2012, doi: 10.1038/nrclinonc.2012.171.

[11] P. Vaupel and M. Höckel, 'Tumor hypoxia and therapeutic resistance', in *Recombinant Human Erythropoietin (rhEPO) in Clinical Oncology: Scientific and Clinical Aspects of Anemia in Cancer*, M. R. Nowrousian, Ed. Vienna: Springer, 2002, pp. 127–146. doi: 10.1007/978-3-7091-7658-0_7.

[12] J. M. Brown, 'Tumor hypoxia in cancer therapy', *Methods Enzymol.*, vol. 435, pp. 297–321, 2007, doi: 10.1016/S0076-6879(07)35015-5.

[13] L. H. Gray, A. D. Conger, M. Ebert, S. Hornsey, and O. C. A. Scott, 'The Concentration of Oxygen Dissolved in Tissues at the Time of Irradiation as a Factor in Radiotherapy', *Br. J. Radiol.*, vol. 26, no. 312, pp. 638–648, Dec. 1953, doi: 10.1259/0007-1285-26-312-638.

[14] R. H. Thomlinson and L. H. Gray, 'The Histological Structure of Some Human Lung Cancers and the Possible Implications for Radiotherapy', *Br. J. Cancer*, vol. 9, no. 4, pp. 539–549, Dec. 1955.

[15] C. Bayer, K. Shi, S. T. Astner, C.-A. Maftei, and P. Vaupel, 'Acute versus chronic hypoxia: why a simplified classification is simply not enough', *Int. J. Radiat. Oncol. Biol. Phys.*, vol. 80, no. 4, pp. 965–968, Jul. 2011, doi: 10.1016/j.ijrobp.2011.02.049.

[16] D. W. Siemann and M. R. Horsman, 'Modulation of the tumor vasculature and oxygenation to improve therapy', *Pharmacol. Ther.*, vol. 153, pp. 107–124, Sep. 2015, doi: 10.1016/j.pharmthera.2015.06.006.

[17] V. S. Hughes, J. M. Wiggins, and D. W. Siemann, 'Tumor oxygenation and cancer therapy-then and now', *Br. J. Radiol.*, vol. 92, no. 1093, p. 20170955, Jan. 2019, doi: 10.1259/bjr.20170955.

[18] P. Vaupel and L. Harrison, 'Tumor hypoxia: causative factors, compensatory mechanisms, and cellular response', *The Oncologist*, vol. 9 Suppl 5, pp. 4–9, 2004, doi: 10.1634/theoncologist.9-90005-4.

[19] K. R. Luoto, R. Kumareswaran, and R. G. Bristow, 'Tumor hypoxia as a driving force in genetic instability', *Genome Integr.*, vol. 4, p. 5, Oct. 2013, doi: 10.1186/2041-9414-4-5.

[20] B. Muz, P. de la Puente, F. Azab, and A.-A. Hypoxia, 'The role of hypoxia in cancer progression, angiogenesis, metastasis, and resistance to therapy', 2015.

[21] P. Vaupel, D. Kelleher, and H.-M. in oncology, 'Oxygenation status of malignant tumors: pathogenesis of hypoxia and significance for tumor therapy', 2001.

[22] M. Höckel and P. Vaupel, 'Biological consequences of tumor hypoxia', *Semin. Oncol.*, vol. 28, pp. 36–41, 2001, doi: 10.1016/s0093-7754(01)90211-8.

[23] Y. Sheng *et al.*, 'Magnetically responsive microbubbles as delivery vehicles for targeted sonodynamic and antimetabolite therapy of pancreatic cancer.', *J. Control. Release Off. J. Control. Release Soc.*, vol. 262, pp. 192–200, 2017, doi: 10.1016/j.jconrel.2017.07.040.
[24] Y. Sheng *et al.*, 'Oxygen generating nanoparticles for improved photodynamic therapy of hypoxic tumours', *J. Control. Release Off. J. Control. Release Soc.*, vol. 264, pp. 333–340, Oct. 2017, doi: 10.1016/j.jconrel.2017.09.004.
[25] M. Khan *et al.*, 'Engineering oxygen nanobubbles for the effective reversal of hypoxia', *Artif. Cells Nanomedicine Biotechnol.*, vol. 46, no. sup3, pp. 1–10, 2018, doi: 10.1080/21691401.2018.1492420.
[26] M. S. Khan *et al.*, 'Oxygen-Carrying Micro/Nanobubbles: Composition, Synthesis Techniques and Potential Prospects in Photo-Triggered Theranostics.', *Mol. Basel Switz.*, vol. 23, no. 9, 2018, doi: 10.3390/molecules23092210.
[27] E. J. Hall, 'Intensity-modulated radiation therapy, protons, and the risk of second cancers', *Int. J. Radiat. Oncol.*, vol. 65, no. 1, pp. 1–7, 2006, doi: 10.1016/j.ijrobp.2006.01.027.
[28] R. Hodgkiss, I. Roberts, and of … W.-M., 'Rapid-mixing studies of radiosensitivity with thiol-depleted mammalian cells', 1987, doi: 10.1080/09553008714552241.
[29] J. M. Brown, 'Hypoxic cytotoxic agents: a new approach to cancer chemotherapy', *Drug Resist. Updat.*, pp. 7–13, 2000, doi: 10.1054/drup.2000.0120.
[30] Y. Ogawa *et al.*, 'Safety and effectiveness of a new enzyme-targeting radiosensitization treatment (KORTUC II) for intratumoral injection for low-LET radioresistant tumors.', *Int. J. Oncol.*, vol. 39, no. 3, pp. 553–60, 2011, doi: 10.3892/ijo.2011.1069.
[31] S. Rockwell, 'Tumor radiation responses and tumor oxygenation in aging mice', *Exp. Gerontol.*, vol. 24, no. 1, pp. 37–48, 1989, doi: 10.1016/0531-5565(89)90033-8.
[32] P. M. Tibbles and J. S. Edelsberg, 'Hyperbaric-Oxygen Therapy', *N. Engl. J. Med.*, vol. 334, no. 25, pp. 1642–1648, 1996, doi: 10.1056/NEJM199606203342506.
[33] G. Lippi, M. Franchini, and G. Banfi, 'Red blood cell-mimicking synthetic biomaterial particles: the new frontier of blood doping?', *Int. J. Sports Med.*, vol. 31, no. 02, pp. 75–76, 2010.
[34] G. Shenouda *et al.*, 'Long-Term Results of Radiation Therapy Oncology Group 9903: A Randomized Phase 3 Trial to Assess the Effect of Erythropoietin on Local-Regional Control in Anemic Patients Treated With Radiation Therapy for Squamous Cell Carcinoma of the Head and Neck', *Int. J. Radiat. Oncol.*, vol. 91, no. 5, pp. 907–915, 2015, doi: 10.1016/j.ijrobp.2014.12.018.
[35] J. R. Wright *et al.*, 'Randomized, Double-Blind, Placebo-Controlled Trial of Erythropoietin in Non–Small-Cell Lung Cancer With Disease-Related Anemia', *J. Clin. Oncol.*, vol. 25, no. 9, pp. 1027–1032, 2007, doi: 10.1200/JCO.2006.07.1514.
[36] A. Tewarson, 'Nonmetallic Material Flammability in Oxygen Enriched Atmospheres', *J. Fire Sci.*, vol. 18, no. 3, pp. 183–214, 2000, doi: 10.1177/073490410001800303.
[37] J. H. A. M. Kaanders, J. Bussink, and A. J. van der Kogel, 'Clinical studies of hypoxia modification in radiotherapy', *Semin. Radiat. Oncol.*, vol. 14, no. 3, pp. 233–240, 2004, doi: 10.1016/j.semradonc.2004.04.002.
[38] A. L. Farris, A. N. Rindone, and W. L. Grayson, 'Oxygen delivering biomaterials for tissue engineering', *J. Mater. Chem. B*, vol. 4, no. 20, pp. 3422–3432, 2016, doi: 10.1039/C5TB02635K.
[39] D. S. Martin and M. P. W. Grocott, 'Oxygen therapy in critical illness: precise control of arterial oxygenation and permissive hypoxemia', *Crit. Care Med.*, vol. 41, no. 2, pp. 423–432, Feb. 2013, doi: 10.1097/CCM.0b013e31826a44f6.
[40] J. Owen *et al.*, 'Reducing Tumour Hypoxia via Oral Administration of Oxygen Nanobubbles.', *PloS One*, vol. 11, no. 12, p. e0168088, 2016, doi: 10.1371/journal.pone.0168088.
[41] M. Khan, J. Hwang, K. Lee, Y. Choi, K. Kim, and H. Koo, 'Applications of Oxygen-Carrying Micro/Nanobubbles: a Potential Approach to Enhance Photodynamic Therapy and Photoacoustic Imaging', 2018.
[42] A. C. Anselmo and S. Mitragotri, 'An overview of clinical and commercial impact of drug delivery systems.', *J. Control. Release Off. J. Control. Release Soc.*, vol. 190, pp. 15–28, 2014, doi: 10.1016/j.jconrel.2014.03.053.
[43] J. Wu, G. Gong, Y. Cui, and R. Li, 'Intratumor partitioning and texture analysis of dynamic contrast-enhanced (DCE)-MRI identifies relevant tumor subregions to predict pathological response of breast cancer to neoadjuvant chemotherapy', *J. Magn. Reson. Imaging JMRI*, vol. 44, no. 5, pp. 1107–1115, Nov. 2016, doi: 10.1002/jmri.25279.

[44] S. B. Feinstein *et al.*, ‘Two-dimensional contrast echocardiography. I. In vitro development and quantitative analysis of echo contrast agents’, *J. Am. Coll. Cardiol.*, vol. 3, no. 1, pp. 14–20, Jan. 1984, doi: 10.1016/s0735-1097(84)80424-6.
[45] E. Stride *et al.*, ‘Microbubble Agents: New Directions’, *Ultrasound Med. Biol.*, vol. 46, no. 6, pp. 1326–1343, Jun. 2020, doi: 10.1016/j.ultrasmedbio.2020.01.027.
[46] J. N. Kheir *et al.*, ‘Oxygen gas-filled microparticles provide intravenous oxygen delivery.’, *Sci. Transl. Med.*, vol. 4, no. 140, p. 140ra88, 2012, doi: 10.1126/scitranslmed.3003679.
[47] J. A. Feshitan, N. D. Legband, M. A. Borden, and B. S. Terry, ‘Systemic oxygen delivery by peritoneal perfusion of oxygen microbubbles’, *Biomaterials*, pp. 2600–2606, 2014, doi: 10.1016/j.biomaterials.2013.12.070.
[48] F. Gerber, G. Waton, M. P. Krafft, and T. F. Vandamme, ‘Long Lived Microbubbles for Oxygen Delivery’, *Artif. Cells Blood Substit. Biotechnol.*, vol. 35, no. 1, pp. 119–124, 2009, doi: 10.1080/10731190600974939.
[49] C. McEwan *et al.*, ‘Oxygen carrying microbubbles for enhanced sonodynamic therapy of hypoxic tumours’, *J. Control. Release Off. J. Control. Release Soc.*, vol. 203, pp. 51–56, Apr. 2015, doi: 10.1016/j.jconrel.2015.02.004.
[50] C. Yang *et al.*, ‘Lipid Microbubbles as Ultrasound-Stimulated Oxygen Carriers for Controllable Oxygen Release for Tumor Reoxygenation’, *Ultrasound Med. Biol.*, vol. 44, no. 2, pp. 416–425, 2018, doi: 10.1016/j.ultrasmedbio.2017.08.1883.
[51] W. Zhu *et al.*, ‘Modulation of Hypoxia in Solid Tumor Microenvironment with MnO2 Nanoparticles to Enhance Photodynamic Therapy’, *Adv. Funct. Mater.*, vol. 26, no. 30, pp. 5490–5498, 2016, doi: 10.1002/adfm.201600676.
[52] J. Owen *et al.*, ‘Orally administered oxygen nanobubbles enhance tumor response to sonodynamic therapy’, *Nano Sel.*, p. nano.202100038, Jun. 2021, doi: 10.1002/nano.202100038.
[53] J. R. Eisenbrey *et al.*, ‘Sensitization of hypoxic tumors to radiation therapy using ultrasound sensitive oxygen microbubbles’, *Int. J. Radiat. Oncol.*, 2018, doi: 10.1016/j.ijrobp.2018.01.042.
[54] J. R. Eisenbrey *et al.*, ‘Development of an ultrasound sensitive oxygen carrier for oxygen delivery to hypoxic tissue’, *Int. J. Pharm.*, vol. 478, no. 1, pp. 361–367, 2015, doi: 10.1016/j.ijpharm.2014.11.023.
[55] M. Lakshman and A. Needles, ‘Screening and quantification of the tumor microenvironment with micro-ultrasound and photoacoustic imaging’, *Nat. Methods*, vol. 12, no. 4, pp. iii–v, 2015, doi: 10.1038/nmeth.f.381.
[56] A. Needles *et al.*, ‘Development of a combined photoacoustic micro-ultrasound system for estimating blood oxygenation’, *2010 IEEE Int. Ultrason. Symp.*, pp. 390–393, 2010, doi: 10.1109/ultsym.2010.5935920.
[57] M. Weiner, ‘Concepts of “tissue PO2” in relation to O2 delivery’, *Artif. Cells. Blood Substit. Immobil. Biotechnol.*, vol. 22, no. 3, pp. 763–768, 1994, doi: 10.3109/10731199409117909.
[58] A. L. Klibanov and S. Hu, ‘Monitoring Oxygenation Levels Deep in the Tumor Core: Noninvasive Imaging of Hypoxia, Now in Real-Time 3D’, *Cancer Res.*, vol. 79, no. 18, pp. 4577–4579, 2019, doi: 10.1158/0008-5472.CAN-19-2151.
[59] A. E. Greijer, ‘The role of hypoxia inducible factor 1 (HIF-1) in hypoxia induced apoptosis’, *J. Clin. Pathol.*, vol. 57, no. 10, pp. 1009–1014, Oct. 2004, doi: 10.1136/jcp.2003.015032.
[60] O. V. Razorenova and A. J. Giaccia, *Hypoxia, Gene Expression, and Metastasis*. doi: 10.1007/978-1-4419-6615-5_3.
[61] D. M. Brizel, G. S. Sibley, L. R. Prosnitz, R. L. Scher, and M. W. Dewhirst, ‘Tumor hypoxia adversely affects the prognosis of carcinoma of the head and neck’, *Int. J. Radiat. Oncol.*, vol. 38, no. 2, pp. 285–289, 1997, doi: 10.1016/s0360-3016(97)00101-6.
[62] A. Fyles *et al.*, ‘Long-term performance of interstial fluid pressure and hypoxia as prognostic factors in cervix cancer’, *Radiother. Oncol.*, vol. 80, no. 2, pp. 132–137, Aug. 2006, doi: 10.1016/j.radonc.2006.07.014.
[63] Q.-T. Le *et al.*, ‘An Evaluation of Tumor Oxygenation and Gene Expression in Patients with Early Stage Non–Small Cell Lung Cancers’, *Clin. Cancer Res.*, vol. 12, no. 5, pp. 1507–1514, Mar. 2006, doi: 10.1158/1078-0432.CCR-05-2049.
[64] C. Menon and D. L. Fraker, ‘Tumor oxygenation status as a prognostic marker’, *Cancer Lett.*, vol. 221, no. 2, pp. 225–235, Apr. 2005, doi: 10.1016/j.canlet.2004.06.029.
[65] A. Turaka, M. K. Buyyounouski, A. L. Hanlon, E. M. Horwitz, R. E. Greenberg, and B. Movsas, ‘Hypoxic Prostate/Muscle Po2 Ratio Predicts for Outcome in Patients With Localized Prostate Cancer: Long-Term Results’, *Int. J. Radiat. Oncol.*, vol. 82, no. 3, pp. e433–e439, Mar. 2012, doi: 10.1016/j.ijrobp.2011.05.037.

[66] P. Vaupel and A. Mayer, ‘Hypoxia in cancer: significance and impact on clinical outcome’, *Cancer Metastasis Rev.*, vol. 26, no. 2, pp. 225–239, Jul. 2007, doi: 10.1007/s10555-007-9055-1.
[67] S. B. Bader, M. W. Dewhirst, and E. M. Hammond, ‘Cyclic Hypoxia: An Update on Its Characteristics, Methods to Measure It and Biological Implications in Cancer’, *Cancers*, vol. 13, no. 1, p. 23, Dec. 2020, doi: 10.3390/cancers13010023.
[68] P. Bonnitcha, S. Grieve, and G. Figtree, ‘Clinical imaging of hypoxia: Current status and future directions’, *Free Radic. Biol. Med.*, vol. 126, pp. 296–312, 2018, doi: 10.1016/j.freeradbiomed.2018.08.019.
[69] F. Colliez, B. Gallez, and B. F. Jordan, ‘Assessing Tumor Oxygenation for Predicting Outcome in Radiation Oncology: A Review of Studies Correlating Tumor Hypoxic Status and Outcome in the Preclinical and Clinical Settings’, *Front. Oncol.*, vol. 7, p. 10, 2017, doi: 10.3389/fonc.2017.00010.
[70] R. A. D’Alonzo *et al.*, ‘In vivo noninvasive preclinical tumor hypoxia imaging methods: a review’, *Int. J. Radiat. Biol.*, pp. 1–39, Apr. 2021, doi: 10.1080/09553002.2021.1900943.
[71] E. M. Hammond, M.-C. C. Asselin, D. Forster, J. P. O’Connor, J. M. Senra, and K. J. Williams, ‘The meaning, measurement and modification of hypoxia in the laboratory and the clinic.’, *Clin. Oncol. R. Coll. Radiol. G. B.*, vol. 26, no. 5, pp. 277–88, 2014, doi: 10.1016/j.clon.2014.02.002.
[72] P. L. Olive, J. P. Banáth, and C. Aquino-Parsons, ‘Measuring Hypoxia in Solid Tumours&Is There a Gold Standard?’, *Acta Oncol.*, vol. 40, no. 8, pp. 917–923, 2001, doi: 10.1080/02841860152708189.
[73] J. A. Raleigh, M. W. Dewhirst, and D. E. Thrall, ‘Measuring tumor hypoxia’, *Semin. Radiat. Oncol.*, vol. 6, no. 1, pp. 37–45, 1996, doi: 10.1016/s1053-4296(96)80034-8.
[74] I. N. Fleming *et al.*, ‘Imaging tumour hypoxia with positron emission tomography’, *Br. J. Cancer*, vol. 112, no. 2, pp. 238–250, Jan. 2015, doi: 10.1038/bjc.2014.610.
[75] K. Wang, E. Yorke, S. A. Nehmeh, J. L. Humm, and C. C. Ling, ‘Modeling acute and chronic hypoxia using serial images of 18F-FMISO PET’, *Med. Phys.*, vol. 36, no. 10, pp. 4400–4408, Oct. 2009, doi: 10.1118/1.3213092.
[76] L. S. Mortensen *et al.*, ‘Accessing radiation response using hypoxia PET imaging and oxygen sensitive electrodes: A preclinical study’, *Radiother. Oncol.*, vol. 99, no. 3, pp. 418–423, 2011, doi: 10.1016/j.radonc.2011.06.034.
[77] J. C. Walsh, A. Lebedev, E. Aten, K. Madsen, L. Marciano, and H. C. Kolb, ‘The Clinical Importance of Assessing Tumor Hypoxia: Relationship of Tumor Hypoxia to Prognosis and Therapeutic Opportunities’, *Antioxid. Redox Signal.*, vol. 21, no. 10, pp. 1516–1554, Oct. 2014, doi: 10.1089/ars.2013.5378.
[78] S. Valable *et al.*, ‘Imaging of brain oxygenation with magnetic resonance imaging: A validation with positron emission tomography in the healthy and tumoural brain’, *J. Cereb. Blood Flow Metab.*, vol. 37, no. 7, pp. 2584–2597, Jul. 2017, doi: 10.1177/0271678X16671965.
[79] D. Paech *et al.*, ‘Quantitative Dynamic Oxygen 17 MRI at 7.0 T for the Cerebral Oxygen Metabolism in Glioma’, *Radiology*, vol. 295, no. 1, pp. 181–189, Apr. 2020, doi: 10.1148/radiol.2020191711.
[80] M. Gerling *et al.*, ‘Real-time assessment of tissue hypoxia in vivo with combined photoacoustics and high-frequency ultrasound.’, *Theranostics*, vol. 4, no. 6, pp. 604–13, 2014, doi: 10.7150/thno.7996.
[81] M. Chen *et al.*, ‘Simultaneous photoacoustic imaging of intravascular and tissue oxygenation’, *Opt. Lett.*, vol. 44, no. 15, p. 3773, 2019, doi: 10.1364/ol.44.003773.
[82] A. L. Bendinger, C. Glowa, J. Peter, and C. P. Karger, ‘Photoacoustic imaging to assess pixel-based sO2 distributions in experimental prostate tumors’, *J. Biomed. Opt.*, vol. 23, no. 3, p. 036009, Mar. 2018, doi: 10.1117/1.JBO.23.3.036009.
[83] S. Ogawa, T. Lee, A. S. Nayak, and P. Glynn, ‘Oxygenation-sensitive contrast in magnetic resonance image of rodent brain at high magnetic fields’, *Magn. Reson. Med.*, pp. 68–78, 1990, doi: 10.1002/mrm.1910140108.
[84] S. Ogawa, T. Lee, A. Kay, and D. Tank, ‘Brain magnetic resonance imaging with contrast dependent on blood oxygenation’, *Proc. Natl. Acad. Sci.*, pp. 9868–9872, 1990, doi: 10.1073/pnas.87.24.9868.
[85] E. Tadamura, H. Hatabu, W. Li, P. V. Prasad, and R. R. Edelman, ‘Effect of oxygen inhalation on relaxation times in various tissues’, *J. Magn. Reson. Imaging*, pp. 220–225, 1997, doi: 10.1002/jmri.1880070134.

[86] I. R. Young, G. J. Clarke, D. R. Baffles, J. M. Pennock, F. H. Doyle, and G. M. Bydder, 'Enhancement of relaxation rate with paramagnetic contrast agents in NMR imaging', *J. Comput. Tomogr.*, vol. 5, no. 6, pp. 543–547, 1981, doi: 10.1016/0149-936X(81)90089-8.
[87] K. Breuer *et al.*, 'Feasibility of 4D T2* quantification in the lung with oxygen gas challenge in patients with non-small cell lung cancer', *Phys. Med.*, vol. 72, pp. 46–51, 2020, doi: 10.1016/j.ejmp.2020.03.009.
[88] F. A. Howe, S. P. Robinson, D. J. O. McIntyre, M. Stubbs, and J. R. Griffiths, 'Issues in flow and oxygenation dependent contrast (FLOOD) imaging of tumours', *NMR Biomed.*, vol. 14, no. 7–8, pp. 497–506, 2001, doi: 10.1002/nbm.716.
[89] S. Chopra *et al.*, 'Comparing oxygen-sensitive MRI (BOLD R2*) with oxygen electrode measurements: A pilot study in men with prostate cancer', *Int. J. Radiat. Biol.*, vol. 85, no. 9, pp. 805–813, Jan. 2009, doi: 10.1080/09553000903043059.
[90] P. J. Hoskin *et al.*, 'Hypoxia in Prostate Cancer: Correlation of BOLD-MRI With Pimonidazole Immunohistochemistry—Initial Observations', *Int. J. Radiat. Oncol.*, vol. 68, no. 4, pp. 1065–1071, 2007, doi: 10.1016/j.ijrobp.2007.01.018.
[91] C. Baudelet and B. Gallez, 'How does blood oxygen level-dependent (BOLD) contrast correlate with oxygen partial pressure (pO2) inside tumors?', *Magn. Reson. Med.*, vol. 48, no. 6, pp. 980–986, 2002, doi: 10.1002/mrm.10318.
[92] R. R. Hallac *et al.*, 'Oxygenation in cervical cancer and normal uterine cervix assessed using blood oxygenation level-dependent (BOLD) MRI at 3T: OXYGEN-SENSITIVE MRI OF HUMAN CERVICAL CANCER', *NMR Biomed.*, vol. 25, no. 12, pp. 1321–1330, Dec. 2012, doi: 10.1002/nbm.2804.
[93] R. Alonzi *et al.*, 'Carbogen breathing increases prostate cancer oxygenation: a translational MRI study in murine xenografts and humans', *Br. J. Cancer*, vol. 100, no. 4, pp. 644–648, Feb. 2009, doi: 10.1038/sj.bjc.6604903.
[94] A. Müller *et al.*, 'Analysing the response in R2* relaxation rate of intracranial tumours to hyperoxic and hypercapnic respiratory challenges: initial results', *Eur. Radiol.*, vol. 21, no. 4, pp. 786–798, Apr. 2011, doi: 10.1007/s00330-010-1948-7.
[95] M. Rijpkema, J. H. A. M. Kaanders, F. B. M. Joosten, A. J. van der Kogel, and A. Heerschap, 'Effects of breathing a hyperoxic hypercapnic gas mixture on blood oxygenation and vascularity of head-and-neck tumors as measured by magnetic resonance imaging', *Int. J. Radiat. Oncol.*, vol. 53, no. 5, pp. 1185–1191, 2002, doi: 10.1016/s0360-3016(02)02825-0.
[96] N. P. Blockley, L. Jiang, A. G. Gardener, C. N. Ludman, S. T. Francis, and P. A. Gowland, 'Field strength dependence of R 1 and R2* relaxivities of human whole blood to prohance, vasovist, and deoxyhemoglobin', *Magn. Reson. Med.*, vol. 60, no. 6, pp. 1313–1320, 2008, doi: 10.1002/mrm.21792.
[97] J. S. Burrell *et al.*, 'Exploring ΔR(2) * and ΔR(1) as imaging biomarkers of tumor oxygenation.', *J. Magn. Reson. Imaging JMRI*, vol. 38, no. 2, pp. 429–34, 2013, doi: 10.1002/jmri.23987.
[98] D. A. White *et al.*, 'Developing oxygen-enhanced magnetic resonance imaging as a prognostic biomarker of radiation response.', *Cancer Lett.*, vol. 380, no. 1, pp. 69–77, 2016, doi: 10.1016/j.canlet.2016.06.003.
[99] M. M. Costa *et al.*, 'Quantitative photoacoustic imaging study of tumours in vivo: Baseline variations in quantitative measurements', *Photoacoustics*, vol. 13, pp. 53–65, 2019, doi: 10.1016/j.pacs.2018.12.002.
[100] K. Matsumoto *et al.*, 'MR assessment of changes of tumor in response to hyperbaric oxygen treatment.', *Magn. Reson. Med.*, vol. 56, no. 2, pp. 240–6, 2006, doi: 10.1002/mrm.20961.
[101] G. Chiarotti, G. Cristiani, and L. Giulotto, 'Proton relaxation in pure liquids and in liquids containing paramagnetic gases in solution', *Il Nuovo Cimento 1955-1965*, vol. 1, no. 5, pp. 863–873, 1955, doi: 10.1007/bf02731333.
[102] B. A. Berkowitz and C. A. Wilson, 'Quantitative Mapping of Ocular Oxygenation Using Magnetic Resonance Imaging', *Magn. Reson. Med.*, vol. 33, no. 4, pp. 579–581, Apr. 1995, doi: 10.1002/mrm.1910330419.
[103] E. R. Muir, Y. Zhang, O. S. E. Nateras, Q. Peng, and T. Q. Duong, 'Human Vitreous: MR Imaging of Oxygen Partial Pressure', *Radiology*, vol. 266, no. 3, pp. 905–911, 2013, doi: 10.1148/radiol.12120777.
[104] A. R. H. Simpson, N. G. Dowell, T. L. Jackson, P. S. Tofts, and E. H. Hughes, 'Measuring the Effect of Pars Plana Vitrectomy on Vitreous Oxygenation Using Magnetic Resonance ImagingEffects of PPV on pO2 Using MRI', *Invest. Ophthalmol. Vis. Sci.*, vol. 54, no. 3, pp. 2028–2034, 2013, doi: 10.1167/iovs.12-11258.

[105] G. Zaharchuk, R. F. Busse, G. Rosenthal, G. T. Manley, O. A. Glenn, and W. P. Dillon, 'Noninvasive Oxygen Partial Pressure Measurement of Human Body Fluids In Vivo Using Magnetic Resonance Imaging', *Acad. Radiol.*, vol. 13, no. 8, pp. 1016–1024, 2006, doi: 10.1016/j.acra.2006.04.016.
[106] Z. J. Wang, B. N. Joe, F. V. Coakley, G. Zaharchuk, R. Busse, and B. M. Yeh, 'Urinary Oxygen Tension Measurement in Humans Using Magnetic Resonance Imaging', *Acad. Radiol.*, vol. 15, no. 11, pp. 1467–1473, Nov. 2008, doi: 10.1016/j.acra.2008.04.013.
[107] G. Zaharchuk, A. J. Martin, G. Rosenthal, G. T. Manley, and W. P. Dillon, 'Measurement of cerebrospinal fluid oxygen partial pressure in humans using MRI', *Magn. Reson. Med.*, vol. 54, no. 1, pp. 113–121, 2005, doi: 10.1002/mrm.20546.
[108] D. T. Pilkinton, T. Hiraki, J. A. Detre, J. H. Greenberg, and R. Reddy, 'Absolute cerebral blood flow quantification with pulsed arterial spin labeling during hyperoxia corrected with the simultaneous measurement of the longitudinal relaxation time of arterial blood', *Magn. Reson. Med.*, vol. 67, no. 6, pp. 1556–1565, 2012, doi: 10.1002/mrm.23137.
[109] S. Portnoy, M. Seed, J. G. Sled, and C. K. Macgowan, 'Non-invasive evaluation of blood oxygen saturation and hematocrit from T1 and T2 relaxation times: In-vitro validation in fetal blood', *Magn. Reson. Med.*, vol. 78, no. 6, pp. 2352–2359, 2017, doi: 10.1002/mrm.26599.
[110] M. J. Silvennoinen, M. I. Kettunen, and R. A. Kauppinen, 'Effects of hematocrit and oxygen saturation level on blood spin-lattice relaxation', *Magn. Reson. Med.*, vol. 49, no. 3, pp. 568–571, 2003, doi: 10.1002/mrm.10370.
[111] A. P. Crawley and R. M. Henkelman, 'A comparison of one-shot and recovery methods in T1 imaging', *Magn. Reson. Med.*, vol. 7, no. 1, pp. 23–34, 1988, doi: 10.1002/mrm.1910070104.
[112] I. Kay and R. M. Henkelman, 'Practical Implementation and Optimization of One-shot T1 imaging', *Magn. Reson. Med.*, vol. 22, no. 2, pp. 414–424, 1991, doi: 10.1002/mrm.1910220249.
[113] D. R. Messroghli, A. Radjenovic, S. Kozerke, D. M. Higgins, M. U. Sivananthan, and J. P. Ridgway, 'Modified Look-Locker inversion recovery (MOLLI) for high-resolution T1 mapping of the heart', *Magn. Reson. Med.*, vol. 52, no. 1, pp. 141–146, Jul. 2004, doi: 10.1002/mrm.20110.
[114] S. K. Piechnik *et al.*, 'Shortened Modified Look-Locker Inversion recovery (ShMOLLI) for clinical myocardial T1-mapping at 1.5 and 3 T within a 9 heartbeat breathhold', *J. Cardiovasc. Magn. Reson. Off. J. Soc. Cardiovasc. Magn. Reson.*, vol. 12, p. 69, Nov. 2010, doi: 10.1186/1532-429X-12-69.
[115] H. Cheng and W.-G. in An, 'Rapid high-resolution T1 mapping by variable flip angles: Accurate and precise measurements in the presence of radiofrequency field inhomogeneity', 2006, doi: 10.1002/mrm.20791.
[116] G. Liberman, Y. Louzoun, and D. B. Bashat, 'T1 Mapping using variable flip angle SPGR data with flip angle correction', *J. Magn. Reson. Imaging*, vol. 40, no. 1, pp. 171–180, 2014, doi: 10.1002/jmri.24373.
[117] E. Fram, R. Herfkens, G. Johnson, and resonance … G.-G., 'Rapid calculation of T1 using variable flip angle gradient refocused imaging', 1987.
[118] N. Stikov, M. Boudreau, I. R. Levesque, C. L. Tardif, J. K. Barral, and B. G. Pike, 'On the accuracy of T1 mapping: Searching for common ground', *Magn. Reson. Med.*, vol. 73, pp. 514–522, 2015, doi: 10.1002/mrm.25135.
[119] A. Corroyer-Dulmont *et al.*, 'Imaging Modalities to Assess Oxygen Status in Glioblastoma.', *Front. Med.*, vol. 2, p. 57, 2015, doi: 10.3389/fmed.2015.00057.
[120] B. F. F. Jordan *et al.*, 'Mapping of oxygen by imaging lipids relaxation enhancement: a potential sensitive endogenous MRI contrast to map variations in tissue oxygenation.', *Magn. Reson. Med.*, vol. 70, no. 3, pp. 732–44, 2013, doi: 10.1002/mrm.24511.
[121] F. Colliez *et al.*, 'Oxygen Mapping within Healthy and Acutely Infarcted Brain Tissue in Humans Using the NMR Relaxation of Lipids: A Proof-Of-Concept Translational Study', *PloS One*, vol. 10, no. 8, p. e0135248, 2015, doi: 10.1371/journal.pone.0135248.
[122] F. Colliez, M. Neveu, J. Magat, T. Pham, and G.-B. Cancer …, 'Qualification of a noninvasive magnetic resonance imaging biomarker to assess tumor oxygenation', 2014, doi: 10.1158/1078-0432.CCR-13-3434.
[123] T.-T. Cao-Pham *et al.*, 'Combined endogenous MR biomarkers to assess changes in tumor oxygenation induced by an allosteric effector of hemoglobin.', *NMR Biomed.*, vol. 33, no. 2, p. e4181, 2019, doi: 10.1002/nbm.4181.
[124] J. P. B. O'Connor, A. Jackson, G. J. M. Parker, C. Roberts, and G. C. Jayson, 'Dynamic contrast-enhanced MRI in clinical trials of antivascular therapies.', *Nat. Rev. Clin. Oncol.*, vol. 9, no. 3, pp. 167–77, 2012, doi: 10.1038/nrclinonc.2012.2.

[125] P. S. Tofts *et al.*, ‘Estimating kinetic parameters from dynamic contrast-enhanced T(1)-weighted MRI of a diffusable tracer: standardized quantities and symbols’, *J. Magn. Reson. Imaging JMRI*, vol. 10, no. 3, pp. 223–232, Sep. 1999, doi: 10.1002/(sici)1522-2586(199909)10:3<223::aid-jmri2>3.0.co;2-s.
[126] T. A. M. Egeland, T. G. Simonsen, J.-V. Gaustad, K. Gulliksrud, C. Ellingsen, and E. K. Rofstad, ‘Dynamic contrast-enhanced magnetic resonance imaging of tumors: preclinical validation of parametric images.’, *Radiat. Res.*, vol. 172, no. 3, pp. 339–47, 2009, doi: 10.1667/rr1787.1.
[127] S. Liu *et al.*, ‘Quantitative tissue oxygen measurement in multiple organs using 19F MRI in a rat model’, *Magn. Reson. Med.*, vol. 66, no. 6, pp. 1722–1730, 2011, doi: 10.1002/mrm.22968.
[128] R. P. Mason, S. Ran, and P. E. Thorpe, ‘Quantitative assessment of tumor oxygen dynamics: Molecular imaging for prognostic radiology’, *J. Cell. Biochem.*, vol. 87, no. S39, pp. 45–53, 2002, doi: 10.1002/jcb.10404.
[129] V. D. Kodibagkar, X. Wang, and R. P. Mason, ‘Physical principles of quantitative nuclear magnetic resonance oximetry’, *Front. Biosci.*, vol. 13, no. 13, p. 1371, 2008, doi: 10.2741/2768.
[130] K. R. Thulborn and I. C. Atkinson, ‘Chapter 4.1 - Quantitative Metabolic Magnetic Resonance Imaging of Sodium, Oxygen, Phosphorus and Potassium in the Human Brain: A Rationale for Bioscales in Clinical Applications’, in *Magnetic Resonance Spectroscopy*, C. Stagg and D. Rothman, Eds. San Diego: Academic Press, 2014, pp. 291–311. doi: 10.1016/B978-0-12-401688-0.00022-7.
[131] J. Pekar, T. Sinnwell, L. Ligeti, A. S. Chesnick, J. A. Frank, and A. C. McLaughlin, ‘Simultaneous Measurement of Cerebral Oxygen Consumption and Blood Flow Using 17O and 19F Magnetic Resonance Imaging’, *J. Cereb. Blood Flow Metab.*, vol. 15, no. 2, pp. 312–320, Mar. 1995, doi: 10.1038/jcbfm.1995.36.
[132] A. C. McLaughlin and J. S. Leigh, ‘Relaxation times in systems with chemical exchange: Approximate solutions for the nondilute case’, *J. Magn. Reson. 1969*, vol. 9, no. 2, pp. 296–304, Feb. 1973, doi: 10.1016/0022-2364(73)90046-2.
[133] I. C. Atkinson, R. Sonstegaard, N. H. Pliskin, and K. R. Thulborn, ‘Vital signs and cognitive function are not affected by 23-sodium and 17-oxygen magnetic resonance imaging of the human brain at 9.4 T’, *J. Magn. Reson. Imaging JMRI*, vol. 32, no. 1, pp. 82–87, Jul. 2010, doi: 10.1002/jmri.22221.
[134] B. Gallez, C. Baudelet, and B. F. Jordan, ‘Assessment of tumor oxygenation by electron paramagnetic resonance: principles and applications’, *NMR Biomed.*, vol. 17, no. 5, pp. 240–262, Aug. 2004, doi: 10.1002/nbm.900.
[135] I. Gertsenshteyn, M. Giurcanu, P. Vaupel, and H. Halpern, ‘Biological validation of electron paramagnetic resonance (EPR) image oxygen thresholds in tissue’, *J. Physiol.*, vol. 599, no. 6, pp. 1759–1767, Mar. 2021, doi: 10.1113/JP278816.
[136] J. R. Biller *et al.*, ‘Relaxation times and line widths of isotopically-substituted nitroxides in aqueous solution at X-band’, *J. Magn. Reson. San Diego Calif 1997*, vol. 212, no. 2, pp. 370–377, Oct. 2011, doi: 10.1016/j.jmr.2011.07.018.
[137] A. Matsumoto *et al.*, ‘Absolute oxygen tension (pO2) in murine fatty and muscle tissue as determined by EPR’, *Magn. Reson. Med.*, vol. 54, no. 6, pp. 1530–1535, 2005, doi: 10.1002/mrm.20714.
[138] B. Epel, M. Maggio, C. Pelizzari, and H. J. Halpern, ‘Electron Paramagnetic Resonance pO2 Image Tumor Oxygen-Guided Radiation Therapy Optimization.’, *Adv. Exp. Med. Biol.*, vol. 977, pp. 287–296, 2017, doi: 10.1007/978-3-319-55231-6_39.
[139] M. Šentjurc, M. Čemažar, and G. Serša, ‘EPR oximetry of tumors in vivo in cancer therapy’, *Spectrochim. Acta. A. Mol. Biomol. Spectrosc.*, vol. 60, no. 6, pp. 1379–1385, May 2004, doi: 10.1016/j.saa.2003.10.036.
[140] H. M. Swartz, ‘Using EPR to Measure a Critical but Often Unmeasured Component of Oxidative Damage: Oxygen’, *Antioxid. Redox Signal.*, vol. 6, no. 3, pp. 677–686, Jun. 2004, doi: 10.1089/152308604773934440.
[141] M. C. Krishna *et al.*, ‘Electron Paramagnetic Resonance Imaging of Tumor pO2’, *Radiat. Res.*, vol. 177, no. 4, pp. 376–386, Mar. 2012, doi: 10.1667/RR2622.1.
[142] K. L. Desmond and S. E. Chavez, ‘Editorial for “Effect of Drinking Oxygenated Water Assessed by in vivo MRI Relaxometry”’, *J. Magn. Reson. Imaging*, vol. 52, no. 3, pp. 729–730, 2020, doi: 10.1002/jmri.27239.
[143] S. A. S. Vatnehol, P. K. Hol, A. Bjørnerud, M. Amiry-Moghaddam, C. Haglerød, and T. H. Storås, ‘Effect of Drinking Oxygenated Water Assessed by in vivo MRI Relaxometry’, *J. Magn. Reson. Imaging*, vol. 52, no. 3, pp. 720–728, 2020, doi: 10.1002/jmri.27104.

[144] D. M. Yang, T. J. Arai, J. W. Campbell, J. L. Gerberich, H. Zhou, and R. P. Mason, 'Oxygen-sensitive MRI assessment of tumor response to hypoxic gas breathing challenge', *NMR Biomed.*, vol. 32, no. 7, p. e4101, 2019, doi: 10.1002/nbm.4101.
[145] N. Bloembergen, 'Proton Relaxation Times in Paramagnetic Solutions', *J. Chem. Phys.*, vol. 27, no. 2, pp. 572–573, Aug. 1957, doi: 10.1063/1.1743771.
[146] N. A. Mel'nichenko, 'The solubility of oxygen in sea water and solutions of electrolytes according to the pulse proton NMR data', *Russ. J. Phys. Chem. A*, vol. 82, no. 9, pp. 1533–1539, Sep. 2008, doi: 10.1134/S0036024408090239.
[147] M. E. Mirhej, 'PROTON SPIN RELAXATION BY PARAMAGNETIC MOLECULAR OXYGEN', *Can. J. Chem.*, vol. 43, no. 5, pp. 1130–1138, 1965, doi: 10.1139/v65-150.
[148] D. S. Parker and J. F. Harmon, 'Dipolar spin-lattice relaxation in water containing oxygen', *Chem. Phys. Lett.*, vol. 25, no. 4, pp. 505–506, Apr. 1974, doi: 10.1016/0009-2614(74)85353-4.
[149] I. Solomon, 'Relaxation Processes in a System of Two Spins', *Phys. Rev.*, vol. 99, no. 2, pp. 559–565, Jul. 1955, doi: 10.1103/PhysRev.99.559.
[150] H. C. Torrey, 'Nuclear Spin Relaxation by Translational Diffusion', *Phys. Rev.*, vol. 92, no. 4, pp. 962–969, Nov. 1953, doi: 10.1103/PhysRev.92.962.
[151] B. A. Berkowitz, 'Role of dissolved plasma oxygen in hyperoxia-induced contrast', *Magn. Reson. Imaging*, vol. 15, no. 1, pp. 123–126, 1997, doi: 10.1016/s0730-725x(96)00230-5.
[152] B. J. d'Othée, G. Rachmuth, J. Munasinghe, and E. V. Lang, 'The effect of hyperoxygenation on T1 relaxation time in vitro1', *Acad. Radiol.*, vol. 10, no. 8, pp. 854–860, 2003, doi: 10.1016/s1076-6332(03)00004-7.
[153] R. Hausser and F. Noack, 'Kernmagnetische Relaxation und Korrelation im System Wasser - Sauerstoff', *Z. Für Naturforschung A*, vol. 20, no. 12, pp. 1668–1675, Dec. 1965, doi: 10.1515/zna-1965-1220.
[154] P. Hueckel, W. Schreiber, K. Markstaller, M. Bellemann, H.-U. Kauczor, and M. Thelen, 'Effect of partial oxygen pressure and hematocrit on T1 relaxation in human blood', *Proc. Int. Soc. Magn. Reson. Med.*, p. 1586, 2000.
[155] H. Kramer, A. Corcos, D. Hernando, J. Berry, M. Schiebler, and S. Reeder, 'Effekt von molekularem Sauerstoff auf Relaxationszeiten bei klinischen Feldstärken', *RöFo - Fortschritte Auf Dem Geb. Röntgenstrahlen Bildgeb. Verfahr.*, vol. 185, no. S 01, p. s-0033-1346217, Apr. 2013, doi: 10.1055/s-0033-1346217.
[156] S. A. S. Vatnehol, P. K. Hol, A. Bjørnerud, M. Amiry-Moghaddam, C. Haglerød, and T. H. Storås, 'Determination of oxygen r1 at 3 Tesla using samples with a concentration range of dissolved oxygen', *Magn. Reson. Mater. Phys. Biol. Med.*, vol. 33, no. 3, pp. 447–453, 2020, doi: 10.1007/s10334-019-00783-x.
[157] S. C. Beeman, Y.-B. B. Shui, C. J. Perez-Torres, J. A. Engelbach, J. J. Ackerman, and J. R. Garbow, 'O2 -sensitive MRI distinguishes brain tumor versus radiation necrosis in murine models.', *Magn. Reson. Med.*, vol. 75, no. 6, pp. 2442–7, 2016, doi: 10.1002/mrm.25821.
[158] B. Haddock, H. B. W. Larsson, A. E. Hansen, and E. Rostrup, 'Measurement of brain oxygenation changes using dynamic T1-weighted imaging', *NeuroImage*, vol. 78, pp. 7–15, Sep. 2013, doi: 10.1016/j.neuroimage.2013.03.068.
[159] E. Moser, E. Winklmayr, P. Holzmüller, and M. Krssak, 'Temperature- and pH-dependence of proton relaxation rates in rat liver tissue', *Magn. Reson. Imaging*, vol. 13, no. 3, pp. 429–440, Jan. 1995, doi: 10.1016/0730-725X(94)00135-P.
[160] W. D. Rooney *et al.*, 'Magnetic field and tissue dependencies of human brain longitudinal1H2O relaxation in vivo', *Magn. Reson. Med.*, vol. 57, no. 2, pp. 308–318, Feb. 2007, doi: 10.1002/mrm.21122.
[161] E. Kaldoudi and S. C. R. Williams, 'Relaxation time measurements in NMR imaging. Part I: Longitudinal relaxation time', *Concepts Magn. Reson.*, vol. 5, no. 3, pp. 217–242, Jul. 1993, doi: 10.1002/cmr.1820050303.
[162] E. Thompson, S. Smart, P. Kinchesh, D. Bulte, and E. Stride, 'Magnetic resonance imaging of oxygen microbubbles', *Healthc. Technol. Lett.*, vol. 6, no. 5, pp. 138–142, 2019, doi: 10.1049/htl.2018.5058.
[163] J. Z. Bojorquez, S. Bricq, C. Acquitter, F. Brunotte, P. M. Walker, and A. Lalande, 'What are normal relaxation times of tissues at 3 T?', *Magn. Reson. Imaging*, vol. 35, pp. 69–80, Jan. 2017, doi: 10.1016/j.mri.2016.08.021.
[164] V. L. Yarnykh, 'Actual flip-angle imaging in the pulsed steady state: A method for rapid three-dimensional mapping of the transmitted radiofrequency field', *Magn. Reson. Med.*, vol. 57, no. 1, pp. 192–200, 2006, doi: 10.1002/mrm.21120.

[165] P. Kellman and M. S. Hansen, ‘T1-mapping in the heart: accuracy and precision’, *J. Cardiovasc. Magn. Reson.*, vol. 16, no. 1, p. 2, Jan. 2014, doi: 10.1186/1532-429X-16-2.
[166] A. Shrivastava, ‘Methods for the determination of limit of detection and limit of quantitation of the analytical methods’, *Chron. Young Sci.*, vol. 2, pp. 21–25, Jun. 2011, doi: 10.4103/2229-5186.79345.
[167] J. P. O’Connor *et al.*, ‘Preliminary study of oxygen-enhanced longitudinal relaxation in MRI: a potential novel biomarker of oxygenation changes in solid tumors.’, *Int. J. Radiat. Oncol. Biol. Phys.*, vol. 75, no. 4, pp. 1209–15, 2009, doi: 10.1016/j.ijrobp.2008.12.040.
[168] Q. Zhang *et al.*, ‘Quality assurance of quantitative cardiac T1-mapping in multicenter clinical trials – A T1 phantom program from the hypertrophic cardiomyopathy registry (HCMR) study’, *Int. J. Cardiol.*, vol. 330, pp. 251–258, May 2021, doi: 10.1016/j.ijcard.2021.01.026.
[169] E. Bluemke, E. Stride, and D. Bulte, ‘A simplified empirical model to estimate oxygen relaxivity at different magnetic fields.’, *NMR Biomed.*, 2021, doi: 10.1002/nbm.4625.
[170] A. E. Campbell-Washburn *et al.*, ‘Opportunities in Interventional and Diagnostic Imaging by Using High-performance Low-Field-Strength MRI’, *Radiology*, vol. 293, no. 2, pp. 384–393, 2019, doi: 10.1148/radiol.2019190452.
[171] C. L. Teng, H. Hong, S. Kiihne, and R. G. Bryant, ‘Molecular oxygen spin-lattice relaxation in solutions measured by proton magnetic relaxation dispersion’, *J. Magn. Reson. San Diego Calif 1997*, vol. 148, no. 1, pp. 31–34, Jan. 2001, doi: 10.1006/jmre.2000.2219.
[172] N. D. and M. Singh, ‘Sample Size Calculator for Comparing Paired Differences’. https://statulator.com/SampleSize/ss2PM.html# (accessed Oct. 04, 2021).
[173] X.-L. Qi, P. Burns, J. Hong, J. Stainsby, and G. Wright, ‘Characterizing blood volume fraction (BVF) in a VX2 tumor’, *Magn. Reson. Imaging*, vol. 26, no. 2, pp. 206–214, Feb. 2008, doi: 10.1016/j.mri.2007.05.010.
[174] S. D. Rane and J. C. Gore, ‘Measurement of T1 of human arterial and venous blood at 7T’, *Magn. Reson. Imaging*, vol. 31, no. 3, pp. 477–479, 2013, doi: 10.1016/j.mri.2012.08.008.
[175] R. A. Brooks, J. H. Battocletti, A. Sances, S. J. Larson, R. L. Bowman, and V. Kudravcev, ‘Nuclear Magnetic Relaxation in Blood’, *IEEE Trans. Biomed. Eng.*, vol. BME-22, no. 1, pp. 12–18, 1975, doi: 10.1109/tbme.1975.324533.
[176] N. Nestle, T. Baumann, and R. Niessner, ‘Oxygen determination in oxygen-supersaturated drinking waters by NMR relaxometry’, *Water Res.*, vol. 37, no. 14, pp. 3361–3366, Aug. 2003, doi: 10.1016/S0043-1354(03)00211-2.
[177] M. W. Dewhirst and S. R. Birer, ‘Oxygen-Enhanced MRI Is a Major Advance in Tumor Hypoxia Imaging.’, *Cancer Res.*, vol. 76, no. 4, pp. 769–72, 2016, doi: 10.1158/0008-5472.can-15-2818.
[178] R. A. Little *et al.*, ‘Mapping Hypoxia in Renal Carcinoma with Oxygen-enhanced MRI: Comparison with Intrinsic Susceptibility MRI and Pathology.’, *Radiology*, vol. 288, no. 3, pp. 739–747, 2018, doi: 10.1148/radiol.2018171531.
[179] J. P. B. O’Connor, S. P. Robinson, and J. C. Waterton, ‘Imaging tumour hypoxia with oxygen-enhanced MRI and BOLD MRI.’, *Br. J. Radiol.*, vol. 92, no. 1095, p. 20180642, 2019, doi: 10.1259/bjr.20180642.
[180] ‘WebPlotDigitizer - Extract data from plots, images, and maps’. https://automeris.io/WebPlotDigitizer/citation.html (accessed Jun. 29, 2021).
[181] P. Virtanen *et al.*, ‘SciPy 1.0: fundamental algorithms for scientific computing in Python’, *Nat. Methods*, vol. 17, no. 3, pp. 261–272, Mar. 2020, doi: 10.1038/s41592-019-0686-2.
[182] F. Pedregosa *et al.*, ‘Scikit-learn: Machine Learning in Python’, *J. Mach. Learn. Res.*, vol. 12, no. 85, pp. 2825–2830, 2011.
[183] V. Graf, F. Noack, and G. J. Béné, ‘Proton spin T 1 relaxation dispersion in liquid H 2 O by slow proton-exchange’, *J. Chem. Phys.*, vol. 72, no. 2, pp. 861–863, 1980, doi: 10.1063/1.439240.
[184] A. Tripathi *et al.*, ‘Effect of Oxygen Tension on NMR Spin-Lattice Relaxation Rate of Blood in vivo’, *Invest. Radiol.*, vol. 19, no. 3, pp. 174–178, 1984, doi: 10.1097/00004424-198405000-00004.
[185] H. Bozdogan, ‘Model selection and Akaike’s Information Criterion (AIC): The general theory and its analytical extensions’, *Psychometrika*, vol. 52, no. 3, pp. 345–370, Sep. 1987, doi: 10.1007/BF02294361.
[186] M. Rohrer, H. Bauer, J. Mintorovitch, M. Requardt, and H.-J. Weinmann, ‘Comparison of Magnetic Properties of MRI Contrast Media Solutions at Different Magnetic Field Strengths’, *Invest. Radiol.*, vol. 40, no. 11, pp. 715–724, 2005, doi: 10.1097/01.rli.0000184756.66360.d3.
[187] C.-Y. Chou *et al.*, ‘Ultra-wide range field-dependent measurements of the relaxivity of Gd1-xEuxVO4 nanoparticle contrast agents using a mechanical sample-shuttling relaxometer’, *Sci. Rep.*, vol. 7, p. 44770, Mar. 2017, doi: 10.1038/srep44770.

[188] H. W. Fischer, P. A. Rinck, Y. van Haverbeke, and R. N. Muller, 'Nuclear relaxation of human brain gray and white matter: Analysis of field dependence and implications for MRI', *Magn. Reson. Med.*, vol. 16, no. 2, pp. 317–334, Nov. 1990, doi: 10.1002/mrm.1910160212.
[189] J. E. Kirsch, 'Basic principles of magnetic resonance contrast agents', *Top. Magn. Reson. Imaging TMRI*, vol. 3, no. 2, pp. 1–18, Mar. 1991.
[190] S. H. Koenig, C. Baglin, R. D. Brown, and C. Fred Brewer, 'Magnetic field dependence of solvent proton relaxation induced by Gd3+ and Mn2+ complexes', *Magn. Reson. Med.*, vol. 1, no. 4, pp. 496–501, Dec. 1984, doi: 10.1002/mrm.1910010408.
[191] A. D. Elster, 'How much contrast is enough? Dependence of enhancement on field strength and MR pulse sequence: Dependence of enhancement on field strength and MR pulse sequence', *Eur. Radiol.*, vol. 7, no. S5, pp. S276–S280, Nov. 1997, doi: 10.1007/PL00006908.
[192] P. W. Hales, F. J. Kirkham, and C. A. Clark, 'A general model to calculate the spin-lattice (T1) relaxation time of blood, accounting for haematocrit, oxygen saturation and magnetic field strength', *J. Cereb. Blood Flow Metab. Off. J. Int. Soc. Cereb. Blood Flow Metab.*, vol. 36, no. 2, pp. 370–374, Feb. 2016, doi: 10.1177/0271678X15605856.
[193] Y. Wang, P. van Gelderen, J. A. de Zwart, and J. H. Duyn, 'B0-field dependence of MRI T1 relaxation in human brain', *NeuroImage*, vol. 213, p. 116700, 2020, doi: 10.1016/j.neuroimage.2020.116700.
[194] J. P. Marques, F. F. J. Simonis, and A. G. Webb, 'Low-field MRI: An MR physics perspective', *J. Magn. Reson. Imaging*, vol. 49, no. 6, pp. 1528–1542, 2019, doi: 10.1002/jmri.26637.
[195] M. Sarracanie and N. Salameh, 'Low-Field MRI: How Low Can We Go? A Fresh View on an Old Debate', *Front. Phys.*, vol. 8, p. 172, 2020, doi: 10.3389/fphy.2020.00172.
[196] G. E. Hagberg and K. Scheffler, 'Effect of $r_1$ and $r_2$ relaxivity of gadolinium-based contrast agents on the $T_1$-weighted MR signal at increasing magnetic field strengths: High-field contrast enhanced MRI', *Contrast Media Mol. Imaging*, vol. 8, no. 6, pp. 456–465, Nov. 2013, doi: 10.1002/cmmi.1565.
[197] P. A. Bottomley, T. H. Foster, R. E. Argersinger, and L. M. Pfeifer, 'A review of normal tissue hydrogen NMR relaxation times and relaxation mechanisms from 1-100 MHz: dependence on tissue type, NMR frequency, temperature, species, excision, and age', *Med. Phys.*, vol. 11, no. 4, pp. 425–448, Aug. 1984, doi: 10.1118/1.595535.
[198] P. A. Rinck and R. N. Muller, 'Field strength and dose dependence of contrast enhancement by gadolinium-based MR contrast agents', *Eur. Radiol.*, vol. 9, no. 5, pp. 998–1004, May 1999, doi: 10.1007/s003300050781.
[199] A. K. Featherstone *et al.*, 'Data-driven mapping of hypoxia-related tumor heterogeneity using DCE-MRI and OE-MRI.', *Magn. Reson. Med.*, vol. 79, no. 4, pp. 2236–2245, 2017, doi: 10.1002/mrm.26860.
[200] I. V. Linnik *et al.*, 'Noninvasive tumor hypoxia measurement using magnetic resonance imaging in murine U87 glioma xenografts and in patients with glioblastoma.', *Magn. Reson. Med.*, vol. 71, no. 5, pp. 1854–62, 2014, doi: 10.1002/mrm.24826.
[201] S. Remmele *et al.*, 'Dynamic and simultaneous MR measurement of R1 and R2* changes during respiratory challenges for the assessment of blood and tissue oxygenation.', *Magn. Reson. Med.*, vol. 70, no. 1, pp. 136–46, 2013, doi: 10.1002/mrm.24458.
[202] K. Grgac, P. C. M. Zijl, and Q. Qin, 'Hematocrit and oxygenation dependence of blood 1H2O T1 at 7 tesla', *Magn. Reson. Med.*, vol. 70, no. 4, pp. 1153–1159, 2013, doi: 10.1002/mrm.24547.
[203] J. R. Zimmerman and W. E. Brittin, 'Nuclear Magnetic Resonance Studies in Multiple Phase Systems: Lifetime of a Water Molecule in an Adsorbing Phase on Silica Gel', *J. Phys. Chem.*, vol. 61, no. 10, pp. 1328–1333, Oct. 1957, doi: 10.1021/j150556a015.
[204] W. Li, K. Grgac, A. Huang, N. Yadav, Q. Qin, and P. C. M. van Zijl, 'Quantitative theory for the longitudinal relaxation time of blood water', *Magn. Reson. Med.*, vol. 76, no. 1, pp. 270–281, Jul. 2016, doi: 10.1002/mrm.25875.
[205] D. Goldman, 'Theoretical models of microvascular oxygen transport to tissue', *Microcirc. N. Y. N 1994*, vol. 15, no. 8, pp. 795–811, Nov. 2008, doi: 10.1080/10739680801938289.
[206] Z. Chu *et al.*, 'The $P_{50}$ value detected by the oxygenation-dissociation analyser and blood gas analyser', *Artif. Cells Nanomedicine Biotechnol.*, vol. 48, no. 1, pp. 867–874, Jan. 2020, doi: 10.1080/21691401.2020.1770272.
[207] S. Kindvall, 'Pulmonary imaging with quantification of T1-relaxation and oxygen enhanced MRI', Lund University: Faculty of Medicine, 2018. Accessed: May 21, 2021. [Online]. Available: https://lucris.lub.lu.se/ws/portalfiles/portal/54271318/Simon_e_spik_ex.pdf

[208] M. C. Dobre, K. Uğurbil, and M. Marjanska, ‘Determination of blood longitudinal relaxation time (T1) at high magnetic field strengths’, *Magn. Reson. Imaging*, vol. 25, no. 5, pp. 733–735, Jun. 2007, doi: 10.1016/j.mri.2006.10.020.
[209] H. Lu, C. Clingman, X. Golay, and P. C. M. van Zijl, ‘Determining the longitudinal relaxation time (T1) of blood at 3.0 Tesla’, *Magn. Reson. Med.*, vol. 52, no. 3, pp. 679–682, Sep. 2004, doi: 10.1002/mrm.20178.
[210] B. Stefanovic and G. B. Pike, ‘Human whole-blood relaxometry at 1.5 T: Assessment of diffusion and exchange models’, *Magn. Reson. Med.*, vol. 52, no. 4, pp. 716–723, Oct. 2004, doi: 10.1002/mrm.20218.
[211] J. P. B. O’Connor *et al.*, ‘Organ-specific effects of oxygen and carbogen gas inhalation on tissue longitudinal relaxation times’, *Magn. Reson. Med.*, vol. 58, no. 3, pp. 490–496, 2007, doi: 10.1002/mrm.21357.
[212] S. S. I. Kindvall, S. Diaz, J. Svensson, P. Wollmer, and L. E. Olsson, ‘The change of longitudinal relaxation rate in oxygen enhanced pulmonary MRI depends on age and BMI but not diffusing capacity of carbon monoxide in healthy never-smokers’, *PloS One*, vol. 12, no. 5, p. e0177670, 2017, doi: 10.1371/journal.pone.0177670.
[213] K. Holliday, ‘Oxygen-enhanced MRI in cancer’, The University of Manchester, 2013. Accessed: Aug. 13, 2021. [Online]. Available: https://www.research.manchester.ac.uk/portal/files/54548076/FULL_TEXT.PDF
[214] M. Welter, T. Fredrich, H. Rinneberg, and H. Rieger, ‘Computational Model for Tumor Oxygenation Applied to Clinical Data on Breast Tumor Hemoglobin Concentrations Suggests Vascular Dilatation and Compression’, *PLOS ONE*, vol. 11, no. 8, p. e0161267, Aug. 2016, doi: 10.1371/journal.pone.0161267.
[215] A. Gjedde, P. Johannsen, G. E. Cold, and L. Østergaard, ‘Cerebral Metabolic Response to Low Blood Flow: Possible Role of Cytochrome Oxidase Inhibition’, *J. Cereb. Blood Flow Metab.*, vol. 25, no. 9, pp. 1183–1196, Sep. 2005, doi: 10.1038/sj.jcbfm.9600113.
[216] P. Rasmussen, E. A. Dawson, L. Nybo, J. J. van Lieshout, N. H. Secher, and A. Gjedde, ‘Capillary-Oxygenation-Level-Dependent Near-Infrared Spectrometry in Frontal Lobe of Humans’, *J. Cereb. Blood Flow Metab.*, vol. 27, no. 5, pp. 1082–1093, May 2007, doi: 10.1038/sj.jcbfm.9600416.
[217] S. S. Kety, ‘Determinants of tissue oxygen tension’, *Fed. Proc.*, vol. 16, no. 3, pp. 666–671, Sep. 1957.
[218] P. Rasmussen *et al.*, ‘Reduced muscle activation during exercise related to brain oxygenation and metabolism in humans: Central fatigue *versus* brain oxygenation and metabolism’, *J. Physiol.*, vol. 588, no. 11, pp. 1985–1995, Jun. 2010, doi: 10.1113/jphysiol.2009.186767.
[219] J. Cho, J. Lee, H. An, M. S. Goyal, Y. Su, and Y. Wang, ‘Cerebral oxygen extraction fraction (OEF): Comparison of challenge-free gradient echo QSM+qBOLD (QQ) with 15O PET in healthy adults’, *J. Cereb. Blood Flow Metab.*, vol. 41, no. 7, pp. 1658–1668, Jul. 2021, doi: 10.1177/0271678X20973951.
[220] K. L. Leenders *et al.*, ‘CEREBRAL BLOOD FLOW, BLOOD VOLUME AND OXYGEN UTILIZATION: NORMAL VALUES AND EFFECT OF AGE’, *Brain*, vol. 113, no. 1, pp. 27–47, 1990, doi: 10.1093/brain/113.1.27.
[221] C. R. Honig and T. E. Gayeski, ‘Resistance to O2 diffusion in anemic red muscle: roles of flux density and cell PO2’, *Am. J. Physiol.-Heart Circ. Physiol.*, vol. 265, no. 3, pp. H868–H875, Sep. 1993, doi: 10.1152/ajpheart.1993.265.3.H868.
[222] T. K. Nguyen, ‘Mass Transfer, Ch 1-6, CHE313’, Chemical and Material Engineering Department, California State Polytechnic University, 2012, pp. 51–60. [Online]. Available: https://www.cpp.edu/~tknguyen/
[223] B. J. McGuire and T. W. Secomb, ‘A theoretical model for oxygen transport in skeletal muscle under conditions of high oxygen demand’, *J. Appl. Physiol.*, vol. 91, no. 5, pp. 2255–2265, 2001, doi: 10.1152/jappl.2001.91.5.2255.
[224] K. C. Afas, R. Vijay, and D. Goldman, ‘A two-compartment model of oxygen transport in skeletal muscle using continuously distributed capillaries’, *Math. Biosci.*, vol. 333, p. 108535, Mar. 2021, doi: 10.1016/j.mbs.2020.108535.
[225] T. E. Moschandreou, C. G. Ellis, and D. Goldman, ‘Influence of tissue metabolism and capillary oxygen supply on arteriolar oxygen transport: A computational model’, *Math. Biosci.*, vol. 232, no. 1, pp. 1–10, Jul. 2011, doi: 10.1016/j.mbs.2011.03.010.
[226] J. R. Less, T. C. Skalak, E. M. Sevick, and R. K. Jain, ‘Microvascular Architecture in a Mammary Carcinoma: Branching Patterns and Vessel Dimensions’, p. 10.

[227] K. P. Ivanov, M. K. Kalinina, and Yu. I. Levkovich, ‘Blood flow velocity in capillaries of brain and muscles and its physiological significance’, *Microvasc. Res.*, vol. 22, no. 2, pp. 143–155, Sep. 1981, doi: 10.1016/0026-2862(81)90084-4.
[228] J. D. Winter, M. K. Akens, and H.-L. M. L. Cheng, ‘Quantitative MRI assessment of VX2 tumour oxygenation changes in response to hyperoxia and hypercapnia.’, *Phys. Med. Biol.*, vol. 56, no. 5, pp. 1225–42, 2011, doi: 10.1088/0031-9155/56/5/001.
[229] A. A. Bhogal, J. C. Siero, J. Zwanenburg, P. R. Luijten, M. E. Philippens, and H. Hoogduin, ‘Quantitative T1 mapping under precisely controlled graded hyperoxia at 7T’, *J. Cereb. Blood Flow Metab. Off. J. Int. Soc. Cereb. Blood Flow Metab.*, vol. 37, no. 4, pp. 1461–1469, Apr. 2017, doi: 10.1177/0271678X16656864.
[230] H. Lu and Y. Ge, ‘Quantitative evaluation of oxygenation in venous vessels using T2-Relaxation-Under-Spin-Tagging MRI’, *Magn. Reson. Med.*, vol. 60, no. 2, pp. 357–363, Aug. 2008, doi: 10.1002/mrm.21627.
[231] A. P. Fan, T. Benner, D. S. Bolar, B. R. Rosen, and E. Adalsteinsson, ‘Phase-based Regional Oxygen Metabolism (PROM) using MRI’, *Magn. Reson. Med.*, vol. 67, no. 3, pp. 669–678, Mar. 2012, doi: 10.1002/mrm.23050.
[232] F. Carinci *et al.*, ‘Blood volume fraction imaging of the human lung using intravoxel incoherent motion’, *J. Magn. Reson. Imaging JMRI*, vol. 41, no. 5, pp. 1454–1464, May 2015, doi: 10.1002/jmri.24669.
[233] R. Fåhræus and T. Lindqvist, ‘The viscosity of the blood in narrow capillary tubes’, *Am. J. Physiol.-Leg. Content*, vol. 96, no. 3, pp. 562–568, Mar. 1931, doi: 10.1152/ajplegacy.1931.96.3.562.
[234] R. Chebbi, ‘Dynamics of blood flow: modeling of the Fåhræus–Lindqvist effect’, *J. Biol. Phys.*, vol. 41, no. 3, pp. 313–326, Jun. 2015, doi: 10.1007/s10867-015-9376-1.
[235] Y. Ding *et al.*, ‘Simultaneous measurement of tissue oxygen level-dependent (TOLD) and blood oxygenation level-dependent (BOLD) effects in abdominal tissue oxygenation level studies: Simultaneous Measurement of TOLD and BOLD’, *J. Magn. Reson. Imaging*, vol. 38, no. 5, pp. 1230–1236, Nov. 2013, doi: 10.1002/jmri.24006.
[236] Y. Ohno, H. Hatabu, D. Takenaka, S. Adachi, M. Van Cauteren, and K. Sugimura, ‘Oxygen-Enhanced MR Ventilation Imaging of the Lung: Preliminary Clinical Experience in 25 Subjects’, *Am. J. Roentgenol.*, vol. 177, no. 1, pp. 185–194, Jul. 2001, doi: 10.2214/ajr.177.1.1770185.
[237] H. Zhou *et al.*, ‘Examining correlations of oxygen sensitive MRI (BOLD/TOLD) with [18F]FMISO PET in rat prostate tumors.’, *Am. J. Nucl. Med. Mol. Imaging*, vol. 9, no. 2, pp. 156–167, 2019.
[238] H. Hatabu *et al.*, ‘Pulmonary ventilation: dynamic MRI with inhalation of molecular oxygen’, *Eur. J. Radiol.*, vol. 37, no. 3, pp. 172–178, Mar. 2001, doi: 10.1016/S0720-048X(00)00298-9.
[239] E. R. Muir, D. P. Cardenas, and T. Q. Duong, ‘MRI of brain tissue oxygen tension under hyperbaric conditions’, *NeuroImage*, vol. 133, pp. 498–503, 2016, doi: 10.1016/j.neuroimage.2016.03.040.
[240] W.-J. Zhang, R. M. Niven, S. S. Young, Y.-Z. Liu, G. J. M. Parker, and J. H. Naish, ‘Dynamic oxygen-enhanced magnetic resonance imaging of the lung in asthma—Initial experience’, *Eur. J. Radiol.*, vol. 84, no. 2, pp. 318–326, Feb. 2015, doi: 10.1016/j.ejrad.2014.10.021.
[241] D. M. McGrath *et al.*, ‘Oxygen-induced changes in longitudinal relaxation times in skeletal muscle’, *Magn. Reson. Imaging*, vol. 26, no. 2, pp. 221–227, 2008, doi: 10.1016/j.mri.2007.06.011.
[242] J. Qian *et al.*, ‘In vivo Monitoring of Oxygen Levels in Human Brain Tumor Between Fractionated Radiotherapy Using Oxygen-enhanced MR Imaging’, *Curr. Med. Imaging Former. Curr. Med. Imaging Rev.*, vol. 16, no. 4, pp. 427–432, 2020, doi: 10.2174/1573405614666180925144814.
[243] A. Salem *et al.*, ‘Oxygen-enhanced MRI Is Feasible, Repeatable, and Detects Radiotherapy-induced Change in Hypoxia in Xenograft Models and in Patients with Non–small Cell Lung Cancer’, *Clin. Cancer Res.*, vol. 25, no. 13, pp. 3818–3829, 2019, doi: 10.1158/1078-0432.ccr-18-3932.
[244] E. Bluemke *et al.*, ‘Oxygen-enhanced MRI MOLLI T1 mapping during chemoradiotherapy in anal squamous cell carcinoma.’, *Clin. Transl. Radiat. Oncol.*, vol. 22, pp. 44–49, 2020, doi: 10.1016/j.ctro.2020.03.001.
[245] Q. Fan *et al.*, ‘Investigation of hypoxia conditions using oxygen-enhanced magnetic resonance imaging measurements in glioma models.’, *Oncotarget*, vol. 5, no. 0, pp. 31864–31875, 2017, doi: 10.18632/oncotarget.16256.
[246] J. O’Connor *et al.*, ‘Oxygen-Enhanced MRI Accurately Identifies, Quantifies, and Maps Tumor Hypoxia in Preclinical Cancer Models’, *Cancer Res.*, vol. 76, no. 4, pp. 787–795, 2016, doi: 10.1158/0008-5472.can-15-2062.

[247] A. R. Morgan *et al.*, ‘Feasibility assessment of using oxygen-enhanced magnetic resonance imaging for evaluating the effect of pharmacological treatment in COPD’, *Eur. J. Radiol.*, vol. 83, no. 11, pp. 2093–2101, 2014, doi: 10.1016/j.ejrad.2014.08.004.
[248] M. Boudreau, C. L. Tardif, N. Stikov, J. G. Sled, W. Lee, and G. B. Pike, ‘B 1 mapping for bias-correction in quantitative T 1 imaging of the brain at 3T using standard pulse sequences: B 1 Maps for Quantitative T 1’, *J. Magn. Reson. Imaging*, vol. 46, no. 6, pp. 1673–1682, 2017, doi: 10.1002/jmri.25692.
[249] T. Cao-Pham *et al.*, ‘Combined endogenous MR biomarkers to predict basal tumor oxygenation and response to hyperoxic challenge’, *NMR Biomed.*, vol. 30, no. 12, p. e3836, 2017, doi: 10.1002/nbm.3836.
[250] T.-T. Cao-Pham *et al.*, ‘Monitoring Tumor Response to Carbogen Breathing by Oxygen-Sensitive Magnetic Resonance Parameters to Predict the Outcome of Radiation Therapy: A Preclinical Study’, *Int. J. Radiat. Oncol.*, vol. 96, no. 1, pp. 149–160, 2016, doi: 10.1016/j.ijrobp.2016.04.029.
[251] R. R. Edelman, H. Hatabu, E. Tadamura, W. Li, and P. V. Prasad, ‘Noninvasive assessment of regional ventilation in the human lung using oxygen–enhanced magnetic resonance imaging’, *Nat. Med.*, vol. 2, no. 11, pp. 1236–1239, 1996, doi: 10.1038/nm1196-1236.
[252] R. A. Jones, M. Ries, C. T. W. Moonen, and N. Grenier, ‘Imaging the changes in renal T1 induced by the inhalation of pure oxygen: A feasibility study’, *Magn. Reson. Med.*, vol. 47, no. 4, pp. 728–735, 2002, doi: 10.1002/mrm.10127.
[253] L. E. Kershaw, J. H. Naish, D. M. McGrath, J. C. Waterton, and G. J. M. Parker, ‘Measurement of arterial plasma oxygenation in dynamic oxygen-enhanced MRI’, *Magn. Reson. Med.*, vol. 64, no. 6, pp. 1838–1842, 2010, doi: 10.1002/mrm.22571.
[254] Y. Kinoshita, K. Kohshi, N. Kunugita, T. Tosaki, and A. Yokota, ‘Preservation of tumour oxygen after hyperbaric oxygenation monitored by magnetic resonance imaging’, *Br. J. Cancer*, vol. 82, no. 1, pp. 88–92, 2000, doi: 10.1054/bjoc.1999.0882.
[255] R. Löffler *et al.*, ‘Optimization and evaluation of the signal intensity change in multisection oxygen-enhanced MR lung imaging’, *Magn. Reson. Med.*, vol. 43, no. 6, pp. 860–866, 2000, doi: 10.1002/1522-2594(200006)43:6<860::aid-mrm12>3.0.co;2-c.
[256] H. Uematsu *et al.*, ‘Changes in T1 and T2 Observed in Brain Magnetic Resonance Imaging With Delivery of High Concentrations of Oxygen’:, *J. Comput. Assist. Tomogr.*, vol. 31, no. 5, pp. 662–665, Sep. 2007, doi: 10.1097/rct.0b013e3180319114.
[257] D. Zhao *et al.*, ‘Dynamic oxygen challenge evaluated by NMR T1 and T2*–insights into tumor oxygenation.’, *NMR Biomed.*, vol. 28, no. 8, pp. 937–947, 2015, doi: 10.1002/nbm.3325.
[258] Y. Anzai, M. Ishikawa, D. W. W. Shaw, A. Artru, V. Yarnykh, and K. R. Maravilla, ‘Paramagnetic effect of supplemental oxygen on CSF hyperintensity on fluid-attenuated inversion recovery MR images’, *AJNR Am. J. Neuroradiol.*, vol. 25, no. 2, pp. 274–279, Feb. 2004.
[259] F. T. Braga, A. J. da Rocha, G. Hernandez Filho, R. K. Arikawa, I. M. Ribeiro, and R. B. Fonseca, ‘Relationship between the concentration of supplemental oxygen and signal intensity of CSF depicted by fluid-attenuated inversion recovery imaging’, *AJNR Am. J. Neuroradiol.*, vol. 24, no. 9, pp. 1863–1868, Oct. 2003.
[260] A. V. Deliganis, D. J. Fisher, A. M. Lam, and K. R. Maravilla, ‘Cerebrospinal Fluid Signal Intensity Increase on FLAIR MR Images in Patients under General Anesthesia: The Role of Supplemental O $_2$’, *Radiology*, vol. 218, no. 1, pp. 152–156, Jan. 2001, doi: 10.1148/radiology.218.1.r01ja43152.
[261] C. Frigon, D. S. Jardine, E. Weinberger, S. R. Heckbert, and D. W. W. Shaw, ‘Fraction of Inspired Oxygen in Relation to Cerebrospinal Fluid Hyperintensity on FLAIR MR Imaging of the Brain in Children and Young Adults Undergoing Anesthesia’, *Am. J. Roentgenol.*, vol. 179, no. 3, pp. 791–796, Sep. 2002, doi: 10.2214/ajr.179.3.1790791.
[262] C. Frigon, D. W. W. Shaw, S. R. Heckbert, E. Weinberger, and D. S. Jardine, ‘Supplemental Oxygen Causes Increased Signal Intensity in Subarachnoid Cerebrospinal Fluid on Brain FLAIR MR Images Obtained in Children during General Anesthesia’, *Radiology*, vol. 233, no. 1, pp. 51–55, Oct. 2004, doi: 10.1148/radiol.2331031375.
[263] S. Petcharunpaisan, ‘Arterial spin labeling in neuroimaging’, *World J. Radiol.*, vol. 2, no. 10, p. 384, 2010, doi: 10.4329/wjr.v2.i10.384.
[264] J. Chaganti, H. Woodford, S. Tomlinson, S. Dunkerton, and B. Brew, ‘Black blood imaging of intracranial vessel walls’, *Pract. Neurol.*, vol. 21, no. 2, pp. 101–107, Apr. 2021, doi: 10.1136/practneurol-2020-002806.
[265] V. Gulani and N. Seiberlich, ‘Quantitative MRI: Rationale and Challenges’, in *Advances in Magnetic Resonance Technology and Applications*, vol. 1, N. Seiberlich, V. Gulani, F.

Calamante, A. Campbell-Washburn, M. Doneva, H. H. Hu, and S. Sourbron, Eds. Academic Press, 2020, pp. xxxvii–li. doi: 10.1016/B978-0-12-817057-1.00001-9.
[266] L. R. Berry *et al.*, 'Quantification of viable tumor microvascular characteristics by multispectral analysis', *Magn. Reson. Med.*, vol. 60, no. 1, pp. 64–72, Jul. 2008, doi: 10.1002/mrm.21470.
[267] M. D. Blackledge *et al.*, 'Supervised Machine-Learning Enables Segmentation and Evaluation of Heterogeneous Post-treatment Changes in Multi-Parametric MRI of Soft-Tissue Sarcoma', *Front. Oncol.*, vol. 0, 2019, doi: 10.3389/fonc.2019.00941.
[268] E. C. Henning, C. Azuma, C. H. Sotak, and K. G. Helmer, 'Multispectral quantification of tissue types in a RIF-1 tumor model with histological validation. Part I', *Magn. Reson. Med.*, vol. 57, no. 3, pp. 501–512, Mar. 2007, doi: 10.1002/mrm.21161.
[269] P. Katiyar *et al.*, 'A Novel Unsupervised Segmentation Approach Quantifies Tumor Tissue Populations Using Multiparametric MRI: First Results with Histological Validation', *Mol. Imaging Biol.*, vol. 19, no. 3, pp. 391–397, Jun. 2017, doi: 10.1007/s11307-016-1009-y.
[270] T. Torheim *et al.*, 'Cluster analysis of dynamic contrast enhanced MRI reveals tumor subregions related to locoregional relapse for cervical cancer patients', *Acta Oncol. Stockh. Swed.*, vol. 55, no. 11, pp. 1294–1298, Nov. 2016, doi: 10.1080/0284186X.2016.1189091.
[271] P. Wang, A. Popovtzer, A. Eisbruch, and Y. Cao, 'An approach to identify, from DCE MRI, significant subvolumes of tumors related to outcomes in advanced head-and-neck cancer', *Med. Phys.*, vol. 39, no. 8, pp. 5277–5285, Aug. 2012, doi: 10.1118/1.4737022.
[272] F. Moosvi, J. H. E. Baker, A. Yung, P. Kozlowski, A. I. Minchinton, and S. A. Reinsberg, 'Fast and sensitive dynamic oxygen-enhanced MRI with a cycling gas challenge and independent component analysis.', *Magn. Reson. Med.*, vol. 81, no. 4, pp. 2514–2525, 2018, doi: 10.1002/mrm.27584.
[273] C. Cortes and V. Vapnik, 'Support-vector networks', *Mach. Learn.*, vol. 20, no. 3, pp. 273–297, Sep. 1995, doi: 10.1007/BF00994018.
[274] L. I. Cárdenas-Navia, D. Mace, R. A. Richardson, D. F. Wilson, S. Shan, and M. W. Dewhirst, 'The Pervasive Presence of Fluctuating Oxygenation in Tumors', *Cancer Res.*, vol. 68, no. 14, pp. 5812–5819, Jul. 2008, doi: 10.1158/0008-5472.CAN-07-6387.
[275] T. J. Dunn *et al.*, 'The effects of hyperoxic and hypercarbic gases on tumour blood flow', *Br. J. Cancer*, vol. 80, no. 1–2, pp. 117–126, Apr. 1999, doi: 10.1038/sj.bjc.6690330.